Excitations avec texture de spin et de pseudospin dans le graphène

par

Wenchen Luo

Thèse présentée au Département de physique en vue de
l'obtention du grade de Docteur ès sciences (Ph.D.)

FACULTÉ DES SCIENCES
UNIVERSITÉ DE SHERBROOKE

Sherbrooke, Québec, Canada, 22 août 2014

Spin and pseudospin textured excitations in graphene

by

Wenchen Luo

A thesis submitted to the physics department in
accordance with the requirements of the degree of
Doctor of Philosophy in the Faculty of Science.

FACULTÉ DES SCIENCES
UNIVERSITÉ DE SHERBROOKE

Sherbrooke, Québec, Canada, August 22, 2014

Le 22 août 2014

le jury a accepté la thèse de Monsieur Wenchen Luo dans sa version finale.

Membres du jury

Professeur René Côté
Directeur de recherche
Département de physique

Professeur Mario Poirier
Membre interne
Département de physique

Professeur Arun Paramekanti
Membre externe
Département de physique
University of Toronto

Professeur Alexandre Blais
Président rapporteur
Département de physique

To my family

Résumé

Nous étudions dans cette thèse plusieurs propriétés du gaz d'électrons bidimensionnel (GE2D) dans le graphène et la bicouche de graphène (BG). Nous commençons par étudier la nature des excitations à une particule du GE2D dans le graphène près des facteurs de remplissage entiers dans les niveaux de Landau $N \neq 0$. Nous utilisons une approche de type Hartree-Fock (HF) pour comparer l'énergie de l'excitation d'une paire électron-trou à celle d'une paire skyrmion (SK)-antiskyrmion (ASK). Dans le graphène, les excitations SK et ASK sont des excitations chargées avec une texture de spin et/ou de pseudospin de vallée qui est quantifiée topologiquement. Nos calculs montrent que les paires SK-ASK sont les excitations chargées de plus basse énergie jusqu'au niveau de Landau $|N| = 3$. Notre approche permet en plus de calculer le domaine de couplage Zeeman pour lequel les paires SK-ASK sont les excitations de plus basse énergie et de déterminer comment l'énergie de ces paires est modifiée par les corrections d'écrantage.

Le diagramme de phase du GE2D dans la bicouche de graphène a fait l'objet d'intenses recherches théoriques et expérimentales [8, 13, 15, 16], mais jusqu'à maintenant, seuls les états uniformes ont été considérés. Nous adaptons notre approche HF à l'étude des états non uniformes pour montrer que le GE2D dans la BG à remplissage $\nu = -1$ dans le niveau de Landau $N = 0$ subit une série de transitions de phase lorsqu'un champ électrique perpendiculaire à la BG est appliqué. Nous étudions tout particulièrement les phases comportant une texture de pseudospin orbital soit un cristal de skyrmions et une phase spirale. Nous calculons les modes collectifs de ces phases ainsi que leur absorption électromagnétique. Nous poursuivons ensuite avec une étude des phases cristallines autour de certains remplissages entiers dans la BG.

Le GE2D dans la bicouche de graphène a principalement été étudié dans le niveau de Landau $N = 0$. Comme dernier problème, nous étudions le diagramme de phase lorsqu'un nombre entier de niveaux de Landau est occupé dans les niveaux supérieurs

$|N| > 0$. Alors que l'état fondamental du GE2D dans le graphène pour ces mêmes niveaux est un ferroaimant de Hall quantique (FHQ) avec une symétrie SU(2) pour le spin (en l'absence de couplage Zeeman) et le pseudospin de vallée, le GE2D dans la BG a plutôt un comportement FHQ de type Ising avec une symétrie Z_2 à champ électrique nul. Cette différence de comportement a une grande influence sur la nature des transitions de phase possibles ainsi que sur celle des excitations topologiques.

Abstract

In this thesis, we study several properties of the two-dimensional electron gas (2DEG) in graphene and bilayer graphene. We first study the nature of the single-particle excitations in graphene near integer filling factors in Landau levels (LLs) $N \neq 0$. We use a Hartree-Fock approach to compare the energy of an electron-hole excitation pair with that of a Skyrmion-antiskyrmion pair. In graphene, Skyrmions are charged excitations with a topological quantized spin and/or valley pseudo-spin texture. We give the range of Zeeman coupling for which Skyrmion-antiskyrmion has the lowest energy up to LL $N = 3$. Then we discuss how screening corrections modifies these results.

The phase diagram of the 2DEG in bilayer graphene had been studied previously by a number of authors [8, 13, 15, 16] but only uniform states had been considered. Extending the Hartree-Fock approach to non-uniform states, we show that at filling factor $\nu = -1$ in LL $N = 0$, the 2DEG goes through a series of phase transitions as the bias from an external electric field between two layers is increased. We study a crystal phase with orbital SK textures and a spiral state with the orbital pseudospin rotating in space. We compute the collective mode of these phases and their signatures in electromagnetic absorption experiments. We finally extend the Hartree-Fock approach to study the crystal states with valley or orbital textures near integer filling factors. The research on the 2DEG in bilayer graphene has been focussed almost exclusively in LL $N = 0$. As our last problem, we study the phase diagram at quarter and half fillings of the quartet of states in LLs $|N| > 0$. While the ground state of the 2DEG in graphene in $|N| > 0$ is a valley and spin quantum Hall ferromagnet with SU(2) symmetry in the absence of Zeeman coupling, the ground state in bilayer graphene is an Ising quantum Hall ferromagnet with a Z_2 valley symmetry at zero bias. We note that this change has important consequences on the nature of the transport properties and the single-particle excitations at integer fillings.

Acknowledgement

I would like to thank my supervisor Prof. René Côté for his enthusiastic help on my research work and study. I also appreciate his revision of this thesis in content and grammar.

The calculation time is provided by Mammouth, and I have received fruitful help from Dr. Huizhong Lu whom I thank for teaching programming arithmetic. I would like to thank my friends, the team members of Prof. Côté's group, for their helpful discussions.

I also would like to thank my parents, uncle and aunt. Without their help, I could not have reached Canada to continue my studies. My uncle and aunt who live in Sherbrooke also give me much help in my daily life. I appreciate them very much.

At last, I particularly appreciate my wife Juan Zhang, since a lot of help in life comes from her. This thesis can not be achieved smoothly without her lovely care.

Contents

List of Figures

Introduction

Graphene, isolated in 2004 [1], is almost an exact 2-dimensional (2D) system, although there are small ripples on its surface to avoid the collapse of the 2D lattice due to Mermin-Wagner theorem [2]. In this thesis, the third dimension in the system is neglected, so that the carbon atoms form a 2D honeycomb structure and each carbon atom has three σ bonds linking to its neighbors. The last electron in a carbon atom forms a π bond which allows electron to hop between adjacent sites.

In the tight-binding approximation, we only consider electron hopping between the nearest neighbor sites. It then follows that electrons in graphene must be described by the massless Dirac equation and have relativistic properties. The wave function of an electron is a two-component spinor $\begin{pmatrix} \alpha & \beta \end{pmatrix}^T$ in the basis $|A\rangle, |B\rangle$ of the two sublattices of the honeycomb lattice. The electron has chirality since the direction of sublattice pseudo-spin (the angle between the two complex numbers α and β) must be parallel or anti-parallel to its momentum. So the electron gas in graphene is a chiral 2-dimensional electron gas (C2DEG). The chirality plays an important role in the transport properties of graphene [3]. Moreover, the large mobility of electrons make it possible to observe the quantum Hall effect in graphene [4].

In the presence of a magnetic field, the conduction and valence bands of the C2DEG in graphene are quantized into a series of Landau levels $N = 0, \pm 1, \pm 2 \ldots$. In each Landau level (LL), there are four levels because an electron is described by its valley and spin indices. The quantum Hall effect can be observed [5], at room temperature [6] because of the large LL gap and the high electronic mobility. The Hall conductivity is quantized as $\sigma_{xy} = 4(N + 1/2)\frac{e^2}{h}$ [8]. This is different from the quantization $\sigma = 2N\frac{e^2}{h}$ measured in a semiconductor 2-dimensional electron gas (2DEG). The factor 4 comes from the four degeneracy of a LL. In this thesis, we concentrate on the transport properties of graphene in the quantum Hall regions.

We study three aspects of graphene and bilayer graphene (BLG):

> 1) The quasi-particles and topological excitations with spin and/or valley textures in higher LL of graphene at finite Zeeman coupling;
>
> 2)A variety of non-uniform states of the C2DEG in BLG near/at filling factors $\nu = -1, 3$ of LL $N = 0$ where the "orbital" pseudo-spin (a concept we will define later) rotates in space;
>
> 3) The quasi-particles and topological excitations with valley and/or spin texture in higher LLs of BLG and the phase diagram of the 2DEG at integer fillings of these LLs.

Thus, our thesis is concerned with the study of various kinds of topological excitations where the texture is that of spin, valley pseudo-spin, or "orbital" pseudo-spin.

Skyrmion excitations (part 1 above) in graphene has been studied before but only at zero Zeeman coupling [9] or in the form of crystal (skyrmion crystal [38]). Extending the calculation to finite Zeeman coupling requires a new technique.

The phase diagram of the 2DEG for $N = 0$ is the subject of intense research, both theoretical and experimental [8,15,16]. However, our study of the modulated states (part 2) is completely new.

The phase diagram of the 2DEG and its excitations in $|N| > 0$ of BLG (part 3) have not been studied before.

The charged excitations in a quantum Hall system are related to the transport gap Δ_{trans}. Basically, the charged excitation states are obtained by removing or adding one charge from the ground state. The transport gap is obtained by summing the excitation energies of two infinitely separated charged excitations, one consisting in removing one charge and the other one consisting in adding one charge. The transport experiments measure the resistivity $R_{xx} \propto e^{-\Delta_{trans}/(k_B T)}$, where k_B is the Boltzman constant and T is the temperature. Because different types of excitations have different energies, the nature of the charged excitations can be explored by measuring the transport gap.

The simplest case of charged excitation is when an electron or a hole is added to the ground state. More complex charged excitations consist of electron or hole carrying a spin (as we will explain later) or a pseudo-spin texture. An example of textured excitation is a skyrmion which is a solution of the nonlinear σ model (NLσM) which is derived by considering only the Fock interaction in the Hamiltonian. The skyrmion is a topological soliton with a texture that carries a topological charge. In the quantum Hall region, this topological charge is related to the electric charge. The skyrmion is thus a charged excitation, and contains vortex-like spin or pseudo-spin texture. The (pseudo-)spin texture of a skyrmion is such that neighboring spins are almost parallel. This decreases the Coulomb energy and may make the skyrmion energetically more favorable than the bare quasi-particle excitation. To compute the skyrmion energy, we may use the NLσM.

At some integer filling factors, the ground state of the C2DEG has all the spin or pseudo-spin aligned. This state is called a quantum Hall ferromagnet (QHF). The QHF, essentially, is induced by the nature of the exchange interaction of spin or psuedo-spin. There is no exchange interaction between different spins. So the spin must be polarized and be parallel to each other to minimum the exchange energy. In the lowest order of approximation, the excitations of this ground state can be described by the NLσM when the spin $\mathbf{S}$ or pseudo-spin $\mathbf{P}$ is mapped into a classical field $\mathbf{m}$.

The Lagrangian of the Nonlinear σ model (NLσM) [27] is written as:

$$L_{NL\sigma M} = \frac{\rho_s}{2}\int d\mathbf{r}\partial^{\mu}\mathbf{m}\cdot\partial^{\mu}\mathbf{m}, \tag{1}$$

where ρ_s is called spin stiffness and $\mathbf{m}$ is a unitary field, $|\mathbf{m}|^2 = 1$. The spin stiffness characterizes the strength to tilde the spin. Hence, the energy of a skyrmion must be related to this quantity.

The field $\mathbf{m}(\mathbf{r})$ could be the real spin or the valley pseudo-spin field in graphene. The static solutions of the Euler-Lagrangian equation in Eq. (1) are skyrmion and anti-skyrmion which are topological solitons. The skyrmion field can be given by

$$\begin{aligned} m_x(r,\theta) &= \frac{2k^Q r^Q}{r^{2Q}+k^{2q}}\cos(Q\theta), & (2)\\ m_y(r,\theta) &= \pm\frac{2k^Q r^Q}{r^{2Q}+k^{2Q}}\sin(Q\theta), & (3)\\ m_z(r,\theta) &= \frac{r^{2Q}-k^{2Q}}{r^{2Q}+k^{2Q}}, & (4)\end{aligned}$$

where k is related to the radius of the skyrmion, ± represent skyrmion and antiskyrmion respectively, and Q is the topological charge which is an integer defined by [27, 28] the Pontryagin index,

$$Q = \frac{1}{8\pi}\int d\mathbf{r}\epsilon_{abc}\epsilon_{ij}m_a\partial_i m_b\partial_j m_c, \tag{5}$$

where ϵ is the Levi-Civita symbol. Details can be found in Refs. [27] and [29]. The spin textures of a skyrmion and an anti-skyrmion can be found in Fig. 1. The excitation energy of skyrmion in the NLσM is given by [24, 27]

$$\Delta_{NL\sigma M} = 4\pi\rho_s. \tag{6}$$

In the NLσM of a classical field $\mathbf{m}$, the radius of a skyrmion can be arbitrary. But in an electron gas system, the size of a skyrmion is controlled by the classical Coulomb interaction and the Zeeman coupling. The Coulomb repulsive interaction makes the size of the skyrmion as large as possible. On the other hand, the Zeeman energy prevents the spin flipping. Spins are flipped as few as possible at finite Zeeman coupling.

The NLσM only includes partly the Fock interaction of the electron gas. When the Zeeman coupling is zero, the Hartree interaction can be cancelled by the positive background and the skyrmion is infinitely large, then the NLσM can deal with the skyrmion very well. At finite Zeeman coupling, the skyrmion is stabilized by the balance of Hartree, Fock and Zeeman energies. Then it must be described by the microscopic wavefunction. For example, a topological charge 1 skyrmion state can be written as $|SK\rangle = c^\dagger_{1,0}\prod_{m=0}(u_m c^\dagger_{0,m} + v_{m+1}c^\dagger_{1,m+1})|0\rangle$, and the anti-skyrmion state as $|ASK\rangle = \prod_{m=1}(u_m c^\dagger_{0,m} + v_{m-1}c^\dagger_{1,m-1})|0\rangle$, where $c^\dagger_{i,m}$ is the creation operator of electron in state i ($i = 0, 1$ represents two spins or two pseudo-spins) at angular momenta m, and $|0\rangle$ is the vacuum state. The ground state is supposed to be $|GS\rangle = \prod_{m=0} c^\dagger_{0,m}|0\rangle$. The factors $|u_m|^2$ and $|v_m|^2$ represent the electron occupation of the different angular momentum states. We can clearly see that the added charge (electron or hole) flips electrons to level 1, if $v_m \neq 0$. If we set $v_m = 0$, the skyrmion state becomes just a usual electron excitation. In Fig. 1, it is shown that the spin projected to the $x - y$ plane rotates by 2π around the center of the skyrmion or the anti-skyrmion.

The skyrmion requires more than one spin flip ($v_m \neq 0$) to create the spin texture (rotation of the spin), in comparison with the quasi-particle state where only one spin is flipped. The spin texture of a skyrmion is also associated with the larger density modulation than that in a usual electron excitation, since the size of the skyrmion is related to the number of flipped spins. At zero Zeeman coupling, the size of a skyrmion is infinite, when the Coulomb repulsion is taken into account. At finite Zeeman coupling the size of a spin skyrmion (SSK) is restricted since a Zeeman energy must be paid when each spin is flipped. Hence, an optimal size of a SSK is obtained by balancing of the

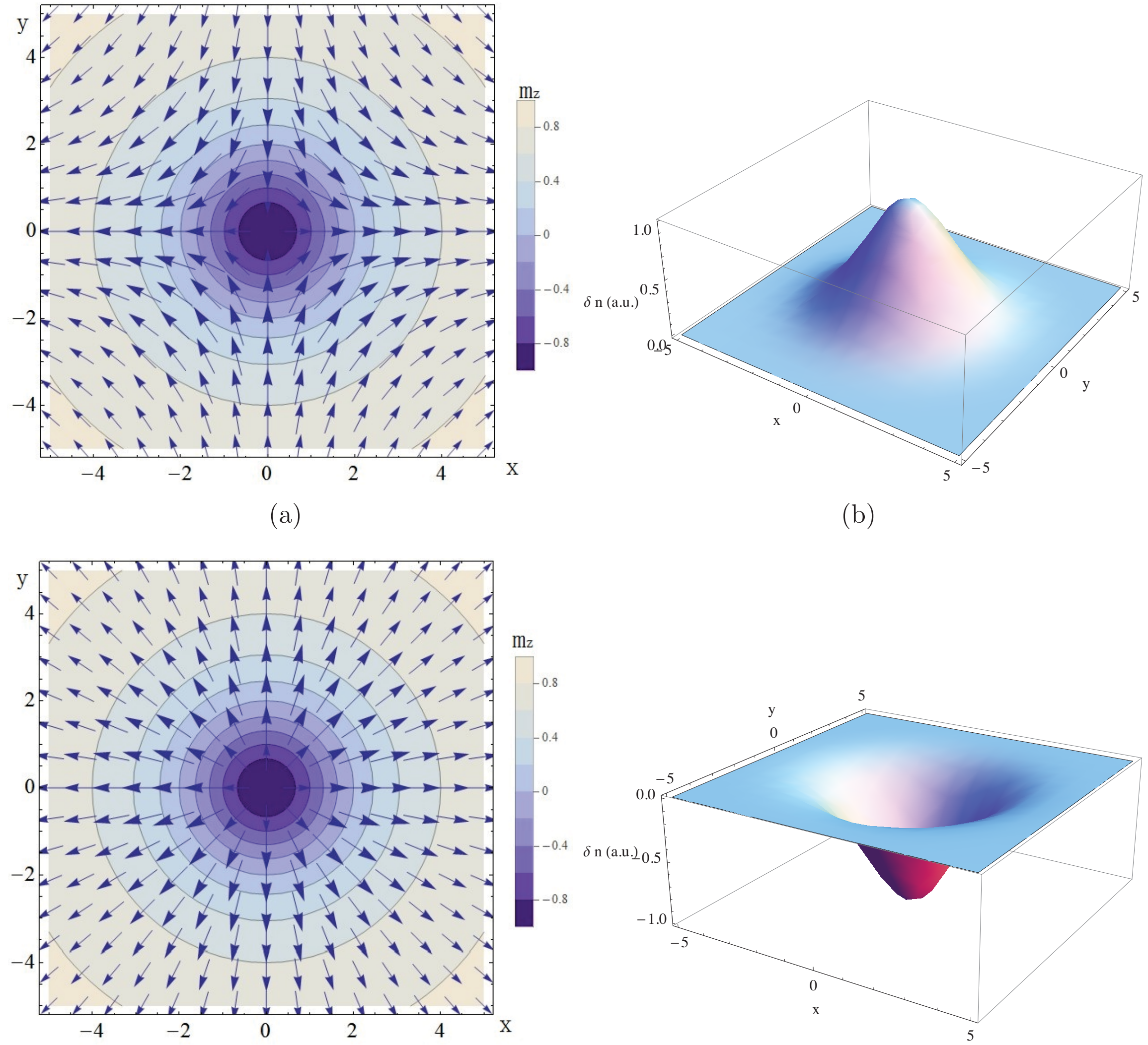

(a) (b)

(c) (d)

FIGURE 1: (a) The spin texture projected to the $x - y$ plane of a skyrmion, and (b) the density profile $\delta n = n_{skyrmion} - n_{groundstate}$ of a skyrmion. (c) The spin texture projected to the $x - y$ plane of an anti-skyrmion and (d) the density profile $\delta n = n_{antiskyrmion} - n_{groundstate}$ of an antiskyrmion. The color contours represent S_z.

Coulomb and Zeeman energies. The textured excitations obtained when considering the Zeeman and Coulomb interactions are no longer exact skyrmions. Nevertheless, in accord with the literature, we will continue to refer to them as “skyrmions”.

Spin skyrmions were first detected by a measurement of the Knight shift which is related to the magnetization of the 2DEG [10]. Moreover, the transport gap is due to the lowest energy excitation of the system at a given temperature. The energy of skyrmions and quasi-particles as a function of the Zeeman coupling are not the same. So the transport gap can be measured at different Zeeman energies to see if the charge excitations are skyrmions or quasi-particles.

In graphene, the valley degree of freedom makes possible to study a perfect valley skyrmion (VSK), since there is no energy gap between the two valleys. For a VSK [11], the valley pseudo-spin field instead of real spin characterizes the nature of the topological soliton. We show in this thesis that the VSK can exist at 1/4 and 3/4 fillings up to Landau level $N = 3$ [9], while the SSK exists only at $\nu = 1$ in the lowest Landau level (LLL) in a conventional semiconductor 2DEG.

We first compute the skyrmion energy by using the Hartree-Fock approximation for the Coulomb interaction. However, to better compare our studies of VSK at 1/4 and 3/4 fillings and the SSK at 1/2 filling with experiment [12], we also consider the LL screening which plays an important role to decrease the Coulomb interaction strength. Essentially, the screening is from the virtual transitions between full filled LLs and the empty (or partially filled) LLs. The LL gap which is given by the cyclotron frequency $\hbar\omega_c$ is of the order of 0.01eV and is much smaller than in a typical insulator. Hence, the Landau level screening is important.

The other system studied in this thesis is the Bernal stacked BLG. It contains richer physics than monolayer graphene, since it is possible to open a gap between two valleys by applying an external electric field. A unique property of BLG is that there are 8 degenerate levels in $N = 0$ due to the presence of an extra “orbital” degeneracy (that will be explained in the thesis) while the other LLs are four-time degenerate. In experiments, this is revealed by a jump in the quantized Hall conductivity σ_{xy} from $-4e^2/h$ to $+4e^2/h$.The ground states of the 2DEG in BLG depend on the electric bias Δ_B, the magnetic field B, the Zeeman coupling Δ_Z and the filling factors. A possible phase diagram at integer filling is presented in Ref. [13]. However, the ground state at some filling factors such as $\nu = 0$ is still the subject of controversy [8, 15, 16].

We know that a quantum Hall ferromagnet, in which all the electrons in the ground state share the same spin or pseudo-spin, in a conventional semiconductor 2DEG or in the C2DEG in graphene supports skyrmion excitations. In graphene bilayer, the orbital degree of freedom may also lead to orbital skyrmions. We have not found a way to compute the energy of an isolated orbital skyrmion for reason that will be explained in the thesis. We have thus decide to study the orbital skyrmion crystal phases instead.

At non integer filling factors, the excitations such as electron, hole or skyrmions can crystallize to form an electron or hole Wigner crystal or a skyrmion crystal. We study several crystal phases associated with valley and/or orbital pseudo-spin texture near integer filling factors. We find bubble orbital skyrmion crystals with charge $q = -e$ or $-2e$ per site at $\nu = 1.2, 3.2$, which are analogous to the bubble Wigner crystals existing in a conventional 2DEG in higher LLs [66]. The reason is intuitive: the orbital $n = 1$ in graphene bilayer is like the LL $N = 1$ in a conventional 2DEG. In a conventional 2DEG, the bubble crystals with charge up to $q = -(N+1)e$ per site exist in Landau level N. So the orbital skyrmion crystals in graphene bilayer support two types of bubbles: $q = -e$ and $-2e$ per site.

Meron, essentially, is half of a skyrmion. It has half-integer topological charge and electric charge. The spin texture of a meron is also vortex-like similar to a skyrmion, but the z component of the spin is zero at infinity. We find a checkerboard valley meron crystal at $\nu = 2.2$, which can be treated as the crystallization of the isolated VSK in orbital $n = 0$ plus another VSK crystal in orbital $n = 1$ [14]. At zero and small bias Δ_B between the two valleys, one skyrmion splits into two merons. So the VSK crystal evolves to a valley meron crystal.

In order to link our numerical studies of crystals to the real experiments, the local density of states (LDOS) is also calculated, since the LDOS can be related to scanning tunneling microscopy experiments.

At integer filling factors $\nu = -1, 3$, the Hamiltonian of the 2DEG contains a Dzyaloshinskii-Moriya (DM) interaction between the orbital pseudo-spin. The DM interaction is able to induce some non uniform phases in the ground state. We derive the phase diagram with respect to the bias, which contains the uniform liquid phase, the orbital skyrmion crystal phase, and the helical phase. In the last two phases, the orbital pseudo-spin is modulated in space. We describe the physics of these phases and in particular the competition between the Heisenberg exchange and the DM interactions.

To characterize the phase transition in the phase diagram, we study the density of states, collective modes and optical absorption. The collective modes of the crystal phases show a skyrmion-like pseudo-spin $x-y$ mode gapped by the DM interaction. And the absorption seems isotropic in the crystal phase. With the increase of the bias, the absorption peaks vary when the phase transition occurs, which might serve as a criterion to observe the phase transitions experimentally.

In higher LLs $N > 0$ in graphene bilayer, there are four-level degenerated (2-spin by 2-valley), which is the same as in monolayer graphene. However, the eigenvectors for each LL depend on the external bias Δ_B. This makes the system interesting and very different from other 2-dimensional systems. By comparison with monolayer graphene, the single-particle excitations in higher LLs in graphene bilayer are even more interesting, since the valley gap can be tuned by an electric field perpendicular to the sample.

We first study the ground states in LLs $N = 1, 2, 3$. The spin is always polarized at 1/4 and 3/4 fillings of a LL, so that we can neglect spin at these fillings. Our calculations show that all the electrons must be in only one valley and neither valley nor spin coherence exists. Particularly, at zero bias, the ground state selects one valley randomly, and the other valley is completely empty. Moreover, the two valleys are absolutely equivalent at zero bias. Hence, we conclude that the symmetry-broken ground state at 1/4 or 3/4 fillings in LLs $n > 0$ has a Z_2 symmetry. It is called an Ising valley quantum Hall ferromagnet (VQHF).

In such an Ising VQHF [79–82], the topological excitation of the VQHF are domain walls (as well as valley skyrmions). A domain wall separates two areas with opposite valley pseudo-spin polarizations. The domain walls increase the entropy of the system to lower the free energy at finite temperature. According to a theory presented in Ref. [80], along the center of a domain wall, a 1D channel where charge diffuses is formed. At very low temperature, the domain wall soup disappears or is very dilute. The charge diffusion in the 1D channel in a domain wall can not dissipate the transport charge. When the temperature is sufficiently high (below a critical temperature), the density of the domain wall soup is high enough, so that the domain walls could connect with each other and dissipate the transport charge. Above the critical temperature, the domain wall is as large as the size of the sample, so that the domain wall does not affect to the charge transport. This charge in dissipation gives rise to a resistance spike in R_{xx} that is detectable experimentally [81, 82]. In graphene bilayer, such resistance spikes are also observed [77].

The Ising behavior of the ground state at 1/4 and 3/4 fillings does not only exists in graphene bilayer. We demonstrate that it also exists at 1/4 and 3/4 fillings in any LL

$|N| > 0$ in chirally-stacked multi-layer graphene. Consequently, we predict that there is also a resistance spike in R_{xx} in these multi-layer graphene systems.

The phase diagram is richer at 1/2 filling of a LL in BLG. Both experiment and our numerical calculations indicate phase transitions between a spin-polarized state and a valley-polarized state when the bias is changed. At zero bias, the ground state is a spin-polarized state in which the $|K, \uparrow\rangle$ and $|K', \uparrow\rangle$ are full and the other two spin-down levels are empty (we suppose the magnetic field points up). In the spin language, $S_Z = 1/2(\langle\rho_{K,\uparrow}\rangle + \langle\rho_{K',\uparrow}\rangle - \langle\rho_{K,\downarrow}\rangle - \langle\rho_{K,\downarrow}\rangle) = 1/2$, where $\langle\rho_{i,j}\rangle$ represents the electron distribution in the level with valley index i and spin index j. At finite bias, the ground state will be converted to a valley pseudo-spin polarized state where $P_Z = 1/2(\langle\rho_{K,\uparrow}\rangle + \langle\rho_{K,\downarrow}\rangle - \langle\rho_{K',\uparrow}\rangle - \langle\rho_{K',\downarrow}\rangle) = \pm 1/2$ (the ± depends on the magnetic field, dielectric constant and LL index). Therefore, the C2DEG in graphene bilayer is a system where the (pseudo-)spin can be controlled by external electric field. The reason why these phase transitions occur can be simply explained by a minimization of the total energy.

Once the ground states are determined, we can study the charged excitations at 1/4 or 3/4 filling of a LL. The NLσM for spins in which we assume that no valley coherence exists is also applied to figure out that the SSK exists up to LL $N = 4$ in the absence of the Zeeman coupling. However, this NLσM is not enough to study the whole four levels. Moreover, the assumption of no valley coherence may be questioned. In such a $4-$level system, we must use the microscopic Hamiltonian to study a general CP^3 skyrmion [56] which mixes all the four levels and contains both spin and valley coherence in principle.

In the double quantum well, which is similar to the graphene bilayer and also has four levels in a LL (2 spins by 2 layers), the CP^3 skyrmion with both the spin and the layer pseudo-spin textures mixes all four levels in a LL. In general, we use the microscopic Hamiltonian to calculate the CP^3 skyrmion at finite Zeeman coupling and zero bias. Unexpectedly, the CP^3 skyrmion degenerates to a SSK without valley coherence at weak Zeeman coupling and to a VSK (only for $N = 1$) without spin coherence at strong Zeeman coupling, and there is no intermediate region between the SSK and the VSK containing the spin-valley mixed texture. For $N \geq 2$, the CP^3 skyrmion degenerates to a quasi-particle when the Zeeman coupling is large. This supports our assumption that we can neglect valley coherence in the NLσM for spins at small Zeeman coupling.

The VSK can not be obtained by the NLσM for valley pseudo-spin, since the ground state has a Z_2 symmetry for the two valleys. The spinor that describes an electronic state in BLG mixes different LL orbitals (see Eq. (1.33) in Chapter 1). It is thus, in some sense, surprising to find skyrmion excitation in BLG since it has been shown [62] that inter-LL skyrmions (charged excitation in a Ising QHF system where two LLs cross each other) are not the lowest-energy excitations.

To refine our calculation of the phase diagram in LL $|N| > 0$ of BLG, we consider the effect of screening. The Ising behavior of the ground states at $1/4$ and $3/4$ fillings of a LL does not changed. At $1/2$ filling of the LLs $N = \pm 1, \pm 2, \pm 3$, we compare the critical biases of the phase transitions calculated with and without screening. The critical bias with screening correction can explain the experiment qualitatively for $|N| > 0$. We also study how the screening changes the SSK in the NLσM.

Some of our works have been published. Chapter 2 is published in Ref. [29]. The works in Chapter 3 have been published in Refs. [59] and [70]. The papers for Chapter 4 are in preparation.

The thesis is organized as follow: In Chapter 1, the basic concepts and formalism related to the topics of this thesis are presented. Then we introduce the calculations of charged excitations in monolayer graphene in Chapter 2. The excitation energies of skyrmions and quasi-particles with Zeeman coupling and screening correction are calculated in order to compare with the experimental results. In Chapter 3, we study the pseudo-spin textured crystal phases in the LLL of graphene bilayer, as well as the density of states, collective modes and electromagnetic absorptions for experimental proposals. In the last chapter, both the ground states and the charged excitations in graphene bilayer in Landau level $N = 1, 2, 3$ are studied.

Chapter 1

Models and methods

Some basic concepts, models, and the theoretical methods which will be used widely in the thesis are introduced in this chapter.

1.1 Tight-binding model in monolayer graphene

In this section, we introduce the lattice structure of graphene and derive its band structure in the tight-binding approximation. For a general review of the properties of graphene, see, for example, Refs. [8,15,16].

Graphene has a 2-dimensional honeycomb lattice of carbon atoms as shown in Fig. 1.1. There are two carbon atoms per unit cell, which we denote by A (the red dots) and B (the blue dots) in Fig. 1.1. The set of all red or blue dot forms a triangular lattice, of which the basis vectors $\mathbf{a_1}$ and $\mathbf{a_2}$ are in the plane xOy. We choose the atoms A as our triangular lattice whose basis vectors are:

$$\mathbf{a_1} = a_0 \left(\frac{1}{2}, -\frac{\sqrt{3}}{2} \right), \tag{1.1a}$$

$$\mathbf{a_2} = a_0 \left(1, 0 \right), \tag{1.1b}$$

where $a_0 = \sqrt{3}c$, and $c = 1.42\text{Å}$ is the distance between two nearest-neighbor atoms. $\delta_1 = (1/2a_0, 1/(2\sqrt{3})a_0)$, $\delta_2 = (-1/2a_0, 1/(2\sqrt{3})a_0)$, $delta_3 = 0, -a_0$. The reciprocal

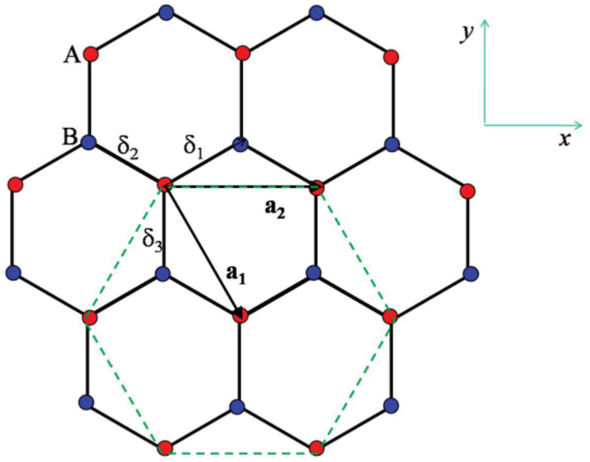

FIGURE 1.1: Graphene crystal lattice. The carbon atoms can be separated into two kinds of atoms in a unit cell. Red dots are classified as atoms A and blue dots are classified as atoms B. Each red atom is linked to its three nearest neighbors by the vectors $\boldsymbol{\delta_1}, \boldsymbol{\delta_2}, \boldsymbol{\delta_3}$.

lattice vectors are given by:

$$\mathbf{b_1} = \frac{2\pi}{a_0}\left(1, \frac{1}{\sqrt{3}}\right), \tag{1.2a}$$

$$\mathbf{b_2} = \frac{2\pi}{a_0}\left(0, -\frac{2}{\sqrt{3}}\right), \tag{1.2b}$$

which is also a regular hexagonal lattice as shown in Fig. 1.2. The first Brillouin zone is the smaller regular hexagon plotted in Fig. 1.2. In the first Brillouin zone, there are two inequivalent points respectively, K and K'. Each K or K' point can be translated to other equivalent K or K' by a combination of the basis vectors of the reciprocal lattice. We choose:

$$\mathbf{K} = \frac{2\pi}{a_0}\left(-\frac{2}{3}, 0\right), \tag{1.3a}$$

$$\mathbf{K}' = \frac{2\pi}{a_0}\left(+\frac{2}{3}, 0\right). \tag{1.3b}$$

Each carbon atom has 4 valence electrons. In graphene, three sp^2 electrons bind covalently with the three nearest neighbor C atoms to form three σ bonds. The last valence electron, in the p_z orbital, makes π bond with other p_z electrons. These electrons are less

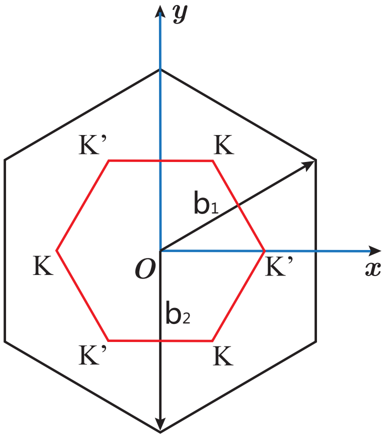

FIGURE 1.2: Reciprocal lattice with lattice vectors $\{\mathbf{b_1}, \mathbf{b_2}\}$ and the first Brillouin zone represented by the red regular hexagon.

localized than the other three sp^2 electrons, and are responsible for the conductivity of graphene. In the simplest model of graphene, we only consider the hopping of π electrons between nearest-neighbor atoms in the tight binding approximation. In this case, we can write the tight-binding hamiltonian as:

$$H = -t \sum_{i,j} \left(a_i^\dagger b_j + h.c. \right), \tag{1.4}$$

where $t \approx 2.8$ eV is the coupling constant between the two nearest-neighbor C atoms in the p_z orbital. The value of the second and third nearest neighbors coupling parameters are 0.1eV and 0.07eV respectively. The are very small in comparison with the first nearest-neighbor hopping. The symbol a_i denotes the annihilation operator of an electron on site A on lattice site i and b_j denotes the annihilation operator of an electron on site B at position j. Actually, a and b are fermion operators so that they satisfy the anti-commutation relation,

$$\left\{ c_i^\dagger, d_j \right\} = \delta_{c,d}\delta_{i,j} \tag{1.5}$$

$$\text{all others} = 0, \tag{1.6}$$

where c and d represent a or b. To analyze the system easily, we define the Fourier transformation of a and b:

$$c_{\mathbf{R_C}} = \frac{1}{\sqrt{N}} \sum_{\mathbf{k}} e^{i\mathbf{k}\cdot\mathbf{R_C}} c_{\mathbf{k}}, \tag{1.7}$$

where N is the total number of crystal sites, $c_{\mathbf{k}}$ is the annihilation operator in momentum space, $\mathbf{R_C}$ represents $\mathbf{R_A}$ for $c = a$, and $\mathbf{R_B}$ for $c = b$. $\mathbf{R_{A(B)}}$ is the coordinate vector for site $A(B)$. We have

$$\begin{aligned} \left\{c_{\mathbf{k}}^{\dagger}, c_{\mathbf{k}'}\right\} &= \delta_{\mathbf{k},\mathbf{k}'}, & (1.8) \\ \text{all others} &= 0. & (1.9) \end{aligned}$$

By a Fourier transformation, the tight binding hamiltonian can be written as,

$$H = \sum_{\mathbf{k}} \begin{pmatrix} a_{\mathbf{k}}^{\dagger} & b_{\mathbf{k}}^{\dagger} \end{pmatrix} \begin{pmatrix} 0 & \Lambda(\mathbf{k}) \\ \Lambda^{*}(\mathbf{k}) & 0 \end{pmatrix} \begin{pmatrix} a_{\mathbf{k}} \\ b_{\mathbf{k}} \end{pmatrix}, \tag{1.10}$$

where $\Lambda(\mathbf{k}) = -t \sum_{\delta} e^{i\mathbf{k}\cdot\delta}$.

Diagonalizing the Hamiltonian in Eq. (1.10), we obtain the band structure,

$$E(\mathbf{k}) = \pm t \sqrt{1 + 4\cos^2\left(\frac{k_x a}{2}\right) + 4\cos\left(\frac{k_x}{2} a\right)\cos\left(\frac{\sqrt{3}}{2} k_y a\right)}. \tag{1.11}$$

This is represented in Fig. 1.3(a). For pristine graphene, the Fermi level is at $E = 0$, the neutrality point. When the electronic doping is small and the Fermi level is close to the neutrality point, we can consider that the electronic properties are determined by electrons in the six valleys K, K' where the dispersion is linear in momentum space. That is

$$E(\mathbf{K}^{(\prime)} + \mathbf{k}) \approx \pm\frac{\sqrt{3}}{2} t |\mathbf{k}| a_0, \;\; (|\mathbf{k}| \ll |\mathbf{K}|), \tag{1.12}$$

where + is for the conduction band and − is for the valence band. This approximation is called the continuum model. In momentum space, the band structure is almost linear in momentum $\mathbf{k}$ near the six valley points at the corners of the Brillouin zone. We call the 6 cones at K and K' points the Dirac's cones because the dispersion relation near K and K' is that of a relativistic $E = \sqrt{p^2c^2 + m_0^2c^4} \to pc$ massless particle. The group

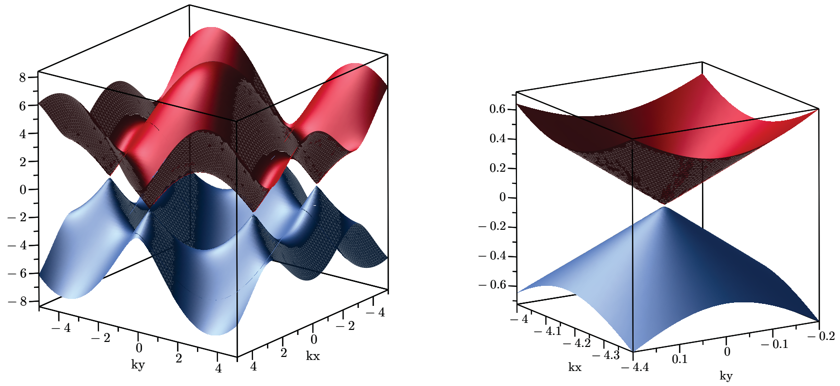

(a) (b)

FIGURE 1.3: (a) The dispersion relation of the energy bands of graphene. There are 6 valleys in the first Brillouin zone. (b) Near each valley, there is a Dirac cone, in which the dispersion relation is linear. The momenta are in units of $1/a_0$ and the energy is in units of eV.

velocity at points K or K' is given by

$$v_F = \frac{1}{\hbar}\frac{\partial E}{\partial |\mathbf{k}|} = \frac{\sqrt{3}}{2\hbar} t a_0. \tag{1.13}$$

It is about 1×10^6 m/s, i.e. 300 times smaller than the velocity of light. We can write the energy in terms of v_F and $|\mathbf{k}|$ as $E(\mathbf{k}) = \pm\hbar v_F |\mathbf{k}|$.

Around points $\mathbf{K}$ and $\mathbf{K}'$, the 2×2 matrix in Eq. (1.10) becomes

$$H_K(\mathbf{k}) = -\frac{\sqrt{3}}{2} a_0 t \begin{pmatrix} 0 & ke^{-i\theta} \\ ke^{i\theta} & 0 \end{pmatrix} = -\hbar v_F \begin{pmatrix} 0 & ke^{-i\theta} \\ ke^{i\theta} & 0 \end{pmatrix}, \tag{1.14a}$$

$$H_{K'}(\mathbf{k}) = +\frac{\sqrt{3}}{2} a_0 t \begin{pmatrix} 0 & ke^{i\theta} \\ ke^{-i\theta} & 0 \end{pmatrix} = +\hbar v_F \begin{pmatrix} 0 & ke^{i\theta} \\ ke^{-i\theta} & 0 \end{pmatrix}, \tag{1.14b}$$

where $\theta = \arctan\frac{p_y}{p_x}$. Hence, the total Hilbert space of the system is $\mathbf{K} \bigoplus \mathbf{K}'$. For the isolated K and K' valleys, the eigenfunctions are two-component spinors in the basis

$\{|A\rangle, |B\rangle\}$,

$$\phi_K = \frac{1}{\sqrt{2}} \begin{pmatrix} 1 \\ \mp e^{i\theta} \end{pmatrix}, \tag{1.15}$$

$$\phi_{K'} = \frac{1}{\sqrt{2}} \begin{pmatrix} 1 \\ \pm e^{-i\theta} \end{pmatrix}, \tag{1.16}$$

where the upper signs in both ± and ∓ are for the conduction band and the lower signs are for the valence band. The total wavefunctions including the two valleys are 4-component spinors.

In a pseudo-spin representation where site $|A\rangle \to |\uparrow\rangle$ and $|A\rangle \to |\downarrow\rangle$, the direction of the sublattice pseudo-spin in Eqs. (1.15) and (1.16) is either parallel or antiparallel to the momentum of the electron. This is the property of chirality. The electrons are thus chiral fermions in graphene, and we will refer to the 2DEG as the chiral 2DEG (C2DEG) in graphene.

If we introduce an external perpendicular magnetic field $\mathbf{B} = B\hat{\mathbf{z}}$, the canonical momentum operator $\mathbf{p}$ must be replaced by the covariant momentum $\mathbf{p} + e\mathbf{A}$ where $q = -e$ is the electron charge, and $\mathbf{A}$ is the vector potential of the magnetic field $\mathbf{B}$. The vector potential can be chosen arbitrarily. However, for convenience, we choose the Landau gauge $\mathbf{A} = (0, Bx, 0)$. For the single-particle excitations, which have a circular symmetry, we need to study the Hamiltonian in symmetric gauge $\mathbf{A} = (-\frac{1}{2}By, \frac{1}{2}Bx, 0)$.

It is well known that there are Landau levels with negative kinetic energies in graphene, unlike in a normal 2DEG. The conduction band of graphene is quantized into a series of positive Landau levels, while the valence band gives a series of negative Landau levels. At the Dirac point where the two bands touch each other, there is a LL with zero kinetic energy.

The solutions of the Hamiltonian of Eq. (1.14) in a magnetic field are the Landau levels and the associated wave functions. They are well-known and can be easily found in the literature [8, 15, 16]. In Landau gauge, the kinetic energies of Landau level N in the K valley is given by

$$E_N^K = \mathrm{sgn}(N) \frac{\sqrt{2}\hbar v_F}{\ell} \sqrt{|N|}. \tag{1.17}$$

The Hamiltonian is two-dimensional, so that there are two quantum numbers for the wave functions. One is the Landau level N, and the other is the guiding center X. Electrons do a cyclotron motion in a magnetic field, X is the center of this cyclotron oscillation.

The wave function spinor in the $\{|A\rangle, |B\rangle\}$ basis is then given by

$$\phi_{N,X}^{K}(\mathbf{r}) = \begin{pmatrix} 0 \\ h_0(\mathbf{r}) \end{pmatrix} \delta_{N,0} + \frac{1-\delta_{N,0}}{\sqrt{2}} \begin{pmatrix} -sgn(N)\, h_{|N|-1,X}(\mathbf{r}) \\ h_{|N|,X}(\mathbf{r}) \end{pmatrix}. \tag{1.18}$$

In the K' valley,

$$E_N^{K'} = sgn(N) \frac{\sqrt{2}\hbar v_F}{\ell} \sqrt{|N|}, \tag{1.19}$$

and the spinors are

$$\phi_{N,X}^{K'}(\mathbf{r}) = \begin{pmatrix} h_0(\mathbf{r}) \\ 0 \end{pmatrix} \delta_{N,0} + \frac{1-\delta_{N,0}}{\sqrt{2}} \begin{pmatrix} h_{|N|,X}(\mathbf{r}) \\ sgn(N)\, h_{|N|-1,X}(\mathbf{r}) \end{pmatrix}. \tag{1.20}$$

In the wave function spinors, we use the Landau level wave function for a normal 2DEG in the Landau gauge [17],

$$h_{n,X}(\mathbf{r}) = \frac{1}{\sqrt{L_y \ell \sqrt{\pi} 2^n n!}} e^{-iXy/\ell^2} e^{-\frac{1}{2}\frac{(x+X)^2}{\ell^2}} H_n\left(\frac{x+X}{\ell}\right), \tag{1.21}$$

where L_y is the y direction size of the sample, H_n is the Hermite polynomial of order n, and ℓ is the magnetic length

$$\ell = \sqrt{\frac{\hbar c}{eB}}. \tag{1.22}$$

In the symmetric gauge, the eigenenergies are the same as the ones in the Landau gauge. However, the guiding center index must be replaced by the angular momentum index. The wave functions for different Landau levels are given by

$$\phi_{N,m}^{K} = \begin{pmatrix} 0 \\ h_{0,m} \end{pmatrix} \delta_{N,0} + \frac{1-\delta_{N,0}}{\sqrt{2}} \begin{pmatrix} -sgn(N) h_{|N|-1,m} \\ h_{|N|,m} \end{pmatrix}, \tag{1.23a}$$

$$\phi_{N,m}^{K'} = \begin{pmatrix} h_{0,m} \\ 0 \end{pmatrix} \delta_{N,0} + \frac{1-\delta_{N,0}}{\sqrt{2}} \begin{pmatrix} h_{|N|,m} \\ sgn(N) h_{|N|-1,m} \end{pmatrix}, \tag{1.23b}$$

where the generalized angular momenta takes the values by $m = 0, 1, 2, ...$, and the real angular momenta is $M = m - n$ in the wave function h_n. The wave function of an

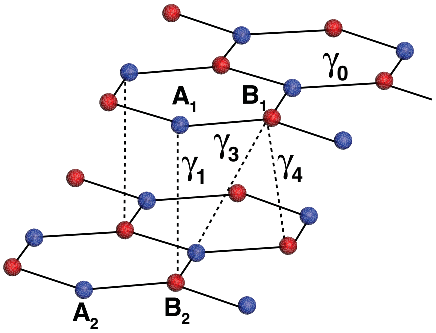

FIGURE 1.4: The crystal structure of a graphene bilayer in Bernal stacking. The numbers denote different layers. The dashed lines represent the hopping interactions: γ_0 is the intra layer nearest neighbor hopping; γ_1 links A_1 and B_2; γ_3 links A_2 and B_1; γ_4 links B_1 and B_2, or A_1 and A_2. Other interactions are much weaker, so they are neglected.

electron in the symmetric gauge is given by

$$h_{n,m}\left(\mathbf{r}\right)=\sqrt{\frac{\left(n+\frac{M-|M|}{2}\right)!}{\ell^{2}\pi 2^{|M|+1}(n+\frac{M+|M|}{2})!}}e^{-iM\varphi}\left(\frac{r}{\ell}\right)^{|M|}e^{-\frac{r^{2}}{4\ell^{2}}}L_{n+\frac{M-|M|}{2}}^{|M|}\left(\frac{r^{2}}{2\ell^{2}}\right), \tag{1.24}$$

where $L_a^b\left(x\right)$ is the Laguerre polynomial, and φ is the angle between $\mathbf{r}$ and the x axis.

An electron must be described by its spin and valley indices in addition to Landau level quantum numbers n, X (or n, m). In the absence of the Zeeman coupling, each level is fourfold degenerate. If we consider the Zeeman coupling, the spin degeneracy is lifted, but the valley degeneracy remains. If the symmetry of site A and site B is broken, then the valley degeneracy could be lifted. This symmetry breaking could be from the spin-orbital coupling. However, in graphene, the spin-orbital coupling of the π bond electron in carbon atom is so weak that the valley degeneracy can not be lifted.

1.2 Tight-binding models of bilayer graphene

We consider a bilayer graphene, i.e. a two-layer graphene with Bernal (or AB) stacking. The crystal structure is shown in Fig. (1.4). For the tight-biding approximation, we only consider the nearest neighbor intra-layer hopping $-\gamma_0 \sum_{\langle i,j \rangle} \left(a_{1i}^\dagger b_{1j} + a_{2i}^\dagger b_{2j} + h.c. \right)$, and inter layer hopping $-\gamma_1 \sum_i \left(a_{1i}^\dagger b_{2i} + h.c. \right)$, $-\gamma_4 \sum_{\langle i,j \rangle} \left(a_{1i}^\dagger a_{2j} + b_{1i}^\dagger b_{2j} + h.c. \right)$, $-\gamma_3 \sum_{\langle i,j \rangle} \left(b_{1i}^\dagger a_{2j} + h.c. \right)$, and the offset energy between sublattices in a layer $\Delta \sum_i \left(a_{1i}^\dagger a_{1i} + b_{2i}^\dagger b_{2i} \right)$. In monolayer graphene, the two sublattices are equivalent, so that there is no offset energy. However, in bilayer graphene, the offset energy represents that the sublattice symmetry is broken so that the electric charge distributes unequally on different sublattices. Here $\langle i, j \rangle$ represents the nearest neighbor pairs. a and b are the operators for sublattice A and B respectively. The number in their lower index means the order of the layer, 1 is the top layer and 2 is the bottom layer. If we couple a perpendicular electric field to the system, we get the bias term $\frac{\Delta_B}{2} \sum_i \left(a_{1i}^\dagger a_{1i} + b_{1i}^\dagger b_{1i} \right) - \frac{\Delta_B}{2} \sum_i \left(a_{2i}^\dagger a_{2i} + b_{2i}^\dagger b_{2i} \right)$, where Δ_B is the bias energy. The bias $\Delta_B = eEd$ is related to the perpendicular electric field E and the distance $d = 3.337\text{Å}$ between two layers. Combining all these terms, we get the full Hamiltonian in the momentum space (in basis $\{|A_1\rangle, |B_1\rangle, |A_2\rangle, |B_2\rangle\}$),

$$H = \sum_{\mathbf{k}} \begin{pmatrix} a_{1\mathbf{k}}^\dagger & b_{1\mathbf{k}}^\dagger & a_{2\mathbf{k}}^\dagger & b_{2\mathbf{k}}^\dagger \end{pmatrix} \begin{pmatrix} \frac{\Delta_B}{2} + \Delta & -\gamma_0 \Lambda & -\gamma_4 \Lambda^* & -\gamma_1 \\ -\gamma_0 \Lambda^* & \frac{\Delta_B}{2} & -\gamma_3 \Lambda & -\gamma_4 \Lambda^* \\ -\gamma_4 \Lambda & -\gamma_3 \Lambda^* & -\frac{\Delta_B}{2} & -\gamma_0 \Lambda \\ -\gamma_1 & -\gamma_4 \Lambda & -\gamma_0 \Lambda^* & \Delta - \frac{\Delta_B}{2} \end{pmatrix} \begin{pmatrix} a_{1\mathbf{k}} \\ b_{1\mathbf{k}} \\ a_{2\mathbf{k}} \\ b_{2\mathbf{k}} \end{pmatrix}, \tag{1.25}$$

where we use the Fourier transformation in Eq. (1.7) for the creation and annihilation operators, and $\Lambda = \sum_\delta e^{i\mathbf{k}\cdot\delta}$. The hopping parameters that we use in this thesis are $\gamma_0 = 3.12\text{eV}$, $\gamma_1 = 0.39\text{eV}$, $\gamma_4 = 0.12\text{eV}$, $\gamma_3 = 0.29\text{eV}$, and $\Delta = 0.0156\text{eV}$. (These values are discussed in Refs. [18–20]). Notice that the value of γ_0 in bilayer graphene is not the same as that in monolayer graphene.

We can diagonalize numerically the Hamiltonian in Eq. (1.25) to obtain its band structure. There are four bands since there are four atoms in a unit cell. Near the valley points, the bands are all quadratic (see for example Ref. [8]). We identify the four bands with the band index $b = 1, 2, 3, 4$ from high to low energy. The middle two bands touch each other at zero energy where the chemical potential lays if the system is without doping. The upper band has a gap γ_1 with the band 2, while the bottom band also has a gap γ_1 with band 3.

A finite bias Δ_B opens the gap between bands 2 and 3 at the neutrality point. When

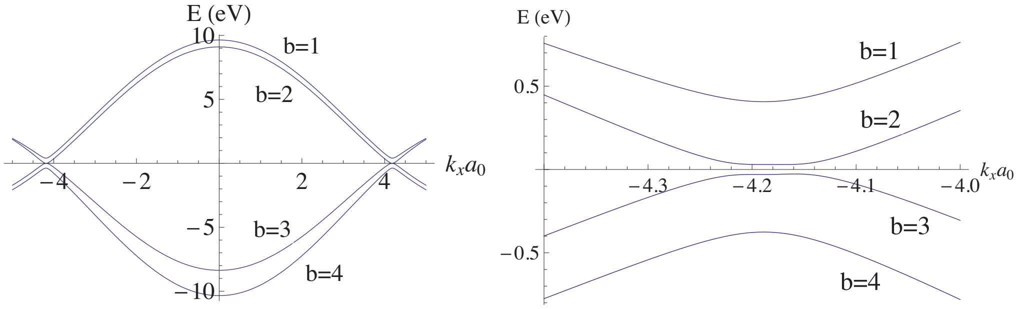

(a) (b)

FIGURE 1.5: (a) The dispersion relation of the energy bands of graphene bilayer along the line $k_y = 0$. The middle two bands touch each other at the K and K' points. (b) The gap between the middle two bands is opened by a bias $\Delta_B = 0.06$eV. The momenta are in units of $1/a_0$ and the energy is in units of eV.

this occurs, the middle two bands no longer touch each other. The bands along the line $k_y = 0$ are shown without bias in Fig. 1.5a, and with bias $\Delta_B = 0.06$eV in Fig. 1.5b. The γ_3 hopping creates a warping of the Fermi surface [21]. Usually, we can neglect the warping term which is the γ_3 hopping term. We will not consider this term in our analysis since it has only a very small effect in the presence of a magnetic field $B > 1$T [21, 76]. Our approximated four-band model without γ_3 is,

$$H = \begin{pmatrix} \frac{\Delta_B}{2} + \Delta & -\gamma_0\Lambda & -\gamma_4\Lambda^* & -\gamma_1 \\ -\gamma_0\Lambda^* & \frac{\Delta_B}{2} & 0 & -\gamma_4\Lambda^* \\ -\gamma_4\Lambda & 0 & -\frac{\Delta_B}{2} & -\gamma_0\Lambda \\ -\gamma_1 & -\gamma_4\Lambda & -\gamma_0\Lambda^* & \Delta - \frac{\Delta_B}{2} \end{pmatrix}. \tag{1.26}$$

If we look at the reciprocal lattice of bilayer graphene, we find that the first Brillouin zone is the same as that of the monolayer graphene (see Fig. 1.2). There are also two inequivalent valleys K and K'. For the same reason that we mentioned in the previous section, we only consider small momentum around the two valleys and so work in the continuum model. We obtain the Hamiltonians around K and K' valleys,

$$H = \begin{pmatrix} \frac{\Delta_B}{2} + \Delta & -\xi u_0 p e^{-\xi i\theta} & -\xi u_4 p e^{\xi i\theta} & -\gamma_1 \\ -\xi u_0 p e^{\xi i\theta} & \frac{\Delta_B}{2} & 0 & -\xi u_4 p e^{\xi i\theta} \\ -\xi u_4 p e^{-\xi i\theta} & 0 & -\frac{\Delta_B}{2} & -\xi u_0 p e^{-\xi i\theta} \\ -\gamma_1 & -\xi u_4 p e^{-\xi i\theta} & -\xi u_0 p e^{\xi i\theta} & \Delta - \frac{\Delta_B}{2} \end{pmatrix}, \tag{1.27}$$

where $\xi = 1$ for valley K, $\xi = -1$ for valley K', and

$$u_i = \gamma_i \frac{\sqrt{3}}{2\hbar} a_0. \tag{1.28}$$

Here the variable p represents the momentum of the electron and not its wave vector, and θ is the angle between the momentum and the x axis.

In presence of magnetic field, the momentum in the Hamiltonian in Eq. (1.27) must be replaced by the canonical one to obtain the LL structure.

1.2.1 Four-band model in the presence of a magnetic field

We have already derived the four-band model without the warping term γ_3 in the previous section. In presence of a magnetic field, as usual, the kinetic momentum $\mathbf{p}$ should be replaced by the canonical one, $\mathbf{P} = \mathbf{p} + \frac{e\mathbf{A}}{c}$, where vector potential $\mathbf{A}$ is defined in the Landau gauge. Since we know the non-interacting Hamiltonian in Eq. (1.27) (in the sublattice basis of $\{|A_1\rangle, |B_1\rangle, |A_2\rangle, |B_2\rangle\}$) without magnetic field, we can write the one in presence of a magnetic field in the K valley as,

$$H_K = \begin{pmatrix} \Delta + \frac{\Delta_B}{2} & iv_0 a & -iv_4 a^\dagger & -\gamma_1 \\ -iv_0 a^\dagger & \frac{\Delta_B}{2} & 0 & -iv_4 a^\dagger \\ iv_4 a & 0 & -\frac{\Delta_B}{2} & iv_0 a \\ -\gamma_1 & iv_4 a & -iv_0 a^\dagger & \Delta - \frac{\Delta_B}{2} \end{pmatrix}. \tag{1.29}$$

In the K' valley (also in the sublattice basis of $\{|A_1\rangle, |B_1\rangle, |A_2\rangle, |B_2\rangle\}$),

$$H_{K'} = \begin{pmatrix} \Delta + \frac{\Delta_B}{2} & iv_0 a & -iv_4 a^\dagger & -\gamma_1 \\ -iv_0 a^\dagger & \frac{\Delta_B}{2} & 0 & -iv_4 a^\dagger \\ iv_4 a & 0 & -\frac{\Delta_B}{2} & iv_0 a \\ -\gamma_1 & iv_4 a & -iv_0 a^\dagger & \Delta - \frac{\Delta_B}{2} \end{pmatrix}, \tag{1.30}$$

where we define

$$v_i = \gamma_i \sqrt{\frac{3}{2}} \frac{a_0}{\ell}, \tag{1.31}$$

and use the Landau level ladder operators a and $a^\dagger$

$$pe^{i\theta} = \frac{\sqrt{2}\hbar}{\ell} i a^\dagger, \tag{1.32a}$$

$$pe^{-i\theta} = -\frac{\sqrt{2}\hbar}{\ell} i a. \tag{1.32b}$$

To justify the approximation of neglecting the warping term γ_3, we remark that McCann and Fal'ko [21] have proved that the warping can be neglected in the effective two-component model (to be derived below) when the magnetic field is strong enough (> 1T). And also, for the four-band model, Côté and Barrette [76] have proved that both the eigenenergy and eigenvector are well approximated without γ_3 in the method of exact diagonalization of the full Hamiltonian when we only consider low Landau levels ($|N| < 10$).

To diagonalize the Hamiltonians in Eqs, (1.29) and (1.30), we use the eigenspinors

$$\begin{pmatrix} y_{1,n}^{K,b} h_{n-1}(\mathbf{r}) \\ y_{2,n}^{K,b} h_n(\mathbf{r}) \\ y_{3,n}^{K,b} h_{n-2}(\mathbf{r}) \\ y_{4,n}^{K,b} h_n(\mathbf{r}) \end{pmatrix}, \begin{pmatrix} y_{1,n}^{K',b} h_{n-1}(\mathbf{r}) \\ y_{2,n}^{K',b} h_{n-2}(\mathbf{r}) \\ y_{3,n}^{K',b} h_n(\mathbf{r}) \\ y_{4,n}^{K',b} h_n(\mathbf{r}) \end{pmatrix}$$

for the K and K' valley respectively, where we define $h_{n<0} = 0$. For $n = 0$, there is only one solution that we identify in the band $b = 3$. For $n = 1$, there are three solutions which are in bands $b = 1, 2, 4$, respectively. For $n > 1$, there are four solutions with band indices $b = 1, 2, 3, 4$. We explain these levels in Fig. 1.6.

Note that the LL index $N \in [0, \infty)$ in bands 1 and 2, while $N \in (-\infty, 0]$ in bands 3 and 4. This is because that the kinetic energies $E_N^{k,b}$, where k is the valley index, in bands 1 and 2 are positive, while the kinetic energies in bands 3 and 4 are negative at zero bias.

We notice that without magnetic field, there are four bands and the middle two bands touch each other at the center of the two valleys. In the presence of a magnetic field, this property still holds. It means that the lowest Landau levels of the middle two bands are very close to each other. In the last chapter, when we study the pseudo-spin textured coherence, we call them orbitals 0 and 1 in the lowest Landau level. In the four-band model, we thus use the index of band b to replace the orbital index, because different orbitals belong to different bands in the LL $N = 0$. We notice that the property of the

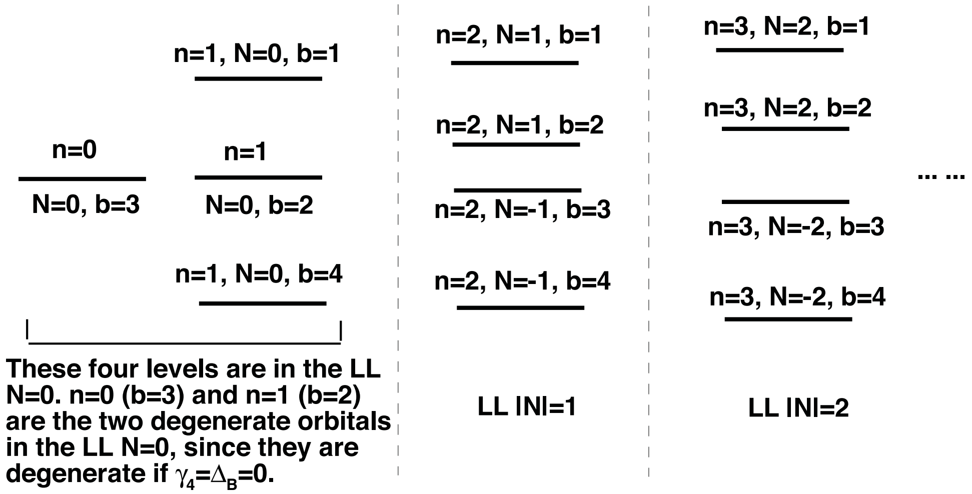

FIGURE 1.6: The schematic diagram of the solutions of the 4-band model. This schematic diagram is valid for both two valleys.

band-orbital corresponding is only valid in bilayer graphene. In *ABC* trilayer graphene, there are three obitals in $N = 0$, although two bands touch each other at zero energy.

Next, we can write all the wave function spinors in a uniform format. In the LL $N = 0$, we use $b = 1, 2, 3, 4$ to distinguish four orbitals in one valley, in which two are near zero-energy and the other two are far away from zero. In other LLs, $b = 1, 2$ belong to positive LL $|N|$ and $b = 3, 4$ belong to negative LL $-|N|$, and we define $E^{k,1}_{|N|} > E^{k,2}_{|N|} > E^{k,3}_{-|N|} > E^{k,4}_{-|N|}$ at zero bias. We conclude the eigenenergies and eigenvectors with band index b instead of orbital as follows:

$$\begin{aligned} \sigma &= (k,s,b) \\ k &: K=1, K'=-1 \\ \begin{pmatrix} y^{k,b}_{1,N} h_{|n|} \\ y^{k,b}_{2,n} h_{|n|+k-\delta_{n,0}\delta_{k,K}\delta_{b,3}} \\ y^{k,b}_{3,n} h_{|n|-k-\delta_{n,0}\delta_{k,K'}\delta_{b,3}} \\ y^{k,b}_{4,n} h_{|n|} \end{pmatrix} &\rightarrow E^{\sigma}_{n} = \frac{-(-1)^s}{2} E_z + k\frac{\Delta_B}{2} + E^{k,b}_{n}, \end{aligned} \tag{1.33}$$

where we have defined

$$h_{i<0} = 0. \tag{1.34}$$

1.2.2 Effective two-component model (2CM)

The four-band model is a solvable system. As we saw, however, the Hamiltonian is a 4×4 matrix and this complicates the calculations. McCann developed a reduced Hamiltonian to describe the system [21], which is called the effective two-component model. The reduced model not only keeps the middle two bands which are the most important when we consider the low energy excitations, but also integrates the information of the other two bands that are far away from the Fermi surface. The effective two-component model is valid for the lowest Landau level, but not for the higher LLs. An analysis of the validity of this model has been done in Ref. [76].

We give here the results of the effective two-component model including terms $\gamma_0, \gamma_1, \gamma_4$, Δ, Δ_B and dropping the warping term γ_3, since it does not affect to the band structure much in the presence of a strong magnetic field ($B \gtrsim 1$T). In the basis of $\{|A_2\rangle, |B_1\rangle\}$, the effective two-component Hamiltonian, in a magnetic field, is given by,

$$H_K = \begin{pmatrix} \frac{2\hbar^2}{\ell^2}\left[2\frac{u_0 u_4}{\gamma_1} + (\Delta + \Delta_B)\frac{u_0^2}{\gamma_1^2}\right] a a^\dagger - \frac{\Delta_B}{2} & \frac{2\hbar^2}{\ell^2}\frac{u_0^2}{\gamma_1} a^2 \\ \frac{2\hbar^2}{\ell^2}\frac{u_0^2}{\gamma_1}\left(a^\dagger\right)^2 & \frac{2\hbar^2}{\ell^2}\left[2\frac{u_0 u_4}{\gamma_1} - (\Delta_B - \Delta)\frac{u_0^2}{\gamma_1^2}\right] a^\dagger a + \frac{\Delta_B}{2} \end{pmatrix}, \tag{1.35}$$

$$H_{K'} = \begin{pmatrix} \frac{2\hbar^2}{\ell^2}\left[2\frac{u_0 u_4}{\gamma_1} + (\Delta + \Delta_B)\frac{u_0^2}{\gamma_1^2}\right] a^\dagger a - \frac{\Delta_B}{2} & \frac{2\hbar^2}{\ell^2}\frac{u_0^2}{\gamma_1}\left(a^\dagger\right)^2 \\ \frac{2\hbar^2}{\ell^2}\frac{u_0^2}{\gamma_1} a^2 & \frac{2\hbar^2}{\ell^2}\left[2\frac{u_0 u_4}{\gamma_1} - (\Delta_B - \Delta)\frac{u_0^2}{\gamma_1^2}\right] a a^\dagger + \frac{\Delta_B}{2} \end{pmatrix}. \tag{1.36}$$

In the LL $N = 0$, there are two degenerate eigenstates when Δ_B, γ_4 and Δ are all zero. We name the two degenerate eigenstates orbital 0 and 1, since the eigenvectors are related to the 0 and 1 Landau level wave functions h_0 and h_1, respectively. It follows that there is a 8-fold degeneracy of this LL when including spin and valley. Experimentally, the eightfold degeneracy of the LL is revealed by a jump in the quantized Hall conductivity from $-4(e^2/h)$ to $+4(e^2/h)$ when the charge density is tuned across neutrality in moderately disordered samples [22]. For finite $\Delta_B, \Delta, \gamma_4$, the energies of $n = 0, 1$ states are given by

$$E^{N=0}_{K,0} = \frac{\Delta_B}{2} \rightarrow \begin{pmatrix} 0 \\ h_0 \end{pmatrix}, \tag{1.37}$$

$$E^{N=0}_{K,1} = \frac{\Delta_B}{2} - \Delta_B\beta + \beta_4 + \Delta\beta \rightarrow \begin{pmatrix} 0 \\ h_1 \end{pmatrix}, \tag{1.38}$$

where we also gave the associated spinor in the $\{A_2, B_1\}$ basis. In the K' valley:

$$E^{N=0}_{K',0} = -\frac{\Delta_B}{2} \rightarrow \begin{pmatrix} h_0 \\ 0 \end{pmatrix}, \tag{1.39}$$

$$E^{N=0}_{K',1} = -\frac{\Delta_B}{2} + \Delta_B\beta + \beta_4 + \Delta\beta \rightarrow \begin{pmatrix} h_1 \\ 0 \end{pmatrix}. \tag{1.40}$$

In these eigenvectors, $h_n = h_n(\mathbf{r})$. From the eigenvectors, we find that the valley index is equivalent to layer index since the electrons in K valley are all on site B_1 of layer 1, while the electrons in K' valley are all on site A_2 of layer 1.

In the minimal model (i.e. $\Delta_B = \Delta = \gamma_4 = 0$) the LL energy spectrum is given by

$$E_N = \sqrt{N\,(N+1)}\hbar\omega_c^*, \tag{1.41}$$

where $\omega_c^* = \frac{\hbar}{m^*\ell^2}$ is the cyclotron frequency and the effective mass $m^* = \frac{2\hbar^2\gamma_1}{3a_0^2\gamma_0^2}$. This quantization has been observed experimentally [23].

In the effective two-component model, we integrate bands 1 and 4. The energies of the LL $N = 0$ in the 2CM are very close to these of the four-band model, and also to those of an exact diagonalization of the full Hamiltonian [76] that includes γ_3. But the energies of effective 2CM is far away from the four-band model in other LLs. And more, the first and last components in the wave function spinors are neglected in the 2CM, which is unacceptable sometimes. In summary, the effective two-component model is only reliable in $N = 0$ and it is necessary to use the four-band model in the case of higher LLs.

1.3 Many-body Hamiltonian in the Hartree-Fock approximation for graphene (monolayer)

The kinetic energy of the electrons is frozen in a Landau level of which the degeneracy is given by $N_\phi = \frac{m^* \omega_c^* S}{h} = \frac{S}{2\pi\ell^2}$ where S is the area of the sample. But the kinetic energy can not describe the system completely. The Coulomb interaction is also very important. Moreover, transport properties are closely related to the Coulomb interaction. To deal with Coulomb interaction, we write the second quantization Hamiltonian as,

$$U = \frac{1}{2}\sum_{\alpha,\beta} \int d\mathbf{r} d\mathbf{r}' \Psi_\alpha^\dagger(\mathbf{r}) \Psi_\beta^\dagger(\mathbf{r}') V(\mathbf{r}-\mathbf{r}') \Psi_\beta(\mathbf{r}') \Psi_\alpha(\mathbf{r}), \tag{1.42}$$

where α, β could be spin and valley indices, the field operator Ψ is defined by

$$\Psi_\alpha(\mathbf{r}) = \sum_{n,k} \phi_{\alpha,n,k}(\mathbf{r})\, c_{\alpha,n,k}, \tag{1.43}$$

with wave function $\phi_{\alpha,n,k}$ and annihilation operator $c_{\alpha,n,k}$ in LL n and guiding center k. The Coulomb potential is given by

$$V(\mathbf{r}-\mathbf{r}') = \frac{1}{S}\sum_{\mathbf{q}} \frac{2\pi e^2}{\kappa q} e^{i\mathbf{q}\cdot(\mathbf{r}-\mathbf{r}')} \equiv \frac{1}{S}\sum_{\mathbf{q}} V(\mathbf{q}) e^{i\mathbf{q}\cdot(\mathbf{r}-\mathbf{r}')}. \tag{1.44}$$

In the Hartree-Fock approximation (HFA), the Hamiltonian is given by the summation of the Hartree term U_H and the Fock term U_F,

$$\begin{aligned}
U &= U_H + U_F, && (1.45)\\
U_H &= \frac{1}{S}\sum_{\mathbf{q}} V(\mathbf{q}) \sum_{\alpha,\beta} \int d\mathbf{r} \int d\mathbf{r}' \left\langle \Psi_\alpha^\dagger(\mathbf{r}) \Psi_\alpha(\mathbf{r}) \right\rangle \Psi_\beta^\dagger(\mathbf{r}') \Psi_\beta(\mathbf{r}') e^{i\mathbf{q}\cdot(\mathbf{r}-\mathbf{r}')}, && (1.46)\\
U_F &= -\frac{1}{S}\sum_{\mathbf{q}} V(\mathbf{q}) \sum_{\alpha,\beta} \int d\mathbf{r} \int d\mathbf{r}' \left\langle \Psi_\alpha^\dagger(\mathbf{r}) \Psi_\beta(\mathbf{r}') \right\rangle \Psi_\beta^\dagger(\mathbf{r}') \Psi_\alpha(\mathbf{r}) e^{i\mathbf{q}\cdot(\mathbf{r}-\mathbf{r}')}. && (1.47)
\end{aligned}$$

We write the Hamiltonian in terms of creation and annihilation operators to obtain

$$\begin{aligned} U_H &= \frac{1}{S}\sum_{\mathbf{q}} V(\mathbf{q}) \sum_{\alpha,\beta} \sum_{n_1\cdots n_4} \sum_{k_1\cdots k_4} \int d\mathbf{r}\phi^*_{\alpha,n_1,k_1}(\mathbf{r})\, e^{i\mathbf{q}\cdot\mathbf{r}}\phi_{\alpha,n_2,k_2}(\mathbf{r}) \\ &\quad \int d\mathbf{r}'\phi^*_{\beta,n_3,k_3}(\mathbf{r}')\, e^{-i\mathbf{q}\cdot\mathbf{r}'}\phi_{\beta,n_4,k_4}(\mathbf{r}') \left\langle c^\dagger_{\alpha,n_1,k_1} c_{\alpha,n_2,k_2}\right\rangle c^\dagger_{\beta,n_3,k_3} c_{\beta,n_4,k_4}, \quad (1.48) \\ U_F &= -\frac{1}{S}\sum_{\mathbf{q}} V(\mathbf{q}) \sum_{\alpha\beta,ss'} \sum_{n_1\cdots n_4} \sum_{k_1\cdots k_4} \int d\mathbf{r}\phi^*_{\alpha,n_1,k_1}(\mathbf{r})\, e^{i\mathbf{q}\cdot\mathbf{r}}\phi_{\alpha,n_4,k_4}(\mathbf{r}) \\ &\quad \int d\mathbf{r}'\phi^*_{\beta,n_3,k_3}(\mathbf{r}')\, e^{-i\mathbf{q}\cdot\mathbf{r}'}\phi_{\beta,n_2,k_2}(\mathbf{r}') \left\langle c^\dagger_{\alpha,n_1,k_1} c_{\beta,n_2,k_2}\right\rangle c^\dagger_{\beta,n_3,k_3} c_{\alpha,n_4,k_4}. \quad (1.49) \end{aligned}$$

The integrals in U_H and U_F can be simplified by defining a function Ξ,

$$\int d\mathbf{r}\phi^*_{\alpha,n_1,k_1}(\mathbf{r})\, e^{i\mathbf{q}\cdot\mathbf{r}}\phi_{\beta,n_2,k_2}(\mathbf{r}) \equiv \Xi^{\alpha,\beta}_{n_1,n_2}(\mathbf{q})\,\delta_{k_1,k_2-q_y}. \quad (1.50)$$

We define the density matrix elements,

$$\rho^{\sigma,\sigma'}_{n,n'}(\mathbf{q}) \equiv \frac{1}{N_\phi}\sum_{k,k'} e^{-\frac{i}{2}q_x(k+k')\ell^2}\delta_{k,k'+q_y} c^\dagger_{\sigma,n,k} c_{\sigma',n',k'}, \quad (1.51)$$

and

$$c^\dagger_{\sigma,n,k} c_{\sigma',n',k'} = \sum_{\mathbf{p}} \rho^{\sigma,\sigma'}_{n,n'}(\mathbf{p})\, e^{\frac{i}{2}p_x(k+k')\ell^2}\delta_{k,k'+p_y}, \quad (1.52)$$

so that any phase of the system is well described by the average value $\langle\rho^{\sigma,\sigma'}_{n,n'}(\mathbf{q})$. All the coherences between electrons are given by these order parameters. Then we can write the Hartree and Fock terms in terms of density matrix elements,

$$\begin{aligned} U_H &= \frac{e^2}{\kappa\ell}\sum_{\mathbf{q}}\sum_{\alpha,\beta}\sum_{n_1\cdots n_4} H^{\alpha,\beta}_{n_1,n_2,n_3,n_4}(\mathbf{q}) \left\langle \rho^{\alpha,\alpha}_{n_1,n_2}(-\mathbf{q})\right\rangle \rho^{\beta,\beta}_{n_3,n_4}(\mathbf{q}), \quad (1.53) \\ U_F &= -\frac{e^2}{\kappa\ell}\sum_{\mathbf{q}}\sum_{\alpha,\beta}\sum_{n_1\cdots n_4} X^{\alpha,\beta}_{n_1,n_4,n_3,n_2}(\mathbf{q}) \left\langle \rho^{\alpha,\beta}_{n_1,n_2}(-\mathbf{q})\right\rangle \rho^{\beta,\alpha}_{n_3,n_4}(\mathbf{q}), \quad (1.54) \end{aligned}$$

where $H^{\alpha,\beta}_{n_1,n_2,n_3,n_4}$ and $X^{\alpha,\beta}_{n_1,n_4,n_3,n_2}$ are Hartree and Fock interaction functions respectively,

$$\begin{aligned} H^{\alpha,\beta}_{n_1,n_2,n_3,n_4}(\mathbf{q}) &= \frac{1}{2\pi\ell^2} V(\mathbf{q})\,\Xi^{\alpha,\alpha}_{n_1,n_2}(\mathbf{q})\,\Xi^{\beta,\beta}_{n_3,n_4}(-\mathbf{q}), \quad (1.55) \\ X^{\alpha,\beta}_{n_1,n_4,n_3,n_2}(\mathbf{q}) &= \frac{1}{S}\sum_{\mathbf{p}} V(\mathbf{p})\,\Xi^{\alpha,\alpha}_{n_1,n_4}(\mathbf{p})\,\Xi^{\beta,\beta}_{n_3,n_2}(-\mathbf{p})\, e^{-i\mathbf{q}\times\mathbf{p}\ell^2}, \quad (1.56) \end{aligned}$$

with $\mathbf{q} \times \mathbf{p} \equiv (\mathbf{q} \times \mathbf{p}) \cdot \widehat{\mathbf{z}}$.

Usually, we do not consider Landau level mixing, since the Landau gap is large enough to avoid inter Landau level coherence, i.e. $\left\langle \rho_{n,n'}^{\alpha,\beta}(\mathbf{q}) \right\rangle\Big|_{n \neq n'} = 0$. In this case, $n_1 = n_2 = n_3 = n_4$, so that the Landau level index can be neglected and the Hartree and Fock interaction functions can be simplified to $H_{\alpha,\beta}$ and $X_{\alpha,\beta}$, respectively. Note that the Hartree interaction functions diverge at zero momenta, $\lim_{q \to 0} H_{\alpha,\beta}(\mathbf{q}) \to \frac{1}{q}$. However, these diverging terms $H_{\alpha,\beta}(\mathbf{0})$ are usually cancelled by the postive background. If the system is a bilayer 2DEG, then there would be a capacitive term left, which can be combined into the Zeeman term. The capacitive energy is induced by the imbalance of the charge of the two layers. It forces the charge distributes equally on the two layers. Hence, we obtain the total Hamiltonian with Zeeman coupling in the second quantization:

$$\begin{aligned} H &= \sum_{\alpha} E_\alpha \rho_{\alpha,\alpha}(0) + \frac{e^2}{\kappa \ell} \overline{\sum_{\mathbf{q}}} \sum_{\alpha,\beta} H_{\alpha,\beta}(\mathbf{q}) \left\langle \rho_{\alpha,\alpha}(-\mathbf{q}) \right\rangle \rho_{\beta,\beta}(\mathbf{q}) \\ &\quad - \frac{e^2}{\kappa \ell} \sum_{\mathbf{q}} \sum_{\alpha,\beta} X_{\alpha,\beta}(\mathbf{q}) \left\langle \rho_{\alpha,\beta}(-\mathbf{q}) \right\rangle \rho_{\beta,\alpha}(\mathbf{q}), \end{aligned} \tag{1.57}$$

where E_α includes the Zeeman energy, the kinetic energy of level α and the capacity energy if it is a bilayer system. The sum symbol with a bar represents the summation excluding $\mathbf{q} = \mathbf{0}$. This Hamiltonian does not apply to BLG with $N = 0$. For $N > 0$, the index α or β should be a spin-valley index.

1.4 Green's functions and correlation functions

In this thesis, the theoretical tools are the Green's functions and the correlation functions, which are introduced in this section.

The single-particle Matsubara Green's function is defined by

$$G_{a,b}(\tau) = -\left\langle T_\tau c_a(\tau) c_b^\dagger(0) \right\rangle = -\left\langle c_a(\tau) c_b^\dagger(0) \right\rangle \theta(\tau) + \left\langle c_b^\dagger(0) c_a(\tau) \right\rangle \theta(-\tau), \tag{1.58}$$

where T_τ is the time ordering operator, and $\theta(x)$ is the step function. The indices in the Green's function, a and b, could be Landau level, spin, valley, layer, orbital, etc.. The equation of motion for the Green's function in the Matsubara formalism is obtained by using the Heisenberg equation of motion

$$\hbar\frac{\partial}{\partial\tau}\left(\ldots\right)=\left[H_{HF}-\mu N,\left(\ldots\right)\right], \tag{1.59}$$

where H_{HF} is the many-body Hamiltonian in the HFA (for example, the Hamiltonian in Eq. (2.8)), μ is the chemical potential, and N is the particle number. On the left hand side of Eq. (1.59), we have

$$\hbar\frac{\partial}{\partial\tau}G_{a,b}\left(\tau\right)=-\hbar\delta(\tau)\delta_{a,b}-\hbar\left\langle T\left[\frac{\partial}{\partial\tau}c_{a}(\tau)\right]c_{b}^{\dagger}(0)\right\rangle . \tag{1.60}$$

And the right part depends on the Hamitonian H_{HF}.

We can derive the equation of motion in Eq. (1.59) as

$$\begin{aligned}
&\left(-i\hbar\omega_{n}+E_{a}-\mu\right)G_{a,b}\left(\mathbf{q},\omega_{n}\right)\\
=\;&-\hbar\delta_{a,b}\delta_{\mathbf{q},0}-\frac{e^{2}}{\kappa\ell}\overline{\sum_{\mathbf{q}'}}\sum_{c}H_{c,a}\left(\mathbf{q}'\right)\left\langle\rho_{c,c}\left(-\mathbf{q}'\right)\right\rangle e^{-\frac{i}{2}\mathbf{q}\times\mathbf{q}'\ell^{2}}G_{a,b}\left(\mathbf{q}+\mathbf{q}',\omega_{n}\right)\\
&+\frac{e^{2}}{\kappa\ell}\sum_{\mathbf{q}'}\sum_{c}X_{c,a}(\mathbf{q}')\left\langle\rho_{c,a}\left(-\mathbf{q}'\right)\right\rangle e^{-\frac{i}{2}\mathbf{q}\times\mathbf{q}'\ell^{2}}G_{c,b}\left(\mathbf{q}+\mathbf{q}',\omega_{n}\right)
\end{aligned} \tag{1.61}$$

where we define $\mathbf{q}\times\mathbf{q}'\equiv\left(\mathbf{q}\times\mathbf{q}'\right)\cdot\widehat{z}$ and use the Fourier transformations:

$$G(\tau) = \frac{1}{\beta\hbar}\sum_{\omega_{n}}\exp(-i\omega_{n}\tau)G(\omega_{n}) \tag{1.62}$$

$$G(\omega_{n}) = \int_{0}^{\beta\hbar}\exp(i\omega_{n}\tau)G(\tau)d\tau, \tag{1.63}$$

with the Fermion Matsubara frequencies $i\omega_{n}=\frac{(2n+1)\pi}{\beta\hbar}$. The $H_{c,a}$ and $X_{c,a}$ are Hartree and Fock interaction fucntions, respectively.

If we only consider the case of electron crystal, then the electron gas forms a periodic structure. The order parameters $\left\langle\rho\left(\mathbf{q}\right)\right\rangle$'s are nonzero only at the reciprocal lattice vectors in the momentum space. And the value of $\left\langle\rho\left(\mathbf{q}\right)\right\rangle$ decreases when $\mathbf{q}$ increases. These properties make it possible to study the system at finite momenta. So, a set of vectors $\{\mathbf{q}\}$ can well describe the ordered phases which are defined by all the density matrix elements $\left\langle\rho_{\alpha,\beta}\left(\mathbf{q}\right)\right\rangle$. On the other hand, the Green's function can be solved to describe completely the system, because of the relation between order parameters and Green's functions,

$$\langle \rho_{a,b}(\mathbf{q}) \rangle = G_{b,a}\left(\mathbf{q},\tau = 0^{-}\right). \tag{1.64}$$

In the case of electron crystal phases, we can write the Eq. (1.61) in a matrix form,

$$\left(i\hbar\omega_n I - F\right) G = B, \tag{1.65}$$

where I is the unitary matrix. Assume, for example, that a, b, c can all take four values, then

$$B(\mathbf{q}) = \hbar \begin{pmatrix} \overrightarrow{1} & \overrightarrow{0} & \overrightarrow{0} & \overrightarrow{0} \\ \overrightarrow{0} & \overrightarrow{1} & \overrightarrow{0} & \overrightarrow{0} \\ \overrightarrow{0} & \overrightarrow{0} & \overrightarrow{1} & \overrightarrow{0} \\ \overrightarrow{0} & \overrightarrow{0} & \overrightarrow{0} & \overrightarrow{1} \end{pmatrix}_{4n\times 4}, \tag{1.66}$$

where n is the number of reciprocal lattice vectors and

$$\begin{aligned} \overrightarrow{1} &= (1,0,0,...,0)^{T}, && (1.67) \\ \overrightarrow{0} &= (0,0,0,...,0)^{T}. && (1.68) \end{aligned}$$

The F matrix can be obtained from Eq. (1.61). The matrix F is Hermitian, and so it can be diagonalized by a unitary transformation $F = UDU^{\dagger}$ where D is a diagonal matrix and the Hermitian matrix U is the unitary transformation matrix satisfying $UU^{\dagger} = I$. So the Eq. (1.65) can be calculated by

$$\begin{aligned} U\left(i\hbar\omega_n I - D\right) U^{\dagger} G &= B, && (1.69) \\ G &= U\left(i\hbar\omega_n I - D\right)^{-1} U^{\dagger} B, && (1.70) \\ G_{ij}(\omega_n) &= \sum_{k,l,p} U_{ik}\left(i\hbar\omega_n I - D\right)^{-1}_{kl} U^{\dagger}_{lp} B_{pj} \\ &= \sum_{k,l,p} \frac{U_{ik}U^{\dagger}_{lp}\delta_{p,j}\delta_{k,l}}{i\hbar\omega_n - D_{kl}} = \sum_{k} \frac{U_{ik}U^{\dagger}_{kj}}{i\hbar\omega_n - D_{kk}}. && (1.71) \end{aligned}$$

Hence,

$$\begin{aligned}\left\langle \rho_{ji}\left(\mathbf{q}\right)\right\rangle &= G_{ij}\left(\tau=0^{-},\mathbf{q}\right)=\frac{1}{\beta\hbar}\sum_{\omega_n}e^{-i\omega_n\tau}G_n^{ij}\\ &= \frac{1}{\beta\hbar}\sum_{\omega_n}\sum_{k}e^{+i\omega_n\delta}\frac{U_{m+(i-1)N,k}U^{*}_{(j-1)N+1,k}}{i\hbar\omega_n-D_{kk}}\\ &= \sum_{k}\frac{1}{e^{\beta d_{kk}}+1}U_{m+(i-1)N,k}U^{*}_{(j-1)N+1,k}. \qquad (1.72)\end{aligned}$$

In Eq. (1.72), $\left\langle \rho_{ji}\left(\mathbf{q}\right)\right\rangle$ is given in terms of the matrix U which itself depends on the set of $\left\{\left\langle \rho_{ji}\left(\mathbf{q}\right)\right\rangle\right\}$. It is thus a self-consistent equation that must be solved numerically. The numerical procedure is described in details in Ref. [26].

The poles of $G\left(\tau=0^{-},\mathbf{q}\right)$ give the energies of the quasi-particle in the system. For example, consider a liquid phase where $\left\langle \rho_{ji}\left(\mathbf{q}\neq\mathbf{0}\right)\right\rangle=0$. The equation of motion of the Green's function can then be simplified to,

$$\begin{aligned}&\left[-i\hbar\omega_n+E_a-\frac{e^2}{\kappa\ell}X_{a,a}(0)\left\langle \rho_{a,a}\left(0\right)\right\rangle\right]G_{a,b}\left(\mathbf{q},\omega_n\right)\\ =&\ -\hbar\delta_{a,b}\delta_{\mathbf{q},0}+\frac{e^2}{\kappa\ell}\sum_{c\neq a}X_{c,a}(0)\left\langle \rho_{c,a}\left(0\right)\right\rangle G_{c,b}\left(\mathbf{q},\omega_n\right). \qquad (1.73)\end{aligned}$$

We do the analytical continuation $i\omega_n\rightarrow\omega+i\delta$, then the poles are given by $\hbar\omega=E_a-\frac{e^2}{\kappa\ell}X_{a,a}(0)\left\langle \rho_{a,a}\left(0\right)\right\rangle$ which are the energies of the quasi-particles in the system.

To study the collective excitations of the system, the single-particle Green's function is not enough. We need to compute the two-particle Green's functions as well, which are defined as

$$\chi_{AB}\left(q,\tau\right)=-\frac{1}{\hbar}\left\langle T_\tau A\left(q,\tau\right)B\left(-q,0\right)\right\rangle, \qquad (1.74)$$

where τ is the imaginary time, and A and B are the operators of two observable quantities. Fourier transforming and making the analytical continuation $i\omega_n\rightarrow\omega+i\delta$, we get the space and time Fourier transform of the retarded function:

$$\chi^{R}_{AB}\left(q,t\right)=-\frac{i}{\hbar}\left\langle\left[A\left(q,t\right),B\left(-q,0\right)\right]\right\rangle\theta\left(t\right). \qquad (1.75)$$

In the linear response theory, we need to set A,B as density field when we calculate the collective mode, absorption and dielectric function. Then we can write the Eq. (1.74) in terms of the operators of density field,

$$\begin{aligned}\chi_{n_i n_j}\left(q,\tau\right) &= -\frac{i}{\hbar}\left\langle T_\tau n_i\left(q,\tau\right)n_j\left(-q,0\right)\right\rangle \\ &= -\frac{i}{\hbar}\sum_{n,n',m,m'}\Xi_{n,n'}\left(q\right)\Xi_{m,m'}\left(-q\right)\left\langle T_\tau c^\dagger_{i,a}(\tau)c_{i,b}(\tau)c^\dagger_{j,c}(0)c_{j,d}(0)\right\rangle,\end{aligned} \tag{1.76}$$

where the density field (n_x, n_y, n_z) is defined by $n_i = \sum_{a,b}\Xi_{a,b}c^\dagger_{i,a}c_{i,b}$.

In a 2DEG system in a magnetic field, an electronic state is defined by the Landau level, guiding center, spin and valley indices (in some cases, more indices may be needed). We thus write $c_{n,X,a}$ for the electron annihilation operator, where n is Landau level index, X is guiding center index, and a includes all the other indices. It will be useful to define the density operator

$$\rho_{(n,a);(n',b)}\left(\mathbf{q}\right) = \frac{1}{N_\phi}\sum_{X,X'}e^{-\frac{i}{2}q_x(X+X')}\delta_{X,X'+q_y\ell^2}c^\dagger_{n,X,a}c_{n',X',b}, \tag{1.77}$$

where N_ϕ is the Landau level degeneracy. A general two-particle Green's function can be written as,

$$\begin{aligned}\chi^{a,b,c,d}_{n_1,n_2,n_3,n_4}\left(\mathbf{p},\mathbf{p}';\tau_1-\tau_3\right) &= -N_\phi\left\langle T_\tau\delta\rho_{(n_1,a);(n_2,b)}\left(\mathbf{p},\tau_1\right)\delta\rho_{(n_3,c);(n_4,d)}\left(-\mathbf{p}',\tau_3\right)\right\rangle \\ &= -N_\phi\left\langle T_\tau\rho_{(n_1,a);(n_2,b)}\left(\mathbf{p},\tau_1\right)\rho_{(n_3,c);(n_4,d)}\left(-\mathbf{p}',\tau_3\right)\right\rangle \\ &\quad +N_\phi\left\langle\rho_{(n_1,a);(n_2,b)}\left(\mathbf{p}\right)\right\rangle\left\langle\rho_{(n_3,c);(n_4,d)}\left(-\mathbf{p}'\right)\right\rangle.\end{aligned} \tag{1.78}$$

These Green's functions share the same poles as the response functions. Moreover, the poles of these Green's functions correspond to the frequency of the collective excitations of the C2DEG. In the generalized random phase approximation (GRPA), we can obtain the self-consistent equation for the two-particle Green's function,

$$\begin{aligned}&\chi^{a,b,c,d}_{n_1,n_2,n_3,n_4}\left(\mathbf{q},\mathbf{q}';i\Omega_n\right) = \chi^{0,a,b,c,d}_{n_1,n_2,n_3,n_4}\left(\mathbf{q},\mathbf{q}';i\Omega_n\right) \\ &+\frac{1}{\hbar}\frac{e^2}{\kappa\ell}\sum_{e,g}\sum_{\mathbf{q}''}\sum_{m_1,m_2,m_3,m_4}\chi^{0,a,b,e,e}_{n_1,n_2,m_1,m_2}\left(\mathbf{q},\mathbf{q}'';i\Omega_n\right)H^{e,g}_{m_1,m_2,m_3,m_4}\left(\mathbf{q}''\right)\chi^{g,g,c,d}_{m_3,m_4,n_3,n_4}\left(\mathbf{q}'',\mathbf{q}';i\Omega_n\right) \\ &-\frac{1}{\hbar}\frac{e^2}{\kappa\ell}\sum_{e,f}\sum_{m_1,m_2,m_3,m_4}\sum_{\mathbf{q}''}\chi^{0,a,b,e,f}_{n_1,n_2,m_1,m_2}\left(\mathbf{q},\mathbf{q}'';i\Omega_n\right)X^{e,f}_{m_1,m_4,m_3,m_2}\left(\mathbf{q}''\right)\chi^{f,e,c,d}_{m_3,m_4,n_3,n_4}\left(\mathbf{q}'',\mathbf{q}';i\Omega_n\right),\end{aligned} \tag{1.79}$$

where $H^{e,g}$ and $X^{e,f}$ are Hartree and Fock interaction functions, and $\chi^0_{a,b,c,d}$ is called the

Hartree-Fock two-particle Green's function. It is given by the equation of motion,

$$\begin{aligned}
&\left[-i\hbar\Omega_n-\left(E_{n_1,a}-E_{n_2,b}\right)\right]\chi^{0,a,b,c,d}_{n_1,n_2,n_3,n_4}\left(\mathbf{q},\mathbf{q}',\Omega_n\right) \qquad (1.80)\\
&=-\hbar\left[\delta_{b,c}\delta_{n_2,n_3}\left\langle\rho^{a,d}_{n_1,n_4}\left(\mathbf{q}-\mathbf{q}'\right)\right\rangle e^{\frac{i}{2}\mathbf{q}\times\mathbf{q}'\ell^2}-\delta_{a,d}\delta_{n_1,n_4}\left\langle\rho^{c,b}_{n_3,n_2}\left(\mathbf{q}-\mathbf{q}'\right)\right\rangle e^{-\frac{i}{2}\mathbf{q}\times\mathbf{q}'\ell^2}\right]\\
&+\frac{e^2}{\kappa\ell}\sum_{m_1,m_2,m_3}\sum_{e}\overline{\sum_{\mathbf{q}''}}H^{e,a}_{m_1,m_2,m_3,n_1}\left(\mathbf{q}''-\mathbf{q}\right)\left\langle\rho^{e,e}_{m_1,m_2}\left(\mathbf{q}-\mathbf{q}''\right)\right\rangle e^{-\frac{i}{2}\mathbf{q}''\times\mathbf{q}\ell^2}\chi^{0,a,b,c,d}_{m_3,n_2,n_3,n_4}\left(\mathbf{q}'',\mathbf{q}',\Omega_n\right)\\
&-\frac{e^2}{\kappa\ell}\sum_{m_1,m_2,m_4}\sum_{e}\overline{\sum_{\mathbf{q}''}}H^{e,b}_{m_1,m_2,n_2,m_4}\left(\mathbf{q}''-\mathbf{q}\right)\left\langle\rho^{e,e}_{m_1,m_2}\left(\mathbf{q}-\mathbf{q}''\right)\right\rangle e^{\frac{i}{2}\mathbf{q}''\times\mathbf{q}\ell^2}\chi^{0,a,b,c,d}_{n_1,m_4,n_3,n_4}\left(\mathbf{q}'',\mathbf{q}',\Omega_n\right)\\
&-\frac{e^2}{\kappa\ell}\sum_{m_1,m_2,m_3}\sum_{e}\sum_{\mathbf{q}''}X^{a,e}_{m_1,n_1,m_3,m_2}\left(\mathbf{q}''-\mathbf{q}\right)\left\langle\rho^{a,e}_{m_1,m_2}\left(\mathbf{q}-\mathbf{q}''\right)\right\rangle e^{-\frac{i}{2}\mathbf{q}''\times\mathbf{q}\ell^2}\chi^{0,e,b,c,d}_{m_3,n_2,n_3,n_4}\left(\mathbf{q}'',\mathbf{q}',\Omega_n\right)\\
&+\frac{e^2}{\kappa\ell}\sum_{m_1,m_2,m_4}\sum_{e}\sum_{\mathbf{q}''}X^{e,b}_{m_1,m_4,n_2,m_2}\left(\mathbf{q}''-\mathbf{q}\right)\left\langle\rho^{e,b}_{m_1,m_2}\left(\mathbf{q}-\mathbf{q}''\right)\right\rangle e^{\frac{i}{2}\mathbf{q}''\times\mathbf{q}\ell^2}\chi^{0,a,e,c,d}_{n_1,m_4,n_3,n_4}\left(\mathbf{q}'',\mathbf{q}',\Omega_n\right),
\end{aligned}$$

where $E_{n_1,a}$ is the kinetic energy of level (n_1,a), and the bar over the sum symbol means that the summation excludes $\mathbf{q}''=\mathbf{q}$. If we neglect the Hartree-Fock interactions in Eq. (1.80), the χ^0 is called bare bubble approximation to the two-particle Green's function. These equations are derived in Chapter 4 of Ref. [25].

The equation of motion of the two-particle's Green function in Eq. (1.79) can be also written in a matrix form [26],

$$(i\Omega_n I-F)\chi=B, \qquad (1.81)$$

where the F matrix contains the Hartree-Fock interactions and the densities $\langle\rho\rangle$, and the B matrix contains only the $\langle\rho\rangle$'s. In the matrix form, χ can be easily solved by diagonalizing the matrix F.

In this thesis, we will use the self-consistent equation of the two-particle Green's function to compute the dispersion relations of the collective modes and their contribution to the electromagnetic absorption. We will use the bare bubble approximation to derive the dielectric function of the C2DEG.

1.5 Nonlinear σ model and its topological solution

If we look for an excitation of the QHF that varies slowly in space, the main contribution to the energy, in the absence of Zeeman or other coupling, comes from the Fock or exchange term in Hartree-Fock (HF) Hamiltonian since it is the term that keeps the spin parallel. To get the NLσM from the HF Hamiltonian we write the Fock term in the gradient approximation, i.e. we expand the densities $\langle \rho_{i,j}(\mathbf{r})\rangle$ (which are related to the classical field $\mathbf{m}$) around the ground state solution. We start with the Fock energy,

$$E = -\frac{N_\phi}{2}\sum_{ss'}\sum_{\mathbf{q}} X_{s,s'}\left(\mathbf{q}\right)\left\langle \rho_{s,s'}\left(\mathbf{q}\right)\right\rangle \left\langle \rho_{s',s}\left(-\mathbf{q}\right)\right\rangle , \tag{1.82}$$

where s and s' are the spin or valley indices of the system. Notice that, for the Fock interaction function, $X_{s,s'} = X_{s',s}$. In real space,

$$E = -\frac{1}{2}\sum_{ss'}\int d\mathbf{r}\int d\mathbf{r}' X_{s,s'}\left(\mathbf{r}-\mathbf{r}'\right)\left\langle \rho_{s,s'}\left(\mathbf{r}\right)\right\rangle \left\langle \rho_{s',s}\left(\mathbf{r}'\right)\right\rangle . \tag{1.83}$$

Now, let us suppose there is a weak pertubation in the density matrix, or say, the density matrix elements vary slowly in real space. Using a Taylor expansion for $\nabla\left\langle \rho_{s',s}\left(\mathbf{r}'\right)\right\rangle$, the energy functional becomes,

$$\begin{aligned} E &= -\frac{1}{2}\sum_{ss'}\int d\mathbf{r}d\mathbf{r}' X_{s,s'}\left(\mathbf{r}-\mathbf{r}'\right)\left\langle \rho_{s,s'}\left(\mathbf{r}\right)\right\rangle \\ &\quad\times\left[\left\langle \rho_{s',s}\left(\mathbf{r}\right)\right\rangle + \left(\mathbf{r}'-\mathbf{r}\right)\cdot\nabla_{\mathbf{r}'}\left\langle \rho_{s',s}\left(\mathbf{r}'\right)\right\rangle|_{\mathbf{r}'=\mathbf{r}} + \frac{1}{2}\left(\mathbf{r}'-\mathbf{r}\right)^2\nabla^2_{r'}\left\langle \rho_{s',s}\left(\mathbf{r}'\right)\right\rangle|_{\mathbf{r}'=\mathbf{r}} + \ldots\right] \\ &= -\frac{1}{2}\sum_{ss'}\int d\mathbf{r}' X_{s,s'}\left(-\mathbf{r}'\right)\int d\mathbf{r}\left\langle \rho_{s,s'}\left(\mathbf{r}\right)\right\rangle \left\langle \rho_{s',s}\left(\mathbf{r}\right)\right\rangle \\ &\quad -\frac{1}{4}\sum_{ss'}\int d\mathbf{r}\int d\mathbf{r}' X_{s,s'}\left(\mathbf{r}-\mathbf{r}'\right)\left\langle \rho_{s,s'}\left(\mathbf{r}\right)\right\rangle \left(\mathbf{r}'-\mathbf{r}\right)^2\nabla^2\left\langle \rho_{s',s}\left(\mathbf{r}\right)\right\rangle , \end{aligned} \tag{1.84}$$

where

$$\begin{aligned} &\int d\mathbf{r}\int d\mathbf{r}' X_{s,s'}\left(\mathbf{r}-\mathbf{r}'\right)\left\langle \rho_{s,s'}\left(\mathbf{r}\right)\right\rangle \left(\mathbf{r}'-\mathbf{r}\right)\cdot\nabla_{\mathbf{r}}\left\langle \rho_{s',s}\left(\mathbf{r}\right)\right\rangle \\ = &\int d\mathbf{r}\int d\mathbf{r}' X_{s,s'}\left(-\mathbf{r}'\right)\left\langle \rho_{s,s'}\left(\mathbf{r}\right)\right\rangle \mathbf{r}'\cdot\nabla_{\mathbf{r}}\left\langle \rho_{s',s}\left(\mathbf{r}\right)\right\rangle = 0, \end{aligned} \tag{1.85}$$

because, in our case, $X_{s,s'}\left(-\mathbf{r}'\right)$ is even and $\mathbf{r}'$ is odd. Notice that we neglect the higher orders because of the condition that $\rho_{i,j}$ vary slowly in real space. Hence, the excitation energy is given by

$$\delta E = \frac{1}{4}\int d\mathbf{r}' X_{s,s'}\left(\mathbf{r}'\right)\mathbf{r}'^2\sum_{ss'}\int d\mathbf{r}\nabla\left\langle \rho_{s,s'}\left(\mathbf{r}\right)\right\rangle \cdot\nabla\left\langle \rho_{s',s}\left(\mathbf{r}\right)\right\rangle , \tag{1.86}$$

which has the form of Eq. (1). In the spin language,

$$S_x = \frac{1}{2}\mathrm{Re}\left\langle \rho_{\uparrow,\downarrow}\left(\mathbf{r}\right)\right\rangle, \tag{1.87}$$

$$S_y = \frac{1}{2}\mathrm{Im}\left\langle \rho_{\uparrow,\downarrow}\left(\mathbf{r}\right)\right\rangle, \tag{1.88}$$

$$S_z = \frac{1}{2}(\left\langle \rho_{\uparrow,\uparrow}\left(\mathbf{r}\right)\right\rangle - \left\langle \rho_{\downarrow,\downarrow}\left(\mathbf{r}\right)\right\rangle), \tag{1.89}$$

so the term

$$\sum_{s,s'} \nabla\left\langle \rho_{s,s'}\left(\mathbf{r}\right)\right\rangle \cdot \nabla\left\langle \rho_{s',s}\left(\mathbf{r}\right)\right\rangle = 2\sum_{i=x,y,z}\nabla S_i\cdot\nabla S_i = 2\partial^\mu\mathbf{S}\cdot\partial^\mu\mathbf{S}, \tag{1.90}$$

where we use Einstein's summation convention. Notice in the nonlinear sigma model, the field is a unit vector, while $\mathbf{S}$ here is not, since $\left|\mathbf{S}\left(\mathbf{r}\right)\right|$ is in units of $\frac{1}{2}\frac{1}{2\pi\ell^2} = \frac{1}{2}\frac{N_\phi}{S}$, so we define

$$\mathbf{m} = 2\frac{S}{N_\phi}\mathbf{S} = 4\pi\ell^2\mathbf{S}, \tag{1.91}$$

to keep $\mathbf{m}^2 = 1$. So $\sum_{ss'}\nabla\left\langle \rho_{s,s'}\left(\mathbf{r}\right)\right\rangle \cdot \nabla\left\langle \rho_{s',s}\left(\mathbf{r}\right)\right\rangle = \frac{1}{2}\left(\frac{N_\phi}{S}\right)^2\partial^\mu\mathbf{m}\cdot\partial^\mu\mathbf{m}$. Hence, the excitation energy functional becomes,

$$\delta E = -\frac{1}{8}\frac{N_\phi}{S}\nabla_q^2 X_n\left(\mathbf{q}\right)|_{q=0}\int d\mathbf{r}\partial^\mu\mathbf{m}\cdot\partial^\mu\mathbf{m}, \tag{1.92}$$

which is consistent with the Lagrangian of the NLσM in Eq. (1). From this expression, we get the spin stiffness,

$$\rho_s = -\frac{1}{4}\frac{1}{2\pi\ell^2}\nabla_q^2 X_n\left(\mathbf{q}\right)|_{q=0}. \tag{1.93}$$

The charged excitation energy $\delta E = 4\pi\rho_s$ only depends on the Fock interaction $X_{s,s'}\left(\mathbf{q}\right)$. For a more realistic model, the Hartree energy must also be considered since a modulation of the charge density costs energy. In the quantum Hall system, skyrmions carry a charge $q_e = Qe$.

1.5.1 Anisotropic Nonlinear σ model and bimeron

Not all the 2DEG systems are described by the NLσM. In bilayer 2DEG, the single-particle excitation with a layer texture is described by the anisotropic NLσM (ANLσM) [30]. Here the 2DEG is assumed to be spin polarized and the important degree of freedom is the layer index. Because of the finite distance between the two layers, the inter-layer and intra-layer Coulomb interactions are not identical. Hence, the O(3) symmetry of the NLσM Lagrangian is broken. The spin stiffnesses for different components of the field are not the same. The Lagrangian of an ANLσM is given by

$$L_{ANL\sigma M} = \frac{1}{2} \sum_{i=x,y,z} \rho_i \int d\mathbf{r}\, (\nabla m_i) \cdot (\nabla m_i)\,. \tag{1.94}$$

If $\rho_x = \rho_y \neq \rho_z$, then the solutions of the Lagrangian in Eq. (1.94) are no longer skyrmions or anti-skyrmions. They are called bimerons and anti-bimerons. The excitation energy of a bimeron or anti-bimeron is given by

$$\Delta_{ANL\sigma M} = \frac{4\pi}{3}(\rho_x + \rho_y + \rho_z). \tag{1.95}$$

The bimeron field, for example, is given by [30]

$$\begin{aligned} m_x \pm i m_y &= \frac{2w}{1+|w|^2}, & (1.96)\\ m_z &= \frac{|w|^2-1}{|w|^2+1}, & (1.97) \end{aligned}$$

which is the same as skyrmion, but, the w field is different. In a skyrmion, $w = \left(\frac{z}{k}\right)^q = \left(\frac{r}{k}\right)^q e^{iq\theta}$, where $z = x + iy$, $\theta = \arctan \frac{y}{x}$. But in the bimeron, $w = \frac{z-z_L}{z-z_R} e^{i\phi}$, where ϕ is an arbitrary angle, z_L and z_R are the positions of the left and right cores in a bimeron, where $S_z = \pm 1$ respectively.

The spin textures and density profiles of a skyrmion and an antiskyrmion are shown in Fig. 1. A bimeron projected on the $x-y$ plane are shown in Fig. 1.7a, while the spin textures of an anti-skyrmion and an anti-bimeron projected on the $x-y$ plane are shown in Fig. 1.7c. The density profiles of a bimeron and an anti-bimeron are shown in Figs. 1.7b and 1.7d, respectively. The two cores, which are located at $x = z_l = -5$ and $x = z_r = 5$, in the bimeron and anti-bimeron are clearly seen in these figures. Notice that the spin points up at infinity in an anti-skyrmion (or skyrmion) while the spin points along the x direction and there is no z component in the spin field in an anti-bimeron (or bimeron) at infinity. This is due to the fact that in a bilayer 2DEG, the capacitive energy forces the electrons to occupy both layers equally at zero bias. In a layer pseudo-spin language, this is equivalent to having all the layer pseudo-spin point in the same direction in the $x - y$ plane.

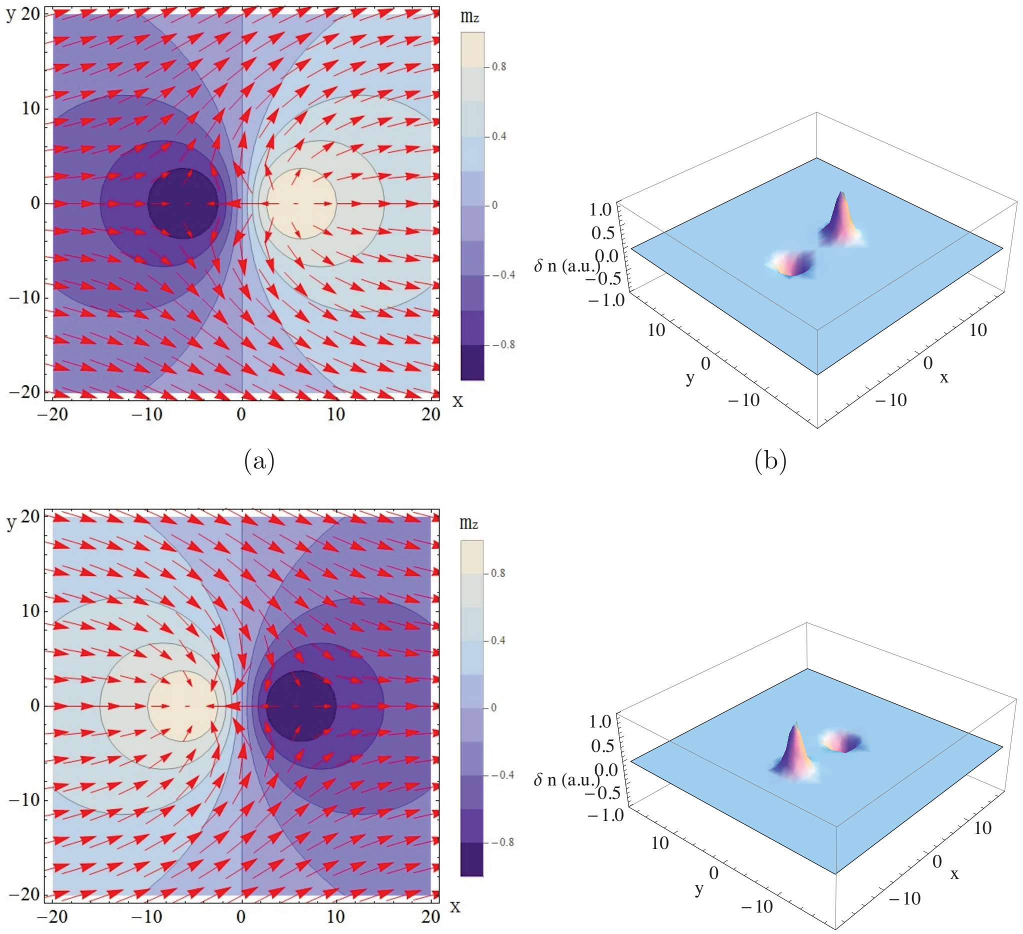

(a) (b)

(c) (d)

FIGURE 1.7: (a) The spin texture projected to the $x - y$ plane of a bimeron, and (b) the density profile $\delta n = n_{bimeron} - n_{groundstate}$ of a bimeron. (c) The spin texture projected to the $x - y$ plane of an anti-bimeron and (d) the density profile $\delta n = n_{anti-bimeron} - n_{groundstate}$ of an anti-bimeron. The color contours represent m_z.

Chapter 2

Skyrmions in monolayer graphene

In the previous chapter, we have studied the Landau quantization in graphene. The conduction and valence bands are replaced by a series of Landau levels with positive and negative energies. The kinetic energy for each Landau level is given by Eq. (1.17). When counting spin and valley degrees of freedom, each Landau level is four-time degenerate.

If we do not consider Landau level mixing, the many-body Hamiltonian in the lowest Landau level (LLL) in graphene is the same as the LLL of a conventional 2DEG in a quantum well. This is because the form factors of the wave functions of graphene are equivalent to those of a conventional 2DEG in the LLL. However, the form factors in higher LLs in graphene are different from those in a conventional 2DEG. Hence, the many-body Hamiltonian of graphene gives a different excitation energy functional, which can be described by a nonlinear σ model (NLσM), from the conventional 2DEG. The difference is represented by the spin stiffness in the NLσM. The spin stiffness is a constant which is related to the form factors of the wave functions, and represents the excitation energy of a spin system if there is a slow twist of the spins in the ground state. It is already known that the spin twisted excitation states (skyrmions) only exist in the LLL in a conventional 2DEG. In higher LLs, the spin stiffness is so large that the spin textured excitations have higher energies than the quasi-particle excitations where only one spin is flipped and there is no spin texture. However, it is possible that the spin textured excitation states survive in higher LLs in graphene system due to the different spin stiffness [9]. This is what we wanted to find out.

Recently, an experimental paper [12] studied the single-particle excitations in graphene in the presence of a magnetic field. In a high-quality sample, which was fabricated on the boron nitride (BN) substrate, the four plateaus of the Hall conductivity σ_{xy} coming from the lifting of the four-fold degeneracy of a LL were observed if the filling factors could be well controlled [5]. The experiment allowed to study the nature of the quantum Hall ground states of the C2DEG as well as their single-particle excitations. The authors measure the resistivity to determine the energy gap of the single-particle excitation, due to the relation in the Quantum Hall states

$$R_{xx} \propto e^{-\Delta_{gap}/(2k_B T)}, \tag{2.1}$$

where R_{xx} is the resistivity, Δ_{gap} is the transport gap of a single-particle pair, k_B is the Boltzman constant, and T is the temperature. Here, the single-particle excitation could be quasi-particle states, or (pseudo-)spin textured excitations. The former one is trivial and the latter one is more interesting in both theoretical and experimental physics. The authors have proved experimentally that the spin and valley skyrmions exist in higher LLs in graphene (see the Figs. 2, 3, and 4 in Ref. [12]). In this work, we will figure out what type of single-particle excitation is preferred in certain conditions, and compare our numerical calculations with the experimental results.

2.1 Hartree-Fock Hamiltonian in symmetric gauge

To study the single-particle excitations, it is more convenient to work in the symmetric gauge. This is because the excitations have a rotational symmetry, just like the wave functions in the symmetric gauge.

In the lowest Landau level of graphene, the Coulomb interaction is identical to that of the LLL in a conventional 2DEG. Skyrmion excitations in this case have been studied in details [31,32]. For this reason, the LLL is not taken into consideration in this section.

Due to the electron-hole (EH) symmetry, the ground state at positive filling factor ν is the same as the ground state at negative filling factor $-\nu$, even when screening effect is taken into account. Without loss of generality, we can thus take the filling factor as positive in our calculations.

At filling factors $\nu = 4, 8, 12$, which correspond to half-filling of the Landau levels $n = 1, 2, 3$, the Landau level gap (which is about $\hbar\omega_c = 0.033\sqrt{B}$eV, where ω_c is the cyclotron frequency and B is the magnetic field) is much larger than the Zeeman ($\Delta_Z = 1.2 \times 10^{-4} B$ eV) or Coulomb gap (which is typically $e^2/(\kappa\ell) = 0.056(\sqrt{B}/\kappa)$eV where

κ is the dielectric constant of the substrate), so that we can neglect the Landau level mixing. Only the partially filled Landau level is considered. The ground states at these fillings should be a spin polarized ferromagnet, since the spin polarized state can minimize the exchange interaction [33]. However, both in experiment [12] and in theory [42], the ground state in the LLL in graphene is more complicated and is probably not fully spin polarized. We will not consider the LLL.

With a magnetic field $\mathbf{B} = B\hat{\mathbf{z}}$, the ground states of the C2DEG at $\nu = 4, 8, 12$ should be that $|K, \uparrow\rangle$ and $|K', \uparrow\rangle$ are fully filled, while the other two levels $|K, \downarrow\rangle$ and $|K', \downarrow\rangle$ are empty levels. In an interacting picture, the four levels in a single Landau level should be instead the symmetric states $|S, \uparrow\rangle = \alpha|K, \uparrow\rangle + \beta|K', \uparrow\rangle$, $|S, \downarrow\rangle = \alpha|K, \downarrow\rangle + \beta|K', \downarrow\rangle$, and antisymmetric states $|AS, \uparrow\rangle = \alpha|K, \uparrow\rangle - \beta|K', \uparrow\rangle$, $|AS, \downarrow\rangle = \alpha|K, \downarrow\rangle - \beta|K', \downarrow\rangle$. For a half-filling state, $|S, \uparrow\rangle$ and $|AS, \uparrow\rangle$ are full and the other are empty. The α, β are the arbitrary parameters which satisfy $|\alpha|^2 + |\beta|^2 = 1$ due to the SU(2) symmetry of the valley pseudo-spin. Hence, the two basis, K, K' and S, AS are equivalent, since we could choose $\alpha = 1$ and $\beta = 0$. So the single particle problem in both two basis is equivalent, i.e. the energy would not change if we change the basis. It means that the spin skyrmion at half-filling could be considered to occur in only one valley and we can simplify our problem by working with a two-level system. This assumption has been verified by the experiments [12], which we will discuss later. Based on this approximation, we write the Hamiltonian for single-particle excitation at half filling as

$$H = E_Z + U + H_{e-b} + H_{b-b}, \tag{2.2}$$

where E_Z is the Zeeman coupling, U is the Coulomb interaction between electrons

$$U = \frac{1}{2} \sum_{s,s'} \int d\mathbf{r} d\mathbf{r}' \Psi_s^\dagger (\mathbf{r}) \Psi_{s'}^\dagger (\mathbf{r}') V (\mathbf{r} - \mathbf{r}') \Psi_{s'} (\mathbf{r}') \Psi_s (\mathbf{r}), \tag{2.3}$$

H_{e-b} is the Coulomb interaction between the electrons and the background, and H_{b-b} is the Coulomb interaction between the positive charges in the background. Notice that in Eq. (2.3), we keep the spin indices s, s' and drop the valley index since we consider only one valley. We do not consider Landau level mixing, so the field operator Ψ is defined by

$$\Psi_s(\mathbf{r}) = \sum_{M=-n}^{N_\phi - n} \phi_{n,M} (\mathbf{r}) c_{s,n,M} = \sum_{m=0}^{N_\phi} \phi_{n,m} (\mathbf{r}) c_{s,n,m}, \tag{2.4}$$

where $\phi_{n,M}$ is the wave function in symmetric gauge (defined in Eq. (1.23)) in either K or K' valley (the two valleys are equivalent, we choose one arbitrarily), and c is the annihilation operator of electrons with Landau level index n and angular momenta M. Notice that there are N_ϕ electrons in the ground state. However, N_ϕ is so large that we can approximately set $M \to \infty$ in the upper limit. We define m as the generalized angular momenta, $m = M + n$. Hence, m has values from zero to infinity for any Landau level, which simplifies the analysis in the following. In practice, we need to consider a finite system with finite m, since the skyrmion is localized if the Zeeman coupling is nonzero. The maximum of m controls the size of the system. The background charge is uniform with density $n_b = n_e$, where n_e is the average electronic density. So,

$$H_{e-b} = -n_b \int d\mathbf{r} \Psi_s^\dagger(\mathbf{r}) \Psi_s(\mathbf{r}) V(\mathbf{r}), \tag{2.5}$$

$$H_{b-b} = \frac{n_b^2}{2} \int d\mathbf{r} V(\mathbf{r}), \tag{2.6}$$

$$E_Z = E_s \int d\mathbf{r} \Psi_s^\dagger(\mathbf{r}) \Psi_s(\mathbf{r}), \tag{2.7}$$

where the Zeeman coupling $E_s = \frac{1}{2} s g \mu_B B$. The index $s = \pm 1$ is for spin down and up respectively, $g = 2$ is the Landé factor in graphene, μ_B is the Bohr magneton.

In the Hartree-Fock approximation, we obtain the full Hamiltonian

$$\begin{aligned}
H = {} & \sum_{s,m} \frac{1}{2} s g \mu_B B c_{s,m}^\dagger c_{s,m} \qquad (2.8)\\
& + \frac{1}{4} \sum_{s,s'} \sum_{m_1,\ldots,m_4} \left(V_{m_1,m_2,m_3,m_4}^{n-1,n-1,n-1,n-1} + V_{m_1,m_2,m_3,m_4}^{n,n,n,n} + V_{m_1,m_2,m_3,m_4}^{n-1,n-1,n,n} \right. \\
& \left. + V_{m_1,m_2,m_3,m_4}^{n,n,n-1,n-1} \right) \left(\left\langle c_{s,m_1}^\dagger c_{s,m_2} \right\rangle c_{s',m_3}^\dagger c_{s',m_4} - \left\langle c_{s,m_1}^\dagger c_{s',m_4} \right\rangle c_{s',m_3}^\dagger c_{s,m_2} \right) \\
& - \frac{1}{4} \sum_{s} \sum_{m',m} \left(V_{m',m',m,m}^{n-1,n-1,n,n} + V_{m',m',m,m}^{n-1,n-1,n-1,n-1} + V_{m',m',m,m}^{n,n,n-1,n-1} + V_{m',m',m,m}^{n,n,n,n} \right) c_{s,m}^\dagger c_{s,m} \\
& + \frac{1}{8} \sum_{m,m'} \left(V_{m',m',m,m}^{n-1,n-1,n,n} + V_{m',m',m,m}^{n-1,n-1,n-1,n-1} + V_{m',m',m,m}^{n,n,n-1,n-1} + V_{m',m',m,m}^{n,n,n,n} \right),
\end{aligned}$$

where we use the generalized angular momenta m_i and the Coulomb interaction elements are defined by the general equation

$$
\begin{aligned}
V_{m_1,m_2,m_3,m_4}^{n_1,n_2,n_3,n_4} &= \frac{e^2}{\kappa\ell}\delta_{M_1-M_2+M_3-M_4}\sqrt{\frac{\min(m_1,m_2)!\,\min(m_3,m_4)!}{\max(m_1,m_2)!\,\max(m_3,m_4)!}} \\
&\times\sqrt{\frac{\min(n_1,n_2)!\,\min(n_3,n_4)!}{\max(n_1,n_2)!\,\max(n_3,n_4)!}}\int dke^{-k^2}\left(\frac{k^2}{2}\right)^{|n_1-n_2|+|m_1-m_2|} \\
&\times(-1)_{n_1<n_2}^{|n_1-n_2|}(-1)_{n_3\geq n_4}^{|n_3-n_4|}i^{|m_1-m_2|}(-i)^{|m_3-m_4|} \\
&\times L_{\min(n_1,n_2)}^{|n_1-n_2|}\left(\frac{k^2}{2}\right)L_{\min(n_3,n_4)}^{|n_3-n_4|}\left(\frac{k^2}{2}\right)L_{\min(m_1,m_2)}^{|m_1-m_2|}\left(\frac{k^2}{2}\right)L_{\min(m_3,m_4)}^{|m_3-m_4|}\left(\frac{k^2}{2}\right) \qquad (2.9)
\end{aligned}
$$

with

$$(-1)_{n_1<n_2}^{|n_1-n_2|} = \left\{\begin{array}{cc} (-1)^{|n_1-n_2|} & n_1<n_2 \\ 1 & n_1\geq n_2 \end{array}\right., \qquad (2.10)$$

$$(-1)_{n_3\geq n_4}^{|n_3-n_4|} = \left\{\begin{array}{cc} (-1)^{|n_3-n_4|} & n_3\geq n_4 \\ 1 & n_3<n_4 \end{array}\right.. \qquad (2.11)$$

In Eq. (2.8), we have used the relation $\sum_m \phi_{n,m}^*(\mathbf{r})\,\phi_{n,m}(\mathbf{r}) = \frac{1}{2\pi\ell^2}$.

The Hamiltonian in Eq. (2.8) is very general. It contains all possible coherences $\left\langle c_{s,m}^{\dagger}c_{s',m'}\right\rangle$ between different angular momenta and spins. These order parameters are used to describe the spin textured states. For example, if the coherence $\left\langle c_{\uparrow,m}^{\dagger}c_{\downarrow,m+\delta}\right\rangle$ is nonzero, then a $2\delta\pi$ rotation of the spin field in real space will occur.

2.2 Single-particle excitations

In the higher Landau levels, the ground state is a quantum Hall ferromagnet and is given by,

$$|GS\rangle = \prod_{m=0}^{\infty} c_{n,\uparrow,m}^{\dagger}|0\rangle. \qquad (2.12)$$

We choose the valley K for our calculation in order to specify the Hamiltonian in Eq. (2.8). The ground state is shown in Fig. (2.1). Each dot represents an electron at certain angular momentum. According to the wave functions in Eq. (1.23), one electron is split into two parts, one part is located at site A and the other is located at site B. Hence, an entire electron should be represented by a two-component spinor. The upper element represents the part at site A, and the lower element represents the part at site B. The

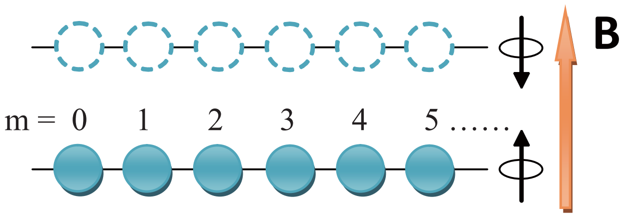

FIGURE 2.1: The spin degenerate ground state (in one valley of an arbitrary Landau level $n > 0$) is split by the Zeeman energy due to external magnetic field **B**. The gap between the two levels is the Zeeman energy $\Delta_B = g\mu_B B$. Each blue ball represents one electron at generalized angular momentum $m = 0, 1, 2, \ldots$ from left to right respectively.

two parts at sites A and B are described by the wave functions of Landau levels $n-1$ and n, respectively. The generalized angular momenta for the two elements of a spinor are the same, although the real angular momenta are different. For convenience, we use the generalized angular momenta to identify the spinor of the entire electron.

For the ground state in Eq. (2.12), the energy per electron is given by

$$\begin{aligned}\frac{E_{GS}}{N_\phi} &= -\frac{1}{2}g\mu_B B \\ &\quad -\frac{1}{8}\sum_{m=0}^{\infty}\left(V_{m,0,0,m}^{n-1,n-1,n-1,n-1} + V_{m,0,0,m}^{n,n,n,n} + 2V_{m,0,0,m}^{n-1,n-1,n,n}\right). \qquad (2.13)\end{aligned}$$

For example, in LL 1 at zero Zeeman coupling,

$$\frac{E_{GS,n=1}}{N_\phi} = -\frac{1}{8}\left(\sqrt{\frac{\pi}{2}} + \frac{3}{4}\sqrt{\frac{\pi}{2}} + \sqrt{\frac{\pi}{2}}\right)\frac{e^2}{\kappa\ell} = -0.430\,83\frac{e^2}{\kappa\ell}. \qquad (2.14)$$

For LL=2,

$$\frac{E_{GS,n=2}}{N_\phi} = -\frac{1}{8}\left(\frac{3}{4}\sqrt{\frac{\pi}{2}} + \frac{41}{64}\sqrt{\frac{\pi}{2}} + \frac{7}{8}\sqrt{\frac{\pi}{2}}\right)\frac{e^2}{\kappa\ell} = -0.354\,94\frac{e^2}{\kappa\ell}. \qquad (2.15)$$

For LL=3,

$$\frac{E_{GS,n=3}}{N_\phi} = -\frac{1}{8}\left(\frac{41}{64}\sqrt{\frac{\pi}{2}} + \frac{147}{256}\sqrt{\frac{\pi}{2}} + \frac{51}{64}\sqrt{\frac{\pi}{2}}\right)\frac{e^2}{\kappa\ell} = -0.315\,16\frac{e^2}{\kappa\ell}. \qquad (2.16)$$

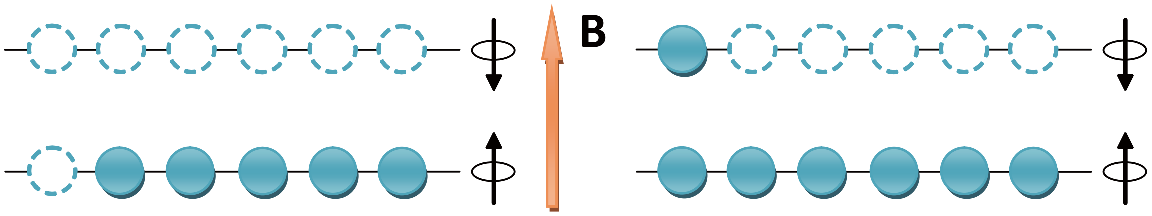

FIGURE 2.2: Quasi-hole state (left) and quasi-electron state (right). Each blue dot represents an entire electron.

2.2.1 Quasi-particle states

Now, we consider the charge excitations without spin texture. If we remove or add one electron from the ground state, we make a quasi-hole or quasi-electron state, respectively. The quasi-particle states are represented in Fig. (2.2). In the symmetric gauge, the quasi-hole and quasi-electron states can be written as

$$|h\rangle = \prod_{m=0,m\neq i}^{\infty} c^{\dagger}_{n,\uparrow,m}\,|0\rangle\,, \tag{2.17}$$

$$|e\rangle = c^{\dagger}_{n,\downarrow,i}\prod_{m=0}^{\infty} c^{\dagger}_{n,\uparrow,m}\,|0\rangle\,, \tag{2.18}$$

respectively. Notice that we put the quasi-particle at $m = i$ (or $M = -n+i$). Physically, the quasi-particle energy is independent of the value of i. In fact, the summation,

$$\sum_{m=0}^{\infty} V^{n,n,n',n'}_{i,m,m,i} = C\left(n,n'\right), \tag{2.19}$$

gives a constant, where C is a constant which does not depend on i, it only depends on the Landau level indices n and n'.

We obtain the excitation energy of a quasi-hole Δ_h and the excitation energy of a quasi-electron Δ_e from the Hamiltonian in Eq. (2.8),

$$\begin{aligned}\Delta_h &= \frac{1}{2}g\mu_B B + \frac{1}{4}\sum_{m=0}^{\infty}\left(V_{i,m,m,i}^{n-1,n-1,n-1,n-1} + V_{i,m,m,i}^{n,n,n,n} + 2V_{m,i,i,m}^{n-1,n-1,n,n}\right), &(2.20)\\ \Delta_e &= \frac{1}{2}g\mu_B B. &(2.21)\end{aligned}$$

Note that adding an electron with opposite spin to the ground state costs no Coulomb energy, the Hartree electron-electron interaction is cancelled by the electron-background interaction and there is no Fock interaction between different spins. For convenience, we set $i = 0$. Hence, the excitation energy of a quasi-particle pair is given by

$$\Delta_{eh} = g\mu_B B + \frac{1}{4}\sum_{m=0}^{\infty}\left(V_{0,m,m,0}^{n-1,n-1,n-1,n-1} + V_{0,m,m,0}^{n,n,n,n} + 2V_{m,0,0,m}^{n-1,n-1,n,n}\right), \quad (2.22)$$

The energy Δ_{eh} is valid when the quasi-hole and quasi-electron are infinitely separated so that there is no interaction between these two quasi-particles.

We can also calculate the excitation energy of quasi-particle in the Landau gauge. The results are identical to Eq. (2.22). The excitation energy Δ_{eh} is directly related to the resistivity measured in a transport experiment by Eq. (2.1). Therefore, the energy gap can be measured by the transport experiment at finite temperature.

2.2.2 Spin-textured excitations

Besides the quasi-particles, another way to excite the system involves spin textures. Yang et al. [9] have proved, using a field theory approach (the nonlinear σ model that we discussed in Sec. 1.5), that the skyrmion can exist up to Landau level $n = 3$ in graphene, while the transport gaps are due to quasi-particle states in higher Landau levels. By contrast, in a semiconductor 2DEG, skyrmions are the lowest-energy charged excitations only in $n = 0$ at filling factor $\nu = 1$ (when the width of the quantum well is neglected) [31, 32].

The same conclusion for graphene was reached by using the density matrix renormalization group (DMRG) method for $n = 0, 1, 2$. For $n = 3$, the skyrmion-antiskyrmion (S-AS) pair and electron-hole (E-H) pair energies are very close and it was not possible to stabilize a skyrmion solution with the DMRG method [36]. Exact diagonalization studies of valley skyrmions have also been done in Ref. [37]. Crystals of valley skyrmions have been shown to be the ground state of the C2DEG around quarter filling of the Landau levels $n = 0, 1$ [38]. A theoretical study of the possible coherence between the spin and valley pseudo-spin in graphene, which could lead to CP^3 skyrmions, was done in Ref. [39]. This work did not include a calculation of the behavior of the transport gap with Zeeman coupling however.

In quantum Hall system, the spin texture of the skyrmion always includes a charge density modulation. However, the nonlinear σ model (NLσM), applying only to large skyrmions, is valid at zero Zeeman coupling, and neglects the Coulomb energy cost to induce the charge modulation. Our approach that uses the Hamiltonian in section 2.1 can deal with smaller skyrmion at finite Zeeman coupling. It also takes into account the Coulomb energy of the charge distribution. Following Fertig et al. [40], we write down the skyrmion and antiskyrmion states as:

$$\begin{aligned} |\mathrm{sk}\rangle &= c^{\dagger}_{n,\downarrow,0} \prod_{m=0}^{\infty} \left(u_m c^{\dagger}_{n,\uparrow,m} + v_m c^{\dagger}_{n,\downarrow,m+\delta} \right) |0\rangle \,, \qquad (2.23) \\ |\mathrm{antisk}\rangle &= \prod_{m=1}^{\infty} \left(u_m c^{\dagger}_{n,\uparrow,m} + v_m c^{\dagger}_{n,\downarrow,m+\delta} \right) |0\rangle \,, \qquad (2.24) \end{aligned}$$

where δ is positive in $|\mathrm{sk}\rangle$ and negative in $|\mathrm{antisk}\rangle$. The normalization condition requires $u_m^2 + v_m^2 = 1$. Furthermore, δ is related to the topological charge Q of the skyrmion or anti-skyrmion. In a quantum Hall system, the topological charge is associated with the electric charge q by the Pontryagin index Q [27, 28],

$$q = Qe. \qquad (2.25)$$

In the NLσM of Eq. (1), the topological charge is defined by Eq. (5). In the field theory, the skyrmion is an exact solution, and the topological charge is an integer. With Zeeman coupling, the skyrmion is no longer the exact solution, and we will see that the topological charge is not exactly quantized.

We now analyze the spin textured states in Eqs. (2.23) and (2.24). If $u_m = 1$ and $v_m = 0$ for all m, then the quasi-particle states in Eqs. (2.18) and (2.17) are recovered: $|sk\rangle \to |e\rangle$ and $|antisk\rangle \to |h\rangle$.

The Zeeman coupling depends on the total magnetic field B_T. By changing the angle θ between the magnetic field and the 2DEG, keeping the magnetic field $B_\perp$ perpendicular to the 2DEG constant, and enlarge the total magnetic field without changing the filling

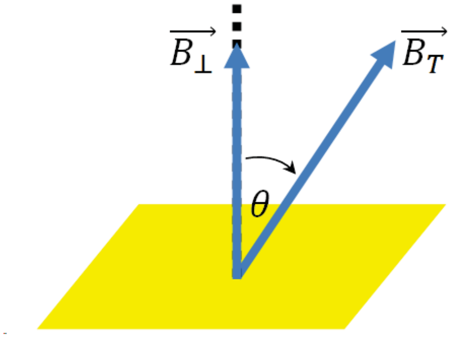

FIGURE 2.3: Rotation of magnetic field from the direction of $\mathbf{B}_\perp$ to the direction $\mathbf{B}_T$. The rotation angle is θ. The perpendicular component of $\mathbf{B}_T$ is $\mathbf{B}_\perp$.

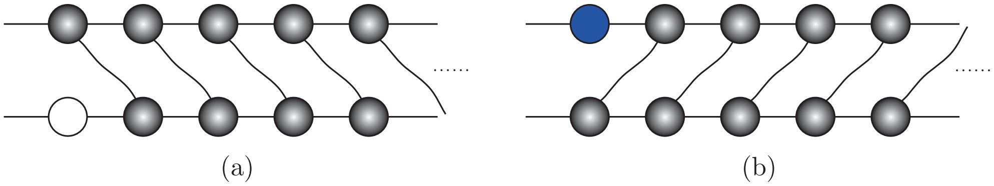

(a)

(b)

FIGURE 2.4: Suppose the topological charge is ±1, i.e. $\delta = -1$ and $+1$ for (a) and (b), respectively. In Landau level n, (a) representsthe antiskyrmion state (Eq. 2.24) where the electron at $m = 0$ ($M = -n$) is removed; (b) represents the skyrmion state (Eq. 2.23), the blue dot is the added electron at $m = 0$ ($M = -n$), but with spin opposite to the electrons in the ground state. The BCS-like pairs are formed in spin texture states. The lines indicate the pairings of states defined by Eqs. (2.23) and (2.24).

factor. The device is shown in Fig. 2.3. In this case, ones can tune the Zeeman coupling without changing the Landau gap or the Coulomb interaction since these quantities are related to the perpendicular component of the magnetic field. At large Zeeman coupling, the quasi-particle states are recovered since the spin flips are too costly.

The added or removed electron flips some spins around it thus making a texture in the spin field. In this case, each spin-up electron with m angular momentum is paired to the spin-down one with $(m \pm 1)$ angular momentum (as shown in Fig. 2.4), so that the projection of spin polarization on the xOy plane rotates by 2π along any path winding around the origin one time. In each pair, there is only one charge or one electron. The electron has a probability u_m^2 to be in the mth angular momentum of spin-up level and a probability v_m^2 to be in the $(m \pm 1)$th angular momentum of spin-down level in a pair. If v_m is nonzero at $m = 0$ and decays to zero as m increases, the direction of spin polarization goes from downward at the origin to upward at infinity and rotates around the origin.

We simplify the general Hamiltonian by inserting the skyrmion states into Eq. (2.8),

$$\begin{aligned} H &= \sum_{s',m'} E_{s'} c^{\dagger}_{n,s',m'} c_{n,s',m'} + \sum_{s',m'} \left(U_{H,m'} - U_{F,s',m'}\right) c^{\dagger}_{n,s',m'} c_{n,s',m'} \\ &\quad - \sum_{m'} U_{sk,m'+\delta} c^{\dagger}_{n,1,m'+\delta} c_{n,0,m'} - \sum_{m'} U^{*}_{sk,m'+\delta} c^{\dagger}_{n,0,m'} c_{n,1,m'+\delta} \\ &\quad - \sum_{s',m'} U_{bg,m'} c^{\dagger}_{n,s',m'} c_{n,s',m'}, \end{aligned} \tag{2.26}$$

where we define

$$E_{s'} = (-1)^{s'} \frac{1}{2} g \mu_B B, \tag{2.27}$$

$$\begin{aligned} U_{H,m'} &= \frac{1}{4} \sum_{s} \sum_{m=0}^{\infty} \left(V^{n-1,n-1,n-1}_{m,m,m',m'} + V^{n,n,n,n}_{m,m,m',m'} + 2V^{n-1,n-1,n,n}_{m,m,m',m'}\right) \\ &\times \left\langle c^{\dagger}_{n,s,m} c_{n,s,m} \right\rangle, \end{aligned} \tag{2.28}$$

$$U_{F,s',m'} = \frac{1}{4} \sum_{m=0}^{\infty} \left(V^{n-1,n-1,n-1}_{m,m',m',m} + V^{n,n,n,n}_{m,m',m',m} + 2V^{n-1,n-1,n,n}_{m,m',m',m}\right) \left\langle c^{\dagger}_{n,s',m} c_{n,s',m} \right\rangle, \tag{2.29}$$

$$\begin{aligned} U_{sk,m'+\delta} &= \frac{1}{4} \sum_{m=0}^{\infty} \left(V^{n-1,n-1,n-1,n-1}_{m,m',m'+\delta,m+\delta} + V^{n,n,n,n}_{m,m',m'+\delta,m+\delta} + 2V^{n-1,n-1,n,n}_{m,m',m'+\delta,m+\delta}\right) \\ &\times \left\langle c^{\dagger}_{n,0,m} c_{n,1,m+\delta} \right\rangle, \end{aligned} \tag{2.30}$$

$$U_{bg,m'} = \frac{1}{4} \sum_{m=0}^{\infty} \left(V^{n-1,n-1,n-1}_{m,m,m',m'} + V^{n,n,n,n}_{m,m,m',m'} + 2V^{n-1,n-1,n,n}_{m,m,m',m'}\right), \tag{2.31}$$

with the spin indices,

$$\uparrow \; = 0, \tag{2.32}$$

$$\downarrow \; = 1. \tag{2.33}$$

In order to find a skyrmion solution, we have to solve for u_m and v_m in Eqs. (2.23) and (2.24). In the HFA, the Hamiltonian in Eq. (2.26) is easy to diagonalize. There are three equivalent methods to do that: (1) minimizing the energy functional of the Hamiltonian; (2) making canonical transformation to diagonalize the Hamiltonian; and (3) using Green's functions. Actually, the three methods are equivalent [41]. In this thesis, only the Green's function method is used.

We define the Green's function:

$$G_{i,j}^{(m)}(\tau) = -\left\langle T_\tau c_{n,i,m+i\delta}(\tau)\, c_{n,j,m+j\delta}^{\dagger}(0)\right\rangle, \tag{2.34}$$

where n is the Landau level and δ is identical to that in Eqs. (2.23) and (2.24). The spin indices $i, j = 0, 1$ according to the Eqs. (2.32) and (2.33). This Green's function is a 2×2 matrix. The number of Green's function matrices is the same as the number of angular momenta used in the system. Since we could not let $m \to \infty$ numerically, it is necessary to put a cut-off on the angular momentum. This approximation is qualified since the order parameters $u_m \to 1$ and $v_m \to 0$ when m is large. Using the same method as in Sec. 1.2, we obtain the matrix equation of motion of the Green's function $G^{(m)}(i\omega_n)$,

$$\left(i\hbar\omega_n I - F^{(m)}\right) G^{(m)} = B^{(m)} \tag{2.35}$$

for each m, since $G^{(m)}$ is not coupled to $G^{(m'\neq m)}$. The elements of the $F^{(m)}$ matrix are given by

$$\begin{aligned}
F_{11}^{(m)} &= E_0 + \left(U_{H,m} - U_{F,0,m} - U_{bg,m}\right), && (2.36)\\
F_{12}^{(m)} &= -U_{sk,m+\delta}^{*}, && (2.37)\\
F_{21}^{(m)} &= -U_{sk,m+\delta}, && (2.38)\\
F_{22}^{(m)} &= E_1 + \left(U_{H,m+\delta} - U_{F,1,m+\delta} - U_{bg,m+\delta}\right). && (2.39)
\end{aligned}$$

We obtain the Green's function self-consistently by diagonalizing the F matrix (see the details in Sec. 1.3). The density matrix at zero temperature is given by

$$\left\langle \rho_{(j,m+j\delta),(i,m+i\delta)}\right\rangle = G_{i,j}^{(m)}\left(\tau = 0^{-}\right), \tag{2.40}$$

where $\rho_{(j,m+j\delta),(i,m+i\delta)} = c_{n,j,m+j\delta}^{\dagger} c_{n,i,m+i\delta}$ is the coherence between an electron with spin j, angular momentum $m + j\delta$ and an electron with spin i, angular momentum $m + i\delta$. The elements of density matrix $\left\langle \rho_{(j,m+j\delta),(i,m+i\delta)}\right\rangle$ are also related to the parameters in Eqs. (2.23) and (2.24) by,

$$\begin{aligned}
\left\langle \rho_{(0,m),(0,m)}\right\rangle &= u_m^2, && (2.41)\\
\left\langle \rho_{(1,m+\delta),(1,m+\delta)}\right\rangle &= v_m^2, && (2.42)\\
\left\langle \rho_{(0,m),(1,m+\delta)}\right\rangle &= u_m v_m. && (2.43)
\end{aligned}$$

In the spin language, we use the wave functions in Eq. (1.23) to calculate the observable quantities: the spin density n_s and the three components of the spin field s_x, s_y, s_z. These order parameters are defined by

$$\begin{aligned}
n_s &= \frac{1}{2}\sum_{m=0}^{\infty}\left(\left|h_{n,m}\right|^2+\left|h_{n-1,m}\right|^2\right)\left\langle\rho_{(s,m+s\delta),(s,m+s\delta)}\right\rangle, & \text{(2.44a)}\\
s_x &= \frac{1}{2}\mathrm{Re}\left[\sum_{m=0}^{\infty}\left(h_{n,m}^{*}h_{n,m+\delta}+h_{n-1,m}^{*}h_{n-1,m+\delta}\right)\right]\left\langle\rho_{(0,m),(1,m+\delta)}\right\rangle, & \text{(2.44b)}\\
s_y &= \frac{1}{2}\mathrm{Im}\left[\sum_{m=0}^{\infty}\left(h_{n,m}^{*}h_{n,m+\delta}+h_{n-1,m}^{*}h_{n-1,m+\delta}\right)\right]\left\langle\rho_{(0,m),(1,m+\delta)}\right\rangle, & \text{(2.44c)}\\
s_z &= \frac{1}{2}\left(n_1-n_0\right). & \text{(2.44d)}
\end{aligned}$$

The spin fields defined here are not normalized to 1, the relation between $\mathbf{s}$ and a unit field $\mathbf{m}$ is given by Eq. (1.91).

2.2.3 Nonlinear σ model for spin skyrmion at zero Zeeman energy or valley skyrmion

According to Sec. 1.4, it is easy to write the excitation energy functional for the QHF. From the Hamiltonian in Eq. (2.26), we obtain the NLσM spin stiffness,

$$\begin{aligned}
\rho_s &= -\frac{1}{4}\frac{1}{2\pi\ell^2}\nabla_q^2 X_n\left(\mathbf{q}\right)|_{q=0}\\
&= \frac{1}{16\pi}\frac{1}{4}\frac{e^2}{\kappa\ell}\int dqq^2e^{\frac{-q^2}{2}}\left[L_n\left(\frac{q^2}{2}\right)+L_{n-1}\left(\frac{q^2}{2}\right)\right]^2, \qquad \text{(2.45)}
\end{aligned}$$

where $X_n\left(\mathbf{q}\right)$ is the Fock interaction written in the Landau gauge, and L_n is a Laguerre polynomial of degree n. The skyrmion or anti-skyrmion excitation energy is given by $\Delta_{skyrmion}=\Delta_{anti-skyrmion}=4\pi\rho_s$, and the excitation energy of a unbound S-AS pair is given by [33]

$$\Delta_{NL\sigma M}=\Delta_{skyrmion}+\Delta_{anti-skyrmion}=8\pi\rho_s. \qquad \text{(2.46)}$$

$\Delta_{skyrmion}$ or $\Delta_{anti-skyrmion}$ gives the energy to make a skyrmion or an anti-skyrmion spin texture and keep the number of electrons constant. These excitations are uncharged. For an isolated skyrmion or antiskyrmion, the energy in field theory is not identical to the charged excitation obtained when one electron is added or removed from the 2DEG.

However, the excitation energy of a S-AS pair given by Eq. (2.46) in field theory is identical to the unbound charged S-AS pair [43]. Hence, we can use Eq. (2.46) to calculate the excitation energy of a unbound charged S-AS pair at zero Zeeman energy.

In a semiconductor 2DEG, it is possible to tune the Zeeman energy by changing the Landé g factor in experiments. It is even possible to change the sign of g. However, in graphene, the Zeeman energy can not be set to zero. It can only be enlarged by tilting the magnetic field. So the excitation energy of a unbound charged S-AS pair at zero Zeeman coupling only exists in theory in graphene. The excitation energy calculated in the microscopic quantum theory should approach the value in Eq. (2.46) when the Zeeman coupling is close to zero.

Due to the SU(2) symmetry, the valley pseudo-spin skyrmion exists around 1/4 and 3/4 fillings of a Landau level. In this case, the analog of the Zeeman energy is the gap between two valleys. It is zero, i.e. the two valleys have the same energy. In this case, the skyrmion excitation must be calculated in NLσM with Eq. (2.46), since the size of skyrmion is infinite and required maximum of m is also infinite, i.e. the microscopic quantum theory fails when the energy difference between the two states considered is zero.

2.2.4 Numerical results at finite Zeeman coupling

The quantum microscopic Hamiltonian and the Green's function method are well suited for calculating the excitation energy and the number of flipped spins at finite Zeeman energy where the size of skyrmion is also finite. However, as we mentioned in the last section, we need to cut off the angular momentum at a large number $m_{\max}$. The single particle orbital with angular momentum m is localized near a ring with radius $\sqrt{2m+1}\ell$, so the size of skyrmion should not exceed a disk of radius $\approx \sqrt{2m_{\max}}\ell$. At the edge of the disk (with radius $\sqrt{2m_{\max}}\ell$), the spin texture should approach that of the ground state outside the disk radius. The associated density profile should also be flat as that of the ground state outside of the disk. However, when the Zeeman coupling decreases below a certain value, the skyrmion size becomes large and $m_{\max}$ becomes too big to handle numerically.

The Landau level wave functions obey the identity

$$\sum_{m=0}^{m_{\max}=\infty} \left|h_{n,m}\left(\mathbf{r}\right)\right|^2 = \frac{1}{2\pi\ell^2}. \tag{2.47}$$

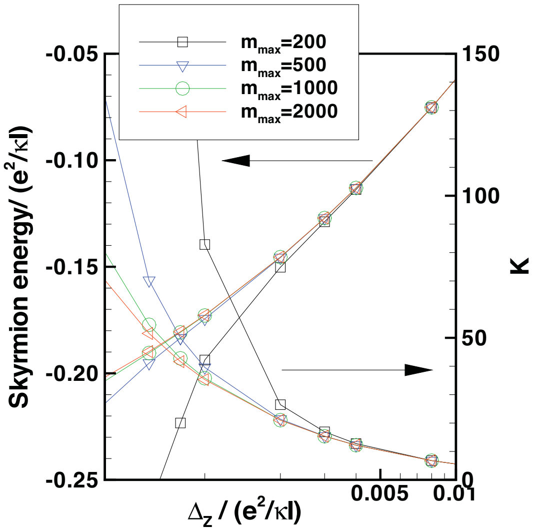

FIGURE 2.5: Energy of one skyrmion E_{sk} and the corresponding number of down spins $N_{\downarrow} = K$ as a function of the Zeeman coupling for different values of the cutoff angular momentum used in the computation. Figure is taken from our publication [29].

In our numerical calculations, we set $m_{\max} = 1000$. It follows that the charged excitation that we compute must be restricted to a disk with radius $r_{\max}/\ell \lesssim 40$. To find out the lowest Zeeman coupling where the calculation with $m_{\max} = 1000$ is reliable, we plot the skyrmion excitation energies E_{sk} as well as the spin flipped number $N_{\downarrow}$ for different $m_{\max}$ in Fig. (2.5). Note that when the Zeeman coupling decreases, the skyrmion energy approaches its asymptotic value much more rapidly with increasing $m_{\max}$. When the Zeeman energy is lower than $0.0005e^2/\kappa\ell$ the calculation with $m_{\max} = 1000$ becomes unreliable.

Because of the electron-hole symmetry around $\nu = 0$ in graphene our calculation for $n > 0$ also applies to Landau levels $n < 0$. In Fig. (2.6), we indicate our numerical results for the excitation energies of a quasi-particle pair and a S-AS pair in Landau levels $|n| = 1, 2, 3$ as a function of the Zeeman coupling. In Fig. (2.6), the lowest Zeeman energy is $0.0004e^2/\kappa\ell$. The excitation energies approach the NLσM results at small Zeeman coupling.

The S-AS energy approaches smoothly the line of the quasi-particle energy in Landau level $|n| = 1$, so that there is a second-order transition between skyrmion and quasi-particle at about Zeeman coupling $\Delta_C^{|n|=1} = 0.048e^2/\kappa\ell$. In Landau level $|n| = 2$, the critical value of the Zeeman energy, where the transition between skyrmion and quasi-

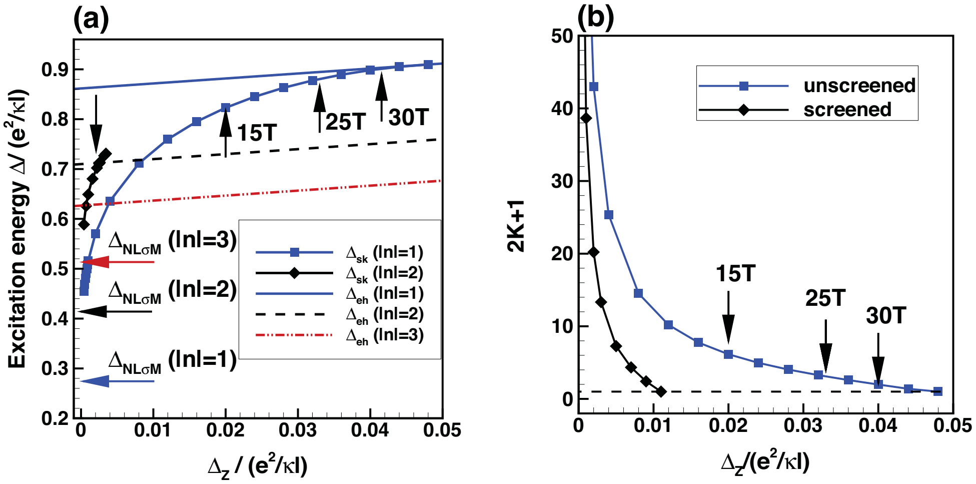

FIGURE 2.6: (a) Excitation energy of a S-AS pair Δ_{S-AS} and an E-H pair Δ_{eh} as a function of the Zeeman coupling Δ_Z in $|n| = 1, 2, 3$. The horizontal arrows indicate the value of the S-AS gap $\Delta_{NL\sigma M}$ calculated in the NLσM. The upward vertical arrows point to values corresponding to total magnetic fields $B = 15, 25, 30$T. The downward arrow points to the value of $\Delta_C^{|n|=2}$. (b) Number of down spins $N_\downarrow = 2K + 1$ in a S-AS pair as a function of Δ_Z in $|n| = 1$ with and without screening. The arrows are placed at $B = 15, 25, 30$T. The dashed line indicates the E-H limit $N_\downarrow = 1$. The results are calculated under the conditions that the perpendicular magnetic field $B_\perp = 15$T and $\kappa = 2.5$. Figures are taken from our publication [29].

particle occurs, is about $\Delta_C^{|n|=2} = 0.0026e^2/\kappa\ell$ which is one order magnitude smaller than the critical Zeeman energy in $|n| = 1$. The existence region of skyrmion is much smaller than $|n| = 1$. The gap Δ_{S-AS} crosses Δ_{eh} at $\Delta_C^{|n|=2}$ and goes over Δ_{eh} when $\Delta_Z > \Delta_C^{|n|=2}$, instead of reaching Δ_{eh} smoothly. Since the number of flipped spins at $\Delta_C^{|n|=2}$ is very large, about 25, there would be an abrupt change of magnitization in the C2DEG at $\Delta_C^{|n|=2}$. A similar first order transition in the magnetization was predicted theoretically for skyrmions in a conventional 2DEG when the finite width of the well was considered at filling factor $\nu = 3$ [32]. This first order transition has been observed in experiments in a conventional 2DEG at $\nu = 1$ [44] and also in a conventional bilayer 2DEG at $\nu = 1$ when the electrons occupy only one of the two layers [45]. Our calculation shows that it can also happen in graphene.

In Landau level $|n| = 3$, the microscopic quantum Hamiltonian calculation is not valid since Δ_{S-AS} is very close to Δ_{eh} even at zero Zeeman coupling. This implies that the existence region of the skyrmion is too small to be calculated numerically. The transition occurs below $0.0002e^2/\kappa\ell$, so the range is approximately one order magnitude smaller than that in $|n| = 2$, based on a rough calculation.

The number of down spins $N_\downarrow > 1$ for a skyrmion-antiskyrmion pair while $N_\downarrow = 1$ for an electron-hole pair. Fig. (2.6b) shows that the rapid increase in energy of Δ_{S-AS} with Δ_Z is associated with a rapid decrease in $N_\downarrow$. At $B_\perp = 15$ T, $N_\downarrow \approx 6$ for n = 1 corresponding to 2.5 flipped spins per skyrmion.

In a skyrmion or an antiskyrmion, a density modulation is always associated with the spin texture, because of the spin charge coupling inherent to quantum Hall ferromagnets. In Fig. (2.7), the density profiles of skyrmions with respects to the ferromagnet ground state density $n_{GS} = 1/(2\pi\ell^2)$ are shown. The induced density is defined as $\delta n = n_{skyrmion} - n_{GS}$. Because of the electron-hole symmetry of the Hamiltonian near half-filling, the density profile of an antiskyrmion is just the opposite to that of the skyrmion, $\delta n_{antisk} = -\delta n$. Fig. (2.7) shows that the size of the skyrmions shrinks with increasing Zeeman coupling and also with increasing Landau level index at fixed Zeeman coupling. Moreover, the size of a skyrmion is proportional to the number of flipped spins. Notice that all skyrmions in Fig. (2.7) are within the calculation limit set by $r_{max} = 35\ell$.

In Fig. (2.8), the spin textures of a skyrmion and an antiskyrmion are indicated. We see that not only the density but also the spin textures are rotationally invariant. This is the reason why we study the skyrmion problem in the symmetric gauge. The in-plane component of the spin winds around the center of the skyrmion counterclockwise

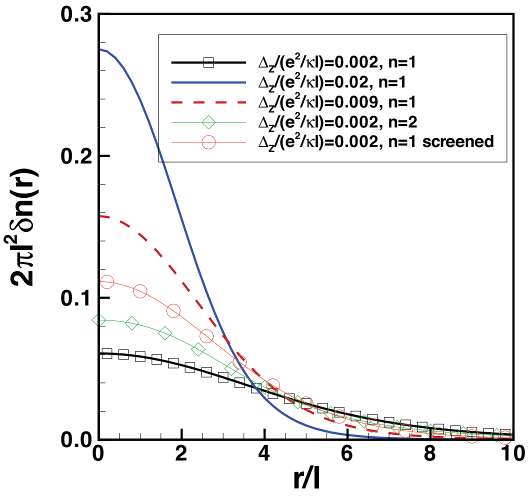

FIGURE 2.7: Profile of the induced density $\delta n\,(r)$ when a skyrmion is added to the ground state in Landau level $n = 1$ for several values of the Zeeman coupling $\Delta_Z/\left(e^2/\kappa\ell\right)$. The profiles for the screened skyrmion in $n = 1$ and the unscreened skyrmion in $n = 2$ are also shown. Because of the electron-hole symmetry, the results in the picture are also valid for the corresponding negative Landau levels. Figure is taken from Ref. [29].

(skyrmion) or clockwise (antiskyrmion). For a topological charge $Q = \pm 1$, the rotation angles are $\pm 2\pi$. At infinity (far enough from the center), the spin texture is that of the ferromagnetic ground state.

We have discussed the topological charge and Pontryagin index in Eqs. (2.25) and (**??**). The skyrmion is defined in the field theory via the NLσM where the topological charge Q is an integer, 1 for skyrmion and -1 for antiskyrmion. However, at finite Zeeman coupling, the skyrmion is not perfect and is not exactly the same as the one defined in NLσM. Hence, the topological charge at nonzero Zeeman coupling is not an integer, but just a number between 0 and 1. Consequently, when the Zeeman coupling $\Delta_Z \to 0$, the topological charge $Q \to \pm 1$. Indeed, a numerical integration of the topological charge defined in Eq. (**??**) proves this point. The integration of the density profile in Fig. (2.7) shows that the total charge by contrast with the topological charge, however, is always $q = -e$ for a skyrmion and $q = e$ for an antiskyrmion. We remark that (anti-)skyrmion can have topological charge $Q = \pm 1, \pm 2, \ldots$. However, creating skyrmion with high $|Q|$ requires more energy than the one with low $|Q|$. We would like to consider the lowest excitation in the C2DEG, so that we do not consider the case of $|Q| > 1$.

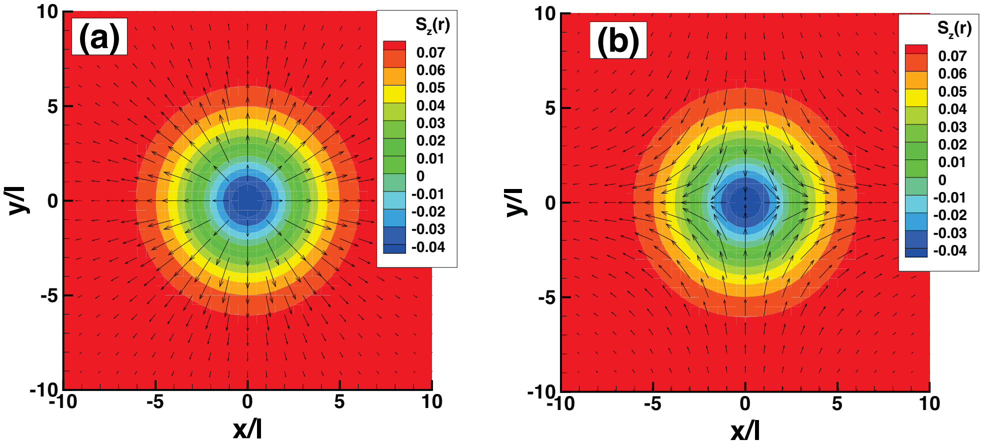

FIGURE 2.8: Spin texture in the $x-y$ plane for a (a) skyrmion and (b) an antiskyrmion in Landau level $|n|=1$ at Zeeman coupling $\Delta_Z = 0.011\left(e^2/\kappa\ell\right)$. The color plot shows $s_z\left(r\right)$ in units of $\hbar/(2\pi\ell^2)$. Figures are taken from Ref. [29].

Our results can be compared with those of Ref. [12] [see Fig. 2(e) of this paper] where the transport gap was measured at total magnetic fields $B=15,25,30$T with the perpendicular magnetic field $B_\perp = 15$T kept fixed. The substrate under graphene in the experiment is Boron Nitride (BN) with a dielectric constant $\kappa = 2.5$ in CGS units. The experiment was carried out at filling factors $\nu = -4,-8,-12$ in Landau levels $n=-1,-2,-3$ respectively. At $B=15,25,30$T, according to our calculations in Fig. (2.6.a), the transport gap is given by the skyrmion-antiskyrmion pair in $n=-1$ and electron-hole pairs in $n=-2,-3$. This result is consistent with the experimental result except for $n=-2$. In this case, the experiment observes a small number of spin flips, $N_\downarrow \approx 1.4$ (in experiment, the flip number is obtained by the differential $N_{flip} = \partial\Delta_{sk}/\partial\Delta_Z$) which is very close to the electron-hole flipping $N_\downarrow^{eh} = 1$ though. It still suggests that $\Delta_{sk}^{|n|=2} < \Delta_{eh}^{|n|=2}$, i.e. the skyrmion is still favored. However, we cannot explain this difference with our model of skyrmion excitations.

Another difference between the experimental and theoretical results is the size of the transport gap. For example, the experimental value of $\Delta_{sk}^{|n|=1} \approx 75$K at $B=30$T, while we find $\Delta_{sk}^{|n|=1} \approx 910$K, one order magnitude higher than the experimental result. Several effects may affect our results such as disorder, Landau level mixing [31], and screening. In a conventional 2DEG, the quantum well width is also considered to decrease the excitation energy, but this effect does not exist in graphene, because the wave function along the z direction is a delta function, since graphene is a one atomic layer material. The important effects must come from disorder, LL mixing and screening. However, disorder and LL mixing are difficult to handle, so we deal with the screening first.

2.3 Landau level screening

Screening in a metal is very important, since there is no gap in a metallic state. For an insulator, the screening effect is weak, since the gap between the valence and conduction bands is large. In a quantum Hall system, the screening effect depends on the value of the LL gap.

To study the effect of screening on the excitation energy of skyrmion and quasi-particle, we need to compute the dielectric function $\epsilon\left(\mathbf{q}\right)$ (we consider the static screening only, leaving the dynamical screening correction to a future work). The bare Coulomb potential $V(q) = 2\pi e^2/\kappa q$ has to be replaced by the screened interaction $V_s(q) = 2\pi e^2/\epsilon(q)\kappa q$. Because of screening, $\epsilon(q) \geq 1$ and the excitation energy of transport gap is reduced.

Next, we calculate the dielectric function in the random phase approximation (RPA). In RPA, the screened Coulomb potential is given by

$$V_s\left(q\right) = \frac{V\left(q\right)}{1 - V\left(q\right)\chi_{nn}\left(q\right)}, \tag{2.48}$$

where χ_{nn} is the density-density response function. The dielectric function is given by

$$\epsilon\left(q\right) = 1 - V\left(q\right)\chi_{nn}\left(q\right) = 1 - \frac{2\pi e^2}{\kappa q}\chi_{nn}\left(q\right). \tag{2.49}$$

We have discussed the response function in Sec. 1.3. The density-density two-particle Green's function is defined by,

$$\begin{aligned}
\chi_{nn}\left(\mathbf{q},\tau\right) &= -\frac{1}{\hbar S}\left\langle T_\tau \delta n\left(\mathbf{q},\tau\right)\delta n\left(-\mathbf{q},0\right)\right\rangle \\
&= \frac{N_\phi}{\hbar S}\sum_{n_1,n_2,n_3,n_4}\Theta_{n_1,n_2}\left(-\mathbf{q}\right)\Theta_{n_3,n_4}\left(\mathbf{q}\right)\sum_{\sigma_1,\sigma_2,\sigma_3,\sigma_4}\chi^{\sigma_1,\sigma_2,\sigma_3,\sigma_4}_{n_1,n_2,n_3,n_4}\left(\mathbf{q},\tau\right),
\end{aligned} \tag{2.50}$$

where we use

$$n\left(\mathbf{q},\tau\right) = N_\varphi\sum_{n_1,n_2}\sum_{\sigma_1,\sigma_2}\Theta_{n_1,n_2}\left(-\mathbf{q}\right)\rho^{\sigma_1,\sigma_2}_{n_1,n_2}\left(\mathbf{q},\tau\right)\delta_{\sigma_1,\sigma_2}, \tag{2.51}$$

and define the two-particle Green's function

$$\chi_{n_1,n_2,n_3,n_4}^{\sigma_1,\sigma_2,\sigma_3,\sigma_4}(\mathbf{q},\tau) = -N_\varphi \left\langle T_\tau \delta\rho_{n_1,n_2}^{\sigma_1,\sigma_2}(\mathbf{q},\tau)\, \delta\rho_{n_3,n_4}^{\sigma_3,\sigma_4}(-\mathbf{q})\right\rangle . \tag{2.52}$$

The index n under χ means density, n_i is the Landau level index and σ_i is the spin-valley index. N_ϕ is the Landau level degeneracy and S is the area of the sample. In the simplest approximation, the correlation function χ_{nn}^0 is given by the noninteracting two-particle Green's function $\chi_{n_1,n_2,n_3,n_4}^{0,\sigma_1,\sigma_2,\sigma_3,\sigma_4}$,

$$\chi_{nn}^0(\mathbf{q},i\Omega_n) = \frac{N_\varphi}{\hbar S} \sum_{n_1,n_2,n_3,n_4} \Theta_{n_1,n_2}(-\mathbf{q})\, \Theta_{n_3,n_4}(\mathbf{q}) \sum_{\sigma_1,\sigma_2,\sigma_3,\sigma_4} \chi_{n_1,n_2,n_3,n_4}^{0,\sigma_1,\sigma_2,\sigma_3,\sigma_4}(\mathbf{q},i\Omega_n)\, \delta_{\sigma_1,\sigma_2}\delta_{\sigma_3,\sigma_4}. \tag{2.53}$$

According to Sec. 1.3, the noninteracting two-particle Green's function is given by

$$\chi_{n_1,n_2,n_3,n_4}^{0,\sigma_1,\sigma_2,\sigma_3,\sigma_4}(\mathbf{q},i\Omega_n) = \frac{\delta_{\sigma_2,\sigma_3}\delta_{n_2,n_3}\left\langle \rho_{n_1,n_4}^{\sigma_1,\sigma_4}(\mathbf{0})\right\rangle - \delta_{\sigma_1,\sigma_4}\delta_{n_1,n_4}\left\langle \rho_{n_3,n_2}^{\sigma_3,\sigma_2}(\mathbf{0})\right\rangle}{i\Omega_n + (E_{n_1,\sigma_1} - E_{n_2,\sigma_2})/\hbar}, \tag{2.54}$$

where E_{n_1,σ_1} is the kinetic energy of Landau level n_1 with spin-valley index σ_1. In this thesis, only the static dielectric function is considered. We first take the analytic continuation $i\Omega_n \to \omega + i\delta$ in Eqs. (2.53) and (4.83) to get the retarded function χ^R. Then we set $\omega \to 0$ to obtain the static dielectric function.

In graphene, the form factor Θ is given by,

$$\Theta_{n,n'}(\mathbf{q}) = \frac{1}{\sqrt{2^{2-\delta_{n,0}-\delta_{n',0}}}}\left[F_{|n|,|n'|}(\mathbf{q}) + sgn(n)\, sgn(n')\, F_{|n|-1,|n'|-1}(\mathbf{q})\right], \tag{2.55}$$

where

$$F_{n,n'}(\mathbf{q}) = \frac{\sqrt{\min(n,n')!}}{\sqrt{\max(n,n')!}} e^{-q^2\ell^2/4} \left[\frac{(sgn(n-n')\, q_y + i q_x)\,\ell}{\sqrt{2}}\right]^{|n-n'|} L_{\min(n,n')}^{|n-n'|}\left(\frac{q^2\ell^2}{2}\right). \tag{2.56}$$

We find that the dielectric function at filling factor ν is the same as that at $-\nu$, i.e. $\epsilon_\nu = \epsilon_{-\nu}$. Hence, the screening effect does not change the electron-hole symmetry in graphene.

The dielectric function $\epsilon(q)$ of the C2DEG has been studied previously [48]. We show our numerical results obtained at different filling factors in Fig. (2.9). In our calculation, we also need to set a cut-off of the Landau levels in the summation in Eq. (2.53). The effects from very high or very low Landau levels are weak (especially at small q). It is

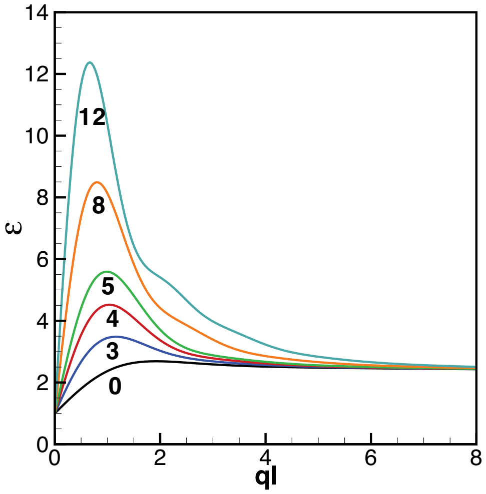

FIGURE 2.9: Static dielectric functions computed in the RPA at different filling factors $|\nu|$ (indicated by the number below each curve) in Landau levels $|n| = 0, 1, 2, 3$. Figure is taken from Ref. [29].

reasonable to restrict the Landau levels to the range $[-800, 800]$, because in this region, the summation in Eq. (2.53) converges below $q\ell < 20$, and the integrand in the Coulomb interaction also approaches zero rapidly when $q\ell \gtrsim 20$. The dielectric function $\epsilon(q) = 1$ at $q = 0$ and $q \to \infty$. The maximal value is around $q\ell \approx 1$ and increases with increasing absolute values of the filling factors (for both electron and hole). In particular, screening is larger at 3/4 filling of a given Landau level than at 1/4 filling for all the Landau levels as shown in Fig. (2.9). This fact is important in the next section when we discuss the valley skyrmion.

To include screening properly, we follow Ref. [49] where it was shown that when all the Landau levels under the partially filled level are integrated out, the low frequency dynamics of the 2DEG is described by the electrons belonging to the partially filled Landau level, but the Coulomb interaction between these electrons as well as the electron-background and background-background interactions are renormalized due to the polarizability of all the other Landau levels. Since the filled Landau levels constitute an ”external” system for the electrons in the partially filled level, both the Hartree and Fock interactions must be screened. Such procedure was used, for example, in the study of inhomogeneous states such as bubble and stripe phases in quantum Hall systems [50]. Our single-particle excitation problem is also an inhomogeneous system. Hence, the way to screen the Coulomb interaction is simply to replace all the Coulomb interaction elements $V^{(s),n_1,n_2,n_3,n_4}_{M_1,M_2,M_3,M_4}$ by the screened ones

$$\begin{aligned}
V^{(s),n_1,n_2,n_3,n_4}_{m_1,m_2,m_3,m_4} &= \frac{e^2}{\kappa\ell}\delta_{M_1-M_2+M_3-M_4}\sqrt{\frac{\min(m_1,m_2)!\min(m_3,m_4)!}{\max(m_1,m_2)!\max(m_3,m_4)!}} \\
&\times\sqrt{\frac{\min(n_1,n_2)!\min(n_3,n_4)!}{\max(n_1,n_2)!\max(n_3,n_4)!}}\int dk\frac{e^{-k^2}}{\epsilon(k)}\left(\frac{k^2}{2}\right)^{|n_1-n_2|+|m_1-m_2|} \\
&\times(-1)^{|n_1-n_2|}_{n_1<n_2}(-1)^{|n_3-n_4|}_{n_3\geq n_4}i^{|m_1-m_2|}(-i)^{|m_3-m_4|} \\
&\times L^{|n_1-n_2|}_{\min(n_1,n_2)}\left(\frac{k^2}{2}\right)L^{|n_3-n_4|}_{\min(n_3,n_4)}\left(\frac{k^2}{2}\right)L^{|m_1-m_2|}_{\min(m_1,m_2)}\left(\frac{k^2}{2}\right)L^{|m_3-m_4|}_{\min(m_3,m_4)}\left(\frac{k^2}{2}\right) \quad (2.57)
\end{aligned}$$

in all the interactions in Eqs. (2.28), (2.27), (2.30), and (2.31). The electron-hole excitation energy in Eq. (2.22) is also screened by replacing V by $V^{(s)}$. Note that if we only screen the Fock interaction as we normally do in a screened exchange approximation, the excitation energies of the quasi-particle states depend on the angular momenta of the added or removed electron, which is unphysical. For the zero Zeeman case, where the NLσM is valid, the spin stiffness in Eq. (2.45) which is from the Fock interaction must be replaced by the screened version:

$$\rho_s^{(s)} = \frac{1}{16\pi}\frac{1}{4}\frac{e^2}{\kappa\ell}\int\frac{dq}{\epsilon(q)}q^2e^{\frac{-q^2}{2}}\left[L_n\left(\frac{q^2}{2}\right)+L_{n-1}\left(\frac{q^2}{2}\right)\right]^2. \quad (2.58)$$

How the screening changes the energies of an electron-hole pair and the skyrmion-antiskyrmion pair is shown in Fig. (2.10). The results are obtain at dielectric constant $\kappa = 2.5$ and magnetic field $B = 10$T. The screening correction significantly decreases the excitation energies. However the highest Landau level in which skyrmion exists is still $|n| = 3$. We see that the $\Delta^{(s)}_{eh}$ is much closer to $\Delta^{(s)}_{NL\sigma M}$ in $|n| = 3$ than that in the unscreened case. So the existence region of a skyrmion at finite Zeeman coupling would be too narrow to calculate in the microscopic quantum method. In Fig. (2.11), we see that the existence regions of skyrmions in all the Landau levels are narrowed very much. In $|n| = 2$, the results in Fig. (2.11) are not very reliable, since the Zeeman energies are too small and the skyrmions are too large. However, we can say that the first order transition occurs at $\Delta_Z \approx 0.0001e^2/\kappa\ell$.

At the end of this section, we would like to compare our results with the experimental measurements. From Figs. and (2.10) and (2.11), we find that the skyrmion still exists

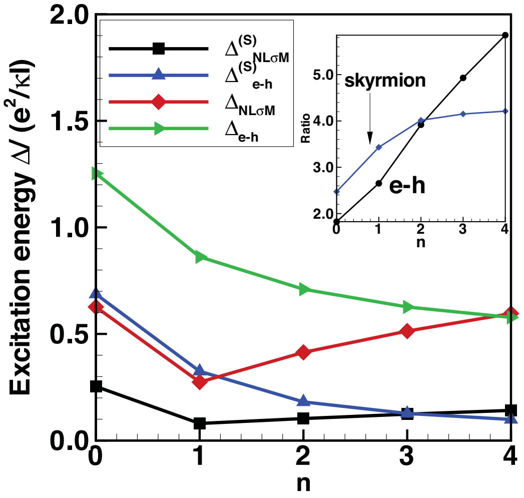

FIGURE 2.10: Evolution of the $NL\sigma M$ and electron-hole transport gaps at zero Zeeman coupling in Landau levels $|n| = 1, 2, 3$. The full lines are only a guide to the eyes. The inset shows the ratios $\Delta_{eh}/\ \Delta_{eh}^{(S)}$ and $\Delta_{NL\sigma M}/\ \Delta_{NL\sigma M}^{(S)}$ with Landau level index. Figure is taken from Ref. [29].

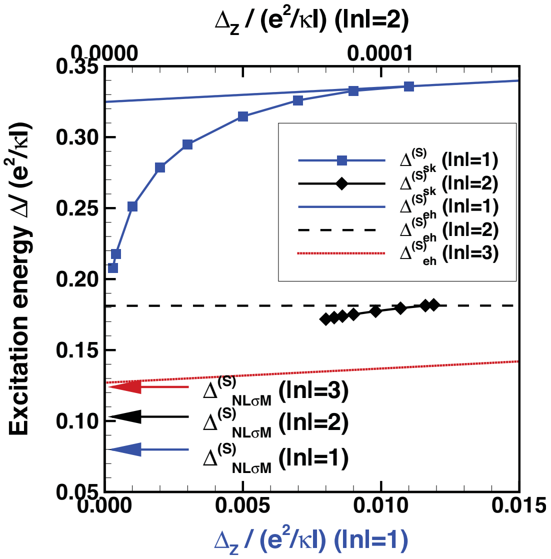

FIGURE 2.11: In HFA, the excitation energies of an electron-hole pair $\Delta_{eh}^{(s)}$ and a spin skyrmion-antiskyrmion pair $\Delta_{sk}^{(s)}$ with screening corrections in Landau levels $|n| = 1$ (lower x axis), $|n| = 2$ (upper x axis) and $|n| = 3$ (lower x axis) at half-filling. The arrow points to the excitation energy of skyrmion-antiskyrmion pair obtained by $NL\sigma$ model at zero Zeeman coupling with a screened spin stiffness. Figure is taken from Ref. [29].

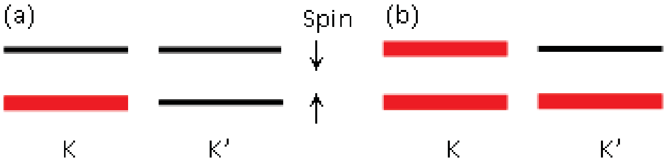

FIGURE 2.12: The ground states at (a) 1/4 and (b) 3/4. Red thicker lines represent filled levels and black ones represent empty levels. The valley pseudo-spin is chosen to be polarized.

even when the screening correction is considered, but the excitation energies are significantly decreased. The energies of a skyrmion-antiskyrmion pair is still 4 times larger than the experimental results [12]. This is mostly due to the Landau level broadening. If we take the broadening into account, the effective Zeeman coupling Δ_Z^{eff} is less than $\Delta_Z = g\mu_B B$. For example, at $B = 15$T, $\Delta_Z = 0.02e^2/\kappa\ell$ the skyrmion does not exist, according to Fig. (2.11). However, the real Zeeman gap, $\Delta_Z^{eff} < 0.02e^2/\kappa\ell$, and the S-AS pair energy is in reality smaller than what we have computed, so that skyrmion could be the lowest charged excitation.

2.4 Valley skyrmion at 1/4 and 3/4 fillings

In the NLσM, we can also study the valley skyrmion at 1/4 and 3/4 fillings. Due to the SU(2) symmetry of valleys, the valley pseudo-spin orientation is arbitrary. So the ground states could be valley polarized, as shown in Fig. (2.12).

In both the 1/4 and 3/4 cases, the four-level system can also be simplified to a two-level system. The Zeeman coupling is finite while the effective Zeeman energy between valleys is zero. So the electrons favor the valley pseudo-spin coherence rather than spin coherence. Experimentally, the lowest-energy charged excitations may be valley skyrmions [12]. Since the excitation energies do not depend on Zeeman energy. Therefore, the 4-level system is reduced to a 2-valley-level system with spin ↑ at 1/4 filling or a 2-valley-level system with spin ↓ at 3/4 filling. In such a system, the effective "Zeeman" coupling is zero, so that the NLσM is valid.

We use the unscreened and screened pseudo-spin stiffnesses in Eqs. (2.45) and (2.58) to calculate the energies of valley skyrmions. In Fig. 2.13, the 1/4 and 3/4 fillings in $|n| = 1$ correspond to $|\nu| = 3, 5$ respectively; the 1/4 and 3/4 fillings in $|n| = 2$ correspond

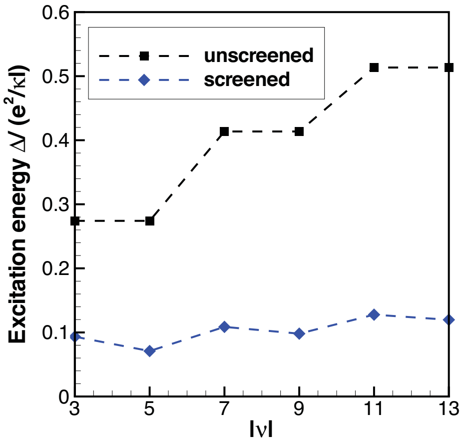

FIGURE 2.13: Excitation energy of a valley skyrmion-antiskyrmion pair for different filling factors with and without screening corrections. The screening is calculated with the parameters: $\kappa = 2.5$, $B = 15$T. The dashed lines are only a guide to the eyes. Figure is taken from Ref. [29].

to $|\nu| = 7, 9$ respectively; the 1/4 and 3/4 fillings in $|n| = 3$ correspond to $|\nu| = 11, 13$ respectively.

The screening at 3/4 filling are stronger than at 1/4 filling. So we see that the electron-hole symmetry in a Landau level is broken, and the valley skyrmion energy at 1/4 is higher than that at 3/4. This conclusion agrees with the experimental results shown in Fig. 2.14. Experimentally, the transport gaps also depend on other effects, such as disorder. Our numerical results can not be exactly equal to the experimental ones.

In fact, the BN substrate is able to flatten the graphene sheet very much [47]. So the impurities are much weaker than those on a SiO_2 substrate. If we do not consider impurities, then the disorder basically renders the background inhomogeneous. These inhomogeneities are also screened. We assume that the disorder is weak, and the disorder at 1/4 filling is the same as that at 3/4 filling without screening. The disorder $|\Gamma| \ll \Delta_{valleysk}$ should be added to the total transport gap Δ_{trans} in absence of screening. If the disorder is screened in the same way as skyrmions are, then we can estimate the ratio of the transport gaps at 1/4 and 3/4 fillings. Because of the screening effect, $\Gamma \to \Gamma^{(s)}$, and

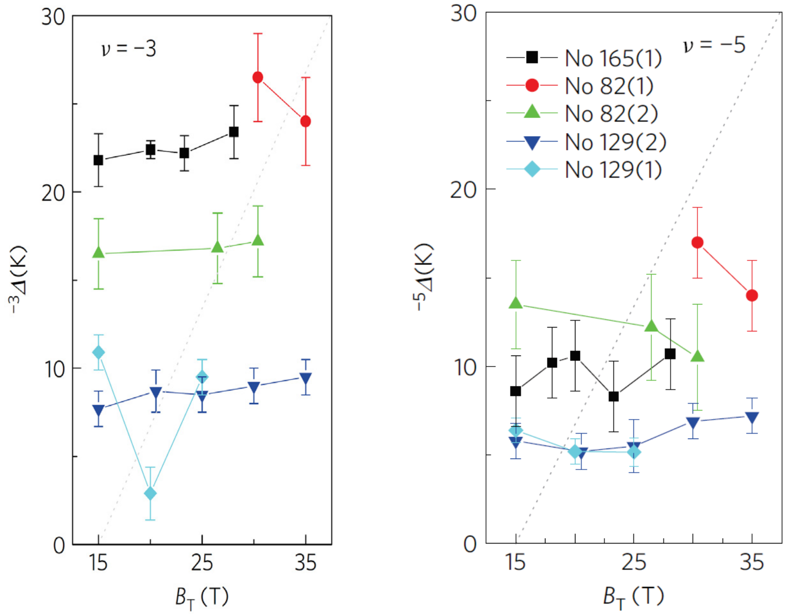

(a) (b)

FIGURE 2.14: The perpendicular magnetic field is 15T. Tilting the magnetic field angle to enlarge the Zeeman coupling. (a) and (b), which are extracted from Figs. 4b and 4c in Ref. [12], are the dependence between the excitation energies and total magnetic field at $\nu = -3$ and -5 for different samples (different dots). The excitation energies are almost independent of the Zeeman coupling.

$\Gamma^{(s)} \approx \frac{\Delta^{(s)}_{valleysk}}{\Delta_{valleysk}}\Gamma$, we obtain the ratio, in the Landau level $n = 1$:

$$
\begin{aligned}
\frac{\Delta^{\nu=3}_{trans}}{\Delta^{\nu=5}_{trans}} &= \frac{\Delta^{(s),\nu=3}_{valleysk} + \Gamma^{(s),\nu=3}}{\Delta^{(s),\nu=5}_{valleysk} + \Gamma^{(s),\nu=5}} \\
&\approx \frac{\frac{\Delta^{(s),\nu=3}_{valleysk}}{\Delta^{\nu=3}_{valleysk}}\left(\Delta^{\nu=3}_{valleysk} + \Gamma\right)}{\frac{\Delta^{(s),\nu=5}_{valleysk}}{\Delta^{\nu=5}_{valleysk}}\left(\Delta^{\nu=5}_{valleysk} + \Gamma\right)} \\
&= \frac{\Delta^{(s),\nu=3}_{valleysk}}{\Delta^{(s),\nu=5}_{valleysk}} = 1.3 \qquad (2.59)
\end{aligned}
$$

in the numerical calculation, which is almost the same as the experimental results in Fig. 2.14 (extracted from Fig. 4 in Ref. [12]).

In this chapter, we study the single skyrmion excitation in graphene system in LL $|N| > 0$ with Zeeman coupling and screening correction. We also try to compare our numerical results with the experiment. Our numerical results for a spin skyrmion around half-filled LL agree with the experiment qualitative. Moreover, we explain quantitatively by the screening effect why the transport gap at 1/4 filling is different from that at 3/4 filling.

Chapter 3

Pseudo-spin textured phases in bilayer graphene in LL $N = 0$

The Bernal-stacked bilayer graphene (BLG) was introduced in Chapter 1. By properly gating the structure, it is possible to control both the total electron density in the BLG as well as the density in each layer. The electric field created by the gates also open a gap between the two degenerate bands at the K and K' points.

In this chapter, we use the HFA to explore the possible crystal phases at and near integer filling factors in the Landau level $N = 0$. We then study some experimental signatures of these phases such as their collective modes and electromagnetic absorption.

In Section 1.2, we have studied the crystal structure of the Bernal stacked graphene bilayer. The tight binding Hamiltonian for the band structure is given in Eq. (1.25). In Section 1.2.1, we have shown that it was possible to derive a simple effective two-component model to analyse the electronic properties in $N = 0$. In the presence of a transverse magnetic field, the two-component model is a particularly good approximation in $N = 0$ [76]. We use this model in this chapter.

In the absence of external electric field and Zeeman coupling and when the small quantities $\gamma_4 = \Delta = 0$ in Eqs. (1.37), (1.38), (1.39) and (1.40), the LL $N = 0$ has 8-fold degeneracy: 2 spins by 2 valleys by 2 orbitals. Consequently, an electron in the $N = 0$ must be described by its spin, valley (or layer), and orbital quantum numbers $n = 0, 1$ in addition to its guiding center index X in the Landau gauge. We remark that the filling factors range from -4 to 4 in $N = 0$. When the Coulomb interaction is taken into account, a rich phase diagram for the bilayer graphene's 2-dimensional electron gas

(2DEG) appears.

In recent works [51–53], it was shown that the octet degeneracy in $N = 0$ is lifted by the Coulomb interaction. The broken symmetry ground states can be described in the pseudo-spin language in which the two valleys (or two orbitals) are supposed to be the pseudo-spin "up" and "down". The coherence between valleys or between orbitals can be represented by a valley or an orbital pseudo-spin. Due to the tunable electric field and the orbital degeneracy, the phase diagram is very rich and interesting. The extra orbital degree of freedom provides different Coulomb interaction from that in a conventional 2DEG when we study the ground states and excitations.

It is known that the topological excitations, such as skyrmion, exist near $\nu = 1$ in a normal 2DEG semiconductor [27]. The spin texture can be found in Sec. 1.3. In bilayer graphene, the orbital pseudo-spin may also be textured in an excitation.

We study the phase diagram of the $N = 0$ LL assuming that the C2DEG is fully spin polarized and neglecting LL mixing. We present several crystal phases with valley or orbital pseudo-spin texture at and near some integer filling factors in $N = 0$.

3.1 Hartree-Fock Hamiltonian

The effective two-component model for the BLG structure is given by

$$H_K = \begin{pmatrix} -\frac{\Delta_B}{2} + (\beta\Delta_B + \zeta_1)\, aa^\dagger & \beta\gamma_1 a^2 \\ \beta\gamma_1 \left(a^\dagger\right)^2 & \frac{\Delta_B}{2} + (-\beta\Delta_B + \zeta_1)\, a^\dagger a \end{pmatrix}, \tag{3.1}$$

$$H_{K'} = \begin{pmatrix} -\frac{\Delta_B}{2} + (\beta\Delta_B + \zeta_1)\, a^\dagger a & \beta\gamma_1 \left(a^\dagger\right)^2 \\ \beta\gamma_1 a^2 & \frac{\Delta_B}{2} + (-\beta\Delta_B + \zeta_1)\, aa^\dagger \end{pmatrix}, \tag{3.2}$$

where we define

$$\zeta_1 = \beta\Delta + \beta_4, \tag{3.3}$$

$$\beta = \frac{u_0^2}{\gamma_1^2}, \tag{3.4}$$

$$\beta_4 = 2\frac{u_0 u_4}{\gamma_1}, \tag{3.5}$$

and u_i is defined in Eq. (1.28). An external electric field lifts both the valley and the orbital degeneracies. It introduces a gap Δ_B between the K and K' valleys. The kinetic energies of the two oribals are given by Eqs. (1.37) and (1.38) in the K valley, and by

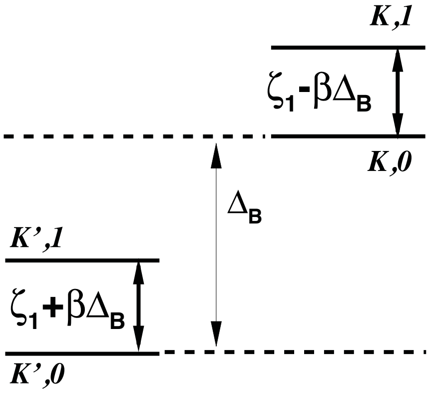

FIGURE 3.1: Noninteracting levels in the LLL with respect to an electric field Δ_B. The spin is neglected here, so there are four levels in all.

Eqs. (1.39) and (1.40) in the K' valley. The positions of the four levels are plotted in Fig. 3.1.

If two states $|0\rangle$ and $|1\rangle$ are coherent, then the order parameter $\langle c_0^\dagger c_1\rangle$ is nonzero, where operators c_i and $c_i^\dagger$ are the annihilation and creation operators of state $|i\rangle$. The Coulomb interaction can induce two coherent states. Let us define the coherence first. If $c^\dagger_{\alpha,n,X}$ is a fermion operator that creates an electron in the state (α, n, X) in the Landau gauge (where the valley index $\alpha = K, K'$, $n = 0, 1$ is the orbital index, and X is the guiding center index), then a state where $\left\langle c^\dagger_{\alpha,n,X} c_{\alpha,n,X}\right\rangle_{\alpha\neq\sigma} \neq 0$ has inter-valley (or interlayer in the LLL) coherence while a state with $\left\langle c^\dagger_{\alpha,n,X} c_{\alpha,m,X}\right\rangle_{m\neq n} \neq 0$ has inter-orbital coherence. In the most general case, both coherences occur.

It is shown in Refs. [51–53] that when $\zeta_1 = 0$, the phase diagram of the 2DEG at integer filling factors $\nu \in [-3, 4]$ contains phases with interlayer and/or inter-orbital coherence. Due to the small interlayer spacing ($d = 3.337$Å$\ll \ell$) in a graphene bilayer, the capacitive energy which balances the charge in two layers (or equivalently in the two valleys) is so small that the interlayer coherence is rapidly lost when the bias Δ_B increases i.e. for $\Delta_B \gtrsim 0.001\,(e^2/\kappa\ell)$ according to Ref. [51–53] (κ is the effective dielectric constant of the substrate). Above this value, inter-orbital coherence sets in when $E^{N=0}_{K,0} = E^{N=0}_{K,1}$. Since the orbital index is not necessarily conserved, the Coulomb interaction can make the two orbitals coherent. If the C2DEG is assumed fully spin polarized, orbital coherence is only possible when valley K is partially filled and valley K' is fully filled. This is because, as Fig. 3.1, the state $|K, 1\rangle$ can be made lower in energy than the state $|K, 0\rangle$. When the Coulomb exchange energy is optimal in $|K, 0\rangle$, there is in this case a competition between bias and Coulomb energies, and obital coherence sets in. This possibility does not exist in valley K' since $E_{K',1} \geq E_{K',0}$ for any bias.

We would like to study the pure orbital coherence crystal phases, so that we need to apply a sufficient electric field ($\Delta_B > 0.001e^2/\kappa\ell$) to avoid the valley coherence. At $\nu = -1, 3$, i.e. three or seven levels are filled in the LL, the valley pseudo-spin is polarized, since the gap between two valleys Δ_B is large enough. For other filling factors, the orbital coherence may be disappeared or mixed with other coherence (like valley or spin coherence). Hence, we study the orbital crystal phases at or near $\nu = -1, 3$.

The precise values of the bias for the transitions between the different liquid phases at integer filling factors are very sensitive to the exact values of the hopping parameters. The same is true for the boundaries between various crystal phases at non-integer filling factors. We assume $\zeta_1(\gamma_4, \Delta) = 0$ for all our calculations. In fact, this simplification is acceptable since both γ_4 and Δ are much smaller than γ_0, and the finite γ_4 and Δ are equivalent to a finite shift of Δ_B. In our opinion, reliable determination of the phase boundary characterizing the many possible crystalline phases will require experimental input.

Whether at filling factor -1 or 3, there is a 4-level system if the spin degree of freedom is frozen. We could write down the Coulomb interaction in the second quantization language as,

$$H_{Coulomb} = \frac{1}{2} \sum_{\alpha,\sigma} \int d\mathbf{u} \int d\mathbf{u}' \Phi_\alpha^\dagger (\mathbf{u}) \Phi_\sigma^\dagger (\mathbf{u}') V (\mathbf{u} - \mathbf{u}') \Phi_\sigma (\mathbf{u}') \Phi_\alpha (\mathbf{u}), \tag{3.6}$$

where valley index $\alpha, \sigma = K, K'$ and $\Phi_\alpha (\mathbf{u})$ is the three-dimensional field operator of an electron. In our case, the layers of graphene have no width, so we can write

$$\Phi_\alpha (\mathbf{u}) = \sum_n \sum_X \Psi_{\alpha,n,X} (\mathbf{r}) \chi_\alpha (z) c_{\alpha,n,X}, \tag{3.7}$$

where we neglect the spin degree of freedom, $\chi_\alpha (z)$ is the wave function in the z direction with $|\chi(z)|^2 = \delta(z \pm d/2)$, $n = 0, 1$ is the orbital index, and $\mathbf{r}$ is a vector in the plane of the C2DEG. Ψ is the wave function spinor and is defined by

$$\Psi_{K,n,X}\left(\mathbf{r}\right) = \begin{pmatrix} 0 \\ h_{n,X}\left(\mathbf{r}\right) \end{pmatrix}, \tag{3.8}$$

$$\Psi_{K',n,X}\left(\mathbf{r}\right) = \begin{pmatrix} h_{n,X}\left(\mathbf{r}\right) \\ 0 \end{pmatrix}, \tag{3.9}$$

in the basis of $\{B_2, A_1\}$, where h is the wave function defined by Eq. (1.21). If we take the limit of zero-width layers

$$\chi_K^*\left(z\right)\chi_K\left(z\right) = \delta\left(z-d/2\right), \tag{3.10}$$

$$\chi_{K'}^*\left(z\right)\chi_{K'}\left(z\right) = \delta\left(z+d/2\right), \tag{3.11}$$

and use the Coulomb potential in Fourier transformed is given by by

$$V\left(\mathbf{u}-\mathbf{u}'\right)=\frac{1}{S}\sum_{\mathbf{q}}\frac{2\pi e^2}{\kappa q}e^{i\mathbf{q}\cdot\left(\mathbf{r}-\mathbf{r}'\right)}e^{-q\left|z-z'\right|}, \tag{3.12}$$

where S is the area of the sample, so the Coulomb interaction is given by

$$\begin{aligned} H_{Coulomb} = & \frac{1}{2S}\sum_{\alpha,\sigma}\sum_{\mathbf{q}}\sum_{X_1,\ldots X_4}\frac{2\pi e^2}{\kappa q}e^{-\Delta_{\alpha,\sigma}qd} \\ & \int d\mathbf{r}d\mathbf{r}'\Psi^{\dagger}_{\alpha,n_1,X_1}\left(\mathbf{r}\right)\Psi^{\dagger}_{\sigma,n_2,X_2}\left(\mathbf{r}'\right)e^{i\mathbf{q}\cdot\left(\mathbf{r}-\mathbf{r}'\right)}\Psi_{\sigma,n_3,X_3}\left(\mathbf{r}'\right)\Psi_{\alpha,n_4,X_4}\left(\mathbf{r}\right) \\ & c^{\dagger}_{\alpha,n_1,X_1}c^{\dagger}_{\sigma,n_2,X_2}c_{\sigma,n_3,X_3}c_{\alpha,n_4,X_4}, \end{aligned} \tag{3.13}$$

where we define the function

$$\Delta_{\alpha,\sigma}=1-\delta_{\alpha,\sigma}, \tag{3.14}$$

to distinguish the intra- and inter-layer Coulomb interactions.

The substrate of the graphene bilayer also plays an important role in the system. We suppose that the sample is deposited on a substrate, which could be SiO_2 or Boron Nitride (BN) with effective dielectric constant κ. We define the density matrix,

$$\rho_{\alpha,n_1;\sigma,n_2}\left(\mathbf{q}\right)\equiv\frac{1}{N_\phi}\sum_{X_1,X_2}e^{-\frac{i}{2}q_x\left(X_1+X_2\right)}\delta_{X_1,X_2+q_y\ell^2}c^{\dagger}_{\alpha,n_1,X_1}c_{\sigma,n_2,X_2}, \tag{3.15}$$

where N_ϕ is the degeneracy of a level. The average value of the density matrix is related to observable quantities. In the LLL, there are 8 degenerate levels, so that the total degeneracy of the LLL is $8N_\phi$. The effect of the positive background is discussed in Appendix B. The interaction of the 2DEG with the positive background is given by

$$H_+ = n_0 N_\phi \left[\frac{\pi e^2 d}{\kappa} - V\left(q=0\right) \right] \sum_\alpha \sum_{n_1,n_2} \rho_{\alpha,n_1;\alpha,n_2}\left(\mathbf{q}=\mathbf{0}\right) + \frac{1}{2} S n_0^2 V\left(q=0\right). \qquad (3.16)$$

The background term can cancel the diverging part of the Hartree interaction at $q = 0$. The non-diverging part is the so-called capacitive energy $E_{cap} \propto \frac{d}{\ell}$ which favors a uniform distribution of charge between the two layers (or valleys). Although the capacitive energy which is related to the distance between two layers is weak, it plays an important role in the phase diagram. In the Hartree-Fock approximation (HFA), taking the Eq. (3.16) into account, the total Hamiltonian is then given by

$$\begin{aligned} H &= H_{Coulomb} + H_+ = N_\phi \sum_{\alpha,n} \widetilde{E}_{\alpha,n} \rho_{\alpha,n;\alpha,n}\left(0\right) \qquad (3.17) \\ &+ N_\phi \frac{e^2}{\kappa\ell} \sum_{\alpha,\sigma} \overline{\sum_{\mathbf{q}}} \sum_{n_1,\ldots,n_4} H_{\alpha,\sigma}\left(n_1,n_2,n_3,n_4;\mathbf{q}\right) \left\langle \rho_{\alpha,n_1;\alpha,n_2}\left(-\mathbf{q}\right)\right\rangle \rho_{\sigma,n_3;\sigma,n_4}\left(\mathbf{q}\right) \\ &- N_\phi \frac{e^2}{\kappa\ell} \sum_{\alpha,\sigma} \sum_{n_1,\ldots,n_4} \sum_{\mathbf{q}} X_{\alpha,\sigma}\left(n_1,n_4,n_3,n_2;\mathbf{q}\right) \left\langle \rho_{\alpha,n_1;\sigma,n_2}\left(-\mathbf{q}\right)\right\rangle \rho_{\sigma,n_3;\alpha,n_4}\left(\mathbf{q}\right). \end{aligned}$$

We define the energies,

$$\begin{aligned} \widetilde{E}_{\alpha,n} &= E^{LLL}_{\alpha,n} + E_{cap} \\ &= \alpha \frac{\Delta_B}{2} - \alpha \Delta_B \beta n + \left(\frac{e^2}{\kappa\ell} \right) \frac{d}{\ell} \left[\frac{\nu}{2} - \nu_{\overline{\alpha}} \right], \qquad (3.18) \end{aligned}$$

where $\alpha = -1, 1$ corresponds to K' and K valley respectively, and $\overline{\alpha}$ is the opposite valley of α. The symbol $\overline{\sum_{\mathbf{q}}}$ means the summation over $\mathbf{q}$ except $\mathbf{q} = \mathbf{0}$. The reason that $\overline{\sum}$ only appears in the Hartree term is that the terms at $\mathbf{q} = \mathbf{0}$ are cancelled by the background H_+. Also, the Hartree and Fock interaction functions $H_{\alpha,\sigma}$ and $X_{\alpha,\sigma}$ are defined by

$$
\begin{aligned}
H_{\alpha,\sigma}\left(n_1,n_2,n_3,n_4;\mathbf{q}\right) &= e^{-\Delta_{\alpha,\sigma}qd}\frac{1}{q\ell}F_{n_1,n_2}\left(\mathbf{q}\right)F_{n_3,n_4}\left(-\mathbf{q}\right), & (3.19)\\
X_{\alpha,\sigma}\left(n_1,n_4,n_3,n_2;\mathbf{q}\right) &= \int\frac{d\mathbf{p}\ell^2}{2\pi}e^{-\Delta_{\alpha,\sigma}pd}\frac{1}{p\ell}F_{n_1,n_4}\left(\mathbf{p}\right)F_{n_3,n_2}\left(-\mathbf{p}\right)e^{i\mathbf{q}\times\mathbf{p}\ell^2}, & (3.20)
\end{aligned}
$$

where the F function is defined by Eq. (2.56).

3.1.1 Single-particle Green's function

Once we obtain the Hamiltonian, the next step is to solve for the observable quantities $\left\langle\rho_{\alpha,n_1;\sigma,n_2}\right\rangle$ using the equation of motion of the single-particle Green's function. The method has been introduced in Sec. 1.3. According to Eq. (1.58), We define the Green's function in imaginary time,

$$
\begin{aligned}
G_{\alpha,n;\sigma,n'}\left(X,X',\tau\right) &= -\left\langle T_\tau c_{\alpha,n,X}\left(\tau\right)c^\dagger_{\sigma,n',X'}\left(0\right)\right\rangle & (3.21)\\
&= -\left\langle c_{\alpha,n,X}\left(\tau\right)c^\dagger_{\sigma,n',X'}\left(0\right)\right\rangle\theta\left(\tau\right)+\left\langle c^\dagger_{\sigma,n',X'}\left(0\right)c_{\alpha,n,X}\left(\tau\right)\right\rangle\theta\left(-\tau\right).
\end{aligned}
$$

We define the Fourier transform of the Green's function by,

$$
G_{\alpha,n;\sigma,n'}\left(\mathbf{q},\tau\right)=\frac{1}{N_\phi}\sum_{X,X'}e^{-\frac{i}{2}q_x\left(X+X'\right)}\delta_{X,X'-q_y\ell^2}G_{\alpha,n;\sigma,n'}\left(X,X',\tau\right). \tag{3.22}
$$

When $\tau\to 0^-$, we have

$$
G_{\alpha,n;\sigma,n'}\left(\mathbf{q},\tau=0^-\right)=\left\langle\rho_{\sigma,n';\alpha,n}\left(\mathbf{q}\right)\right\rangle. \tag{3.23}
$$

Following the procedure for calculating the Green's function explained in Sec. 1.3, we obtain the equation of motion of the Green's function

$$
\begin{aligned}
&\left[\hbar i\omega_n-\left(\widetilde{E}_{\alpha,n}-\mu\right)\right]G_{\alpha,n;\sigma,n'}\left(\mathbf{q},\omega_n\right)=\hbar\delta_{\mathbf{q},0}\delta_{n,n'}\delta_{\alpha,\sigma} & (3.24)\\
&+\frac{e^2}{\kappa\ell}\sum_{\gamma}\sum_{n_1,n_2,n_4}\overline{\sum_{\mathbf{q}'}}H_{\gamma,\alpha}\left(n_1,n_2,n,n_4;\mathbf{q}'-\mathbf{q}\right)\left\langle\rho_{\gamma,n_1;\gamma,n_2}\left(\mathbf{q}-\mathbf{q}'\right)\right\rangle e^{-i\mathbf{q}\times\mathbf{q}'\ell^2/2}G_{\alpha,n_4;\sigma,n'}\left(\mathbf{q}',\omega_n\right)\\
&-\frac{e^2}{\kappa\ell}\sum_{\gamma}\sum_{n_1,n_2,n_4}\sum_{\mathbf{q}'}X_{\gamma,\alpha}\left(n_1,n_4,n,n_2;\mathbf{q}'-\mathbf{q}\right)\left\langle\rho_{\gamma,n_1;\alpha,n_2}\left(\mathbf{q}-\mathbf{q}'\right)\right\rangle e^{-i\mathbf{q}\times\mathbf{q}'\ell^2/2}G_{\gamma,n_4;\sigma,n'}\left(\mathbf{q}',\omega_n\right).
\end{aligned}
$$

The matrix form of Eq. (3.24) can be also written in the form of Eq. (1.59),

$$\left(i\hbar\omega_n I - F\right) G = B. \tag{3.25}$$

Notice that we need to combine the valley and orbital indices together in the subscript of the Green's function: $(K,0) \to 1; (K,1) \to 2; (K',0) \to 3; (K',1) \to 4$. Consequently, the F matrix, in this case, can be written in details:

$$\begin{aligned} F_{11}\left(\mathbf{q},\mathbf{q}'\right) &= \left(\widetilde{E}_1 - \mu\right)\delta_{\mathbf{q},\mathbf{q}'} - \frac{e^2}{\kappa\ell}\sum_{n_1,n_2} X_{K,K}\left(n_1,0,0,n_2;\mathbf{q}'-\mathbf{q}\right)\left\langle \rho_{K,n_1;K,n_2}\left(\mathbf{q}-\mathbf{q}'\right)\right\rangle \\ &+\frac{e^2}{\kappa\ell}\sum_{\gamma,n_1,n_2} e^{-i\mathbf{q}\times\mathbf{q}'\ell^2/2}\left\langle \rho_{\gamma,n_1;\gamma,n_2}\left(\mathbf{q}-\mathbf{q}'\right)\right\rangle H_{\gamma,K}\left(n_1,n_2,0,0;\mathbf{q}'-\mathbf{q}\right)\left(1-\delta_{\mathbf{q},\mathbf{q}'}\right), \end{aligned} \tag{3.26}$$

$$\begin{aligned} F_{12}\left(\mathbf{q},\mathbf{q}'\right) &= \frac{e^2}{\kappa\ell}\sum_{\gamma,n_1,n_2} e^{-i\mathbf{q}\times\mathbf{q}'\ell^2/2}\left\langle \rho_{\gamma,n_1;\gamma,n_2}\left(\mathbf{q}-\mathbf{q}'\right)\right\rangle H_{\gamma,K}\left(n_1,n_2,0,1;\mathbf{q}'-\mathbf{q}\right)\left(1-\delta_{\mathbf{q},\mathbf{q}'}\right) \\ &-\frac{e^2}{\kappa\ell}\sum_{n_1,n_2} X_{K,K}\left(n_1,1,0,n_2;\mathbf{q}'-\mathbf{q}\right)\left\langle \rho_{K,n_1;K,n_2}\left(\mathbf{q}-\mathbf{q}'\right)\right\rangle e^{-i\mathbf{q}\times\mathbf{q}'\ell^2/2}, \end{aligned} \tag{3.27}$$

$$F_{13}\left(\mathbf{q},\mathbf{q}'\right) = -\frac{e^2}{\kappa\ell}\sum_{n_1,n_2} X_{K',K}\left(n_1,0,0,n_2;\mathbf{q}'-\mathbf{q}\right)\left\langle \rho_{K',n_1;K,n_2}\left(\mathbf{q}-\mathbf{q}'\right)\right\rangle e^{-i\mathbf{q}\times\mathbf{q}'\ell^2/2}, \tag{3.28}$$

$$F_{14}\left(\mathbf{q},\mathbf{q}'\right) = -\frac{e^2}{\kappa\ell}\sum_{n_1,n_2} X_{K',K}\left(n_1,1,0,n_2;\mathbf{q}'-\mathbf{q}\right)\left\langle \rho_{K',n_1;K,n_2}\left(\mathbf{q}-\mathbf{q}'\right)\right\rangle e^{-i\mathbf{q}\times\mathbf{q}'\ell^2/2}, \tag{3.29}$$

$$\begin{aligned} F_{22}\left(\mathbf{q},\mathbf{q}'\right) &= \left(\widetilde{E}_2 - \mu\right)\delta_{\mathbf{q},\mathbf{q}'} \\ &-\frac{e^2}{\kappa\ell}\sum_{n_1,n_2} X_{K,K}\left(n_1,1,1,n_2;\mathbf{q}'-\mathbf{q}\right)\left\langle \rho_{K,n_1;K,n_2}\left(\mathbf{q}-\mathbf{q}'\right)\right\rangle e^{-i\mathbf{q}\times\mathbf{q}'\ell^2/2} \\ &+\frac{e^2}{\kappa\ell}\sum_{\gamma,n_1,n_2} e^{-i\mathbf{q}\times\mathbf{q}'\ell^2/2}\left\langle \rho_{\gamma,n_1;\gamma,n_2}\left(\mathbf{q}-\mathbf{q}'\right)\right\rangle H_{\gamma,K}\left(n_1,n_2,1,1;\mathbf{q}'-\mathbf{q}\right)\left(1-\delta_{\mathbf{q},\mathbf{q}'}\right), \end{aligned} \tag{3.30}$$

$$F_{23}\left(\mathbf{q},\mathbf{q}'\right) = -\frac{e^2}{\kappa\ell}\sum_{n_1,n_2} X_{K',K}\left(n_1,0,1,n_2;\mathbf{q}'-\mathbf{q}\right)\left\langle \rho_{K',n_1;K,n_2}\left(\mathbf{q}-\mathbf{q}'\right)\right\rangle e^{-i\mathbf{q}\times\mathbf{q}'\ell^2/2}, \tag{3.31}$$

$$F_{24}\left(\mathbf{q},\mathbf{q}'\right) = -\frac{e^2}{\kappa\ell}\sum_{n_1,n_2} X_{K',K}\left(n_1,1,1,n_2;\mathbf{q}'-\mathbf{q}\right)\left\langle \rho_{K',n_1;K,n_2}\left(\mathbf{q}-\mathbf{q}'\right)\right\rangle e^{-i\mathbf{q}\times\mathbf{q}'\ell^2/2}, \tag{3.32}$$

$$
\begin{aligned}
&F_{33}\left(\mathbf{q},\mathbf{q}'\right) = \left(\widetilde{E}_3 - \mu\right)\delta_{\mathbf{q},\mathbf{q}'} \\
&-\frac{e^2}{\kappa\ell}\sum_{n_1,n_2} X_{K',K'}\left(n_1,0,0,n_2;\mathbf{q}'-\mathbf{q}\right)\left\langle \rho_{K',n_1;K',n_2}\left(\mathbf{q}-\mathbf{q}'\right)\right\rangle e^{-i\mathbf{q}\times\mathbf{q}'\ell^2/2} \\
&+\left(\frac{e^2}{\kappa\ell}\right)\sum_{\gamma}\sum_{n_1,n_2}\left\langle \rho_{\gamma,n_1;\gamma,n_2}\left(\mathbf{q}-\mathbf{q}'\right)\right\rangle e^{-i\mathbf{q}\times\mathbf{q}'\ell^2/2} H_{\gamma,K'}\left(n_1,n_2,0,0;\mathbf{q}'-\mathbf{q}\right)\left(1-\delta_{\mathbf{q},\mathbf{q}'}\right),
\end{aligned}
\tag{3.33}
$$

$$
\begin{aligned}
F_{34}\left(\mathbf{q},\mathbf{q}'\right) &= \frac{e^2}{\kappa\ell}\sum_{\gamma}\sum_{n_1,n_2}\left\langle \rho_{\gamma,n_1;\gamma,n_2}\left(\mathbf{q}-\mathbf{q}'\right)\right\rangle e^{-i\mathbf{q}\times\mathbf{q}'\ell^2/2} H_{\gamma,K'}\left(n_1,n_2,0,1;\mathbf{q}'-\mathbf{q}\right)\left(1-\delta_{\mathbf{q},\mathbf{q}'}\right) \\
&\quad -\frac{e^2}{\kappa\ell}\sum_{n_1,n_2} X_{K',K'}\left(n_1,1,0,n_2;\mathbf{q}'-\mathbf{q}\right)\left\langle \rho_{K',n_1;K',n_2}\left(\mathbf{q}-\mathbf{q}'\right)\right\rangle e^{-i\mathbf{q}\times\mathbf{q}'\ell^2/2},
\end{aligned}
\tag{3.34}
$$

$$
\begin{aligned}
&F_{44}\left(\mathbf{q},\mathbf{q}'\right) = \left(\widetilde{E}_4 - \mu\right)\delta_{\mathbf{q},\mathbf{q}'} \\
&-\frac{e^2}{\kappa\ell}\sum_{n_1,n_2} X_{K',K'}\left(n_1,1,1,n_2;\mathbf{q}'-\mathbf{q}\right)\left\langle \rho_{K',n_1;K',n_2}\left(\mathbf{q}-\mathbf{q}'\right)\right\rangle e^{-i\mathbf{q}\times\mathbf{q}'\ell^2/2} \\
&+\frac{e^2}{\kappa\ell}\sum_{\gamma}\sum_{n_1,n_2}\left\langle \rho_{\gamma,n_1;\gamma,n_2}\left(\mathbf{q}-\mathbf{q}'\right)\right\rangle e^{-i\mathbf{q}\times\mathbf{q}'\ell^2/2} H_{\gamma,K'}\left(n_1,n_2,1,1;\mathbf{q}'-\mathbf{q}\right)\left(1-\delta_{\mathbf{q},\mathbf{q}'}\right),
\end{aligned}
\tag{3.35}
$$

where γ is the valley index. Since the F matrix is a Hermitian matrix, the other elements which have not been listed here obey the relations, $F_{ji}(\mathbf{q}',\mathbf{q}) = [F_{ij}(\mathbf{q},\mathbf{q}')]^*$.

At last, the sum rules for $\langle\rho\rangle$ are given by

$$
\begin{aligned}
\left\langle \rho_{\alpha,n;\alpha,n}(\mathbf{0})\right\rangle &= \nu_{\alpha,n}, && (3.36)\\
\sum_n \left\langle \rho_{\alpha,n;\alpha,n}(\mathbf{0})\right\rangle &= \sum_n \nu_{\alpha,n} = \nu_\alpha, && (3.37)\\
\sum_{\alpha',n'}\sum_{\mathbf{q}} \left|\left\langle \rho_{\alpha,n;\alpha',n'}\left(\mathbf{q}\right)\right\rangle\right|^2 &= \left\langle \rho_{\alpha,n;\alpha,n}(\mathbf{0})\right\rangle = \nu_{\alpha,n}, && (3.38)
\end{aligned}
$$

where ν_α is the filling factor in the valley α, and $\nu_{\alpha,n}$ is the filling factor in the orbital n in the α valley.

3.1.2 Order parameters and pseudo-spin language

Following the algorithm introduced in Sec. 1.3, we can calculate the 16 components of the Green's function which give the set of order parameters $\langle \rho_{\alpha,n;\sigma,n'}(\mathbf{q}) \rangle$. These order parameters characterize the system completely. In a uniform ground state, which mostly happens at integer filling factors, $\langle \rho_{\alpha,n;\sigma,n'}(\mathbf{q} \neq \mathbf{0}) \rangle = 0$. The state is called a liquid state because of its uniform density. However, at non-integer filling factors, the ground state is not necessarily uniform. In this chapter, we study crystal states occurring at non-integer filling factor ν where we expect a finite fraction of the electrons, usually $N_\phi(\nu - \lfloor \nu \rfloor)$, to crystallize. $\lfloor x \rfloor$ is the floor function which is the largest integer not greater than x. In the crystal phases, $\langle \rho_{\alpha,n;\sigma,n'}(\mathbf{q}) \rangle \neq 0$ only at some discrete $\mathbf{q} = \mathbf{G}$, where $\mathbf{G}$ is the reciprocal lattice vector of the crystal lattice. Notice that the lattice constant of the electron crystal is much larger than the lattice constant of graphene, so that we are justified to use the continuum approximation explained in Chapter 1.

A combination of order parameters $\langle \rho \rangle$ can be used to construct the pseudo-spin language. We associate the two valleys (or two orbitals) with the two components of valley pseudo-spin, according to $|K\rangle \rightarrow |\uparrow\rangle$ and $|K'\rangle \rightarrow |\downarrow\rangle$. In the momentum space, the density is defined by

$$n_\alpha(\mathbf{q}) = N_\phi \sum_{n,n'=0}^{1} F_{n,n'}(-\mathbf{q}) \langle \rho_{\alpha,n;\alpha,n'}(\mathbf{q}) \rangle . \tag{3.39}$$

The density in real space $n_\alpha(\mathbf{r})$ is just the Fourier transform of $n_\alpha(\mathbf{q})$. We also define another expression for the density,

$$\widetilde{n}_\alpha(\mathbf{q}) = \sum_{n=0}^{1} \langle \rho_{\alpha,n;\alpha,n}(\mathbf{q}) \rangle , \tag{3.40}$$

which is called the guiding-center density. By definition, $\widetilde{n}_\alpha(\mathbf{q} = \mathbf{0}) = \nu_\alpha$ is just the filling factor in the α valley. Notice that the guiding center density is not the real density of electrons, because of the form factor $F_{n,n'}(-\mathbf{q})$ in Eq. (3.39).

If we take the mapping orbital 0 as orbital pseudo-spin up, and orbital 1 as orbital pseudo-spin down, then in the orbital pseudo-spin language:

$$\begin{aligned} s_{\alpha,z} &= \frac{1}{2}\left(\left\langle \rho_{\alpha,0;\alpha,0}\right\rangle - \left\langle \rho_{\alpha,1;\alpha,1}\right\rangle\right), && (3.41a)\\ s_{\alpha,x} &= \operatorname{Re}\left\langle \rho_{\alpha,0;\alpha,1}\right\rangle, && (3.41b)\\ s_{\alpha,y} &= \operatorname{Im}\left\langle \rho_{\alpha,0;\alpha,1}\right\rangle. && (3.41c) \end{aligned}$$

For the valley pseudo-spin,

$$\begin{aligned} p_{n,z} &= \frac{1}{2}\left(\left\langle \rho_{K,n;K,n}\right\rangle - \left\langle \rho_{K',n;K',n}\right\rangle\right), && (3.42a)\\ p_{n,x} &= \operatorname{Re}\left\langle \rho_{K,n;K',n}\right\rangle, && (3.42b)\\ p_{n,y} &= \operatorname{Im}\left\langle \rho_{K,n;K',n}\right\rangle. && (3.42c) \end{aligned}$$

All the pseudo-spin fields ($\mathbf{s}_\alpha$ and $\mathbf{p}_n$) are defined in the guiding center representation (GCR). If we want to get the pseudo-spin fields in real space, we only need to multiply all the density matrix elements $\langle \rho_{\alpha,n;\sigma,n'}(\mathbf{q})\rangle$ by $F_{n,n'}(\mathbf{q})$ and sum over $\mathbf{q}$ i.e.

$$\left\langle \rho_{\alpha,n;\sigma,n'}\left(\mathbf{r}\right)\right\rangle = \frac{1}{S}\sum_{\mathbf{q}} e^{i\mathbf{q}\cdot\mathbf{r}} F_{n,n'}\left(-\mathbf{q}\right)\left\langle \rho_{\alpha,n;\sigma,n'}\left(\mathbf{q}\right)\right\rangle. \tag{3.43}$$

Even though the real density $n_\alpha\left(\mathbf{r}\right)$ is the observable quantity, the guiding center definition is useful, since it does not contain the form factor $F_{n,n'}$ that reflects the character of the different orbitals. In fact, plots of the guiding-center density are often easier to understand physically.

The two fields defined in Eqs. (3.41)-(3.42) only provide simple physical pictures of the system, but can not describe the four-level system completely. If we want to describe the full system, we need to use a 4-component field which is called CP^3 spinor [55]. However, in our system, the fields $\mathbf{s}$ and $\mathbf{p}$ are sufficient to understand the physics.

3.2 Crystal phases at non-integer filling factors

Skyrmion crystals with intervalley or interlayer pseudo-spin textures have been studied extensively in semiconductor 2DEG in double quantum well systems as well as in graphene monolayer [38, 56, 57]. In the LL $N = 0$ in bilayer graphene, there is the additional possibility of orbital pseudo-spin texture as we describe above. This orbital pseudo-spin field, $\mathbf{s}_\alpha$, is particularly interesting because it gives rise to textures of electric dipoles in the plane of the layer [13, 53, 58, 59]. The orientation of the electric dipole in space is given by the orientation of the orbital pseudo-spin vector. It follows that the crystals with orbital pseudo-spin texture also have electric dipole textures. Orbital skyrmion crystals are the electric analog of spin skyrmions crystals where it is the magnetization that varies in space. Electrons can change their orbital indices by the Coulomb interaction, so that the orientation of electric dipoles which are related to the orbital coherence can be tuned by the Coulomb interaction and bias Δ_B, as well as by an in-plane electric field [13].

For graphene, we have studied the energy of an isolated skyrmion in the last chapter. In the BLG, isolated skyrmion can also be written in a way similar to Eqs. (2.23) and (2.24) in the symmetric gauge. An antiskyrmion is given by

$$|ASK\rangle = \prod_{m=-1} \left(u_m c^\dagger_{0,m+2} + v_m c^\dagger_{1,m} \right) |0\rangle \,, \tag{3.44}$$

where $c^\dagger_{n,m}$ is a creation operator of an electron in orbital n and real angular momenta m. The electric charge of the excitation $|ASK\rangle$ in Eq. (3.44) is $q = e$ ($e > 0$) and the topological charge is $Q = -2$, because the lowest angular momenta state in orbital $n = 1$ is -1. For topological charge $Q = 2$, there are three possible states for the skyrmion:

$$|SK\rangle = c^\dagger_{1,i} \prod_{m=0} \left(u_m c^\dagger_{0,m} + v_m c^\dagger_{1,m+2} \right) |0\rangle \,, i = -1, 0, 1. \tag{3.45}$$

In this case, the relation between topological charge and electric charge is $q = Qe/2$ which is different from a spin skyrmion. In such a skyrmion or antiskyrmion, the orbital pseudo-spin rotates by 4π along a path that circles the origin once, because its topological charge is ± 2. We remark that skyrmions with topological charge $|Q| > 1$ have been studied in a semiconductor 2DEG [61,62]. It was found that inter-LL skyrmion between the LL $n = 0$ with spin down and $n = 1$ with spin up was not the lowest-energy excitation. Because the Coulomb interaction is different in LL $N = 0$ in BLG, orbital skyrmions may be the lowest-energy charged excitations in the system. We have studied such skyrmion before [41], but in the valley K' where orbital $n = 0$ is always below orbital $n = 1$. In valley K, when $E_{K,0} > E_{K,1}$, not all the electrons are occupied in $n = 0$ in the ground state and the study of such skyrmion is more difficult.

In this thesis, we decide for these reasons to study orbital skyrmion crystal instead

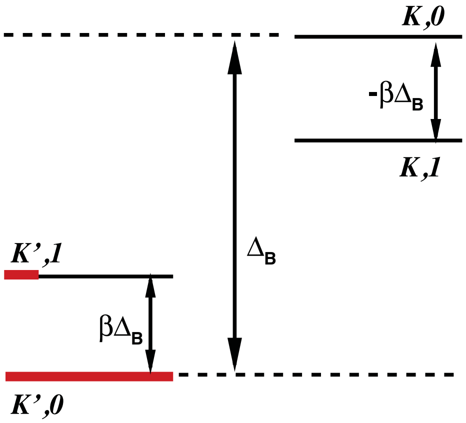

FIGURE 3.2: The occupation of the levels at $\tilde{\nu} = 1.2$ is shown schematically. The spin is frozen so that the four levels are only associated with valley and orbital states. The black lines are empty levels, while the red line indicates the occupied level. The state $|K', 1\rangle$ is only partially occupied.

of isolated skyrmion. This work can be found in Ref. [59] where, however, the density profiles and pseudo-spin textures of the triangular crystals are incorrect. The corrected ones are shown in this thesis.

3.2.1 Orbital skyrmion crystal at large bias

In this chapter, we set the magnetic field at 10T, and dielectric constant $\kappa = 5$ for SiO$_2$ substrate. For the validation of the effective two-component model, the bias required is $\Delta_B \ll \gamma_1 = 0.39eV\approx 10e^2/\kappa\ell$.

The simplest crystalline structure occurs at large bias near filling factor $\nu = -3$, where there is only one level fully filled. We define the effective filling factor as $\tilde{\nu} = \nu + 4 = 1$, which indicates that only one level is filled and all the other 7 levels in the LL $N = 0$ are empty. In this case, the valley pseudo-spin is polarized by the large Δ_B. All the charge is in the K' valley. The occupation of the levels is shown in Fig. 3.2.

The ground state at $\tilde{\nu} = 1$ is a liquid with electrons in $|K', 0\rangle$. At $\tilde{\nu} > 1$, the filling factor of the $|K', 1\rangle$ level is $\tilde{\nu} - 1$. The electrons in this level crystallize in a triangle lattice, flipping the orbital pseudo-spin in the process to create an orbital pseudo-spin texture. The crystal lattice is shown in Fig. 3.3 for $\tilde{\nu} = 1.2$ and $\Delta_B = 1.28e^2/\kappa\ell$. Note that only the pseudo-spin texture of the orbital skyrmion crystal represented in the guiding

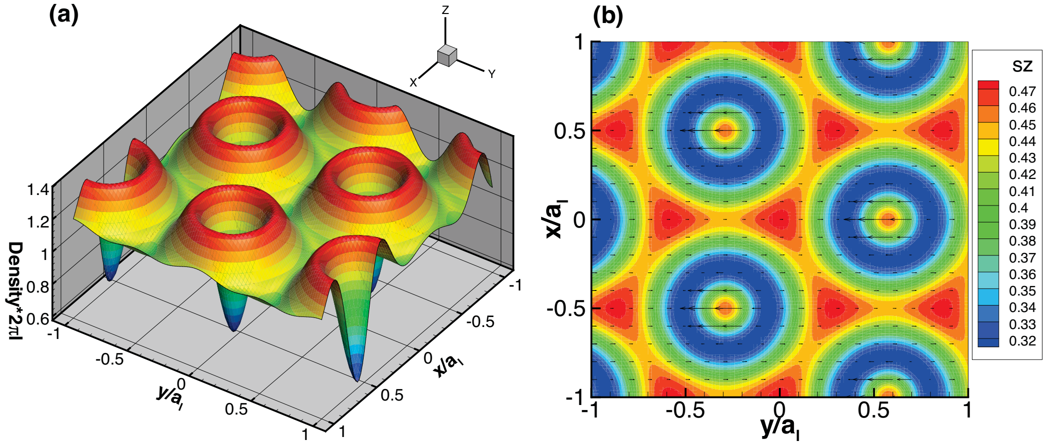

FIGURE 3.3: The crystal phase at $\tilde{\nu} = 1.2$ and $\Delta_B = 1.28e^2/\kappa\ell$ in the real space representation. (a) Space density profile, and (b) orbital pseudo-spin field in real space representation.

center density is similar to the spin texture of a spin skyrmion crystal in a conventional 2DEG [24,64]. In the real space representation, the orbital pseudo-spin texture looks like that of a Wigner crystal, i.e. there is no rotation of the pseudo-spin. The ground state is an orbital quantum Hall ferromagnet, so that the pseudo-spin field of the electrons in the inter-site regions points in the same direction as the field in the ground state. The field points in the opposite direction at the center of each crystal site. The ring structure at the crystal site is induced by the added electrons in the orbital $n = 1$ with angular momenta $m = -1$. In the symmetric gauge, the density profile of wave functions $h_{1,m}$ given in Eq. (1.24) at $m = -1, 0, 1$ is shown in Fig. 3.4. The wave function at $m = -1$ has a ring structure, which is similar to the rings in Fig. 3.3.

The lattice constant of electron crystal is defined by a_l which is much larger than the lattice constant of graphene. In fact, from the Fig. 3.3a, the density is from 0.576 to 1.4 (in units of $1/(2\pi\ell^2)$). The minimum of the density is smaller than 1. This is because the total density is not equal to the sum of the density in oribtal 0 and the density in orbital 1, according to Eq. (3.39). If we look at the density profile and pseudo-spin texture in the guiding center representation in Fig. 3.5, then the skyrmion-like texture is very clear. It is also clear in Fig. 3.5a that there is one skyrmion per site of the crystal.

The existence region of the skyrmion crystal is about $\Delta_B/(e^2/\kappa\ell) \in [0.96, 30]$. We note the lower critical bias as $\Delta_B^{C2} = 0.96e^2/\kappa\ell$. Below this value the crystal phases will

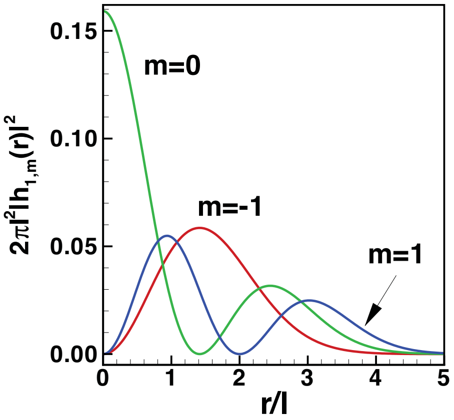

FIGURE 3.4: The density profile of the wave functions in orbital $n = 1$, $h_{1,m}$, $m = -1, 0, 1$ [59].

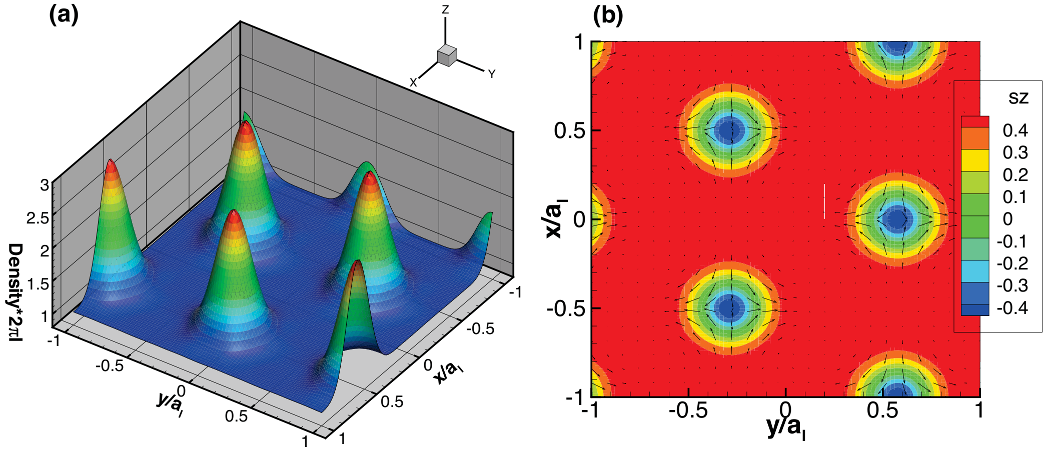

FIGURE 3.5: The crystal phase at $\tilde{\nu} = 1.2$ and $\Delta_B = 1.28e^2/\kappa\ell$ in the guiding center representation. (a) Density profile, and (b) orbital pseudo-spin field.

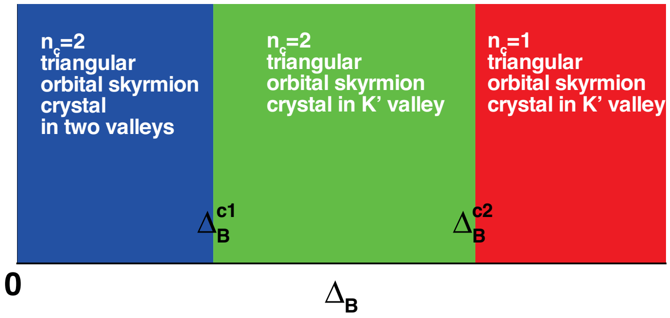

FIGURE 3.6: The crystal phase diagram at $\tilde{\nu} = 1.2$. The $\Delta_B^{c1} = 0.0013e^3/\kappa\ell$ and $\Delta_B^{c2} = 0.96e^2/\kappa\ell$ are the critical biases of the two phase transitions.

be discussed in the next section. The Wigner crystal solution i.e., no orbital pseudo-spin texture in both real space and guiding center representation can be found if the bias is taken to be extremely large, i.e., on the order of $\Delta_B \approx 30e^2/\kappa\ell$ which is well beyond the limit of validity of the effective two-component model. Just as for spin skyrmions, the orbital texture is gradually lost when the bias is increased.

3.2.2 Orbital skyrmion crystal at small bias

In this section, we discuss the orbital crystal phases at zero and small bias at $\tilde{\nu} = 1.2$. Including the $n_c = 1$ orbital skyrmion crystal that we discussed in the last section, the phase diagram is shown in Fig. 3.6. The red region in Fig. 3.6 has been discussed in the last section. It occurs for $\Delta_B > \Delta_B^{c2}$. In the green region, the orbital skyrmion crystal phase is almost the same as the one in the red region, except that there are two electrons per site, i.e. $n_c = 2$. At extremely small bias (in the blue region), the orbital skyrmion crystal distributes itself in both two valleys.

We have mentioned that above a critical bias $\Delta_B^{c0} \approx 0.0011e^2/\kappa\ell$ which is of the same order as Δ_B^{c1}, the ground state at $\tilde{\nu} = 1$ is the valley polarized state, which means $|K', 0\rangle = 1$ and all other three levels are empty. Below Δ_B^{c0}, valley coherence sets in, so that electrons are partly in the K valley and partly in the K' valley. When the filling factor increases to $\tilde{\nu} = 1.2$, the electrons that crystallize have both valley and orbital coherences at small bias. Because the orbital coherence sets in, the critical bias Δ_B^{c1} to

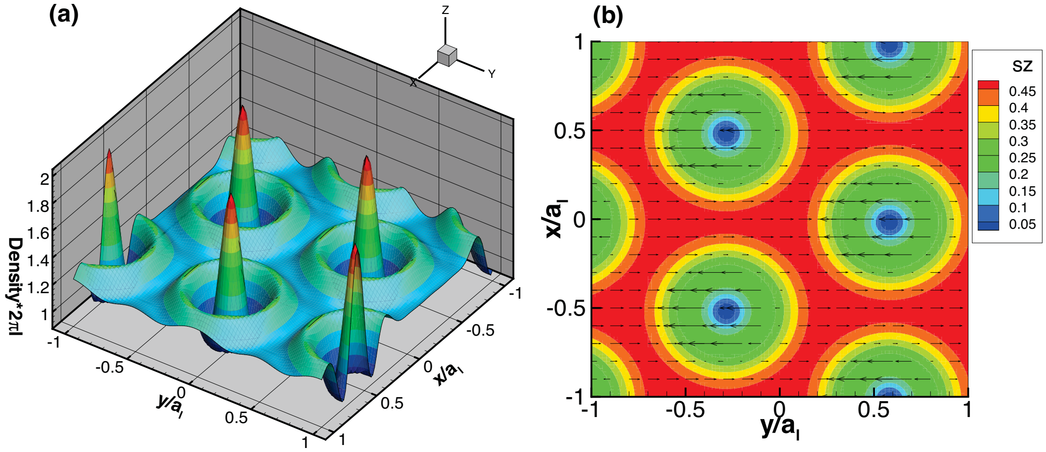

FIGURE 3.7: The crystal phase at $\tilde{\nu} = 1.2$ and $\Delta_B = 0.002e^2/\kappa\ell$. All charge is in the K' valley. We show that (a)the density profile, and (b)the orbital pseudo-spin field in real space representation.

polarize the valley pseudo-spin is increased a little to $0.0013e^2/\kappa\ell$.

If the bias is between $\Delta_B^{c1} = 0.0013e^2/\kappa\ell$ and $\Delta_B^{c2} = 0.96e^2/\kappa\ell$, the phase of electron state falls into the green region in Fig. 3.6. In Fig. 3.7, we show the crystal phase at $\Delta_B = 0.002e^2/\kappa\ell$ in real space. Notice that there is an extra peak at each site of the electron crystal in Fig. 3.7. This peak comes from an electron with angular momenta $m = 0$ (see the density profile of $h_{1,0}$ in Fig. 3.4), while the ring comes from electron with angular momenta $m = -1$. The two electrons are superimposed at the same site. Hence, the electron number per site n_c is 2. In Fig. 3.8, we show the orbital skyrmion texture. Intuitively, an isolated skyrmion with charge $q = 2e$ can be written in the symmetric gauge as

$$|sk^{2e}\rangle = c^{\dagger}_{1,-1}c^{\dagger}_{1,0}\prod_{m=0}(u_m c^{\dagger}_{0,m} + v_m c^{\dagger}_{1,m+1})|0\rangle. \tag{3.46}$$

The rotation of the orbital pseudo-spin is still 2π around the center of the skyrmion.

Skyrmions with charge $q = -2e$ were also studied in Ref. [63]. At small density, there is an attractive force, which is from the Fock interaction, between two skyrmions that goes like $1/R$, where R is the separation between the two skyrmions. So the crystal is constructed by the balance between this attractive force and the Coulomb repulsion. Also, in previous studies of spin and pseudo-spin skyrmions in conventional semiconductor's 2DEG, it was found that lattices with skyrmion pairs occurred for small value of the

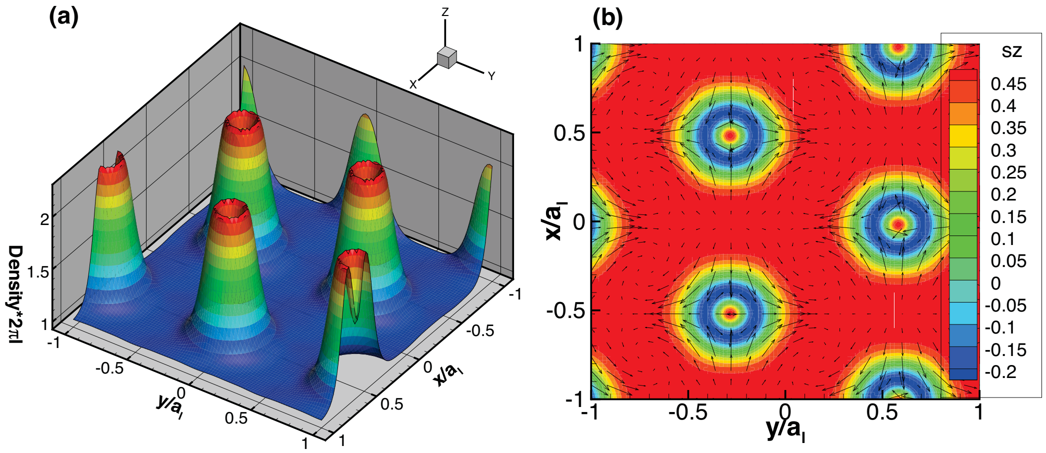

FIGURE 3.8: The crystal phase at $\tilde{\nu} = 1.2$ and $\Delta_B = 0.002e^2/\kappa\ell$. All charge is in the K' valley. We show that (a)the density profile, and (b)the orbital pseudo-spin field in guiding center representation.

Zeeman or bias (effective Zeeman) couplings [56]. Our work shows that the same physics seems to occur in BLG.

However, the orbital skyrmion crystal in Figs. 3.7 and 3.8 is not the same as this skyrmion-pair crystal. Instead, it is analogous to the bubble crystal that occurs in higher Landau levels in semiconductor's 2DEG [65]. The bubble crystals were studied in the Hartree-Fock approximation in Ref. [66]. In this approximation, if we increase the filling factor ν in Landau level N, the ground state of the 2DEG evolves from a Wigner crystal at small filling factor into a succession of bubble crystals with increasing number of electrons per bubble (site), M with $M = 1, 2, \ldots, N + 1$. The wave functions of the electrons in the higher Landau levels have a ring structure in the symmetric gauge if the angular momenta $m \neq 0$. The Coulomb interaction between these rings has a special feature: for $r > 2R_0$, where R_0 is the ring radius, it decreases as $1/R$, where R is the separation between the ring centers. When $R \leq 2R_0$, however, the Coulomb interaction has a sort of plateau. As the filling factor increases, the density of electrons increases, then the density of electron rings increases and the rings start to touch each another, it becomes energetically preferable to make a crystal of clusters (or bubbles) of electrons. For example, in Landau level 1, the bubble crystal can have $M = 2$. The two electrons per site occupy the angular momenta $m = -1, 0$ respectively. So that the isolated bubble state can be written as $|2e\rangle = c^{\dagger}_{1,-1,\uparrow} c^{\dagger}_{1,0,\uparrow} \prod_{m=-1} c^{\dagger}_{1,m,\downarrow} |0\rangle$. The density profile can be found in Fig. 2 of Ref. [66], which can be compared with the bubble skyrmion crystal of Fig. 3.7a.

In our orbital system, the filling factor and the density of electrons are fixed. However, if we decrease the bias between $|K', 0\rangle$ and $|K', 1\rangle$, the size of the skyrmion increases and the number of flipped orbital pseudo-spins increases. When the skyrmion becomes too large, it becomes more favorable to increase the distance between them and so the number of skyrmions per site is increased. The bubble orbital skyrmion crystal with $M = 1$ is transformed to a bubble orbital skyrmion crystal with $M = 2$ when the bias is decreased. The transition is of first-order.

The crystal phase at extremely small bias $\Delta_B < \Delta_B^{c1} = 0.0013e^2/\kappa\ell$ at $\tilde{\nu} = 1.2$ is more interesting since it contains both the valley and orbital coherence. The phase is shown in the blue region in the phase diagram of Fig. 3.6. The four states with Coulomb interaction in order of increasing energy are symmetric state $|S, 0\rangle$ in orbital 0, symmetric state $|S, 1\rangle$ in orbital 1, anti-symmetric state $|AS, 0\rangle$ in orbital 0, and anti-symmetric state $|S, 1\rangle$ in orbital 1:

$$|S, 0\rangle = \frac{1}{\sqrt{2}} \left(|K, 0\rangle + |K', 0\rangle\right) \tag{3.47a}$$

$$|S, 1\rangle = \frac{1}{\sqrt{2}} \left(|K, 1\rangle + |K', 1\rangle\right) \tag{3.47b}$$

$$|AS, 0\rangle = \frac{1}{\sqrt{2}} \left(|K, 0\rangle - |K', 0\rangle\right) \tag{3.47c}$$

$$|AS, 1\rangle = \frac{1}{\sqrt{2}} \left(|K, 1\rangle - |K', 1\rangle\right) \tag{3.47d}$$

So the ground state at $\tilde{\nu} = 1$ has $|S, 0\rangle$ fully occupied and the three other levels are empty. When the filling factor increases to 1.2, the extra electrons are added to $|S, 1\rangle$. Hence, the crystal phase contains the coherences between the valleys $|K\rangle$ and $|K'\rangle$, and between the orbitals $|0\rangle$ and $|1\rangle$. Indeed, our numerical calculations show that the crystal contains orbital skyrmion texture in both valleys. In each valley, the orbital skyrmion texture is similar to that of Fig. 3.7 in real space and Fig. 3.8 in guiding center representation. The valley pseudo-spin textures are shown in Figs. 3.9 and 3.10. The valley pseudo-spin texture in orbital 0 is almost uniform. On the other hand, the valley pseudo-spin texture in orbital 1 indicates a Wigner crystal.

We also need to mention that there is a similar phase as the blue region of Fig. 3.6 at $\tilde{\nu} = 3.2$ when the bias is very small. In the region where $\Delta_B \in [0, 0.0021]e^2/\kappa\ell$, however,

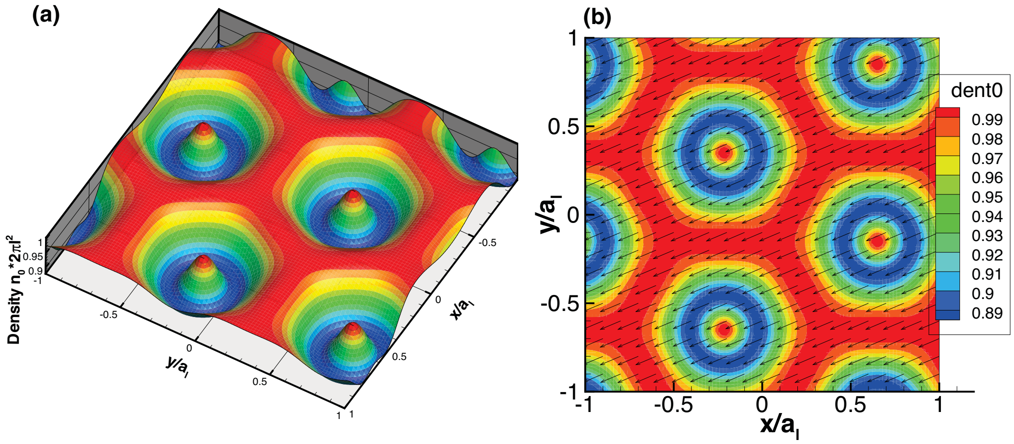

FIGURE 3.9: The crystal phase at $\tilde{\nu} = 1.2$ and $\Delta_B = 0$ is shown in real space. The electron density in orbital 0 is shown in (a), and the valley pseudo-spin texture in orbital 0 is shown in (b).

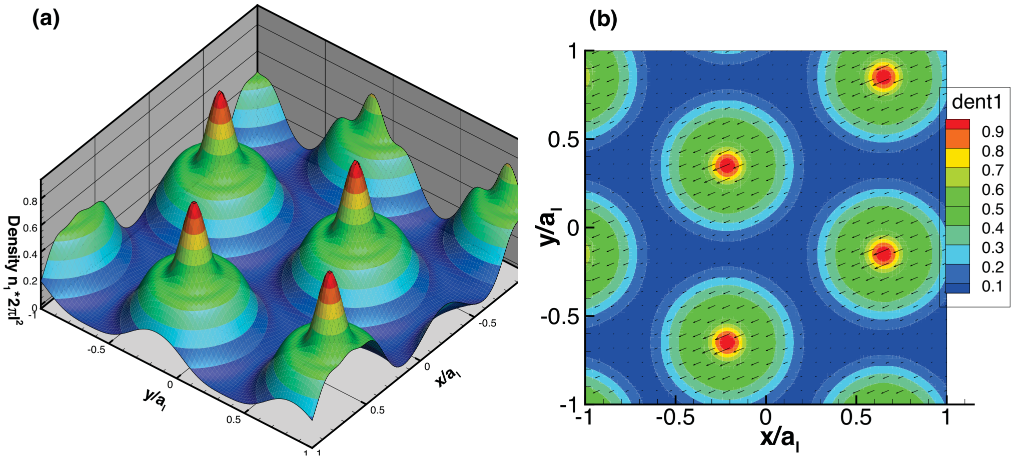

FIGURE 3.10: The crystal phase at $\tilde{\nu} = 1.2$ and $\Delta_B = 0$ is shown in real space. The electron density in orbital 1 is shown in (a), and the valley pseudo-spin texture in orbital 1 is shown in (b).

the coherence is between the states $|AS, 0\rangle$ and $|AS, 1\rangle$. The orbital skyrmion textures which exists in both two valleys are similar to those in Fig. 3.7 in real space and Fig. 3.8 in the guiding center representation, while the valley pseudo-spin texture is like that in Figs. 3.9 and 3.10. When the bias increases from zero, the gap $-\beta\Delta_B$ between $|K, 0\rangle$ and $|K, 1\rangle$ is negative (see Fig. 3.1). However, the valley coherence disappear completely when $\Delta_B > 0.0021e/\kappa\ell$. When $\Delta_B \gtrsim 0.0021e^2/\kappa\ell$, we still get a triangular crystal of orbital skyrmion with charge $q = -2e$ per site, where electrons are in majority in orbital $n = 0$ and there is not much difference with the $\tilde{\nu} = 1.2$ case. The orbital texture is similar to that in Fig. 3.7 in real space and Fig. 3.8 in the guiding center representation. The only difference with $\tilde{\nu} = 1.2$ is that the orbital texture occurs in the K valley. When the bias is sufficiently strong, the crystal phase is much more complex since the majority electrons are flipped into the $n = 1$ orbital. However, the orbital pseudo-spin texture still persists. We do not discuss this limit further in this chapter, because the bias is beyond the limit of the effective two-component model, and it is also difficult to achieve experimentally.

3.2.3 Valley skrymion crystal near $\tilde{\nu} = 2$

At $\tilde{\nu} = 2$, the uniform ground state at zero bias has inter-layer (or say inter-valley) coherence in both orbitals $n = 0$ and $n = 1$ [14,61]. In this case, according to Eq. (3.47), the occupied states are $|S, 0\rangle$ and $|S, 1\rangle$. The other two states are empty. Above a critical bias $\Delta_B^{(c)} = 0.003e^2/\kappa\ell$, all charge are transferred to the K' valley, the valley pseudo-spin is polarized, i.e. the states $|K', n = 0\rangle$ and $|K', n = 1\rangle$ are fully occupied, and states in K valley are empty. Inter-layer as well as orbital coherences vanish. Coherence between two states can only occur if they are both partially filled.

The 2-electron charge excitation at $\tilde{\nu} = 2$ and $\Delta_B < \Delta_B^{(c)}$ is predicted to be skyrmions with superposition of $n = 0$ and $n = 1$ inter-layer pseudo-spin textures, i.e. the combination of a valley skyrmion in $n = 0$ and another valley skyrmion in $n = 1$ in Ref. [14] (the small contribution $\beta\Delta_B$ between orbitals was neglected in that paper). The authors have concluded that such a $q = -2e$ skyrmion would have lower energy than the quasi-particle states at filling factor $\tilde{\nu} = 2$.

If the filling factor increases a little from 2, for example at $\tilde{\nu} = 2.2$, the charge excitation can crystallize at $T = 0$K. At zero or very small bias, the gap between $|K, 0\rangle$ and $|K', 0\rangle$ is very small or even zero. In this case, the skyrmion crystal should be replaced

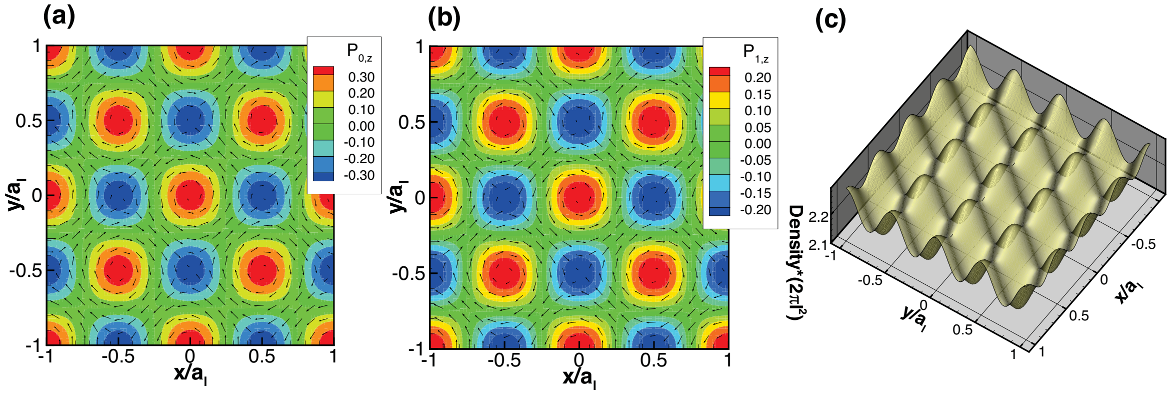

FIGURE 3.11: (a) The valley pseudo-spin texture in orbital $n = 0$; (b) the valley pseudo-spin texture in orbital $n = 1$; (c) the total density profile of the checkerboard meron crystal phase. All three pictures are represented in real space.

by a meron crystal (see below for its definition) [33,67]. Our numerical calculations show the layer pseudo-spin meron crystals with each meron carrying charge $q = -e/2$ at zero bias in Fig. 3.11. We find that at each site of the crystal, there is charge $-e$ associated with vortex-like texture on each blue and red dots. Hence, there are 4 electrons per unit cell of the crystal. If we separate the two orbitals, we obtain that the density profile for each orbital is similar to that in Fig. 3.11c. It means that the crystal in either orbital 0 or 1 is a square lattice with charge $q = -e/2$ per site. The total crystal is thus a superposition of the square lattice in orbital 0 and 1, so that there is charge $q = -e$ per site and 4 electrons per unit cell in Fig. 3.11c.

The valley pseudo-spin field is defined by Eq. (3.42). In Fig. 3.11, each red dot is a meron with positive p_z, while blue dots are anti-merons with negative p_z. If we look at a path that circles counterclockwise around the center of the charge (each red or blue dot), a meron's (at red dot) pseudo-spin texture winds around the charge with a 2π counterclockwise rotation and an anti-meron's (at blue dot) pseudo-spin texture winds around the charge with a 2π clockwise rotation. A meron (or an anti-meron) is similar to a half-charge skyrmion (or anti-skyrmion). There is a phase difference of π between the two nearest merons, i.e. the two nearest red dots in Fig. 3.11 (or two nearest anti-meron, i.e. two nearest blue dots). This phase difference decreases the energy of the crystal because the gradient of the pseudo-spin texture between two adjacent sites is minimized in this configuration. The orbital coherence also exists, however, there is no

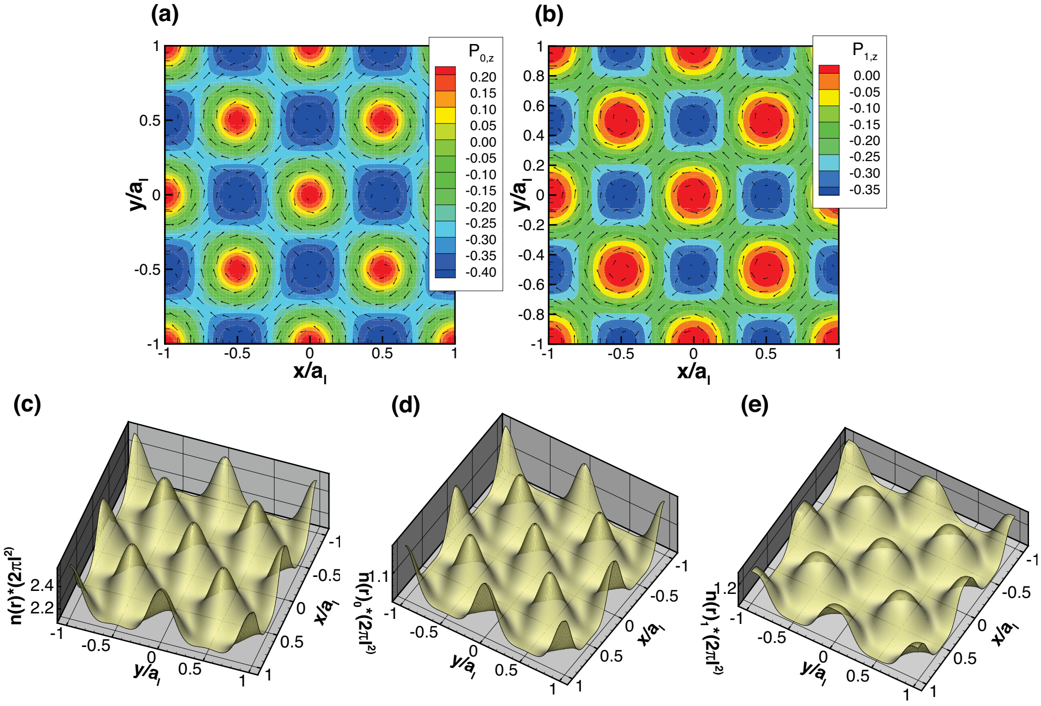

FIGURE 3.12: (a) The valley pseudo-spin texture in orbital $n = 0$; (b) the valley pseudo-spin texture in orbital $n = 1$; (c) the total density profile of the valley skyrmion cyrstal phase; (d) the density in orbital 0, $2\pi\ell^2 n_0$; (e) the density in orbital 1, $2\pi\ell^2 n_1$. All the three pictures are represented in real space.

orbital pseudo-spin texture.

When the bias increase, the gaps between valleys also increase. The gap between $|K', 0\rangle$ and $|K, 0\rangle$ is $\Delta_0 = \Delta_B$, and the gap between $|K', 1\rangle$ and $|K, 1\rangle$ is $\Delta_1 = \Delta_B - 2\beta\Delta_B$. Due to the finite gaps, the valley meron crystal evolves to the real skyrmion crystal. In our numerical calculations, the charge is transformed from the blue dots to the red dots. At finite bias, the perfect valley meron crystal in Fig. 3.11 evolves to a unperfect checkerboard meron crystal where the red dot is larger than the blue dot in density profile as well as the valley pseudo-spin texture is slightly changed. After a critical bias of about $\Delta^{c0}_{B,\tilde{\nu}=2.2} = 0.02e^2/\kappa\ell$, the meron crystal evolves to a skyrmion crystal. This phase transition is smooth. It is a second order phase transition. We show the valley skyrmion crystal in Fig. 3.2.3. All the charge concentrate on red dots. There is charge $q = -e$ in each red dot and still 4 electrons per unit cell in the crystal of Fig.3.2.3c.

However, in our numerical calculation, we find that the crystal phase turns into

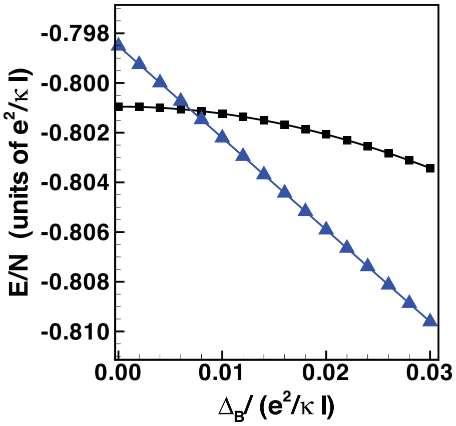

FIGURE 3.13: Comparison of the Hartree-Fock energy per electron at $\tilde{\nu} = 2.2$ of the valley meron crystal (black squares) and orbital skyrmion crystal (blue triangles). There is a first order phase transition between the valley meron crystal and orbital skyrmion crystal at $\Delta^{c1}_{B,\tilde{\nu}=2.2} = 0.007e^2/\kappa\ell$ [59].

an orbital skyrmion phase before the valley meron crystal could evolve to the valley skyrmion crystal. The phase transition is at $\Delta^{c1}_{B,\tilde{\nu}=2.2} \approx 0.007e^2/\kappa\ell$. The energies of these two crystals are plotted in Fig. 3.2.3. There is only one skyrmion per site in the ortibal skyrmion crystal. It contains no valley coherence. The states $|K',0\rangle$ and $|K',1\rangle$ are full. The rest $0.2N_\phi$ electrons all crystallize in the K valley with orbital texture. The orbital texture is induced by a Dzyaloshinskii-Moriya interaction between the different orbital pseudo-spin [70]. This type of crystal will be discussed in details in Sec. 3.3.

We conclude that the phase diagram at $\nu = 2.2$ is as follows: a checkerboard valley meron crystal when $\Delta_B \in [0, 0.007]e^2/\kappa\ell$; then an orbital skyrmion crystal in K valley when $\Delta_B > 0.007e^2/\kappa\ell$. If the bias is extremely large, there is a Wigner crystal in level $|K,1\rangle$. Note that, however, our numerical calculations do not cover all the possible crystal phases. The real phase diagram may be different from what we have shown.

3.2.4 Density of states

The crystal phases could be detected in principle by using a scanning tunneling microscope (STM). To link with the experimental observation, we study the local and total density of states (DOS) of the crystal phases in this section. For example, skyrmion lattices with charge $q = -2e$ per site can be distinguished from skyrmion lattices with charge $q = -e$ per site by their DOS.

The total DOS (TDOS) of the system $g(\omega)$ is given by

$$\begin{aligned} g\left(\omega\right) &= -\frac{1}{\pi}\sum_{\alpha,n}\int d\mathbf{r}\,\mathrm{Im}\left[G^{R}_{\alpha,n;\alpha,n}\left(\mathbf{r},\mathbf{r},\omega\right)\right] \qquad (3.48)\\ &= -\frac{1}{\pi}\sum_{\alpha,n}\sum_{X,X'}\mathrm{Im}\left[G^{R}_{\alpha,n;\alpha,n}\left(X,X',\omega\right)\right]\int d\mathbf{r}\,\Psi_{\alpha,n,X}\left(\mathbf{r}\right)\Psi^{*}_{\alpha,n,X'}\left(\mathbf{r}\right)\\ &= -\frac{1}{\pi}\sum_{\alpha,n}\sum_{X}\mathrm{Im}\left[G^{R}_{\alpha,n;\alpha,n}\left(X,X,\omega\right)\right] = -\frac{N_\phi}{\pi}\sum_{\alpha,n}\mathrm{Im}\left[G^{R}_{\alpha,n;\alpha,n}\left(\mathbf{q}=0,\omega\right)\right], \end{aligned}$$

where the wave function Ψ is defined in Eqs. (3.8) and (3.9). The Green's function in real space is defined by associating the Green's function in guiding center in Eq. (3.22) with the wave functions,

$$\begin{aligned} G_{\alpha,n;\alpha,n}\left(\mathbf{r},\mathbf{r},\tau\right) &= -\sum_{X,X'}\Psi_{\alpha,n,X}\left(\mathbf{r}\right)\Psi^{*}_{\alpha,n,X'}\left(\mathbf{r}\right)\left\langle T_\tau c_{\alpha,n,X}\left(\tau\right)c^{\dagger}_{\alpha,n,X}\left(0\right)\right\rangle\\ &= \sum_{X,X'}\Psi^{*}_{\alpha,n,X'}\left(\mathbf{r}\right)\Psi_{\alpha,n,X}\left(\mathbf{r}\right)G_{\alpha,n;\alpha,n}\left(X,X',\tau\right), \qquad (3.49) \end{aligned}$$

and the retarded Green's function $G^{R}_{\alpha,n;\alpha,n}\left(\mathbf{r},\mathbf{r},\omega\right)$ is obtained from $G_{\alpha,n;\alpha,n}\left(\mathbf{r},\mathbf{r},i\omega_n\right)$ which is the Fourier transform of $G_{\alpha,n;\alpha,n}\left(\mathbf{r},\mathbf{r},\tau\right)$ by the analytical continuation,

$$G^{R}_{\mu,\mu}\left(\mathbf{r},\mathbf{r},\omega\right) = \lim_{i\omega_n\to\omega+i0^+}G_{\mu,\mu}\left(\mathbf{r},\mathbf{r},i\omega_n\right). \qquad (3.50)$$

We observe that the number of peaks near the Fermi level in the TDOS is equal to the number of electrons per site in a skyrmion crystal. The curves of TDOS of the skyrmion crystals with $q = -e$ and $q = -2e$ are displayed in Fig (3.14). A similar result was also found for bubble crystals in semiconductor's 2DEG [66].

It was shown by Poplavskyy et al. [68] that the density pattern in the bubble crystal can also be seen in STM. This measure is related to the local DOS (LDOS) which is defined by

$$\begin{aligned} g_L\left(\mathbf{r},\omega\right) &= -\frac{1}{\pi}\sum_{\alpha,n}\mathrm{Im}\left[G^{R}_{\alpha,n;\alpha,n}\left(\mathbf{r},\mathbf{r},\omega\right)\right] \qquad (3.51)\\ &= -\frac{N_\phi}{\pi}\mathrm{Im}\sum_{\alpha,n}\sum_{\mathbf{q}}\sum_{X,X'}e^{\frac{i}{2}q_x\left(X+X'\right)}\delta_{X,X'-q_y l_\perp^2}\phi_{m,X}\left(\mathbf{r}\right)\phi^{*}_{m,X'}\left(\mathbf{r}\right)G^{R}_{\alpha,n;\alpha,n}\left(\mathbf{q},\omega\right), \end{aligned}$$

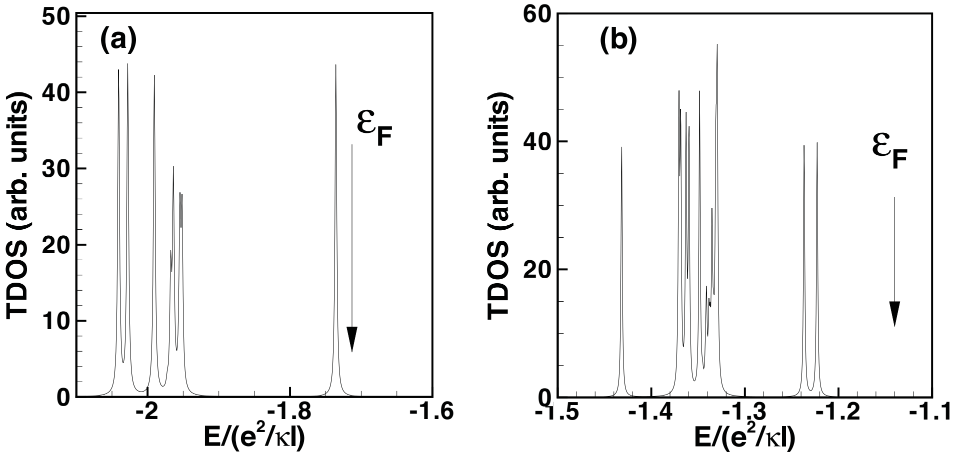

FIGURE 3.14: Total density of states for orbital skyrmion crystals at $\tilde{\nu} = 1.2$. Only the low energy part is shown in the figure. ϵ_F is the Fermi energy. (a) Skyrmion crystal with one electron per site at $\Delta_B = 1.28e^2/\kappa\ell$, which is discussed in Sec. 3.2.1; (b) $\Delta_B = 0.002e^2/\kappa\ell$, the TDOS of skyrmion crystal which is shown in Fig. 3.7, and where there are two electrons per site.

where we use

$$G^R_{\alpha,n;\alpha,n}(X, X', \omega) = N_\phi \sum_{\mathbf{q}} e^{\frac{i}{2}q_x(X+X')}\delta_{X,X'-q_y\ell^2} G^R_{\alpha,n;\alpha,n}(\mathbf{q},\omega), \tag{3.52}$$

so that we obtain

$$g_L(\mathbf{r}, \omega) = -\frac{1}{\pi}\frac{1}{2\pi\ell^2}\sum_{\alpha,n}\mathrm{Im}\sum_{\mathbf{q}} G^R_{\alpha,n;\alpha,n}(\mathbf{q},\omega) F_{n,n}(-\mathbf{q}) e^{i\mathbf{q}\cdot\mathbf{r}}, \tag{3.53}$$

and the function $F_{n,n}$ defined in Eq. (2.56).

We show the LDOS in Fig. 3.15 in valley K' and at the energies of the highest peak in Fig. 3.14a and of the two highest peaks in Fig. 3.14b. The LDOS is almost the same for both peaks in the case of the skyrmion crystal with charge $q = -2e$. The LDOS for the skyrmion crystal with charge $q = -e$ in Fig. 3.15c also looks similar to that in Figs. 3.15a and 3.15b. Following Ref. [68], we can also sum the LDOS evaluated at all the

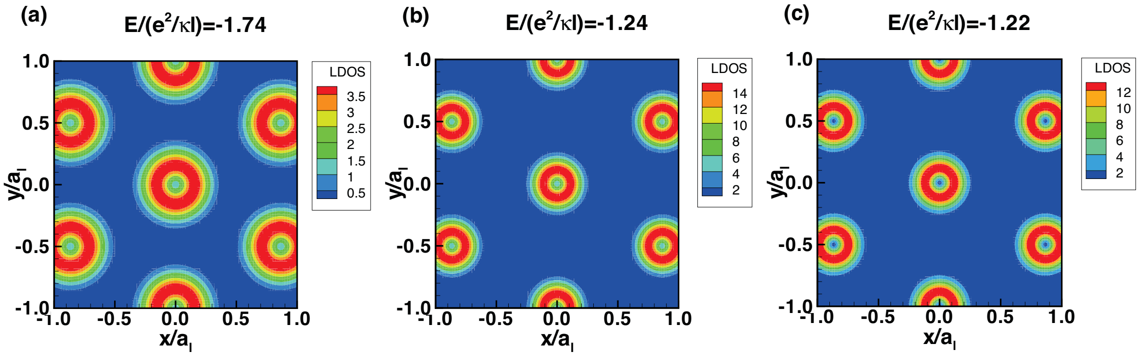

FIGURE 3.15: Local density of states for orbital skyrmion crystals at $\tilde{\nu} = 1.2$. (a) The LDOS for skyrmion crystal in Fig. 3.14a at the energy of the highest peak. Pictures (b) and (c) are the LDOS corresponding to the highest two peaks in Fig. 3.14b. The energies where the LDOS are calculated are listed above the LDOS figures.

peaks below the Fermi energy ϵ_F. The summation gives

$$\int_{-\infty}^{\epsilon_F} g_L(\mathbf{r}, \omega)\, d\omega = N_p(\mathbf{r}), \tag{3.54}$$

where $N_p(\mathbf{r})$ is the density defined in Eq. (3.40) in guiding center representation. It follows that the LDOS is not directly related to the orbital coherence.

We should mention that, however, the lattice constant a_l of the crystals in this section is related to the filling factor. For example, for a triangular crystal shown in Sec. 3.2.1, the lattice constant is given by $a_l = \sqrt{\frac{4\pi}{(\tilde{\nu}-1)\sqrt{3}}}\ell \approx 6\ell$, which is much larger than the lattice constant of graphene. It follows that observing the crystal by STM may not be an easy work.

At the end of this section, we would like to comment on the effect of ζ_1. At $B = 10$T, $\zeta_1 = 0.113e^2/\kappa\ell$, which is not small. The parameter ζ_1 has the possibility to change the phase diagram, especially at small or zero bias. Furthermore, the orbital coherence depends on the gap between the two orbital states. If $\zeta_1 \neq 0$, the state $|K, 1\rangle$ is below $|K, 0\rangle$ in the K valley when $\Delta_B > 1.27e^2/\kappa\ell$. Fortunately, our numerical calculations show that the orbital skyrmions crystal does survive even with a finite ζ_1. At filling factor $\tilde{\nu} = 1.2$, finite ζ_1 eliminates the $q = -2e$ orbital skyrmion crystal in the phase diagram. However the $q = -e$ orbital skyrmion crystal still exists. This is consistent with our conclusion that skyrmion crystal with $q = -2e$ exists at small gap only. At

$\tilde{\nu} = 3.2$, due to the positive ζ_1, state $|K, 1\rangle$ has a chance to be above $|K, 0\rangle$ at small bias, i.e. $\zeta_1 - \beta\Delta_B > 0$. Hence, if the gap $\zeta_1 - \beta\Delta_B$ is tuned from positive to negative, both of the orbital skyrmion crystals can be found.

3.3 Charge-density-wave states at integer filling factors

As we mentioned in Sec. 3.2.3, the phase diagram at $\tilde{\nu} = 2.2$ includes a valley skyrmion crystal which we have not analyzed yet. This crystal phase is special, since it exists even at some integer filling factors. At $\tilde{\nu} = 2.2$ and sufficient large bias ($\Delta_B > 0.007e^2/\kappa\ell$), the K' valley is full, so that there are $2N_\phi$ electrons in the K' valley while $0.2N_\phi$ electrons have crystallized in the K valley. In fact, not only at $\tilde{\nu} = 2.2$, but also when $\tilde{\nu} \in [2.2, 3]$, this orbital skyrmion crystal phase exists in the K valley at sufficient large bias.

At $\nu = -3, 1$, the ground state has all the charge in one layer (or valley) at a sufficient large bias. The ground state is uniform and contains an orbital pseudospin mode that can be viewed as an inter-orbital excitation or a cyclotron resonance [51, 60]. This mode is gapped due to the finite bias and should be detectable in microwave absorption experiments because it involves the fluctuations of electric dipoles [70]. At integer filling factor $\nu = -1$ ($\tilde{\nu} = 3$), we suppose that the 2DEG is spin polarized. Usually, the liquid phase which has a uniform density and polarized (pseudo-)spin texture is the ground state of the system. The liquid phase diagram at $\tilde{\nu} = 3$ is studied in details in Ref. [13, 51, 53]. It was shown that the liquid phase has an instability in the collective modes [13, 70] at finite wavevector above a critical bias. This implies that the ground state above this critical bias may be a charge-density-wave state.

We find that at $\tilde{\nu} = 3$ a crystal phase has lower energy than the liquid phase when the bias is finite. The orbital texture crystal is similar to the orbital skyrmion crystal discussed in Sec. 3.2.3 at $\tilde{\nu} = 2.2$. The only difference is that the crystalline filling $\nu_c = 1$ for $\tilde{\nu} = 3$, while $\nu_c = 0.2$ for $\tilde{\nu} = 2.2$. For convenience and without loss of generality, we study the system at $\tilde{\nu} = 3$ in a four-level system

With the same method we used to study the crystal phase in Sec. 3.2, we write the Hartree-Fock Hamiltonian. Then we use the Green's function method, which is introduced in Sec. 1.3 and is utilized in Sec. 3.2, to calculate the charge-density-wave phases.

In order to be consistent with the first part of this chapter, we still set $\zeta_1 = 0$ in this section. For simplicity and without loss of generality, we simplify the four-level system to a two-orbital system. We neglect the K' valley and keep the two orbitals in the K valley since the K' valley is full and there is no valley coherence at large bias. So the density matrix $\rho_{K,i;K,j}$ $(i, j = 0, 1)$ can be simplified to $\rho_{i,j}$.

3.3.1 Dzyaloshinskii-Moriya interaction in pseudo-spin language

Usually, the uniform liquid state is the ground state in the 2DEG since the Coulomb interaction at $\mathbf{q} = \mathbf{0}$ gives the lowest energy. At integer filling factor $\tilde{\nu} = 3$, ones obtain that there is an instability in the collective mode for the uniform liquid phase (ULP) at some bias, see the Fig. 5 in Ref. [70]. This occurs because effective interaction between electrons has a minimum at finite momenta $\mathbf{q} \neq \mathbf{0}$ instead of $\mathbf{q} = \mathbf{0}$. The order parameters $\langle \rho (\mathbf{q} \neq 0) \rangle$ would be nonzero to minimize the total energy of the system and the ground state is non-uniform.

It was shown recently [53] that there is a Dzyaloshinskii-Moriya (DM) interaction [71] between the orbital pseudo-spins that causes this instability of ULP. Because of the DM interaction, the ground state at integer filling factors $\nu = -1, 3$ may contain helical phases similar to those observed in other magnetic systems [72–74]. Following Ref. [70], we give the DM Hamiltonian and then discuss the phase diagram in the next section. If we define a set of orbital pseudo-spin field

$$
\begin{aligned}
S_x &= \mathrm{Re}\rho_{0,1} = \frac{\rho_{0,1} + \rho_{1,0}}{2}, && (3.55a)\\
S_y &= \mathrm{Im}\rho_{0,1} = \frac{\rho_{0,1} - \rho_{1,0}}{2i}, && (3.55b)\\
S_z &= \frac{\rho_{0,0} - \rho_{1,1}}{2}, && (3.55c)
\end{aligned}
$$

then the total energy functional is similar to a Heisenberg term $\mathbf{S}(-\mathbf{q}) \cdot \mathbf{S}(\mathbf{q})$ plus a DM term $\mathbf{S}(-\mathbf{q}) \times \mathbf{S}(\mathbf{q})$,

$$
\begin{aligned}
& \sum \left\{ f \mathbf{S}(-\mathbf{q}) \cdot \mathbf{S}(\mathbf{q}) + \mathbf{j} \cdot [\mathbf{S}(-\mathbf{q}) \times \mathbf{S}(\mathbf{q})] \right\} \\
= & \sum_i \sum_{\mathbf{q}} f S_i(-\mathbf{q}) \cdot S_i(\mathbf{q}) + \sum_{k,l,m} \sum_{\mathbf{q}} \epsilon_{klm} j_k S_l(-\mathbf{q}) S_m(\mathbf{q}), \qquad (3.56)
\end{aligned}
$$

where f and j_k are all from the Hartree and Fock interactions.

The exchange interactions tend to polarize the pseudo-spins, while the DM term favors the rotation of the pseudo-spins in the guiding center representation. This rotation is associated with charge density wave in real space. The competition between the Heisenberg and DM interactions actually makes the ULP instable. This type of competition also exists in helical magnets such as MnSi and $\mathrm{Fe}_{1-x}\mathrm{Co}_x\mathrm{Si}$. For example, the Hamiltonian in Eq. (3.56) is very similar to that of $\mathrm{Fe}_{0.5}\mathrm{Co}_{0.5}\mathrm{Si}$. Indeed, our numerical calculations give a phase diagram that is similar to what has been found recently in the helical magnet $\mathrm{Fe}_{0.5}\mathrm{Co}_{0.5}\mathrm{Si}$ where skyrmion crystal and a helical phase have been observed by Lorentz transmission electron microscopy [72].

It is important to notice that the DM interaction in our model has nothing to do with spin-orbit coupling. In a magnet system, the DM interaction is due to the spin-orbit coupling of each ion in the crystal lattice. However, it comes entirely from the exchange interaction and the fact that the orbital pseudo-spin involves the coupling between two different orbitals ($n = 0$ and $n = 1$) in graphene bilayer.

3.3.2 Phase diagram in a two-orbital system

When we study the phase diagram at $\tilde{\nu} = 3$ at finite bias, we assume that the filled states in valley K' are inert. The inter valley coherence is consequently neglected. If we use a finite ζ_1, then the phase diagram we present in Eq. (3.57) is still valid, but we need to shift all biases by $1.28e^2/\kappa\ell$. A bias $\Delta_B = 1.28e^2/\kappa\ell$ is able to make the kinetic energy of $|K, 1\rangle$ identical to $|K, 0, \rangle$. Using our Green's function method, we obtain the following phase diagram:

$$\begin{array}{cc} 0 < \Delta_B < 0.1\frac{e^2}{\kappa\ell}, & \mathrm{Uniformliquidphase} \\ 0.1\frac{e^2}{\kappa\ell} < \Delta_B < 0.52\frac{e^2}{\kappa\ell}, & \mathrm{Orbitalskyrmioncrystal} \\ 0.52\frac{e^2}{\kappa\ell} < \Delta_B < 3.02\frac{e^2}{\kappa\ell}, & \mathrm{Helicalphase} \\ 3.02\frac{e^2}{\kappa\ell} < \Delta_B < 3.44\frac{e^2}{\kappa\ell}, & \mathrm{Orbitalskyrmioncrystal} \\ 3.44\frac{e^2}{\kappa\ell} < \Delta_B. & \mathrm{Uniformliquidphase} \end{array} \tag{3.57}$$

The ULP requires that $\langle\rho_{i,j}(q \neq 0)\rangle = 0$. The helical phase (HP) and the orbital skyrmion crystal (OSC) phase are symmetric with respect to the middle of the HP at $\Delta_B^{center} = 1.75e^2/\kappa\ell$. The HP is also called the spiral phase and contains a charge density wave in real space and a spiral orbital pseudo-spin texture in the guiding center representation. An example of HP is shown in Fig. 3.17. The density profile shows

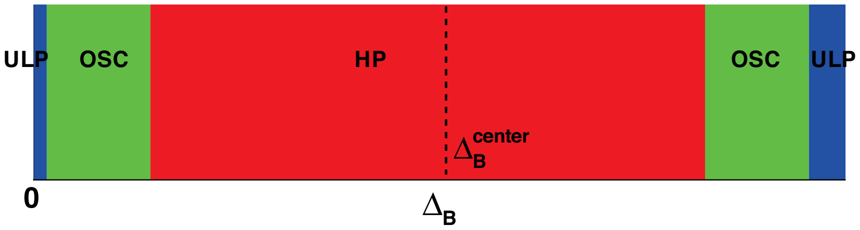

FIGURE 3.16: The phase diagram sketch. Blue represents the ULP, green region is the OSC phase, and red region is the HP. The middle of the HP is Δ_B^{center}.

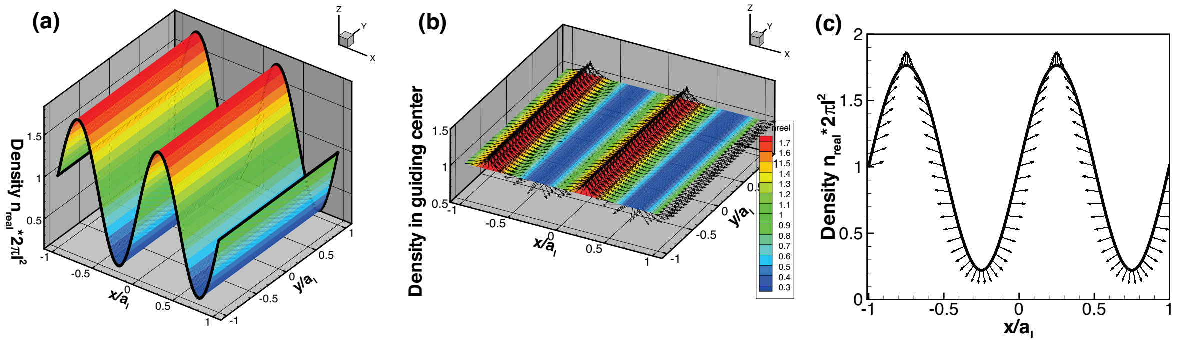

FIGURE 3.17: The ULP at bias $\Delta_B = 0.6e^2/\kappa\ell$. (a) The real density profile. (b) The density in guiding center representation, and the color is the density in real space. The orbital pseudo-spin texture in guiding center is also indicated. (c) The combination of density in real space and the guiding center pseudo-spin texture.

a stripe in the y direction and a sine-like wave in x direction, while the density in the guiding center representation is uniform. Details of the HP can be found in Ref. [70].

The orbital skyrmion crystal phase, as we mentioned in Sec. 3.2.3, also exists at $\tilde{\nu} = 2.2$. Both the helical phase and orbital skyrmion crystal phase are observed in the helical magnet $\mathrm{Fe}_{0.5}\mathrm{Co}_{0.5}\mathrm{Si}$ [72], where the Hamiltonian also contains a DM term similar to that of Eq. (3.56). Therefore, the orbital skyrmion crystal is basically induced by the DM interaction. In this system, however, the DM interaction originates from a spin-orbit coupling.

There is one electron per site in a triangular lattice in the orbital skyrmion crystal phase. So the density is given by $2/(a_l^2\sqrt{3})$, where a_l is the lattice constant of the electron

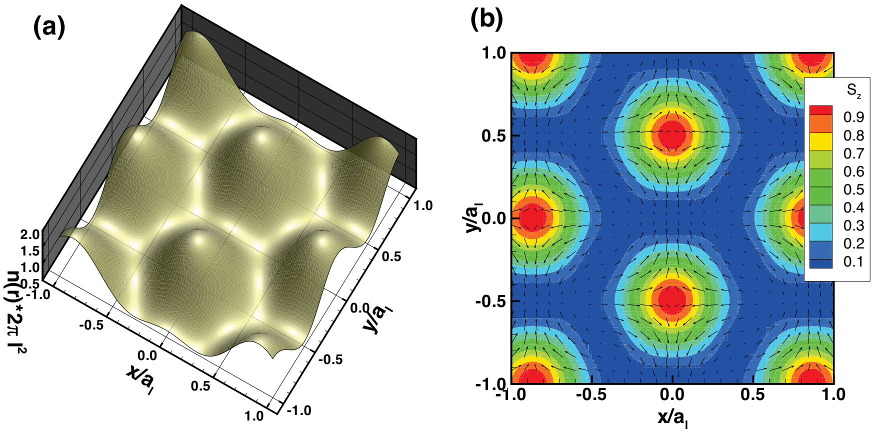

FIGURE 3.18: The OSC phase at bias $\Delta_B = 0.2e^2/\kappa\ell$. (a) The density $n(\mathbf{r})$ in real space, $n(\mathbf{r}) > 0.5\frac{1}{2\pi\ell^2}$. (b) The orbital pseudo-spin texture pattern in the guiding center representation.

crystal. On the other hand, in our system, the filling factor of the crystallized electrons is 1. So the density is also given by $1/(2\pi\ell^2)$. Then we obtain $a_l = \sqrt{4\pi/\sqrt{3}}\ell$. The electron wave function of neighboring sites overlaps strongly (the minimum of $n(\mathbf{r})$ is about $0.5\frac{1}{2\pi\ell^2}$) and the density in real space is shown in Fig. 3.18a, where the true density $n(r)$ defined by Eq. (3.39) is plotted. In Fig. 3.18b, the orbital pseudo-spin around each site (each red dot) displays a typical skyrmion texture.

A crystal structure at integer filling factor $\nu = 1$ is unusual. It occurs in our system because the real density involves the coherence between two different orbitals. If we look at the density in guiding center which is defined in Eq. (3.40), it is a uniform state. With two levels of the same wave function (for example, $n = 0$ and different spins), exchange interaction favors a uniform polarized state, a modulated structure is impossible.

Notice that in the phase diagram in Fig. 3.16, the electron crystal phase occurs on both sides of the helical state in the phase diagram, and is symmetric with respect to Δ_B^{center}. So we have

$$n(\mathbf{r}, 2\Delta_B^{center} - \Delta_B) = \frac{2}{2\pi\ell^2} - n(\mathbf{r}, \Delta_B), \tag{3.58}$$

$$S_z(\mathbf{r}, 2\Delta_B^{center} - \Delta_B) = -S_z(\mathbf{r}, \Delta_B). \tag{3.59}$$

The pseudospin vorticity in the x-y plane is the same for both $2\Delta_B^{center} - \Delta_B$ and Δ_B, since the coherence $\rho_{0,1}$ does not change.

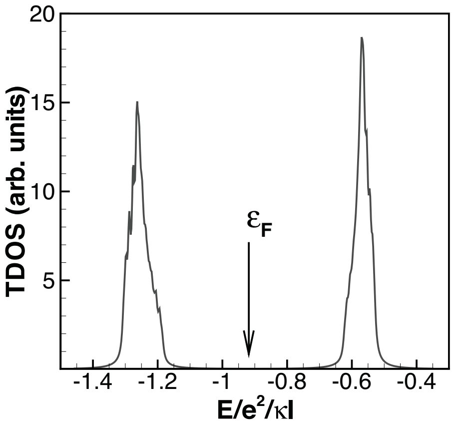

FIGURE 3.19: The total density of states of OSC at bias $\Delta_B = 0.2e^2/\kappa\ell$ [59].

The total density of states can be also calculated in the same way as in Sec. 3.2.4. It is shown in Fig. 3.19.

3.3.3 Collective modes

The collective modes of a given phase are given by the poles of the imaginary part of the retarded response functions. According to the formalism in Sec. 1.3, the poles of the response functions can be obtained by diagonalizing the matrix $(i\Omega_n I - F)$ in the equation of motion of two-particle Green's function in Eq. (1.81). However, in the case considered in this section, the system does not involve the valley index. Hence, in such a two-level system, the equation of motion of the two-particle Green's function is obtained by omitting the indices a, b, c, d, e, f, g in Eqs. (1.79) and (1.80). In our system, the Hartree and Fock interactions in Eqs. (1.79) and (1.80) are defined by Eqs. (3.19) and (3.20), respectively.

Using the pseudo-spin field defined in Eq. (3.55), the response functions $\chi^R_{a,b}(\mathbf{q}, \mathbf{q}', \tau)$ $(a, b = S_x, S_y, S_z, S_n)$ are defined by the combinations of the two particle Green's functions, as shown in Eq. (1.74). The collective modes can be obtained from the poles of the imaginary part of the full GRPA response functions $\chi^R_{a,a}(\mathbf{k}, \mathbf{k}, \omega)$. The retarded correlation function can be obtained by the analytic continuation $i\Omega_n \to \omega + i\delta$ in $\chi(i\Omega_n)$, i.e.

$$\chi^R_{a,b}\left(\mathbf{q}, \mathbf{q}', \omega\right) = \lim_{i\Omega_n \to \omega + i0^+} \chi_{a,b}\left(\mathbf{q}, \mathbf{q}', i\Omega_n\right). \tag{3.60}$$

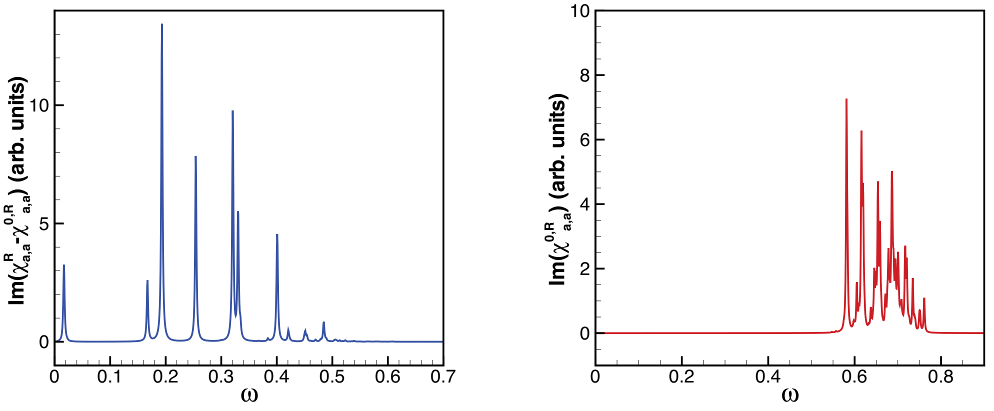

(a)

(b)

FIGURE 3.20: The imaginary parts of (a) the retarded response function $\chi^{R}_{a,a}(\mathbf{q},\omega)-\chi^{0,R}_{a,a}(\mathbf{q},\omega)$ and (b) the single bubble response function $\chi^{0,R}_{a,a}(\mathbf{q},\omega)$ ($a=S_n$) when the momenta $\mathbf{q}=(0.1/\ell,0)$. The electron-hole continuum is mainly from $\chi^{0,R}_{a,a}(\mathbf{q},\omega)$.

Note that the poles of the single bubble response function $\chi^{0,R}_{S_n,S_n}(\mathbf{q},\mathbf{q},\omega)$ contains the electron-hole continuum only, and does not capture the collective modes which are obtained from the GRPA for the response function.

To get the full dispersion relation, we need to sum over all the reciprocal lattice vectors $\mathbf{G}$ of the electron crystal,

$$\chi^{R}_{a,a}\left(\mathbf{q},\omega\right)=\sum_{\mathbf{G}}\chi^{R}_{a,a}\left(\mathbf{q}+\mathbf{G},\mathbf{q}+\mathbf{G},\omega\right). \tag{3.61}$$

$\chi^{R}_{a,a}\left(\mathbf{q},\omega\right)$ does not only contain the collective modes (if $a=S_n$ then the modes correspond to density collective modes; if $a=S_x$ then the modes correspond to pseudo-spin waves), but also the electron-hole continuum. Notice that all response functions are coupled in the GRPA equations in Eqs. (1.79) and (1.80). Consequently, they all share the same poles. However, the weight of a certain pole depends on the nature of the underlying mode (basically the Hartree-Fock Hamiltonian and the ground state) and is not the same in all response functions. Fig. 3.20 shows the imaginary part of the response functions at $q_x=0.1/\ell, q_y=0$. Electron-hole excitations which are provided mostly by the single bubble response function $\chi^{0,R}_{S_n,S_n}(\mathbf{q},\omega)$ appear as very localized excitations and are captured in the response functions at finite $\mathbf{G}$.

We follow the frequencies of the low-energy peaks in Fig. 3.20 as the wave vector is

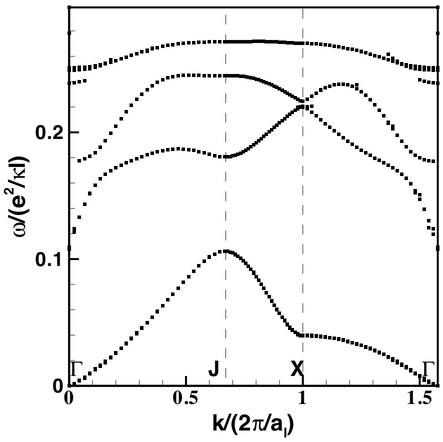

FIGURE 3.21: The low-energy collective modes of the OSC phase at $\Delta_B = 0.2e^2/\kappa\ell$. The x axis is along the path $\Gamma \to J \to X \to \Gamma$ in the first Brillouin zone.

varied in the first Brillouin zone of the electron crystal. Fig. 3.21 shows the low-energy collective modes of the OSC phase at bias $\Delta_B = 0.2e^2/\kappa\ell$. The modes become more and more dense at higher energy until the electron-hole continuum appears. From the DOS in Fig. 3.19, the continuum is in the range $E_{eh} \in [0.47, 0.90]$. The dispersion for $2\Delta_B^{center} - \Delta_B$ is not shown, but is exactly the same as that for Δ_B, as expected.

Since our calculation does not include disorder, the lowest energy mode is a gapless magnetophonon mode. At $\Delta_B = 0.2e^2/\kappa\ell$, the dispersion relation goes as $\omega \sim k^{1.5}$, which is like the magnetophonon mode in Wigner crystal [26].

In the second lowest mode, there are substantial weights in $\chi^R_{S_x,S_x}$ and $\chi^R_{S_y,S_y}$, which means the mode has a pseudo-spin wave character. It seems that this mode is the pseudo-spin $x-y$ mode gapped by the DM Hamiltonian. This mode is gapless in a spin skyrmion crystal [75], since there is no DM interaction in this case.

When disorder is considered, the crystal is pinned by the impurities and magnetophonon mode is gapped. The resulting "pinning" mode is detectable in microwave absorption experiments.

3.3.4 Electromagnetic absorption

The collective modes of the HP and OSC phase can be detected in an electromagnetic absorption experiment. Theoretically, the absorption can be related to the current-

current correlation functions [53], so that we define the current operator as,

$$j_i^\alpha = -c\,\frac{\delta H_\alpha}{\delta A_i}\bigg|_{A_i=0}, \tag{3.62}$$

where α is the valley index, $i = x, y$, and A_i is the i direction component of the vector potential. In the first quantization, the current operators are 2×2 matrices. In second quantization, we have

$$J_i^\alpha = \sum_{n,n'}\sum_{X,X'}\int d\mathbf{r}\Psi^*_{\alpha,n,X}(\mathbf{r})\, j_i^\alpha \Psi_{\alpha,n',X'}(\mathbf{r})\, c^\dagger_{\alpha,n,X} c_{\alpha,n',X'}, \tag{3.63}$$

where the wave function Ψ is defined in Eq. (3.9). Then we obtain in our two-orbital system, in the K valley, that

$$J_i^K = \frac{\sqrt{2}\ell e}{\hbar} N_\phi \Delta_B \beta S_{\bar{i}}^K, \tag{3.64}$$

where the bar over i represents that $\overline{x} = y, \overline{y} = x$. Following the definition of correlation function in Eq. (1.74), we write the current-current two-particle Green's function,

$$\chi_{J_iJ_j}(q,\tau) = -\frac{1}{S}\left\langle T_\tau J_i^K(q,\tau)\, J_j^K(-q,0)\right\rangle = \frac{e^2\Delta_B^2\beta^2}{\pi\hbar}\chi_{S_{\bar{i}}S_{\bar{j}}}(q,\tau),$$

where S is the area of the sample and $i, j = x, y$, and we define

$$\chi_{S_{\bar{i}}S_{\bar{j}}}(q,\tau) = -\frac{N_\phi}{\hbar}\left\langle T_\tau S_{\bar{i}}^K(q,\tau)\, S_{\bar{j}}^K(-q,0)\right\rangle. \tag{3.65}$$

The electromagnetic absorption is given by

$$P_i(\omega) = -\mathrm{Im}\left[\frac{\chi^R_{J_iJ_i}(q=0,\omega)}{\hbar(\omega+i\eta)}\right]E_0^2 = -\frac{1}{\hbar}\frac{e^2\Delta_B^2\beta^2}{\pi\hbar}E_0^2\mathrm{Im}\left[\frac{\chi^R_{S_{\bar{i}}S_{\bar{i}}}(0,\omega)}{\omega+i\eta}\right],$$

where E_0 is the electric field $\mathbf{E}(r,t) = E_0\widehat{\mathbf{i}}e^{i(\mathbf{q}\cdot\mathbf{r}-\omega t)}$ with polarization $\widehat{\mathbf{i}}$ and the retarded response functions are obtained by using the analytic continuation $i\Omega_n \rightarrow \omega + i\eta$ in $\chi_{J_iJ_i}(i\Omega_n)$. $P_i(\omega)$ is the absorption power per unit area.

The absorptions are shown in Fig. 3.22 at $\Delta_B = 0.07e^2/\kappa\ell, 0.2e^2/\kappa\ell, 0.51e^2/\kappa\ell$ for different phases. In these case, all the modes (except the gapless phonon mode) are active in the absorptions. The low energy absorption peaks, actually, correspond to

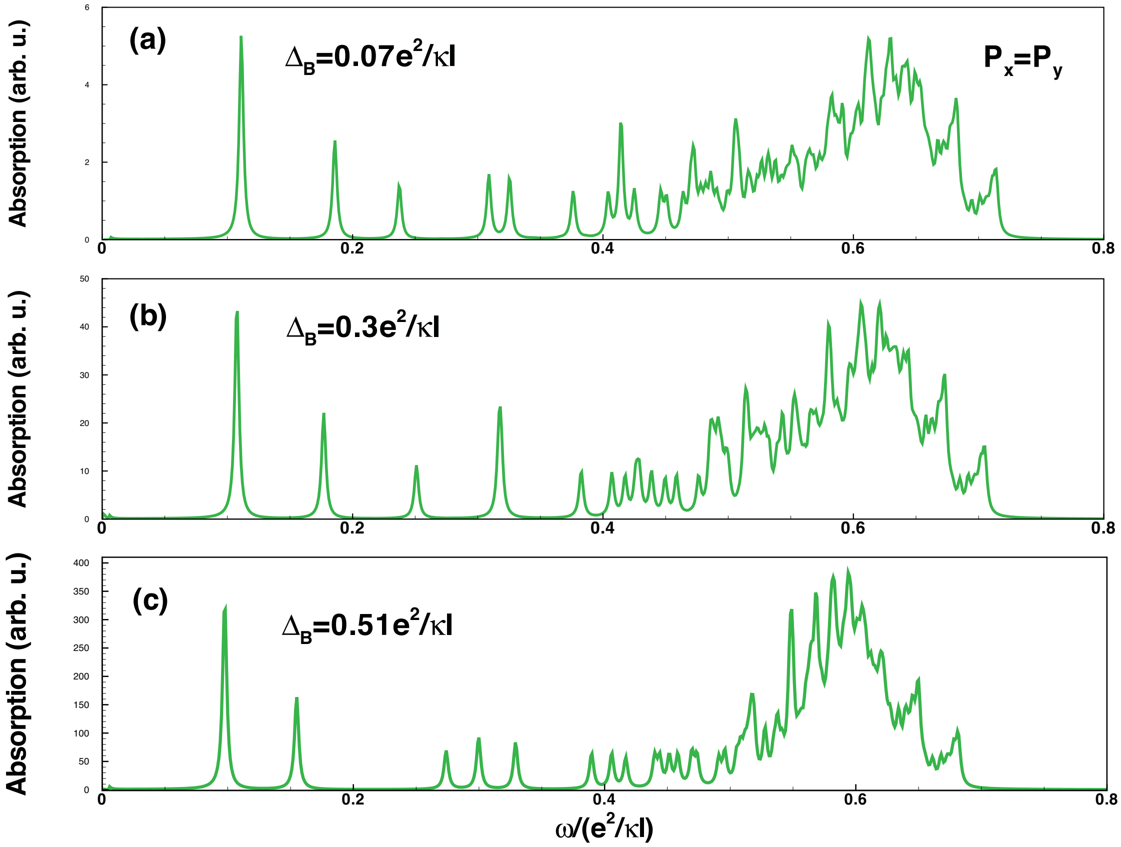

FIGURE 3.22: The electromagnetic absorptions $P_\alpha(\omega)$ of the OSC phase at different bias. The absorption for the polarization of the electromagnetic field in the x direction is identical to that in the y direction.

the gap of the low energy gapped modes at zero momentum. All the absorption peaks are slightly shifted when the bias increases. If we suppose the substrate is SiO_2, the dielectric constant $\kappa = 5$, then the basic frequency $\nu_0 = e^2/(\hbar\kappa\ell) = 0.43\sqrt{B}$THz. For the absorption peaks of the OSC phase, the frequency should be $\nu \in [0.14, 0.54]$THz at $B = 10$T.

It seems that the absorption is isotropic, i.e. $P_x = P_y$. There are qualitative differences between the absorptions in the HP and OSC phase, which may help to observe the transition between these two phases [70]. Notice that, in the ULP, the orbital pseudospin mode is gapless and does not lead to absorption at finite frequency.

In this chapter, we consider a series of crystal phases near or at integer filling factors in LL $N = 0$ in graphene bilayer. We note that the DM interaction which is induced by the orbital exchange interaction crystalize the electron gas even at integer fillings. We also propose a STM and electromagnetic absorption measurements to observe those crystal phases.

Chapter 4

Ground state and excitations in LL $|N| > 0$ of bilayer graphene

In analogy to monolayer graphene, higher Landau levels in bilayer graphene (even chiral stacking multi-layer graphene) also have four-fold degeneracy in the absense of Zeeman coupling. The valley degeneracy, however, can now be lifted by an electric field perpendicular to the sample. The possibility to control the valley degree of freedom makes the phase diagram of the C2DEG in bilayer graphene very rich. As was the case with monolayer graphene, we are interested by the nature of the ground state and by the single-particle excitations in such a four-level system. It is interesting to compare these excitations with those in monolayer graphene.

In higher Landau levels in graphene bilayer, the effective two-component model derived in Sec. 1.2.2 is not accurate. Côté and Barrette [76] have shown that both the eigenenergies and eigenstates of higher Landau levels in the two-component model differ substantially from the four-band model given in Sec. 1.2.1. This is why we will use the four-band model in this chapter. By "four-band" model, we mean the full non-interacting Hamiltonian given in Eq. (1.25) where the warping term γ_3 is set to zero.

4.1 Validity of the four-band model

In order to verify the validity of the four-band model approximation, we diagonalize the full Hamiltonian including the warping γ_3 in basis of the eigenvectors of the four-band model, and compare the exact energies with those of the four-band model [76]. Each element of the new matrix of the full Hamiltonian $C_{i,i'}$ can be written as, for example in the K valley,

$$\begin{aligned} C_{(b,N),(b,N')} &= \left\langle \phi_N^b \right| H_K \left| \phi_{N'}^b \right\rangle \\ &= \begin{pmatrix} y_{1,N}^* h_N^* & y_{2,N}^* h_{N+1}^* & y_{3,N}^* h_{N-1}^* & y_{4,N}^* h_N^* \end{pmatrix} H_K \begin{pmatrix} y_{1,N'} h_{N'} \\ y_{2,N'} h_{N'+1} \\ y_{3,N'} h_{N'-1} \\ y_{4,N'} h_{N'}, \end{pmatrix} \end{aligned} \tag{4.1}$$

where we suppose N is the absolute value of the LL index, H_K given in Eq. (1.29) is the tight-binding Hamiltonian in the valley K, and $\left|\phi_{N'}^b\right\rangle$ is the eigenstate of the four-band model in LL N and band b. The full Hamiltonian gives an infinity large matrix that we need to truncate to a finite one for numerical calculation. For small LL index $|N|$, it was shown in Ref. [76] that an accurate result for the energy was obtained by keeping a relatively small number of matrix elements $C_{(b,N),(b,N')}$.

The energies in Landau levels $N = 1, 2, 3$ in the band 2 in the four-band model have a less than 1% difference from the corresponding exact eigenergies of the full Hamiltonian. Furthermore, the projection of the eigenvector of the four-band model in Landau level 1 $\left|\phi_N^b\right\rangle$ to the corresponding eigenvector of the full Hamiltonian $\left|\psi_N^b\right\rangle$ is given numerically by $\left\langle \phi_{N=1}^b \right| \psi_{N=1}^b \rangle = 0.994$, which is close to 1. Moreover, $\left\langle \phi_{N=2}^b \right| \psi_{N=2}^b \rangle = 0.988$ and $\left\langle \phi_{N=3}^b \right| \psi_{N=3}^b \rangle = 0.985$. (The projections are given at magnetic field $B = 10$T, dielectric constant $\kappa = 2.5$, and zero bias.) It means that not only the eigenenergies but also the eigenstates are well approximated by the four-band model.

In Fig. 4.1 [25], we show the kinetic energies of Landau levels with different bias Δ_B between the two layers of graphene bilayer. It is shown that the Landau levels $N = 1, 2, 3$ separate from each other very well when $\Delta_B < 0.05$eV.

4.2 Hartree-Fock Hamiltonian

In the approximation where the Hilbert space is restricted to one LL (valid at high magnetic field and low temperature), the kinetic energy is effectively frozen. In this case, the Coulomb interaction plays a dominant role and determines the phase diagram of the 2DEG.

When $B = 10$T, $\kappa = 2.5$, and zero bias, we obtain that the kinetic energies of Landau

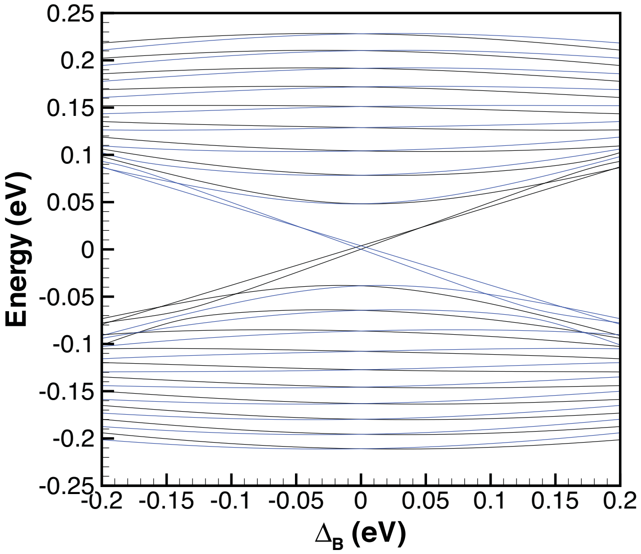

FIGURE 4.1: The energies of Landau levels in the four-band model. The black curves represent the energies of LLs in the K valley, and the blue curves represent the energies of LLs in the K' valley. The four states with linear dispersion belong to the two orbitals in LL $N = 0$. Spin is not taken into account here.

levels $N = 0, 1, 2, 3$ in band 2 are $E_{N=0}^{k,b=2} = 0.039(e^2/\kappa\ell), E_{N=1}^{k,b=2} = 0.67(e^2/\kappa\ell), E_{N=2}^{k,b=2} = 1.095(e^2/\kappa\ell), E_{N=3}^{k,b=2} = 1.465(e^2/\kappa\ell)$, respectively, if the Zeeman coupling is ignored. The Zeeman coupling is usually of the order of $0.01(e^2/\kappa\ell)$. Note that we also neglect Landau level mixing in this chapter when we discuss the ground states and excitations, since the Landau gap is much larger than the Zeeman coupling and we consider small bias only. Although the Zeeman energy is weak, it breaks the SU(2) symmetry of spin. So that we need to take it into account when we consider the ground state phase diagram.

In the four-band model, we define the field operator as

$$\Psi_{\alpha,s}(\mathbf{u}) = \sum_X e^{-i\alpha\cdot\mathbf{r}} \begin{pmatrix} y_{1,N}^{\alpha} h_{N,X}(\mathbf{r}) |A_1\rangle \delta\left(z + \frac{d}{2}\right) \\ y_{2,N}^{\alpha} h_{N+\alpha,X}(\mathbf{r}) |B_1\rangle \delta\left(z + \frac{d}{2}\right) \\ y_{3,N}^{\alpha} h_{N-\alpha,X}(\mathbf{r}) |A_2\rangle \delta\left(z - \frac{d}{2}\right) \\ y_{4,N}^{\alpha} h_{N,X}(\mathbf{r}) |B_2\rangle \delta\left(z - \frac{d}{2}\right) \end{pmatrix} c_{\alpha,s,X}, \tag{4.2}$$

where α is the valley index and $\alpha = \pm 1$ for K and K' valley respectively. The 3D vector $\mathbf{u}$ contains the in-plane component $\mathbf{r}$ and the z direction component. The bilayer graphene is in the xOy plane, and the two layers are at $z = \pm d/2$ respectively. This accounts for the factor $\delta(z \pm d/2)$ in each element of the spinor. Notice that we drop the band index in Ψ and c, since we neglect Landau level mixing so that all electrons are in the same band and the same Landau level.

4.2.1 The effects of positive background

In Chapter 3, we have discussed the effect of a positive background on the bilayer graphene. An important term in Hamiltonian, the capacitive energy comes from this effect. In this section, the same background as we discuss in Chapter 3 and Appendix 1 is applied. The positive charge is distributed uniformly on the two sides of bilayer graphene. So the Hamiltonian of background is given by Eq. (B.21),

$$H_{+} = n_0 N_\phi \left[\frac{\pi e^2 d}{\kappa} - V\left(q=0\right) \right] \sum_{k,s} \rho_{(k,s);(k,s)}\left(\mathbf{q}=\mathbf{0}\right) + \frac{1}{2} S n_0^2 V\left(q=0\right), \tag{4.3}$$

where k, s are valley and spin index respectively. All the parameters have the same definitions as in Appendix B.

4.2.2 Electron-electron interaction

The Coulomb interaction between electrons can be written, in terms of field operators as,

$$U = \frac{1}{2} \sum_{\alpha,\beta} \sum_{s,t} \int d\mathbf{u} \int d\mathbf{u}' \Psi^{\dagger}_{\alpha,s}\left(\mathbf{u}\right) \Psi^{\dagger}_{\beta,t}\left(\mathbf{u}'\right) V\left(\mathbf{u}-\mathbf{u}'\right) \Psi_{\beta,t}\left(\mathbf{u}'\right) \Psi_{\alpha,s}\left(\mathbf{u}\right), \tag{4.4}$$

where α and β are valley indices and s and t are spin indices. The valley and spin are conserved as usual.

With Ψ given by Eq. (4.2), we get,

$$\begin{aligned} U &= \frac{1}{2} N_\phi \sum_{\alpha,\beta} \sum_{s,t} \sum_{\mathbf{q}} \left[U^{H}_{\alpha,\beta}\left(\mathbf{q}\right) \rho_{\alpha,s;\alpha,s}\left(-\mathbf{q}\right) \rho_{\beta,t;\beta,t}\left(\mathbf{q}\right) \right. \\ &\quad \left. - U^{F}_{\alpha,\beta}\left(\mathbf{q}\right) \rho_{\alpha,s;\beta,t}\left(-\mathbf{q}\right) \rho_{\beta,t;\alpha,s}\left(\mathbf{q}\right) \right]. \end{aligned} \tag{4.5}$$

where we have defined the density operator

$$\rho_{\alpha,s;\beta,t}\left(\mathbf{q}\right)\equiv\frac{1}{N_{\phi}}\sum_{X_1,X_2}e^{-\frac{i}{2}q_x\left(X_1+X_2\right)}\delta_{X_1,X_2+q_y\ell^2}c^{\dagger}_{\alpha,X_1,s}c_{\beta,X_2,t}. \tag{4.6}$$

The two important functions $U^H_{\alpha,\beta}$ and $U^F_{\alpha,\beta}$, which we call the Hartree and the Fock factors respectively, define the Hartree and Fock interactions. They are given in LL N by

$$\begin{aligned}U^H_{\alpha,\beta}\left(\mathbf{q}\right) &= \sum_{i,j=1}^{4}\left|y^{\alpha}_{i,N}\right|^2\left|y^{\beta}_{j,N}\right|^2\frac{e^2}{\kappa\ell}\frac{1}{q\ell}e^{-\Delta_{ij}qd}e^{-q^2\ell^2/2}L_{N+\alpha_i}\left(\frac{q^2\ell^2}{2}\right)L_{N+\beta_j}\left(\frac{q^2\ell^2}{2}\right) &(4.7)\\ U^F_{\alpha,\beta}\left(\mathbf{q}\right) &= \sum_{i,j=1}^{4}\left|y^{\alpha}_{i,N}\right|^2\left|y^{\beta}_{j,N}\right|^2\frac{e^2}{\kappa\ell}\\ &\times\int dp\ell e^{-\Delta_{ij}pd}e^{-p^2\ell^2/2}L_{N+\alpha_i}\left(\frac{p^2\ell^2}{2}\right)L_{N+\beta_j}\left(\frac{p^2\ell^2}{2}\right)J_0\left(pq\ell^2\right), &(4.8)\end{aligned}$$

where we define the function Δ_{ij} to distinguish the inter or intra layer interaction,

$$\Delta_{ij}=\begin{cases}0 & i\in\{1,2\},j\in\{1,2\},or,i\in\{3,4\},j\in\{3,4\}\\ 1 & i\in\{1,2\},j\in\{3,4\},or,i\in\{3,4\},j\in\{1,2\}\end{cases}, \tag{4.9}$$

and J_0 is a Bessel function.

In the Hartree-Fock approximation, the Hamiltonian of electron-electron interaction can be written as

$$\begin{aligned}U &= N_{\phi}\sum_{\alpha,\beta}\sum_{s,t}\sum_{\mathbf{q}}U^H_{\alpha,\beta}\left(\mathbf{q}\right)\left\langle\rho_{\alpha,s;\alpha,s}\left(-\mathbf{q}\right)\right\rangle\rho_{\beta,t;\beta,t}\left(\mathbf{q}\right)\\ &-N_{\phi}\sum_{\alpha,\beta}\sum_{s,t}\sum_{\mathbf{q}}U^F_{\alpha,\beta}\left(\mathbf{q}\right)\left\langle\rho_{\alpha,s;\beta,t}\left(-\mathbf{q}\right)\right\rangle\rho_{\beta,t;\alpha,s}\left(\mathbf{q}\right), \qquad (4.10)\end{aligned}$$

where we have used the symmetry properties of the Hartree and Fock factors

$$\begin{aligned}U^H_{\beta,\alpha}\left(\mathbf{q}\right) &= U^H_{\alpha,\beta}\left(\mathbf{q}\right)=U^H_{\alpha,\beta}\left(-\mathbf{q}\right), &(4.11)\\ U^F_{\beta,\alpha}\left(\mathbf{q}\right) &= U^F_{\alpha,\beta}\left(\mathbf{q}\right)=U^F_{\alpha,\beta}\left(-\mathbf{q}\right). &(4.12)\end{aligned}$$

In order to add the contribution of the background in Eq. (B.19), we need to consider the Hartree term, $H_H(\mathbf{q}=\mathbf{0}) = N_\phi \sum_{\alpha,\beta}\sum_{s,t} U^H_{\alpha,\beta}(\mathbf{0})\langle\rho_{\alpha,s;\alpha,s}(\mathbf{0})\rangle \rho_{\beta,t;\beta,t}(\mathbf{0})$, in which

$$\begin{aligned} U^H_{\alpha,\beta}(\mathbf{0}) &= \frac{e^2}{\kappa\ell}\sum_{i,j=1}^{4}\left|y^\alpha_{i,N}\right|^2\left|y^\beta_{j,N}\right|^2\left(\frac{1-\Delta_{ij}qd}{q\ell}\right)_{q=0} \\ &\times \left[e^{-q^2\ell^2/2}L_{N+\alpha_i}\left(\frac{q^2\ell^2}{2}\right)L_{N+\beta_j}\left(\frac{q^2\ell^2}{2}\right)\right]_{q=0} \\ &= \frac{V(q=0)}{2\pi\ell^2} - \frac{e^2}{\kappa\ell}\sum_{i=1}^{4}\left|y^\alpha_{i,N}\right|^2\sum_{j=1}^{4}\left|y^\beta_{j,N}\right|^2\Delta_{ij}\frac{d}{\ell}. \end{aligned} \tag{4.13}$$

Summing the term $H_H(\mathbf{0})$ and the background term H_+, we obtain

$$H_H(\mathbf{0}) + H_+ = N_\phi\sum_{\beta,t}\left(\frac{e^2}{\kappa\ell}\frac{\nu}{2}\frac{d}{\ell} - \sum_{\alpha,s}U^0_{\alpha,\beta}\frac{d}{\ell}\langle\rho_{\alpha,s;\alpha,s}(\mathbf{0})\rangle\right)\rho_{\beta,t;\beta,t}(\mathbf{0}), \tag{4.14}$$

which gives the capacitive energy of the system. Here we have defined a new coefficient

$$U^0_{\alpha,\beta} = \frac{e^2}{\kappa\ell}\sum_{i,j=1}^{4}\left|y^\alpha_{i,N}\right|^2\left|y^\beta_{j,N}\right|^2\Delta_{ij}. \tag{4.15}$$

This term $U^0_{\alpha,\beta}$ has units of energy and is related to the coefficients of wave function spinors. In fact, not only $U^0_{\alpha,\beta}$, but also the Hartree factor $U^H_{\alpha,\beta}$ and Fock factor $U^F_{\alpha,\beta}$ contain the coefficients of wave function spinors, $y^\alpha_{i,N}$. Moreover, $y^\alpha_{i,N}$ not only depends on the structure of graphene bilayer, but also depends on the bias Δ_B. In another words, all the interactions depend on an external electric field Δ_B. This means that a tunable variable Δ_B can change the eigenvectors, eigenenergies and interactions of the system. Hence, it is reasonable to consider that Δ_B significantly influences the properties of the ground states as well as of the excited states.

We combine all the interactions together, and obtain the full Hamiltonian in the HFA including the background,

$$\begin{aligned} H &= N_\phi \sum_{\alpha,s} \left[E_n^{\alpha,s} + \frac{e^2}{\kappa\ell}\frac{\nu}{2}\frac{d}{\ell} - \frac{d}{\ell}\sum_{\beta,t} U^0_{\beta,\alpha} \left\langle \rho_{\beta,t;\beta,t}\left(\mathbf{0}\right)\right\rangle \right] \rho_{\alpha,s,\alpha,s}\left(0\right) \\ &+ N_\phi \sum_{\alpha,\beta}\sum_{s,t}\overline{\sum_{\mathbf{q}}} U^H_{\alpha,\beta}\left(\mathbf{q}\right)\left\langle \rho_{\alpha,s;\alpha,s}\left(-\mathbf{q}\right)\right\rangle \rho_{\beta,t;\beta,t}\left(\mathbf{q}\right) \\ &- N_\phi \sum_{\alpha,\beta}\sum_{s,t}\sum_{\mathbf{q}} U^F_{\alpha,\beta}\left(\mathbf{q}\right)\left\langle \rho_{\alpha,s;\beta,t}\left(-\mathbf{q}\right)\right\rangle \rho_{\beta,t;\alpha,s}\left(\mathbf{q}\right), \end{aligned} \tag{4.16}$$

where $E_n^{\alpha,s}$ calculated numerically is the eigenenergy of LL n in valley α with spin s (the band index $b = 2$ is assumed here), and the bar over the summation sign means that the summation excludes the contribution at $\mathbf{q} = \mathbf{0}$. Note that, although we do not indicate the Landau level N in the interaction terms in Eq. (4.16), the coefficients $y^\alpha_{i,N}$ contained in $U^0_{\beta,\alpha}$, $U^H_{\alpha,\beta}$, and $U^F_{\alpha,\beta}$ include the Landau level index n.

4.3 Ground states at integer filling factors of Landau levels $N = 1, 2, 3$

In order to study the ground states of the C2DEG, we define the Matsubara single particle Green's function, and use the method discussed in Sec. 1.3 to compute the order parameters $\langle \rho_{\alpha,s;\beta,t}\rangle$. The Green's function can also be defined by Eq. (3.21). The relation between the Green's function and the order parameter is given by

$$G_{\alpha,s;\beta,s'}\left(\mathbf{q},\tau = 0^-\right) = \left\langle \rho_{\beta,s';\alpha,s}\left(\mathbf{q}\right)\right\rangle . \tag{4.17}$$

The equation of motion for the Green's function in the Matsubara formalism is obtained by using Eq.(1.59)

$$\hbar\frac{\partial}{\partial\tau}G = \left[H - \mu N, G\right], \tag{4.18}$$

where μ is the chemical potential and H is the Hartree-Fock Hamiltonian of Eq. (4.16). Then we obtain the equation of motion of the Green's function,

$$\begin{aligned}
&-i\omega_n G_{\sigma,s;\sigma',s'}(\mathbf{q},i\omega_n) \\
=\;& -\delta_{\sigma,\sigma'}\delta_{s,s'}\delta_{\mathbf{q},\mathbf{0}} - \left[E_n^{\alpha,s''} - \mu - \sum_{\alpha,s''} U^0_{\alpha,\sigma}\left\langle \rho_{\alpha,s'';\alpha,s''}(\mathbf{0})\right\rangle\right] G_{\sigma,s;\sigma',s'}(\mathbf{q},i\omega_n) \\
& -\sum_{\mathbf{p}\neq\mathbf{q}}\sum_{\alpha,s''} U^H_{\alpha,\sigma}(\mathbf{p}-\mathbf{q})\left\langle \rho_{\alpha,s'';\alpha,s''}(\mathbf{q}-\mathbf{p})\right\rangle G_{\sigma,s;\sigma',s'}(\mathbf{p},i\omega_n)\, e^{-\frac{i}{2}\mathbf{q}\times\mathbf{p}} \\
& +\sum_{\mathbf{p}}\sum_{\alpha,s''} U^F_{\alpha,\sigma}(\mathbf{p}-\mathbf{q})\left\langle \rho_{\alpha,s'';\sigma,s}(\mathbf{q}-\mathbf{p})\right\rangle G_{\alpha,s'';\sigma',s'}(\mathbf{p},i\omega_n)\, e^{-\frac{i}{2}\mathbf{q}\times\mathbf{p}}, \qquad (4.19)
\end{aligned}$$

where $G(\mathbf{q},i\omega_n)$ is the Fourier transform of the time-dependent Green's funtion in Eq. (**??**),

$$G(i\omega_n) = \int_0^{\beta\hbar} e^{i\omega_n\tau} G(\tau) d\tau, \qquad (4.20)$$

$$i\omega_n = \frac{(2n+1)\pi}{\beta\hbar}, \qquad (4.21)$$

where ω_n are the Matsubara frequency for Fermions, and $\beta = 1/k_B T$, where k_B is the Boltzman constant and T is the temperature.

We can write the equation of motion in a matrix form as,

$$\left(i\hbar\omega_n I - F\right) G = B. \qquad (4.22)$$

If we assume a uniform ground state, then only the component $\left\langle \rho_{i;j}(\mathbf{0})\right\rangle \neq 0$ and the F matrix can be written as:

$$F_{11} = E_n^1 - \mu + \frac{\nu}{2}\frac{d}{\ell} - \frac{d}{\ell}\sum_{\alpha,s''} U^0_{\alpha,0}\left\langle \rho_{\alpha,s'';\alpha,s''}(\mathbf{0})\right\rangle - U^F_{0,0}(\mathbf{0})\left\langle \rho_{1;1}(\mathbf{0})\right\rangle, \qquad (4.23)$$

$$F_{12} = -U^F_{0,0}(\mathbf{0})\left\langle \rho_{2;1}(\mathbf{0})\right\rangle, \qquad (4.24)$$

$$F_{13} = -U^F_{1,0}(\mathbf{0})\left\langle \rho_{3;1}(\mathbf{0})\right\rangle, \qquad (4.25)$$

$$F_{14} = -U^F_{1,0}(\mathbf{0})\left\langle \rho_{4;1}(\mathbf{0})\right\rangle, \qquad (4.26)$$

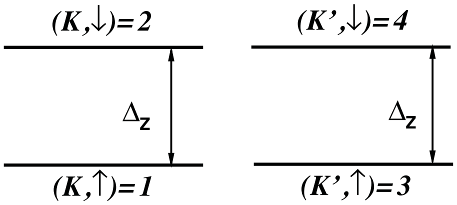

FIGURE 4.2: The sketch of the four levels in a LL ($N > 0$) in graphene bilayer. The valley and spin indices are combined together for convenience.

$$F_{22} = E_n^2 - \mu + \frac{\nu}{2}\frac{d}{\ell} - \frac{d}{\ell}\sum_{\alpha,s''} U^0_{\alpha,0}\left\langle \rho_{\alpha,s'';\alpha,s''}\left(\mathbf{0}\right)\right\rangle - U^F_{0,0}\left(\mathbf{0}\right)\left\langle \rho_{2;2}\left(\mathbf{0}\right)\right\rangle , \tag{4.27}$$

$$F_{23} = -U^F_{1,0}\left(\mathbf{0}\right)\left\langle \rho_{3;2}\left(\mathbf{0}\right)\right\rangle , \tag{4.28}$$

$$F_{24} = -U^F_{1,0}\left(\mathbf{0}\right)\left\langle \rho_{4;2}\left(\mathbf{0}\right)\right\rangle , \tag{4.29}$$

$$F_{33} = E_n^3 - \mu + \frac{\nu}{2}\frac{d}{\ell} - \frac{d}{\ell}\sum_{\alpha,s''} U^0_{\alpha,1}\left\langle \rho_{\alpha,s'';\alpha,s''}\left(\mathbf{0}\right)\right\rangle - U^F_{1,1}\left(\mathbf{0}\right)\left\langle \rho_{3;3}\left(\mathbf{0}\right)\right\rangle , \tag{4.30}$$

$$F_{34} = -U^F_{1,1}\left(\mathbf{0}\right)\left\langle \rho_{4;3}\left(\mathbf{0}\right)\right\rangle , \tag{4.31}$$

and

$$F_{44} = E_n^4 - \mu + \frac{\nu}{2}\frac{d}{\ell} - \frac{d}{\ell}\sum_{\alpha,s''} U^0_{\alpha,1}\left\langle \rho_{\alpha,s'';\alpha,s''}\left(\mathbf{0}\right)\right\rangle - U^F_{1,1}\left(\mathbf{0}\right)\left\langle \rho_{4;4}\left(\mathbf{0}\right)\right\rangle . \tag{4.32}$$

For the indices i and j of matrix elements F_{ij} and of density matrix elements $\left\langle \rho_{i;j}\left(\mathbf{0}\right)\right\rangle$, we combine the valley and spin together as:

$$i,j = 1 \equiv \left(K,\uparrow\right), \tag{4.33a}$$

$$i,j = 2 \equiv \left(K,\downarrow\right), \tag{4.33b}$$

$$i,j = 3 \equiv \left(K',\uparrow\right), \tag{4.33c}$$

$$i,j = 4 \equiv \left(K',\downarrow\right). \tag{4.33d}$$

The index of the combination of valley and spin can be found in Fig. 4.2

The iteration process in Ref. [26] is used to solve the equation of motion in Eq. (4.19) numerically. By solving the equation of motion of the Green's function, we obtain the

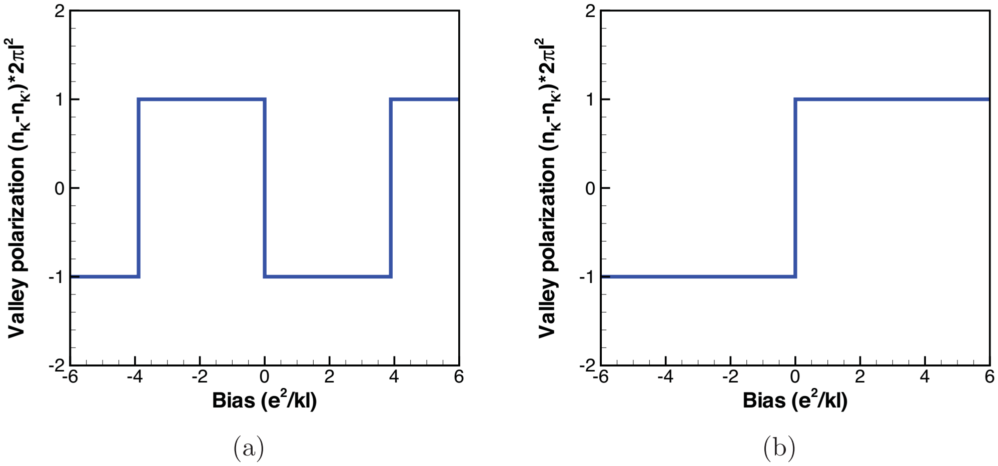

FIGURE 4.3: Valley pseudo-spin polarization of the ground state at $\nu = 1$: (a) in Landau level $N = 1$; and (b) in Landau level $N \geq 2$. The magnetic field $B = 9$T, and the dielectric constant $\kappa = 2.5$.

order parameters of the density matrix $\langle \rho_{\beta,s';\alpha,s}(\mathbf{q} = \mathbf{0}) \rangle$ in the ground state.

4.3.1 Phase diagram at filling factors $\nu = 1$ and 3

We suppose that the graphene sheet is put in a magnetic field pointing up. So the four degenerated states in one Landau level can be described by $|K, \uparrow\rangle = |1\rangle, |K, \downarrow\rangle = |2\rangle, |K', \uparrow\rangle = |3\rangle, |K', \downarrow\rangle = |4\rangle$. The $|\uparrow\rangle$ states have Zeeman energy $-\frac{1}{2} g\mu_B B$, while the $|\downarrow\rangle$ states have Zeeman energy $\frac{1}{2} g\mu_B B$. Fig. 4.3 displays the phase diagram at filling factor $\nu = 1$ in Landau levels $N \geq 1$. Here we define the filling factor in a single Landau level. If we take the zero LL into account, then the total filling factor in Landau level N is $\nu_t = \nu + 4N$.

The ground state is always spin polarized since the exchange interaction of the same spin minimizes the energy. We find that the valley pseudo-spin is also polarized at any bias. This is different from what is found in the LL $N = 0$. In the zero LL, there is always a finite valley coherence at zero bias [13]. But not in higher Landau levels where there is always no valley coherence at any bias at filling factor 1. At zero bias, the ground state has a Z_2 valley symmetry, while there is a SU(2) valley symmetry in the ground state in the LL $N = 0$. The reason for this difference is the distance between the two layers. In the LL $N = 0$, the valley pseudo-spin is equivalent to layer pseudo-spin, and the capacitive energy must balance the charge in two layers (valleys). So at zero or small bias, the

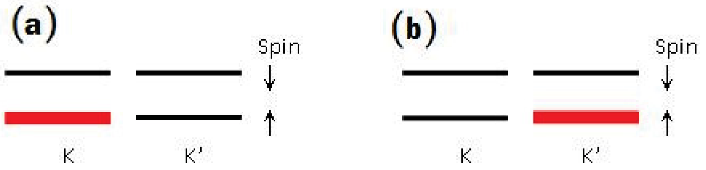

FIGURE 4.4: The ground state at filling factor $\nu = 1$ at zero bias. The red line represents a fully filled level and the black lines are empty levels in a Landau level. The ground state has Z_2 symmetry, so that the two candidates are completely equivalent.

two layers (valleys) must be filled partially to reduce the capacitive energy. However, in higher Landau levels, electrons in one valley can stay in both layers. This can be clearly seen in the wave function spinors in Eq. (1.33). In the numerical calculations, we can see that the capacitive energy is two magnitudes lower than the Fock energy and is too weak to balance the charge in two valleys. Although the kinetic energies in two valleys are identical, the exchange interaction polarizes the valley pseudo-spin automatically, i.e. the exchange energy between valleys is always higher than the intra-valley exchange energy. So the electrons prefer to occupy one valley to minimize the exchange energy. If we set the distance $d = 0$ and $\Delta_B = 0$, the inter-valley interaction is identical to the intra-valley interaction, then the system recovers the SU(2) valley symmetry.

At zero bias, see in Fig. 4.4, state (a) is equivalent to state (b), since the ground state has the Z_2 valley symmetry. At finite bias, the valley pseudo-spin is polarized by the bias. This is shown in the phase diagrams in Fig. 4.3a for the Landau level $N = 1$ and in Fig. 4.3b for Landau levels $n \geq 2$. Interestingly, in the ground state of $N = 1$, the electrons occupy the valley with the higher non-interacting energy when $0 < |\Delta_B| < 3.89(e^2/\kappa\ell)$. But for $N \geq 2$, in the ground states, electrons always occupy the lowest kinetic energy levels in the corresponding LL. Note that the phase diagrams in Fig. 4.3 are obtained when $B = 9$T and $\kappa = 2.5$. If these parameters change, the phase diagram also changes [78].

The calculations in Ref. [78] indicate that no crystal phase (or say density-modulation state) has lower energy than that of the liquid phase. If we suppose the system is spin polarized, then we can simplify the energy functional in the pseudo-spin language [25] at zero bias to,

$$\frac{E}{N_\phi} = -U_F^{K,K}(\mathbf{0})\, P_{z,\uparrow}^2 - U_F^{K,K'}(\mathbf{0})\, \mathbf{P}_{\perp,\uparrow} \cdot \mathbf{P}_{\perp,\uparrow}, \tag{4.34}$$

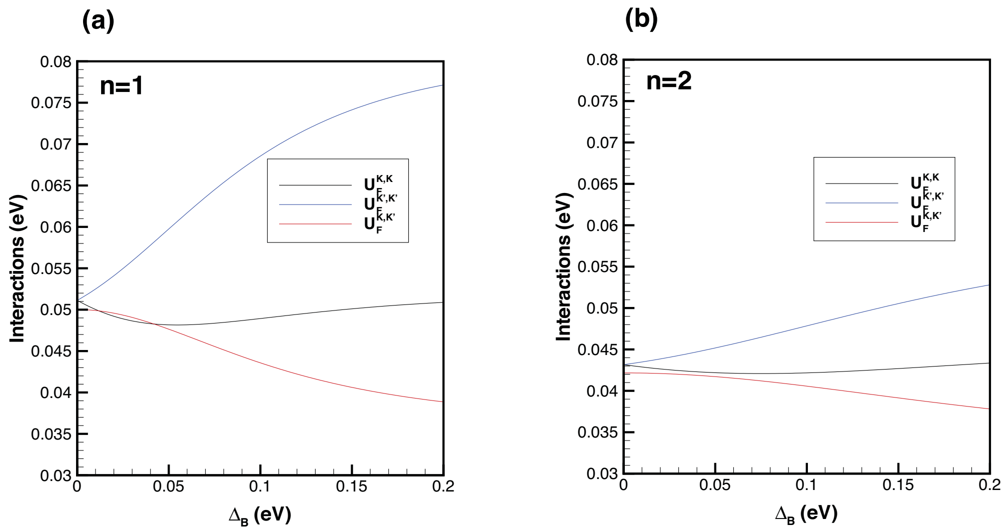

FIGURE 4.5: The Fock interaction functions $U_F^{K,K}$, $U_F^{K',K'}$, and $U_F^{K,K'}$ as functions of bias Δ_B. The functions are calculated at $B = 10$T, $\kappa = 2.5$, and (a) in $n = 1$ and (b) in $n = 2$.

where N_ϕ is the degeneracy of one level, and we neglect the constant term and the capacitive energy which is very small. The valley pseudo-spin field is defined by

$$P_{x,\uparrow} = \frac{1}{2}\left(\langle\rho_{1,3}(\mathbf{0})\rangle + \langle\rho_{3,1}(\mathbf{0})\rangle\right), \tag{4.35a}$$

$$P_{y,\uparrow} = \frac{1}{2i}\left(\langle\rho_{1,3}(\mathbf{0})\rangle - \langle\rho_{3,1}(\mathbf{0})\rangle\right), \tag{4.35b}$$

$$P_{z,\uparrow} = \frac{1}{2}\left(\langle\rho_{1,1}(\mathbf{0})\rangle - \langle\rho_{3,3}(\mathbf{0})\rangle\right), \tag{4.35c}$$

$$\mathbf{P}_{\perp,\uparrow} = \left(P_{x,\uparrow}, P_{y,\uparrow}\right). \tag{4.35d}$$

Fig. 4.5 shows that the $-U_F^{K,K}$ is lower than $-U_F^{K,K'}$ at $q = 0$, so that the system prefer the lower energy state with $P_{z,\uparrow} = \pm\frac{1}{2}$ and $\mathbf{P}_{\perp,\uparrow} = (0,0)$. In the same way, the energy of the system can be written as

$$\frac{E}{N_\phi} = C + \Lambda P_z - J_z P_z^2 - J_\perp P_\perp^2 \tag{4.36}$$

at finite bias. Here, C is a constant,

$$C = \frac{1}{2}\left(E_{N=1}^{K,\uparrow} + E_{N=1}^{K',\uparrow}\right) - \frac{1}{4}\frac{d}{\ell}\left(\frac{e^2}{\kappa\ell}\right)n_1 n_2 - \frac{1}{8}\left[U_F^{K,K}(\mathbf{0}) + U_F^{K',K'}(\mathbf{0})\right], \tag{4.37}$$

and the effective "Zeeman" term for the valleys is

$$\begin{aligned} \Lambda &= \left(E_{N=1}^{K,\uparrow} - \frac{1}{2} U_F^{K,K}(\mathbf{0}) - \frac{d}{\ell}\frac{e^2}{\kappa\ell} n_{1,K} n_{2,K} \right) \\ &\quad - \left(E_{N=1}^{K',\uparrow} - \frac{1}{2} U_F^{K',K'}(\mathbf{0}) - \frac{d}{\ell}\frac{e^2}{\kappa\ell} n_{1,K'} n_{2,K'} \right), \end{aligned} \tag{4.38}$$

where $n_{i,\alpha}$ is the electron density in the layer i and valley α,

$$n_{1,\alpha} = \left| y_{1,N}^{\alpha} \right|^2 + \left| y_{2,N}^{\alpha} \right|^2, \tag{4.39}$$

$$n_{2,\alpha} = \left| y_{3,N}^{\alpha} \right|^2 + \left| y_{4,N}^{\alpha} \right|^2, \tag{4.40}$$

and n_i is the electron density in the layer i, $n_i = n_{i,K} + n_{i,K'}$. The effective pseudo-spin exchange interaction is given by

$$J_z = \frac{d}{\ell}\left(\frac{e^2}{\kappa\ell}\right)\left(n_{1,K'} - n_{1,K}\right)\left(n_{2,K'} - n_{2,K}\right) + \frac{1}{2}\left[U_F^{K,K}(\mathbf{0}) + U_F^{K',K'}(\mathbf{0})\right], \tag{4.41}$$

$$J_\perp = U_F^{K,K'}. \tag{4.42}$$

Note that all the phase transitions at $\nu = 1, 3$ are first-order and there is no valley or spin coherence in the system. This is because $J_\perp < J_Z$, the valley pseudo-spin prefers to be aligned along the z direction. The sign of the effective "Zeeman" Λ determines which valley is occupied in the ground state. For $\Lambda > 0$, P_z must be $-1/2$ to minimize the energy, so valley K' is occupied. For $\Lambda > 0$, $P_z = 1/2$ and valley K is occupied. At zero bias, $\Lambda = 0$, so the ground state has a Z_2 symmetry for valley pseudo-spin. In Fig. 4.6, we find that the behavior of $\Lambda(N = 1)$ is different from that of $\Lambda(N = 2, 3)$. Each zero point of function Λ corresponds to a phase transition in Fig. 4.3.

At filling factor $\nu = 3$, where three of the four levels in a Landau level are filled, the phase diagrams in Fig. 4.3 are still valid. The only difference is that the levels $|1\rangle$ and $|3\rangle$ are full filled, and the valley polarization of the system only depends on if $|2\rangle$ or $|4\rangle$ is filled or not.

4.3.2 Phase diagram at $\nu = 2$

At filling factor $\nu = 2$, the phase diagram is even richer since there are more possibilities of occupying levels. When we solve the equation of motion of the Green's function

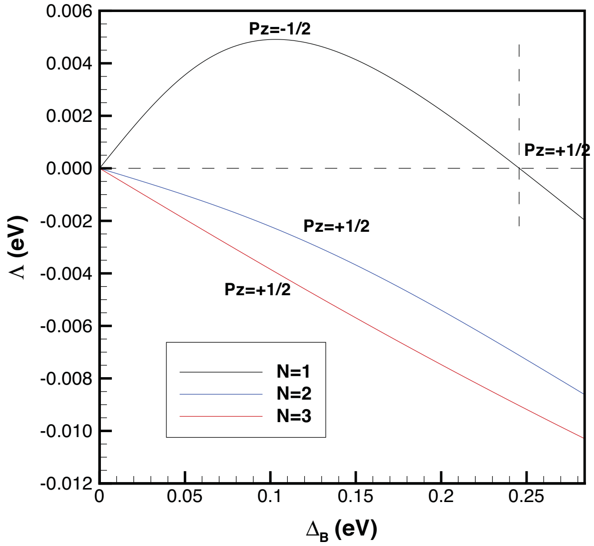

FIGURE 4.6: Function Λ as a function of bias in Landau levels $N = 1, 2, 3$.

in Eq. (4.22), we could not find any coherence between valleys or between spins. The four levels in a LL are either occupied or empty.

By analogy with $\nu = 1, 3$, we find that the phase diagram in $N = 1$ is also richer than that in $n > 1$ when $B = 10$T and $\kappa = 2.5$. The phase diagram of LL $N = 1$ is shown in Fig. 4.7.

The evolution of the phases from $\Delta_B = 0$ to 0.3eV is displayed in Fig. 4.8. Note that the position of the levels in this diagram does not reflect their real kinetic energies. Phases (I), (II) and (III) are also indicated in Fig. 4.7.

At small bias $-\Delta_B^1 < \Delta_B < \Delta_B^1 = 0.015$eV, phase (I) has levels $|1\rangle$ and $|3\rangle$ full while the other two levels are empty. At the critical bias Δ_B^1, there is a first-order phase transition converting the system from spin polarized to valley polarized. When the bias increases, $\Delta_B^1 < \Delta_B < \Delta_B^2 = 0.22$eV, the occupied states are all in the higher energy valley since this decreases more the exchange energy than the increase of the kinetic energy. Phase (II) has levels $|3\rangle$ and $|4\rangle$ full, while the other two levels are empty. When $\Delta_B^2 < \Delta_B < \Delta_B^3 = 0.265$eV, the ground state returns to the spin polarized phase (I). When $\Delta_B > \Delta_B^3$, the lower energy valley is fully filled. In this case, phase (III) indicates that $|1\rangle$ and $|2\rangle$ are full and the other two levels are empty.

In experiment [77], the highest bias is achieved at about 0.2eV. So the critical biases

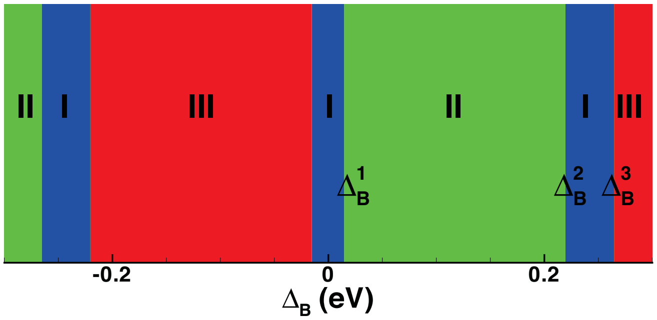

FIGURE 4.7: The phase diagram at $\nu = 2$ in $N = 1$.

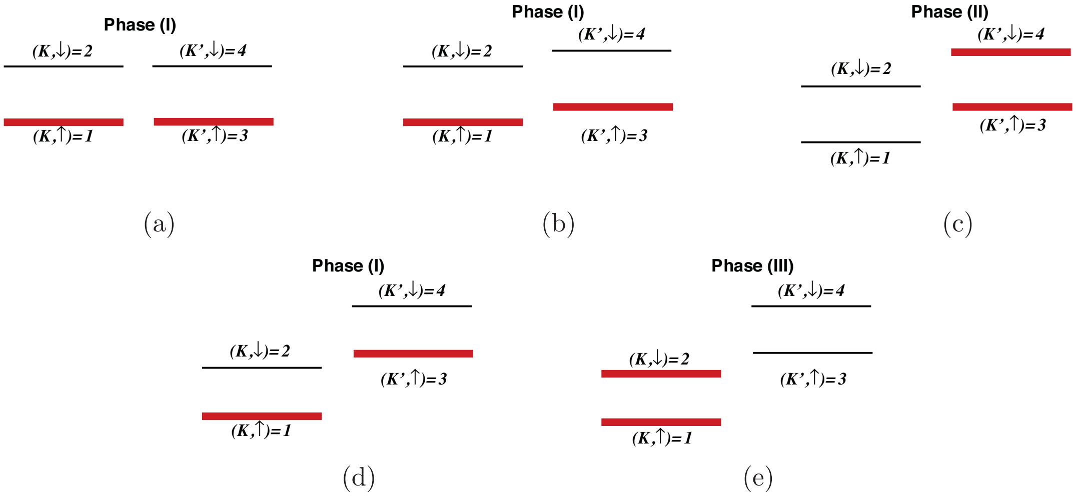

(a) (b) (c) (d) (e)

FIGURE 4.8: The phase evolution at $\nu = 2$ in $N = 1$ is shown from (a) to (e) as the bias Δ_B is increased from 0 to 0.3eV. Red lines represent fully occupied levels and black lines represent empty levels.

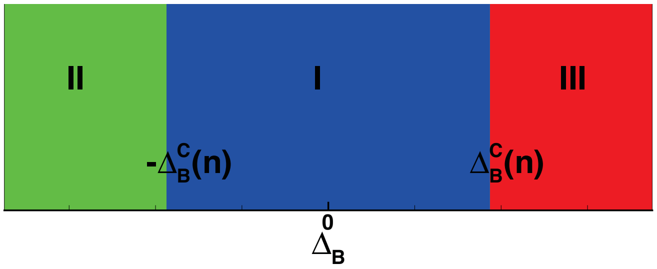

FIGURE 4.9: The phase diagram at $\nu = 2$ in LL $N \geq 2$.

Δ_B^2 and Δ_B^3 are too high to observe experimentally. Moreover, the LL mixing must be considered at these critical biases. For negative bias $-\Delta_B$, the phase is obtained by exchanging the K and K' valleys in the phase at Δ_B.

In LL $N \geq 2$, the phase diagram is simpler. The ground state is spin polarized at small bias $\Delta_B < \Delta_B^C(n)$. At large bias $\Delta_B > \Delta_B^C(n)$, a phase transition occurs to convert the ground state from spin polarized to valley polarized, and the lower energy valley is fully occupied. The phase diagram for $n \geq 2$ is shown in Fig. 4.9. The critical biases calculated in $B = 10$T and $\kappa = 2.5$ are given by $\Delta_B^C(n = 2) = 0.056$eV and $\Delta_B^C(n = 3) = 0.03$eV . The phases (I), (II) and (III) have the same definitions as in Fig. 4.8.

In (pseudo-)spin language, we rewrite the energy per electron as

$$\frac{E}{2N_\phi} = D + \frac{1}{2}\Lambda P_z - J_z P_z^2 - \frac{1}{2}\Delta_Z S_z - J_{K'} S_{z,K'}^2 - J_K S_{z,K}^2, \tag{4.43}$$

where $J_K = \frac{1}{2}U_F^{K,K}(0)$, $J_{K'} = \frac{1}{2}U_F^{K',K'}(0)$, and we have set valley and spin coherence to zero. The constant D is given by,

$$D = \frac{1}{2}\left(E_N^{K,\uparrow} + E_N^{K',\uparrow}\right) + \Delta_Z - \frac{1}{2}\frac{d}{\ell}\left(\frac{e^2}{\kappa\ell}\right) n_1 n_2 - \frac{1}{8}\left[U_F^{K,K}(0) + U_F^{K',K'}(0)\right], \tag{4.44}$$

and Λ and J_z are given by Eqs. (4.38) and (4.42), respectively. The spin field is defined

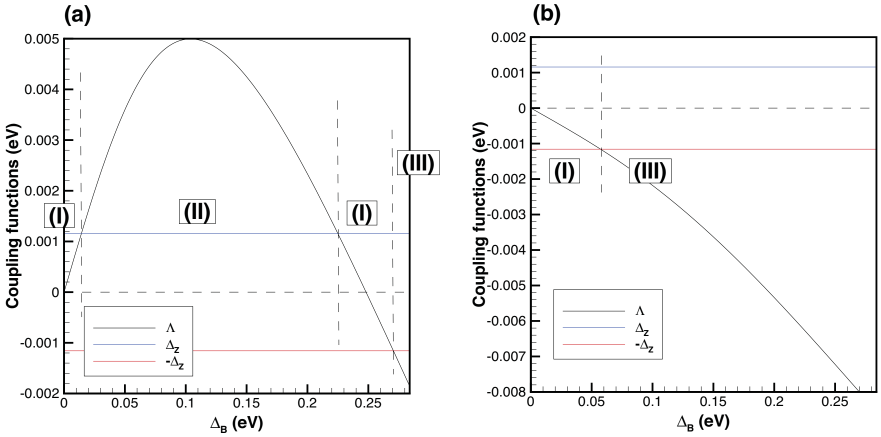

FIGURE 4.10: The coupling functions determine the phase transitions. The crossing points correspond to phase transitions in (a) $N = 1$ and (b) $N = 2$. The functions are calculated for $B = 10$T and $\kappa = 2.5$. Phases (I), (II) and (III) are also given in Fig. 4.8.

by

$$S_{x,K} = \frac{1}{2}\left(\langle\rho_{1,2}(\mathbf{0})\rangle + \langle\rho_{2,1}(\mathbf{0})\rangle\right), \tag{4.45a}$$

$$S_{y,K} = \frac{1}{2i}\left(\langle\rho_{1,2}(\mathbf{0})\rangle - \langle\rho_{2,1}(\mathbf{0})\rangle\right), \tag{4.45b}$$

$$S_{z,K} = \frac{1}{2}\left(\langle\rho_{1,1}(\mathbf{0})\rangle - \langle\rho_{2,2}(\mathbf{0})\rangle\right), \tag{4.45c}$$

$$S_{x,K'} = \frac{1}{2}\left(\langle\rho_{3,4}(\mathbf{0})\rangle + \langle\rho_{4,3}(\mathbf{0})\rangle\right), \tag{4.45d}$$

$$S_{y,K'} = \frac{1}{2i}\left(\langle\rho_{3,4}(\mathbf{0})\rangle - \langle\rho_{4,3}(\mathbf{0})\rangle\right), \tag{4.45e}$$

$$S_{z,K'} = \frac{1}{2}\left(\langle\rho_{3,3}(\mathbf{0})\rangle - \langle\rho_{4,4}(\mathbf{0})\rangle\right), \tag{4.45f}$$

and $S_i = S_{i,K} + S_{i,K'}, (i = x, y, z)$. Although there is a SU(2) symmetry for the spin, the Zeeman coupling breaks this symmetry. So the spin coherence does not exist.

The phase diagrams in Figs. 4.7 and 4.9 can be also explained by the competition between the bias energy Λ and the Zeeman coupling. Fig. 4.10 clearly shows that how the competition changes the phases of the ground state.

4.4 Ising quantum Hall ferromagnet in chiral multilayer graphene

The quantum Hall ferromagnet with Z_2 symmetry discussed in Sec. 4.3 is the so-called easy-axis (or Ising) quantum Hall ferromagnet. In such a system, there might exist domain walls that induce a resistivity (R_{xx}) spike in a transport experiment at finite temperature [80]. The domain walls increase the Coulomb energy of the system. There is no domain wall at zero temperature, so the conductivity R_{xx} is still zero at integer filling factor at zero temperature. At finite temperature, the domain wall could lower the free energy of the system, when we consider the wall entropy. Below a critical temperature T_c, domain walls provide 1D channels carrying extra charges. These charge dissipate the transport charge of the 2DEG, so that the resistance spike appears [81, 82]. Above the critical temperature, the domain wall will be infinity long and expand to the sample perimeter. The charge in the domain wall can not dissipate the transport electrons any more, so the resistance spike disappears.

A recent experiment [77] has indeed observed the conductivity spikes at $\nu = 1$ in higher Landau levels at temperature $T = 1.4$K. The experimental evidence also supports the fact that there is an Ising quantum Hall ferromagnet in graphene bilayer at $\nu = 1$.

We can derive a criteria that determines if the ground state of the system has a SU(2) symmetry or a Z_2 symmetry. The criteria is obtained by comparing the energy of a SU(2) state $E_{SU(2)}$ with that of an Ising quantum Hall ferromagnet E_I,

$$E_I < E_{SU(2)}. \tag{4.46}$$

If this equation is true, the ground state is an Ising quantum Hall ferromagnet, otherwise the ground state is an $x - y$ spin ferromagnet as in monolayer graphene. In graphene bilayer, in the higher Landau levels, the criteria can be written as,

$$D\left(d\right) = U^F_{K,K}\left(\mathbf{0}\right) - U^F_{K,K'}\left(\mathbf{0}\right) - \frac{e^2}{\kappa\ell}\frac{d}{\ell}\left(n_{1,K} - n_{2,K}\right)^2 > 0, \tag{4.47}$$

where the Fock interaction $U^F_{\sigma,\sigma'}$ between valleys σ and σ' is defined in Eq. (4.8). If we set D as a function of the distance between the two layers d, Fig. 4.11 shows that $D\left(d > 0\right) > 0$ and $D\left(d = 0\right) = 0$, which means that if the separation between the two layers is zero, then the ground state recovers SU(2) symmetry.

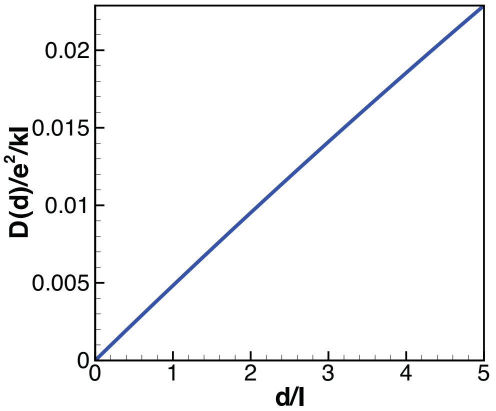

FIGURE 4.11: The Ising quantum Hall ferromagnet discriminant function $D(d) \geq 0$, which means the ground state is an Ising ferromagnet when the two layers of graphene bilayer are separated.

If we apply the effective two-component model to the criteria in Eq. (4.47), we can still obtain that the ground state at $\nu = 1$ is the Ising quantum Hall ferromagnet. Hence, the two-component model may be able to determine this property of the ground state qualitatively in higher Landau levels.

The chiral multi-layer graphene is stacked, in the $\mathbf{z}$ direction, by the layers periodically as $A-B-C-A-B-C\ldots$. In Fig. 4.12, we show the ABC stacking. In the first Brillouin zone, there are also two inequivalent valleys K and K' in a chirally stacked multi-layer graphene. In such a system, the Hamiltonian can be also simplified to a two-component model [83]. It seems reasonable to assume that all the chirally-stacked multi-layer graphene are Ising quantum Hall ferromagnets at $\nu = 1$ in higher Landau levels.

First, we verify this assumption in the two-component model of an ABC trilayer graphene. The Hamiltonian, in the basis of $\{A_1, B_3\}$, is written as [69],

$$H_{K'} = \begin{pmatrix} \Delta_0 - \left(\beta^2\Delta_0 + 2\beta\alpha_4\right) aa^\dagger & \beta^2\alpha_0 a^3 \\ \beta^2\alpha_0 \left(a^\dagger\right)^3 & \Delta_0 - \left(\beta^2\Delta_0 + 2\beta\alpha_4\right) a^\dagger a \end{pmatrix}, \tag{4.48}$$

and

$$H_K = \begin{pmatrix} \Delta_0 - \left(\beta^2\Delta_0 + 2\beta\alpha_4\right) a^\dagger a & -\beta^2\alpha_0 \left(a^\dagger\right)^3 \\ -\beta^2\alpha_0 a^3 & \Delta_0 - \left(\beta^2\Delta_0 + 2\beta\alpha_4\right) aa^\dagger \end{pmatrix}, \tag{4.49}$$

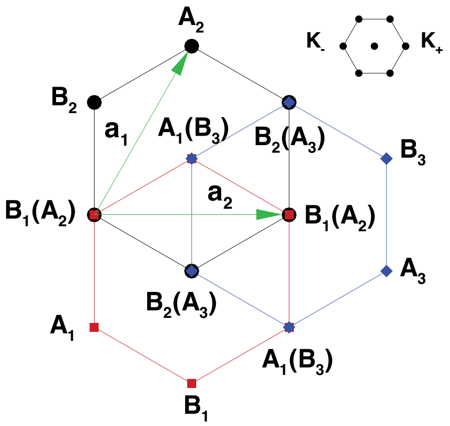

FIGURE 4.12: The top view of a ABC trilayer graphene. A red hexagons represent the first layer, black ones represent the second layer, and blue ones represent the third layer. The vectors $\mathbf{a_1}$ and $\mathbf{a_2}$ are the basis vectors of the lattice. The inset shows the first Brillouin zone which is the same as in monolayer and bilayer graphene. K_- and K_+ are the K and K' valleys, respectively.

when the bias $\Delta_B = 0$. The Landau level ladder operator a is defined in Eq. (1.32), and $\alpha_i = \sqrt{\frac{3}{2}}\frac{a_0}{\ell}\gamma_i, \beta = \frac{\alpha_0}{\gamma_1}$. In the ABC trilayer graphene, $\gamma_0 = 3.16\text{eV}$ is the nearest neighbor coupling in each layer, $\gamma_1 = 0.502\text{eV}$ couples A_1 and B_2, $\gamma_4 = -0.099\text{eV}$ couples B_1 and B_2, and $\Delta_0 = -0.0014\text{eV}$ is the on-site energy. So we obtain that, in the LL $n = 1$, $B = 10\text{T}$, the wave functions in the two valleys are given by

$$\phi_K = \begin{pmatrix} y_1^K h_3 \\ y_2^K h_0 \end{pmatrix} = \begin{pmatrix} 0.746\,19 h_3 \\ -i0.665\,73 h_0 \end{pmatrix}, \tag{4.50}$$

$$\phi_{K'} = \begin{pmatrix} y_1^{K'} h_0 \\ y_2^{K'} h_3 \end{pmatrix} = \begin{pmatrix} i0.665\,73 h_0 \\ 0.746\,19 h_3 \end{pmatrix}, \tag{4.51}$$

where h_i is defined in Eq. (1.21). In this case, the discriminant function $D(d_3)$ becomes

$$D(d_3) = U^F_{K,K}(\mathbf{0}) - U^F_{K,K'}(\mathbf{0}) - \frac{e^2}{\kappa\ell}\frac{d_3}{\ell}(n_{1,K} - n_{2,K})^2, \tag{4.52}$$

where $d_3 = 2d = 6.6374\text{Å}$ is the distance between the two outermost layers, $n_{i,\sigma} = |y_i^\sigma|^2$

and the Fock interaction is given by

$$U^F_{\sigma,\sigma'}(\mathbf{q}) = \sum_{i,j=1}^{2} |y_i^\sigma|^2 \left|y_j^{\sigma'}\right|^2 \frac{e^2}{\kappa\ell} \int dp e^{-\Delta_{ij} p d_3/\ell} e^{-p^2/2} L_{n+\sigma_i}\left(\frac{p^2}{2}\right) L_{n+\sigma'_j}\left(\frac{p^2}{2}\right) J_0(pq\ell), \tag{4.53}$$

with $K_1 = K'_2 = 2, K_2 = K'_1 = -1$ in σ_i, and

$$\Delta_{ij} = \begin{cases} 0 & i = j \\ 1 & i \neq j \end{cases}. \tag{4.54}$$

Note that n_2 here represents the charge density in the third layer. Numerically, we get $D\left(d_3 = 6.6374\text{Å}\right) = 0.0365\frac{e^2}{\kappa\ell} > 0$. Hence, we conclude that the ground states of the ABC trilayer graphene at $\nu = 1$ in higher LLs are Ising ferromagnets.

Second, the Hamiltonian of the minimum two-component model in a chiral stacked m-layer graphene [83] can be written in general as:

$$H^m_\xi = \begin{pmatrix} 0 & \xi\beta^{m-1}\alpha_0 a^m \\ \xi\beta^{m-1}\alpha_0\left(a^\dagger\right)^m & 0 \end{pmatrix}, \tag{4.55}$$

in the basis of $\{B_m, A_1\}$ in the K valley and in the basis of $\{A_1, B_m\}$ in the K' valley, where $\xi = -1$ for K valley and $\xi = 1$ for K' valley. So the wave functions of this system in Landau level n, in the basis of $\{A_1, B_m\}$, are given by,

$$\phi_{K,n} = \begin{pmatrix} y^{K(m)}_{1,n} h_{n+m-1} \\ y^{K(m)}_{2,n} h_{n-1} \end{pmatrix}, \tag{4.56}$$

$$\phi_{K',n} = \begin{pmatrix} y^{K'(m)}_{1,n} h_{n-1} \\ y^{K'(m)}_{2,n} h_{n+m-1} \end{pmatrix}, \tag{4.57}$$

where $\left|y^{\sigma(m)}_{i,n}\right| = \frac{1}{\sqrt{2}}$. Then the discriminant function in the nth Landau level becomes

$$\begin{aligned} D^{(m)}_n(d_m) &= U^{F(m)}_{K,K}(n,\mathbf{0}) - U^{F(m)}_{K,K'}(n,\mathbf{0}) - \frac{e^2}{\kappa\ell}\frac{d_m}{\ell}\left(n^{(m)}_{1,K} - n^{(m)}_{2,K}\right)^2 \\ &= U^{F(m)}_{K,K}(n,\mathbf{0}) - U^{F(m)}_{K,K'}(n,\mathbf{0}), \end{aligned} \tag{4.58}$$

where

$$U^{F(m)}_{\sigma,\sigma'}(n,\mathbf{q}) = \sum_{i,j=1}^{2}\left|y^{\sigma(m)}_{i,n}\right|^2\left|y^{\sigma'(m)}_{j,n}\right|^2\frac{e^2}{\kappa\ell}\int dpe^{-(m-1)\Delta_{ij}pd/\ell}e^{-p^2/2} \times L_{n+\sigma_i}\left(\frac{p^2}{2}\right)L_{n+\sigma'_j}\left(\frac{p^2}{2}\right)J_0\left(pq\ell\right), \tag{4.59}$$

with $K_1 = K_2' = m-1, K_2 = K_1' = -1$ in σ_i. The parameter $d_m = (m-1)\,d$ is the distance between the two outermost layers of the multi-layer graphene. So we obtain that

$$D^{(m)}_n(d_m) = \frac{1}{4}\int dpe^{-p^2/2}\left[1-e^{-pd_m/\ell}\right]\left[L_{n-m+1}\left(\frac{p^2}{2}\right)-L_{n-1}\left(\frac{p^2}{2}\right)\right]^2 > 0, \tag{4.60}$$

which proves that the ground states are Ising quantum Hall ferromagnets in a chirally stacked multi-layer graphene in higher Landau levels. Note that $D^{(0)}_n(d_0 = 0) = 0$, which implies that the ground state of monolayer graphene in any Landau level always has the SU(2) valley symmetry.

4.5 Charged excitations at zero bias

Once we understand the ground state of the system, it is natural to question how the excitations look like. We have studied the excitation problems in details in Ref. [78]. For simplicity, we concentrate on the single-particle excitations at zero bias only. The charged excitation, as what we have shown in the Chapter 2, is related to the transport gap. At 1/4 or 3/4 filling of a Landau level ($N > 0$), the ground state is studied in Sec. 4.3. In this section, the charged excitations around these two filling factors in a few Landau levels will be studied.

4.5.1 Quasi-particle states

We consider the simplest single-particle excitations, quasi-electron and quasi-hole states. They are similar to the quasi-particle studied in Chapter 2, which were represented in Fig. 2.2.

If we work in the Landau gauge, the quasi-particle states can be written as

$$\begin{aligned} |e\rangle &= c^{\dagger}_{n,K',\uparrow,X}\,|GS\rangle\,, && (4.61)\\ |h\rangle &= c_{n,K,\uparrow,X}\,|GS\rangle\,, && (4.62)\end{aligned}$$

where $|GS\rangle$ is the ground state at $\nu = 1$. The ground state could be in either the K or the K' valley, due to the Z_2 valley symmetry. Without loss of generality, we choose the ground state in the K valley here, which is defined by

$$|GS\rangle = \prod_{X'} c^{\dagger}_{N,K,\uparrow,X'}\,|0\rangle\,, \tag{4.63}$$

We insert Eqs. (4.61) and (4.62) into the Hamiltonian in Eq. (4.16), and then obtain the excitation energies of a quasi-electron and a quasi-hole states respectively. Since the capacitive energy is usually very small (of order of $10^{-5}e^2/\kappa\ell$), we can neglect it. So if one removes one electron from the ground state, one obtains the excitation energy of quasi-hole state,

$$\Delta_h = \frac{1}{2}\Delta_Z + U^F_{\alpha,\alpha}\left(\mathbf{0}\right)\left\langle\rho_{\alpha,s;\alpha,s}\left(\mathbf{0}\right)\right\rangle\left\langle\rho_{\alpha,s;\alpha,s}\left(\mathbf{0}\right)\right\rangle, \tag{4.64}$$

where α and s are the valley and the spin indices, respectively. If we set the ground state to be in K valley, then $\alpha = K'$ for the quasi-electron state. If one adds one electron in the $|K',\uparrow\rangle$ state, the extra Hartree interaction (with the exception of the capacitive energy) is cancelled by the background. Also, there is no exchange interaction between different valleys. So the excitation energy of quasi-electron is given by

$$\Delta_e = -\frac{1}{2}\Delta_Z. \tag{4.65}$$

We remark that the excitation energy of a quasi-particle pair, which is composed by a quasi-electron and a quasi-hole, can be measured in a transport experiment. The resistivity $R_{xx} \sim e^{-\Delta_T/k_BT}$ is related to the transport gap Δ_T at low temeprature, where k_B is the Boltzman constant and T is the temperature. Theoretically, this transport gap corresponds to the excitation of a quasi-electron quasi-hole pair with no interaction between them (infinite separation). The total excitation energy is simply the sum of the two quasi-particles energies, $\Delta_{eh} = \Delta_e + \Delta_h$.

There are other possibilities for the quasi-electron state. For example, the extra electron can be put in the opposite spin state $|K, \downarrow\rangle$ or $|K', \downarrow\rangle$. However, the energies of these states are higher than the state in Eq. (4.61). Hence, we choose the state in Eq. (4.61), which has the same spin as the lowest quasi-electron state, but is in the opposite valley to the ground state.

The excitation energy of a quasi-particle pair is given by

$$\begin{aligned} \Delta_{eh}^{\alpha} &= U_{\alpha,\alpha}^{F}(\mathbf{0}) && (4.66) \\ &= \frac{e^2}{\kappa\ell} \sum_{i,j=1}^{4} \left|y_{i,N}^{\alpha}\right|^2 \left|y_{j,N}^{\alpha}\right|^2 \int dp\ell e^{-\Delta_{ij}pd} e^{-p^2\ell^2/2} L_{N+\alpha_i}\left(\frac{p^2\ell^2}{2}\right) L_{N+\alpha_j}\left(\frac{p^2\ell^2}{2}\right), \end{aligned}$$

where $\alpha = 1, -1$ corresponds to valley K or K' respectively, and

$$\begin{aligned} \alpha_1 &= \alpha_4 = 0, && (4.67) \\ \alpha_2 &= \alpha, && (4.68) \\ \alpha_3 &= -\alpha, && (4.69) \end{aligned}$$

according to the wave function spinor in Eq. (1.33). Because of the Z_2 valley symmetry of the ground state at zero bias, we have $\Delta_{eh}^{K} = \Delta_{eh}^{K'}$. We use Eq. (4.66) to calculate the excitation energies of quasi-particle pairs and we then compare the quasi-particle energy with the energy of a spin textured excitation.

4.5.2 Nonlinear σ model and spin skyrmion excitations

In a conventional 2DEG in a semiconductor quantum well and in the chiral 2DEG of monolayer graphene, skyrmion excitations exist that reduces the excitation energy. We have shown that the valley skyrmion is the lowest energy excitation in LL $|n| = 1, 2, 3$ in graphene, since the ground state has the SU(2) symmetry in the two-valley system. However, in graphene bilayer (or multi-layer), the ground states in LL $N \geq 1$ are Ising quantum Hall ferromagnets at 1/4 and 3/4 fillings of a LL. So that we can not apply the NLσM in the two lowest kinetic energy levels, which are $|K, \uparrow\rangle$ and $|K, \downarrow\rangle$.

If we consider spin excitation, the situation is different. Since the ground state has Z_2 symmetry in the valley pseudo-spin at zero bias, we arbitrarily choose the ground state as $|K, \uparrow\rangle$. In the limit of slowly varying spin texture and if we set $\Delta_{Z=0}$, the Coulomb interaction can be described by the NLσM in Eq. (1) where $\mathbf{m}$ is a unitary spin field, $\mathbf{m} = 4\pi\ell^2\mathbf{S}_\alpha$. The spin field $\mathbf{S}_\alpha$ is defined in Eq. (4.45).The spin stiffness ρ_s is calculated

Landau level	Skyrmion	Quasi-particle
1	0.33136	0.721175
2	0.396278	0.608707
3	0.433813	0.548021
4	0.46233	0.506872
5	0.4869	0.476078

Table 4.1: Excitation energies for spin SK-ASK and e-h pairs in Landau levels N =1 to 4. All the energies are in units of $e^2/\kappa\ell$. The system is at magnetic field $B = 9$T, dielectric constant $\kappa = 2.5$.

by the method of Sec. 1.5, and is given by

$$\begin{aligned}
\rho_s &= \rho_s^K = \rho_s^{K'} - \frac{1}{16\pi\ell^2}\nabla_q^2 \sum_\alpha U^F_{K,K}(\mathbf{q})\,|_{q=0} \qquad (4.70)\\
&= \frac{e^2}{\kappa\ell}\frac{1}{32\pi}\sum_\alpha\sum_{i,j=1}^{4}\left|y^K_{i,N}\right|^2\left|y^K_{j,N}\right|^2\int dp p^2 e^{-\Delta_{ij}p\frac{d}{\ell}}e^{-p^2}L_{N+\alpha_i}\left(\frac{p^2}{2}\right)L_{N+\alpha_j}\left(\frac{p^2}{2}\right).
\end{aligned}$$

Note that the spin stiffnesses $\rho_s^K = \rho_s^{K'}$ at zero bias since $U^F_{K,K}(\mathbf{q}) = U^F_{K',K'}(\mathbf{q})$.

Once we know the spin stiffness, the excitation energy of a skyrmion anti-skyrmion pair is given by

$$\Delta_{SK-ASK} = 8\pi\rho_s. \qquad (4.71)$$

As in the monolayer graphene, the skyrmion can be shrinked to a quasi-particle state if the Zeeman coupling increases. If we consider the case of zero Zeeman coupling, then only the NLσM is able to describe the excitation states.

We need to compare Δ_{SK-ASK} with Δ_{eh} to determine which excitation is preferred for a different value of LL N. In the Table 4.5.2, we compare the excitation energies of a SK-ASK (skyrmion-antiskyrmion) and an e-h (quasi-electron-hole) pairs at zero Zeeman coupling. We see that the spin skyrmion energy is lower than the energy of quasi-particle up to Landau level 4. In a normal 2DEG in a quantum well, the skyrmion state only exists in the lowest Landau level. The spin skyrmion state exists up to Landau level 3 in monolayer graphene [9].

4.5.3 Skyrmions in microscopic Hamiltonian language

So far, we have neglected the possibility of the valley coherence in our study of spin skyrmion. The complete excitation states should involve the four levels, i.e. spin and valley texture may be intertwined. If we suppose $|K, \uparrow\rangle = |1\rangle$ is the ground state and do not consider LL mixing, the anti-skyrmion state should be written in the symmetric gauge as [27]:

$$|ASK\rangle = \prod_{m=1}^{\infty} \left(u_{1,m} c_{1,m}^{\dagger} + u_{2,m-1} c_{2,m-1}^{\dagger} + u_{3,m-1} c_{3,m-1}^{\dagger} + u_{4,m-1} c_{4,m-1}^{\dagger} \right) |0\rangle \,, \qquad (4.72)$$

where the index i in $c_{i,m}^{\dagger}$ combines the valley and spin indices together, and is also defined as: $i = 1 = (K, \uparrow); 2 = (K, \downarrow); 3 = (K', \uparrow); 4 = (K', \downarrow)$. $c_{i,m}^{\dagger}$ represents the creation operator of an electron in the level $|i\rangle$ at generalized angular momenta m.

For the skyrmion states, there are three possibilities,

$$\begin{aligned}
|SK\rangle_2 &= c_{2,0}^{\dagger} \prod_{m=0}^{\infty} \left(u_{1,m} c_{1,m}^{\dagger} + u_{2,m+1} c_{2,m+1}^{\dagger} + u_{3,m} c_{3,m}^{\dagger} + u_{4,m} c_{4,m}^{\dagger} \right) |0\rangle \,, && (4.73)\\
|SK\rangle_3 &= c_{3,0}^{\dagger} \prod_{m=0}^{\infty} \left(u_{1,m} c_{1,m}^{\dagger} + u_{2,m} c_{2,m}^{\dagger} + u_{3,m+1} c_{3,m+1}^{\dagger} + u_{4,m} c_{4,m}^{\dagger} \right) |0\rangle \,, && (4.74)\\
|SK\rangle_4 &= c_{4,0}^{\dagger} \prod_{m=0}^{\infty} \left(u_{1,m} c_{1,m}^{\dagger} + u_{2,m} c_{2,m}^{\dagger} + u_{3,m} c_{3,m}^{\dagger} + u_{4,m+1} c_{4,m+1}^{\dagger} \right) |0\rangle \,, && (4.75)
\end{aligned}$$

because there are three possible levels ($|2\rangle$, $|3\rangle$ and $|4\rangle$) that can accept the extra electron.

To calculate the skyrmions at finite Zeeman coupling and finite bias Δ_B, we need to numerically calculate the energies of states in Eqs. (4.72), (4.73), (4.74), and (4.75) with the method that we have used in Chapter 2. From a calculation shown in Fig. 4.13 in the condition that $B = 10\text{T}$ and $\kappa = 2.5$, we find that at small Zeeman coupling, the spin skyrmion can exist without valley coherence. It supports our assumption of neglecting the valley coherence in the NLσM. The spin anti-skyrmion (SASK) can be written as

$$|SASK\rangle = \prod_{m=1}^{\infty} \left(u_{1,m} c_{1,m}^{\dagger} + u_{2,m-1} c_{2,m-1}^{\dagger} \right) |0\rangle \,, \qquad (4.76)$$

which is obtained by simplifying the state $|ASK\rangle$. The spin skyrmion (SSK) can also be

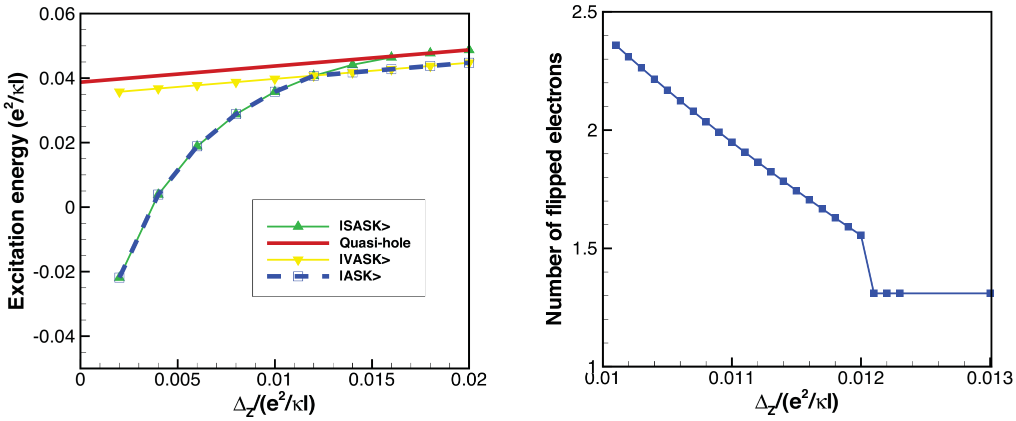

(a) (b)

FIGURE 4.13: (a) The excitation energies of the quasi-hole, spin anti-skyrmion $|SASK\rangle$, valley anti-skyrmion $|VASK\rangle$ and general state $|ASK\rangle$ in $N = 1$. (b) The number of flipped electrons in the lowest-energy anti-skyrmion state in $N = 1$. The step at $\Delta_Z = 0.012e^2/\kappa\ell$ represents the transition from a SASK to a VASK.

obtained by simplifying $|SK\rangle_2$:

$$|SSK\rangle = c^\dagger_{2,0} \prod_{m=0}^{\infty} \left(u_{1,m} c^\dagger_{1,m} + u_{2,m+1} c^\dagger_{2,m+1} \right) |0\rangle \,. \tag{4.77}$$

Fig. 4.13a shows the excitation energies of an anti-skyrmion described by Eq. (4.72) and a quasi-hole at zero bias. At small Zeeman coupling, $\Delta_Z < 0.012e^2/\kappa\ell$, $|ASK\rangle = |SASK\rangle$. When $\Delta_Z > 0.012e^2/\kappa\ell$, $|ASK\rangle$ evolves to the valley anti-skyrmion (VASK) $|VASK\rangle$ directly. Unlike a double quantum well system [56], there is no CP^3 anti-skyrmion state between SASK and VASK. We can also find the first-order transition by the number of electron flipped of the anti-skyrmion states in Fig. 4.13b.

The excitation energies of the skyrmion excitations $|SK\rangle_i, i = 2, 3, 4$ where i represents that an extra electron is added into level $|i\rangle$ are shown in Fig. 4.14. The state $|SK\rangle_4$ always has the highest energy. At small Zeeman coupling, the $|SK\rangle_2$ is degenerated to $|SSK\rangle$ with no valley coherence. This also supports our assumption of neglecting the valley coherence in the NLσM. When $\Delta_Z > 0.0084e^2/\kappa\ell$, the skyrmion state $|SK\rangle_3$ evolves to a valley skyrmion (VSK) and has the lowest energy in the three skyrmion states. There is also a first-order transition between $|SK\rangle_2$ and $|SK\rangle_3$, which can be verified by calculating the number of flipped electrons in Fig. 4.14b.

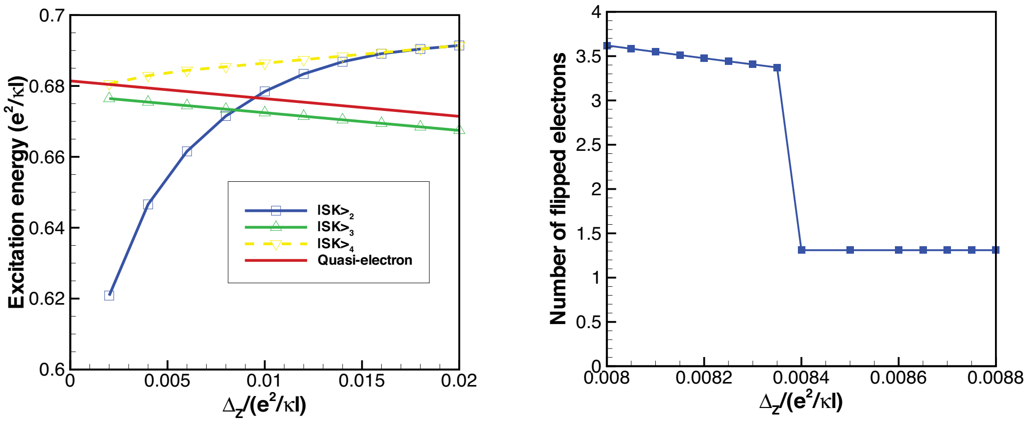

(a) (b)

FIGURE 4.14: (a) The excitation energies of the quasi-electron, and $|SK\rangle_i (i = 1, 2, 3)$. (b) The number of flipped electrons in the lowest-energy skyrmion state. The step at $\Delta_Z = 0.0084e^2/\kappa\ell$ represents the transition from a SSK to a VSK.

Since the level $|4\rangle$ has an energy greater than the ground state $|1\rangle$ by an amount Δ_Z, the preferred VSK should be $|SK\rangle_2$. So the VASK and VSK states can be written in the symmetric gauge as

$$|VASK\rangle = \prod_{m=1}^{\infty} \left(u_{1,m} c^\dagger_{1,m} + u_{3,m-1} c^\dagger_{3,m-1} \right) |0\rangle , \tag{4.78}$$

$$|VSK\rangle = c^\dagger_{3,0} \prod_{m=0}^{\infty} \left(u_{1,m} c^\dagger_{1,m} + u_{3,m+1} c^\dagger_{3,m+1} \right) |0\rangle . \tag{4.79}$$

The VASK (VSK) never be degenerated to the hole (electron) state at zero bias when the Zeeman energy increases. This is because that the valley gap and the Coulomb interaction are not changed by the Zeeman coupling.

Interestingly, the skyrmion-antiskyrmion pair is composed by a SSK and a SASK when $0 < \Delta_Z < 0.0084e^2/\kappa\ell$; by a VSK and a SASK when $0.0084e^2/\kappa\ell < \Delta_Z < 0.012e^2/\kappa\ell$; and by a VSK and a VASK when $\Delta_Z > 0.012e^2/\kappa\ell$. The existence region of a VSK is not the same as a VASK. The reason is that the energy of a VSK increases with Zeeman coupling while the energy of a VASK decreases with Zeeman coupling. The total excitation energies of a skyrmion pair and a quasi-particle pair is shown in Fig. 4.15. Note that, for the SSK and SASK (for both graphene bilayer and monolayer graphene studied in Chapter 2), the existence regions are the same. Also, the numbers of flipped

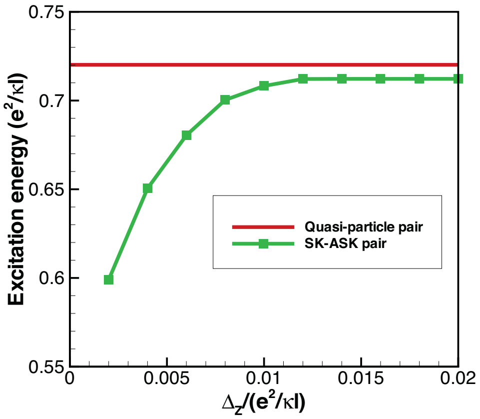

FIGURE 4.15: The excitation energies of a skyrmion pair and a quasi-particle pair at zero Δ_B.

electrons for a SSK and a SASK at the same Zeeman coupling are identical. This is because the two spin levels have the SU(2) symmetry. At zero bias, the flipped electron of a VSK is identical to that of a VASK due to the electron hole symmetry.

To study the VSK and VASK in detail, we calculate the valley (anti-)skyrmion as a function of Δ_B at a large Zeeman coupling $\Delta_Z = 0.03e^2/\kappa\ell$. As we show in Figs. 4.13 and 4.14, the spin coherence does not exist at so high Zeeman coupling, so that we can concentrate on the VSK and VASK only. Figs. 4.16a and 4.16b show the excitation energies of a VASK and a VSK, respectively. Note that, at positive Δ_B the ground state is $|3\rangle$ while the ground state is $|1\rangle$ at negative bias. The existence region of a VASK is $(-0.06, 0.06)e^2/\kappa\ell$, and the existence region of a VSK is $(-0.09, 0.09)e^2/\kappa\ell$. The energy of a VASK-VSK pair is shown in Fig. 4.16c. When the bias is nonzero, the Z_2 symmetry of the two valleys is broken, and the electron hole symmetry is also broken. The electron flipping number of a VSK is larger than that of a VASK at finite bias, which leads the existence region of the VSK larger. In addition, the VSK and VASK are also found in $N = -1$.

The spin textures of a SASK and a SSK are similar to those in monolayer graphene shown in Fig. 2.8. The density profiles are also associated with the spin textures, which are similar to Fig. 2.7. Although the density profiles of a VASK (or a VSK) are similar to a SASK (or a SSK), the spin textures of a VASK and a VSK are very different from any (anti-)skyrmion that we have studied before. Fig. 4.17 shows the valley pseudo-spin textures of a VASK and a VSK.

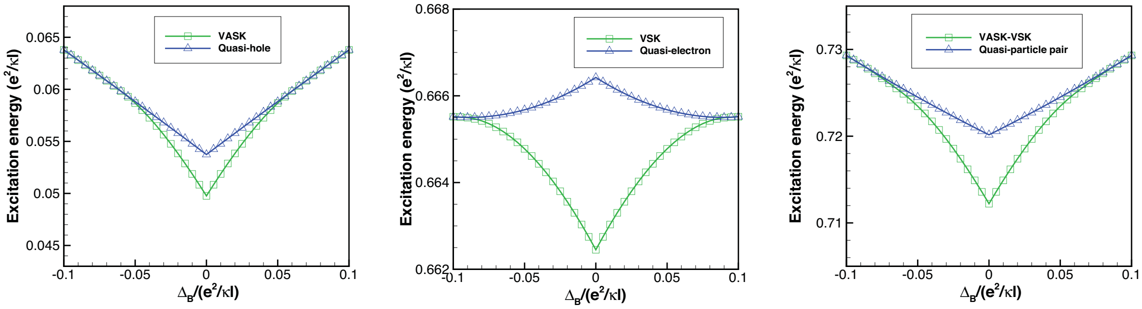

(a) (b) (c)

FIGURE 4.16: (a) The excitation energies of a VASK and a quasi-hole as functions of the bias Δ_B. (b) The excitation energies of a VSK and a quasi-electron. (c) The excitation energies of a VASK-VSK pair and a quasi-particle pair. The calculations are for $B = 10T$ and $\kappa = 2.5$ in $N = 1$.

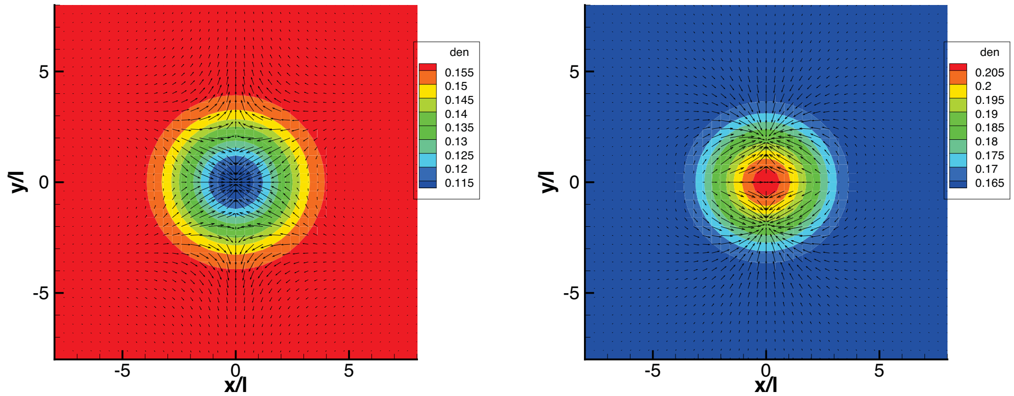

(a) (b)

FIGURE 4.17: (a) The valley pseudo-spin texture of a VASK. (b) The valley pseudo-spin texture of a VSK. The colors represent the density profile which is similar to a SASK or SSK.

The reason why the valley pseudo-spin textures of a VASK and a VSK are so complicated is that the orbital indices in elements with $|B_1\rangle$ and $|A_2\rangle$ are not the same in different valleys. In the symmetric gauge, the wave function spinors are written as

$$\psi_{K,M}(\mathbf{u}) = \begin{pmatrix} y_{1,N}^{K} h_{N,M}(\mathbf{r}) |A_1\rangle \delta\left(z+\frac{d}{2}\right) \\ y_{2,N}^{K} h_{N+1,M-1}(\mathbf{r}) |B_1\rangle \delta\left(z+\frac{d}{2}\right) \\ y_{3,N}^{K} h_{N-1,M+1}(\mathbf{r}) |A_2\rangle \delta\left(z-\frac{d}{2}\right) \\ y_{4,N}^{K} h_{N,M}(\mathbf{r}) |B_2\rangle \delta\left(z-\frac{d}{2}\right) \end{pmatrix}, \tag{4.80}$$

$$\psi_{K',M}(\mathbf{u}) = \begin{pmatrix} y_{1,N}^{K'} h_{N,M}(\mathbf{r}) |A_1\rangle \delta\left(z+\frac{d}{2}\right) \\ y_{2,N}^{K'} h_{N-1,M+1}(\mathbf{r}) |B_1\rangle \delta\left(z+\frac{d}{2}\right) \\ y_{3,N}^{K'} h_{N+1,M-1}(\mathbf{r}) |A_2\rangle \delta\left(z-\frac{d}{2}\right) \\ y_{4,N}^{K'} h_{N,M}(\mathbf{r}) |B_2\rangle \delta\left(z-\frac{d}{2}\right) \end{pmatrix}, \tag{4.81}$$

where M is the real angular momenta. In a SASK or a SSK, the spin field is defined by $S_+ = \sum_M \psi^*_{K,M+\delta}\psi_{K,M} c^\dagger_{K,\uparrow,M+\delta} c_{K,\downarrow,M}$. So there is always a δ factor difference between the angular momenta in $\psi^*_{K,M+\delta}$ and $\psi_{K,M}$. However, in a VASK or VSK, the valley pseudo-spin field is defined by $P_+ = \sum_M \psi^*_{K,M+\delta}\psi_{K',M} c^\dagger_{K,\uparrow,M+\delta} c_{K',\uparrow,M}$. The angular momenta difference between $\psi^*_{K,M+\delta}$ and $\psi_{K',M}$ is not always δ. The complexity of $\psi^*_{K,M+\delta}\psi_{K',M}$ leads to the extraordinary valley pseudo-spin texture.

There is another type of Ising quantum Hall ferromagnet in a two-level system with different Landau level orbitals. In a quantum well, such as ZnO or AlAs, the LL gap can be small and the Zeeman coupling can be tuned widely. For example, the $|n=0,\downarrow\rangle$ can be higher than $|n=1,\uparrow\rangle$ when the Zeeman coupling is tuned to be larger than the LL gap between $n=0$ and $n=1$. If the filling factor $\nu=2$, the 2DEG in the two levels $|n=0,\downarrow\rangle$ and $|n=1,\uparrow\rangle$ is an Ising quantum Hall ferromagnet. When the Zeeman coupling is sufficiently large, all the electrons in $|n=0,\downarrow\rangle$ are flipped to $|n=1,\uparrow\rangle$ as shown in Fig. 4.18. In this case, Lilliehook [62] has proved that there is no skyrmion between the two levels. The charged excitations are only quasi-particles. The VASK and VSK in graphene bilayer are very special since the ground state is also an Ising quantum Hall ferromagnet. The reason why the VASK and VSK exist might be that the two corresponding levels are all in the same Landau level, although the LL orbital indices in the wave function spinors of the two levels are not exactly the same.

We now comment on the single particle excitations at half filling of a Landau level. In this case, the ground state at zero bias has the two states $|K,\uparrow\rangle$ and $|K',\uparrow\rangle$ fully filled

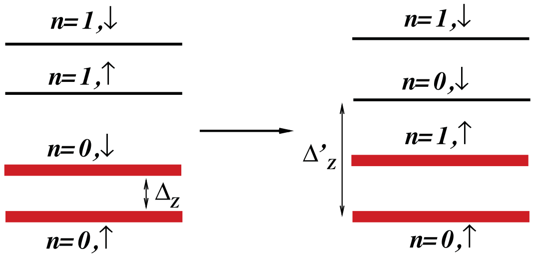

FIGURE 4.18: The Zeeman coupling is tuned to be larger than the LL gap, and the ground state is changed to an Ising quantum Hall ferromagnet.

and the other two states are empty [78]. According to Table (4.5.2), the spin skyrmion, which could occur in any one of the two valleys, has lower energy than a quasi-particle at zero Zeeman coupling up to LL $N = 4$.

4.6 Screening effect

As in Chapter 2, we can also take the screening effect into consideration in our study of quasi-particle and skyrmion excitations. However, the screening is more complicated in a bilayer system, since the dielectric function should be replaced by a dielectric matrix. Misumi and Shizuya [84] discussed the screening effect and calculated the dielectric matrix for bilayer graphene. Gorbar et al. even discussed the dynamic screening effect in graphene bilayer [46]. However, these authors just use the effective two-component model which is not accurate in higher Landau levels. Although the eigen-wavefunctions of the four-band model (with $\gamma_3 = 0$) are not reliable in very high Landau levels, the high Landau levels affect the screening only weakly since they are far away from the partially filled Landau level. In addition, the Landau level gaps in graphene bilayer is smaller than monolayer graphene, so that the screening effect may also be stronger. In this section, we work in the four-band model.

In a bilayer system, the inter-layer and intra-layer Coulomb interactions are screened differently. We use 1 and 2 to denote the two layers in graphene bilayer. A_1, B_1 are on the layer 1, while A_2, B_2 are located on layer 2. The screened Coulomb potential is given by

$$\begin{pmatrix} V_{11,s} & V_{12,s} \\ V_{21,s} & V_{22,s} \end{pmatrix} = \begin{pmatrix} V_{11} & V_{12} \\ V_{12} & V_{11} \end{pmatrix} \left[I + \begin{pmatrix} \Pi_{11} & \Pi_{12} \\ \Pi_{12} & \Pi_{22} \end{pmatrix} \begin{pmatrix} V_{11} & V_{12} \\ V_{12} & V_{11} \end{pmatrix} \right]^{-1}, \tag{4.82}$$

where the index s denotes the screened Coulomb potential. $V_{ij,s}$ is the screened Coulomb potential between layer i and layer j. Π_{ij} is the polarization function between layer i and layer j. It is related to density-density correlation function $\chi_{n_i n_j}$ by $\Pi_{ij} = -\chi_{n_i n_j}$. The Coulomb potential in Eq. (4.82) is a matrix, while the Coulomb potential in a monolayer system is only a function.

We need to calculate four polarization functions to obtain the screened Coulomb potential matrix in Eq. (4.82). Then, the excitation energies of skyrmion and of quasi-particle can be calculated using these screening corrections.

The density-density correlation function in the simplest (RPA) approximation is given by

$$
\begin{align}
\chi_{nn}\left(\mathbf{q}\right) &= \frac{1}{2\pi\ell^2\hbar}\sum_{n_i}\sum_{\sigma_i}\Theta^{\sigma_1,\sigma_2}_{n_1,n_2}\left(-\mathbf{q}\right)\Theta^{\sigma_3,\sigma_4}_{n_3,n_4}\left(\mathbf{q}\right)\chi^{0,\sigma_1,\sigma_2,\sigma_3,\sigma_4}_{n_1,n_2,n_3,n_4}\left(\mathbf{q}\right), \tag{4.83}\\
\chi^{0,\sigma_1,\sigma_2,\sigma_3,\sigma_4}_{n_1,n_2,n_3,n_4}\left(\mathbf{q},i\Omega_n\right) &= \delta_{k_1,k_2}\delta_{k_3,k_4}\delta_{s_1,s_2}\delta_{s_3,s_4} \nonumber\\
&\times\frac{\delta_{\sigma_2,\sigma_3}\delta_{n_2,n_3}\left\langle\rho^{\sigma_1,\sigma_4}_{n_1,n_4}\left(\mathbf{0}\right)\right\rangle-\delta_{\sigma_1,\sigma_4}\delta_{n_1,n_4}\left\langle\rho^{\sigma_3,\sigma_2}_{n_3,n_2}\left(\mathbf{0}\right)\right\rangle}{i\Omega_n+\left(\widetilde{E}_{n_1,\sigma_1}-\widetilde{E}_{n_2,\sigma_2}\right)/\hbar}, \tag{4.84}
\end{align}
$$

where n_i is the Landau level index, and σ is the index combined band b, valley k and spin s. Here we neglect Landau level mixing coherence, so that the density matrix elements $\left\langle\rho^{\sigma,\sigma'}_{n,n'}\left(\mathbf{0}\right)\right\rangle$ are zero when $n \neq n'$ or $\sigma \neq \sigma'$. The form factor Θ is defined by

$$
\begin{align}
\Theta^{\sigma_1,\sigma_2}_{n_1,n_2}\left(-\mathbf{q}\right) &= \begin{pmatrix} y^{k_1,b_1*}_{1,n_1}h^*_{|n_1|} & y^{k_1,b_1*}_{2,n_1}h^*_{|n_1|+f_{2,\sigma_1}} & y^{k_1,b_1*}_{3,n_1}h^*_{|n_1|+f_{3,\sigma_1}} & y^{k_1,b_1*}_{4,n_1}h^*_{|n_1|}\end{pmatrix} \nonumber\\
&\times\begin{pmatrix} y^{k_2,b_2}_{1,n_2}h_{|n_2|}\left\{1\right\}\\ y^{k_2,b_2}_{2,n_2}h_{|n_2|+f_{2,\sigma_2}}\left\{1\right\}\\ y^{k_2,b_2}_{3,n_2}h_{|n_2|+f_{3,\sigma_2}}\left\{2\right\}\\ y^{k_2,b_2}_{4,n_2}h_{|n_2|}\left\{2\right\}\end{pmatrix}, \tag{4.85}
\end{align}
$$

where

$$
\begin{align}
f_{2,\sigma} &= \left(-1\right)^k-\delta_{n,0}\delta_{k,K}\delta_{b,3}, \tag{4.86}\\
f_{3,\sigma} &= -\left(-1\right)^k-\delta_{n,0}\delta_{k,K'}\delta_{b,3}. \tag{4.87}
\end{align}
$$

The symbol $\{i\}$ means that the term involves layer i. So, there are four terms in the density factor $\Theta \cdot \Theta$,

$$
\begin{aligned}
&\Theta^{\sigma_1,\sigma_2}_{n_1,n_2}\left(-\mathbf{q}\right)\Theta^{\sigma_3,\sigma_4}_{n_3,n_4}\left(\mathbf{q}\right) = \\
&\Big\{\Big[y^{k_1,b_1*}_{1,n_1} y^{k_2,b_2}_{1,n_2} F_{|n_1|,|n_2|}\left(-\mathbf{q}\right) + y^{k_1,b_1*}_{2,n_1} y^{k_2,b_2}_{2,n_2} F_{|n_1|+f_{2,\sigma_1},|n_2|+f_{2,\sigma_2}}\left(-\mathbf{q}\right)\Big] \\
&\times \Big[y^{k_3,b_3*}_{1,n_3} y^{k_4,b_4}_{1,n_4} F_{|n_3|,|n_4|}\left(\mathbf{q}\right) + y^{k_3,b_3*}_{2,n_3} y^{k_4,b_4}_{2,n_4} F_{|n_3|+f_{2,\sigma_3},|n_4|+f_{2,\sigma_4}}\left(\mathbf{q}\right)\Big]\{11\} \\
&+ \Big[y^{k_1,b_1*}_{1,n_1} y^{k_2,b_2}_{1,n_2} F_{|n_1|,|n_2|}\left(-\mathbf{q}\right) + y^{k_1,b_1*}_{2,n_1} y^{k_2,b_2}_{2,n_2} F_{|n_1|+f_{2,\sigma_1},|n_2|+f_{2,\sigma_2}}\left(-\mathbf{q}\right)\Big] \\
&\times \Big[y^{k_3,b_3*}_{3,n_3} y^{k_4,b_4}_{3,n_4} F_{|n_3|+f_{3,\sigma_3},|n_4|+f_{3,\sigma_4}}\left(\mathbf{q}\right) + y^{k_3,b_3*}_{4,n_3} y^{k_4,b_4}_{4,n_4} F_{|n_3|,|n_4|}\left(\mathbf{q}\right)\Big]\{12\} \\
&+ \Big[y^{k_1,b_1*}_{3,n_1} y^{k_2,b_2}_{3,n_2} F_{|n_1|+f_{3,\sigma_1},|n_2|+f_{3,\sigma_2}}\left(-\mathbf{q}\right) + y^{k_1,b_1*}_{4,n_1} y^{k_2,b_2}_{4,n_2} F_{|n_1|,|n_2|}\left(-\mathbf{q}\right)\Big] \\
&\times \Big[y^{k_3,b_3*}_{1,n_3} y^{k_4,b_4}_{1,n_4} F_{|n_3|,|n_4|}\left(\mathbf{q}\right) + y^{k_3,b_3*}_{2,n_3} y^{k_4,b_4}_{2,n_4} F_{|n_3|+f_{2,\sigma_3},|n_4|+f_{2,\sigma_4}}\left(\mathbf{q}\right)\Big]\{21\} \\
&+ \Big[y^{k_1,b_1*}_{3,n_1} y^{k_2,b_2}_{3,n_2} F_{|n_1|+f_{3,\sigma_1},|n_2|+f_{3,\sigma_2}}\left(-\mathbf{q}\right) + y^{k_1,b_1*}_{4,n_1} y^{k_2,b_2}_{4,n_2} F_{|n_1|,|n_2|}\left(-\mathbf{q}\right)\Big] \\
&\times \Big[y^{k_3,b_3*}_{3,n_3} y^{k_4,b_4}_{3,n_4} F_{|n_3|+f_{3,\sigma_3},|n_4|+f_{3,\sigma_4}}\left(\mathbf{q}\right) + y^{k_3,b_3*}_{4,n_3} y^{k_4,b_4}_{4,n_4} F_{|n_3|,|n_4|}\left(\mathbf{q}\right)\Big]\{22\}\Big\},
\end{aligned}
\tag{4.88}
$$

where each $\{ij\}$ corresponds to the density-density correlation function $\chi_{n_in_j}$ respectively. The F function is given by Eq. (2.56).

Now we can define the screened dielectric function,

$$\epsilon_{ij}(q) = \frac{V_{ij}(q)}{V_{ij,s}(q)}, \tag{4.89}$$

where ϵ_{ij} is used to calculate the screened Coulomb interaction between layer i and layer j. Notice that in Eq. (4.88), the $\{12\}$ part is identical to the $\{21\}$ part. Consequently, we find that $\chi_{n_1n_2} = \chi_{n_2n_1} \in \mathbb{R}$ in the system. So we obtain the property of the screened Coulomb potential,

$$V_{12,s} = V_{21,s}, \epsilon_{12} = \epsilon_{21}, \tag{4.90}$$

which means the inter-layer Coulomb potentials are always identical with or without screening correction. Note that without screening, $V_{11} = V_{22}$, while $V_{11,s}$ is not necessary the same as $V_{22,s}$ at $\nu = 1, 3$. This is because the charge is not balanced in the two layers at $\nu = 1, 3$. However, at zero bias, the electron charge is balanced in two layers at $\nu = 2, 4$. So, we find that $V_{11} = V_{22}$ and $V_{11,s} = V_{22,s}$ in this case. In Fig. 4.19, we show the dielectric functions as a function of momentum at $\nu = 1$ in Landau level $N = 1$ ($\nu_t = 5$). The magnetic field is 10T, and the sample is suspended, the dielectric constant for the substrate $\kappa = 1$. Moreover, we are able to find similar results as in monolayer

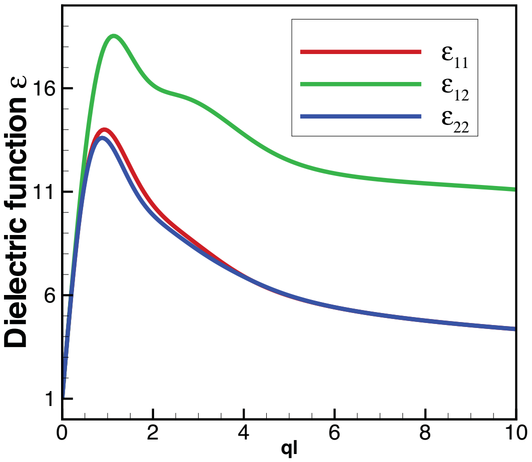

FIGURE 4.19: The screening effect and dielectric functions at $\nu_t = 5$, in Landau level $N = 1$.

graphene in Fig. 2.9. For example, screening is stronger and the dielectric functions $(\epsilon_{11}, \epsilon_{12}, \epsilon_{22})$ increase when the total filling factor increases.

4.6.1 Phase transitions at integer filling factors with screening corrections in Landau levels $N \neq 0$

To study the ground state with screening correction, we need to modify the interaction functions U^H and U^F in the equation of motion of the Green's function in Eq. (4.19). Note that U^0 does not have to be screened, because U^0 is from $U^H(q=0)$, and $\epsilon(q=0)=1$. If we only consider the liquid phase, the Hartree interaction can be neglected. It follows that the screened Fock interaction function $U^{F(s)}_{\alpha,\beta}$ is given by

$$\begin{aligned} U^{F(s)}_{\alpha,\beta}(\mathbf{q}) &= \frac{e^2}{\kappa\ell}\sum_{i,j=1}^{4}\left|y^{\alpha}_{i,N}\right|^2\left|y^{\beta}_{j,N}\right|^2 \\ &\times \int \frac{dp}{\epsilon_{\mu\nu}(p)} e^{-\Delta_{ij}pd/\ell} e^{-p^2/2} L_{N+\alpha_i}\left(\frac{p^2}{2}\right) L_{N+\beta_j}\left(\frac{p^2}{2}\right) J_0(pq\ell), \end{aligned} \quad (4.91)$$

where μ, ν are the layer indices and are defined by

$$\mu = 1 \quad \text{if} \quad i = 1, 2, \tag{4.92}$$

$$\mu = 2 \quad \text{if} \quad i = 3, 4, \tag{4.93}$$

$$\nu = 1 \quad \text{if} \quad j = 1, 2, \tag{4.94}$$

$$\nu = 2 \quad \text{if} \quad j = 1, 2. \tag{4.95}$$

Note that $\epsilon_{\mu\nu}$ contains the density matrix elements $\langle \rho \rangle$, so the calculation of $\epsilon_{\mu\nu}$ must be included in the self-consistent iterations of solution of the equation of motion of the Green's function.

Our numerical calculations indicate that the Ising behavior of the ground states at $\nu = 1$ in LLs $|N| = 1, 2, 3$ is not changed by screening. However, there is no other phase transition in $N = 1$ except at $\Delta_B = 0$. So the phase diagrams with screening at $\nu = 1$ in $N = 1, 2, 3$ are similar to those that have been shown in Fig. 4.3b. Since the ground state is still an Ising quantum Hall ferromanget, the resistance spike of R_{xx} still exists at zero bias. The experiment also supports our calculations. In Fig. 4.20 (from Fig. 3a in Ref. [77]), it is clear that there are resistance spikes at zero bias at $\nu_t = -5, -9, -13$ which correspond to $\nu = 1$ in LL $N = -1, -2, -3$. The black square and circle are spin-polarized to valley-polarized phase transitions at $\nu = 2$ in $N = -1, -2$.

At $\nu = 2$, the phase diagram in Fig. 4.7 for $N = 1$ is also changed to that similar to Fig. 4.9. There are only three phases and two phase transitions in the whole diagram of $N = 1, 2, 3$. All the phase transitions are from a spin polarized state to a valley pseudo-spin polarized state in which the lower-energy valley is occupied. The critical biases of phase transitions $\Delta_B^{C(s)}(n)$ for different LL N also changed. We calculate $\Delta_B^{C(s)}(N = 1, 2, 3)$ (only the positive ones are calculated since the negative critical bias $-\Delta_B^C$ has the same absolute value as Δ_B^C) and compare them with the unscreened ones: Δ_B^1 (for $N = 1$) and $\Delta_B^C(N = 2, 3)$ in Fig. 4.21. If we do not consider screening, the critical bias in $N = 1$ is always higher than those in $N = 2, 3$. And the critical biases decrease when the magnetic field increases.

In Ref. [77], which is shown in Fig. 4.22 (Fig. 3d in Ref. [77]), the authors measured the critical biases in LLs $N = -1, -2, -3$. In each of these negative LLs (they all belong to the band $b = 3$) with or without screening, there are two critical biases ($|\Delta_B^C(N)|$ and $-\Delta_B^C(N)$) in the phase diagram similar to that of LL $N = 2$. All the two phase transitions are corresponding to the transition between the spin-polarized

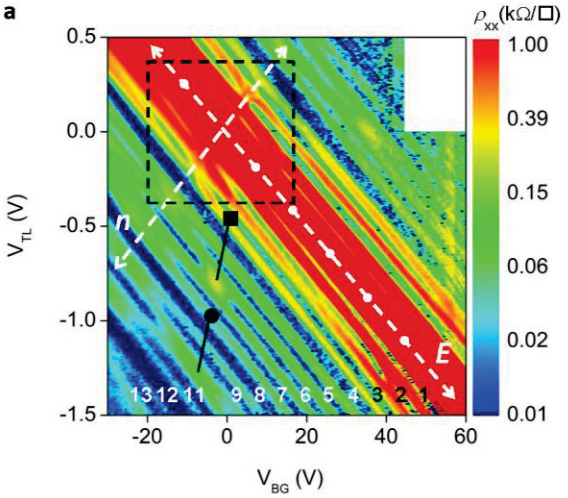

FIGURE 4.20: The experimental picture extracted in Ref. [77]. The white dashed line for E is the axis of electric field $E = \Delta_B/(ed)$. The dots along this line represent an increment of 0.1V/nm of E. The black square and circle are the phase transitions at $\nu = 2$.

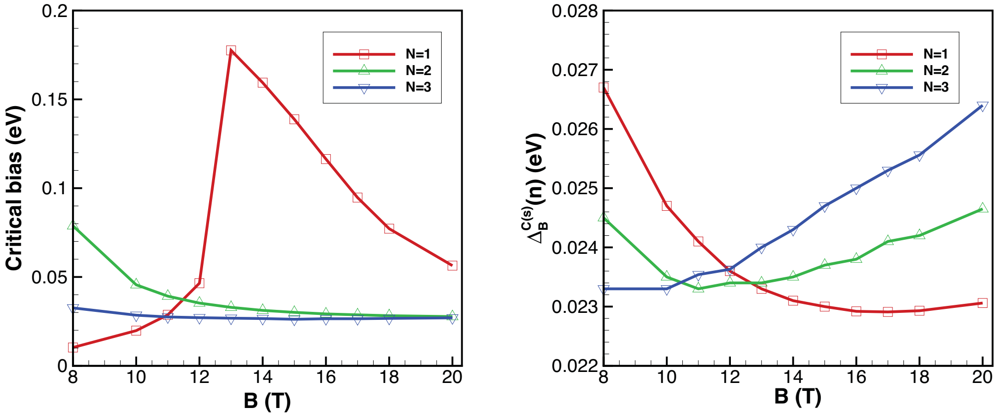

(a) (b)

FIGURE 4.21: (a) The critical biases Δ_B^1 (for $n = 1$) and Δ_B^C $(N = 2, 3)$. (b) The critical bias with screening correction, $\Delta_B^{C(s)}$ $(N = 1, 2, 3)$. The dielectric constant of the substrate $\kappa = 3$ is given by experimental parameter.

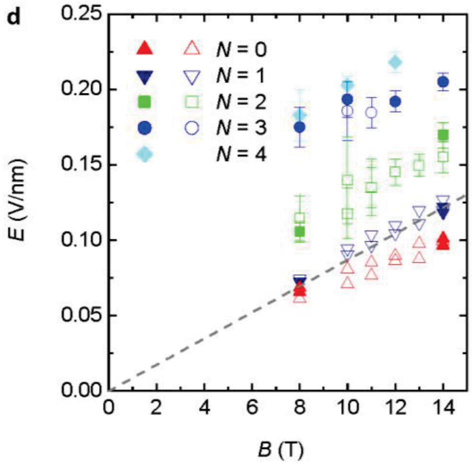

FIGURE 4.22: The critical biases of phase transitions at $\nu = 2$ in LL $n = 0, 1, 2, 3$ measured in Ref. [77]. The LL indices here $N = 0, 1$ belong to the two orbitals of LL $N = 0$, and "$N = 2, 3, 4$" in the picture actually belong to LL $-1, -2, -3$, respectively.

and valley-polarized states. In Fig. 4.23, we indicate our numerical calculations of these critical biases at different magnetic fields in $N = -1, -2, -3$ with and without screening. We find that the critical biases increase with the magnetic field and $\Delta_B^C (N = -1) < \Delta_B^C (N = -2) < \Delta_B^C (N = -3)$, which agrees with the experiment qualitatively. The screening effect helps the numerical results closer to the experiment. However, the experimental results are still three to four times larger than the numerical results with screening. Note that, in $N = 0$, the experimental critical biases are also three to four times larger than the numerical results [13].

4.6.2 Skyrmions in Nonlinear σ model with screening correction

In the following, we use a symbol (s) in the upper index of variables to represent the screened excitation energies. Hence, we obtain the screened excitation energy of a quasi-electron quasi-hole pair,

$$\Delta_{eh}^{(s)N,\alpha} = \frac{e^2}{\kappa\ell} \int dq e^{\frac{-q^2}{2}} \xi_{\alpha,\alpha}^{N} (q) , \tag{4.96}$$

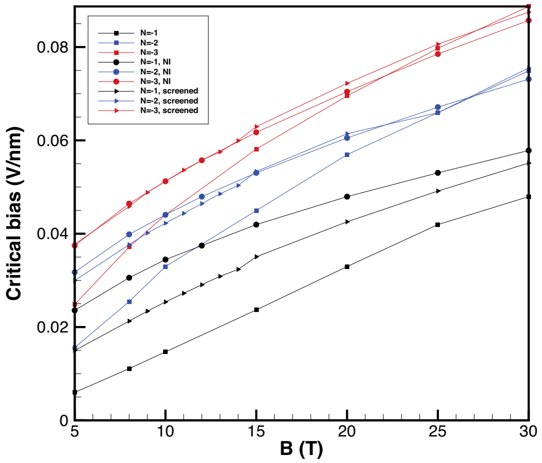

FIGURE 4.23: The critical electric fields $E_C = \Delta_B^C/d$ of phase transitions at $\nu = 2$ in LL $N = -1, -2, -3$ with and without screening at $\kappa = 2.5$. In comparison, we add the numerical results calculated in the non-interacting (NI) model. All the phase transitions are from a spin-polarized state to a valley-polarized state in the K valley.

where we define the function of ξ,

$$\begin{aligned}\xi^N_{\alpha,\alpha'}(q) &= \frac{1}{\epsilon_{11}(q)} \sum_{i,j=1}^{2} \left|y^{\alpha}_{i,N}\right|^2 L_{N+\alpha_i}\left(\frac{q^2}{2}\right) \left|y^{\alpha'}_{j,N}\right|^2 L_{N+\alpha'_j}\left(\frac{q^2}{2}\right) \\ &+ \frac{1}{\epsilon_{12}(q)} \sum_{i=1}^{2} \left|y^{\alpha}_{i,N}\right|^2 L_{N+\alpha_i}\left(\frac{q^2}{2}\right) \sum_{j=3}^{4} \left|y^{\alpha'}_{j,N}\right|^2 L_{N+\alpha'_j}\left(\frac{q^2}{2}\right) e^{-q\frac{d}{\ell}} \\ &+ \frac{1}{\epsilon_{12}(q)} \sum_{i=3}^{4} \left|y^{\alpha}_{i,N}\right|^2 L_{N+\alpha_i}\left(\frac{q^2}{2}\right) \sum_{j=1}^{2} \left|y^{\alpha'}_{j,N}\right|^2 L_{N+\alpha'_j}\left(\frac{q^2}{2}\right) e^{-q\frac{d}{\ell}} \\ &+ \frac{1}{\epsilon_{22}(q)} \sum_{i,j=3}^{4} \left|y^{\alpha}_{i,N}\right|^2 L_{N+\alpha_i}\left(\frac{q^2}{2}\right) \left|y^{\alpha'}_{j,N}\right|^2 L_{N+\alpha'_j}\left(\frac{q^2}{2}\right). \end{aligned} \tag{4.97}$$

Note that $\Delta^{(s)N,K}_{eh} = \Delta^{(s)n,K'}_{eh}$ at zero bias. For the spin stiffness in the NLσM,

$$\rho_s^{(s)n} = \frac{1}{16\pi} \frac{e^2}{\kappa\ell} \sum_{\alpha} \int dq q^2 e^{\frac{-q^2}{2}} \xi^n_{\alpha,\alpha}(q), \tag{4.98}$$

where α is the an arbitrary valley at zero bias.

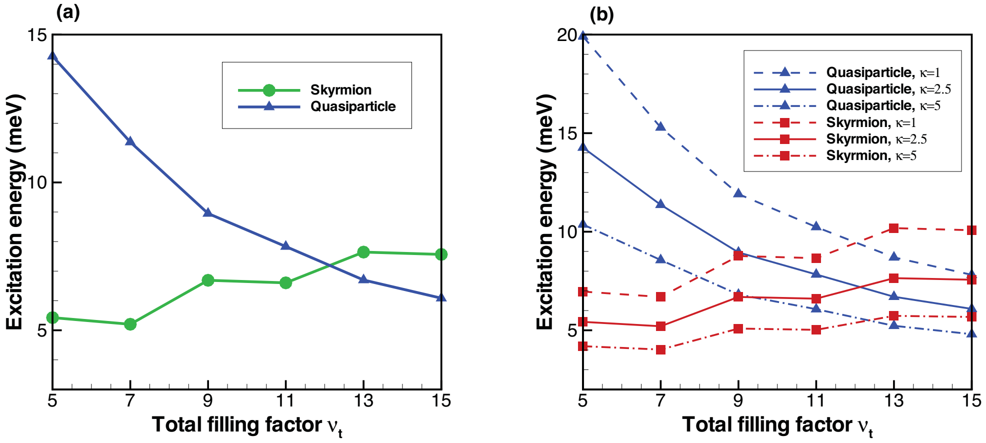

FIGURE 4.24: Excitation energies of the SSK pair and the quasi-particle pairs at $B = 9$T. The electrons are at $1/4$ and $3/4$ fillings in LLs $N = 1, 2, 3$. (a) The comparison of a SSK pair and a quasi-particle pairs when the dielectric constant of the substrate is fixed to $\kappa = 2.5$. (b) The excitation energies are changed as functions of the dielectric constant.

We can compare the excitation energy of the quasi-particle with that of the spin skyrmion by computing Eqs. (4.96) and (4.98). The screening strength is dependent on many parameters, such as magnetic field, filling factor, bias, and dielectric constant of the substrate.

Since the four-band model is not reliable in very high Landau levels, we concentrate on the screening effect in Landau levels $N = 1, 2, 3$. The $1/4$ and $3/4$ fillings in Landau level $N = 1$ correspond to the total filling factor $\nu_t = 5, 7$, respectively. The $1/4$ and $3/4$ fillings in $n = 2$ correspond to $\nu_t = 9, 11$, and the $1/4$ and $3/4$ fillings correspond to $\nu_t = 13, 15$ in $n = 3$.

From Fig. 4.24, it is clear that the excitation energy of the spin skyrmion anti-skyrmion pair is lower than that of a quasi-particle pair in Landau levels $N = 1, 2$. In contrast with the unscreened case, the skyrmion does not exist in $N = 3, 4$. In the same Landau level, the energy at $1/4$ filling is always higher than that at $3/4$ filling. If the screening is neglected, these two energies should be identical because of the electron hole symmetry. This symmetry is broken by the screening. The same effect was seen in monolayer graphene in Chapter 2. In addition, we find that the ratio of the energy at $1/4$ to the energy at $3/4$ is much different from that of the quasi-particles. We list the

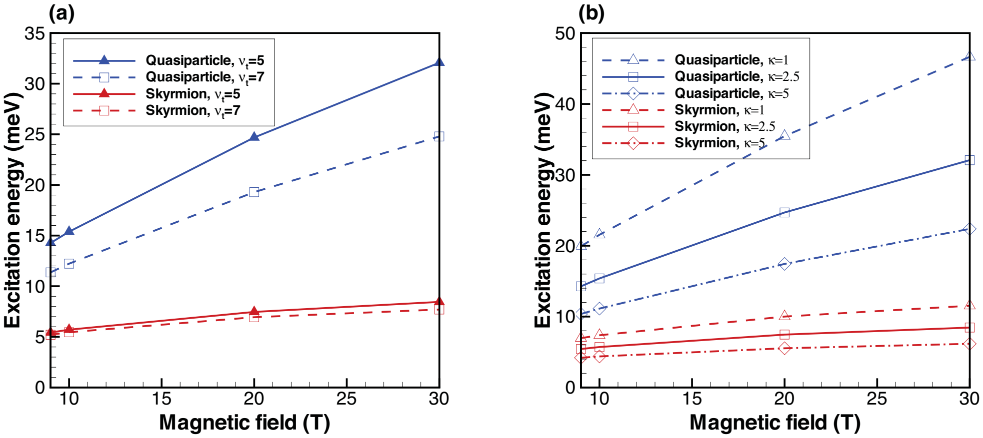

FIGURE 4.25: The excitation energies of the spin skyrmion and quasi-particle are changed by the magnetic field. (a) The dielectric constant is fixed at $\kappa = 2.5$. The excitation energies at filling factor $\nu = 1, 3$ ($\nu_t = 5, 7$) in LL 1 are plotted. (b) The filling factor is fixed at $\nu = 1$ in LL $N = 1$, and the dielectric constant changes the excitation energies.

ratios of skyrmion pairs and quasi-particles:

$$\frac{\Delta^{(s)N=1,\nu=1}_{S-AS}}{\Delta^{(s)N=1,\nu=3}_{S-AS}} = 1.05, \quad \frac{\Delta^{(s)N=1,\nu=1}_{eh}}{\Delta^{(s)N=1,\nu=3}_{eh}} = 1.26, \tag{4.99a}$$

$$\frac{\Delta^{(s)N=2,\nu=1}_{S-AS}}{\Delta^{(s)N=2,\nu=3}_{S-AS}} = 1.01, \quad \frac{\Delta^{(s)N=2,\nu=1}_{eh}}{\Delta^{(s)N=2,\nu=3}_{eh}} = 1.15, \tag{4.99b}$$

where we take $B = 10$T and $\kappa = 2.5$. The excitation energies of the spin skyrmions are strongly reduced by the screening. Note that the energies of skyrmion pairs at 1/4 and 3/4 fillings are very close ($\Delta^{(s)\nu=1}_{S-AS} \approx \Delta^{(s)\nu=3}_{S-AS}$), while the energies of quasi-particle pairs at 1/4 and 3/4 fillings are very different. In contrast, the ratios are about 1.3 for both the skyrmion pair and the quasi-particle pair in monolayer graphene (see Eq. (2.59)). The excitation energies at different filling factors can be measured in a transport experiment. Based on Eq. (4.99), we predict that the difference of the energies between 1/4 and 3/4 fillings might be used to distinguish between skyrmion and quasi-particle excitations.

Next, we study how the magnetic field affects the screening and changes the energy of a single particle excitation. We see from Fig. 4.25 that the excitation energy increases almost linearly with the magnetic field. If we do not consider screening, the Coulomb energy in a excitation state $E \propto \sqrt{B}$ since the energy scale $e^2/\kappa\ell \propto \sqrt{B}$. However, we see in Fig. 4.25, the curve of excitation energy is not proportional to $\sqrt{B}$, but is almost linear to B. In fact, the screening effect flattens the energy curve to make it proportional to B approximately. The fact that the excitation energy is linear with the magnetic field was observed in Ref. [85]. And the screening effect is indeed one of the explanations of this experimental results.

We extend our research to the higher LLs in graphene bilayer (even multi-layer graphene). The ground states indicate Ising behavior with a Z_2 symmetry of the valley pseudo-spin. We study this interesting Ising property of the material and compare with other LL Ising QHF. We also study a valley skyrmion with an extraordinary valley pseudo-spin texturein the Ising quantum Hall ferromagnetism bilayer graphene .

Conclusion

The main objective of this thesis is to study the topological solitons in monolayer and bilayer graphene. The topological solitons, especially skyrmions, associated with both density profile and (pseudo-)spin texture, were studied in the quantum Hall regions.

In graphene, the ground state at half filling in a Landau level $n > 0$ is a spin ferromagnet in the presence of a magnetic field. The excitation energies of the charged excitations are related to the resistivity R_{xx} which can be measured in transport experiments. The charged excitations in this case could be quasi-particle states or skyrmions. It is known that the skyrmion has lower energy than quasi-particle at zero Zeeman coupling up to $n = 3$ [9] in the nonlinear σ model. However, the nonlinear σ model is not valid when the Zeeman coupling is finite. Instead, we developed a microscopic Hamiltonian in the symmetric gauge to calculate the excitation energies of skyrmions and quasi-particles. At half filling in Landau level $n = 1, 2$, we compared the energy of a skyrmion with a quasi-particle at finite Zeeman coupling, and obtained the Zeeman coupling region where the spin skyrmion exists. However, in $n = 3$, the region is too small for a calculation to be valid.

Our numerical results can be compared with experimental results [12] qualitatively. However, the transport gap of skyrmions is about one order of magnitude higher than the experimental measurements, if we do not consider disorder and screening effects. In fact, the screening may be important in graphene, since the Landau gaps are much smaller than the gap between valence and conduction bands in a conventional insulator. Virtual transitions between Landau levels are strong enough to screen the Coulomb interaction effectively. We considered this Landau level screening, by calculating the static dielectric function. Then we first obtained that the transport gap is decreased significantly. Although the numerical results with screening still do not agree with the experimental results exactly, the screening effect is able to make the numerical calculations much closer to the experiments. If disorder is included, the transport gap may decrease more. Secondly, the Zeeman coupling region where skyrmions exist is also decreased a lot, about one order magnitude lower than without screening.

At 1/4 and 3/4 fillings in a Landau level, the single-particle excitation is called valley skyrmion up to $n = 3$. We studied the valley skyrmion in the Nonlinear σ model, since the effective "Zeeman" gap between two valleys is zero. The spin coherence is thus neglected since the real Zeeman coupling is large. Because of the electron-hole symmetry, it is clear that the transport gaps at the two fillings are identical, $\Delta_{1/4} = \Delta_{3/4}$. However the screening effect is stronger at 3/4 than that at 1/4, so that the electron-hole symmetry is broken by the screening. The proof of this broken symmetry is that $\Delta^{(s)}_{1/4} > \Delta^{(s)}_{3/4}$. If we consider that the disorder correction Γ in the total excitation energy is weak and is screened at the same strength as the skyrmion energy, then the numerical transport gap ratio $\Delta^{(s)}_{1/4}/\Delta^{(s)}_{3/4} = 1.3$ in Landau level $n = 1$, which is the same as the experimental results.

In Chapter 3, we study the orbital pseudo-spin textured states in graphene bilayer in an effective two-component model in which we assume $\gamma_3 = \gamma_4 = 0$. This model is particularly good for the Landau level $N = 0$ of graphene bilayer. Moreover, we discuss how γ_4 changes the phase transition of crystal phases.

A few crystal phases with valley and/or orbital pseudospin textures that can occur near the integer filling factors were presented in the Hartree-Fock approximation. The orbital skyrmion crystal can be associated with one electron per site at large bias and two electrons per site at small bias at $\tilde{\nu} = 1.2$. The $q = -2e$ skyrmion crystal is also analogous to the bubble Wigner crystal phase which is found in higher Landau levels in a conventional 2DEG. The orbital skyrmion crystals have a Wigner-crystal-like orbital pseudo-spin texture in real space representation and a skyrmion-like orbital pseudo-spin texture in the guiding-center representation.

At $\tilde{\nu} = 2.2$, we explore the checkerboard valley meron crystal at zero and small bias and another orbital skyrmion crystal at large bias. A meron is essentially half a skyrmion. At larger bias, the valley meron crystal is able to evolve to the valley skyrmion crystal. However, the electron gas is crystallized into the orbital skyrmion crystal by the orbital Dzyaloshinskii-Moriya interaction before the valley skyrmion crystal is formed. We propose a STM experiment to observe these crystal phases, which leads us to study the density of states of the crystal phases.

The orbital skyrmion crystal induced by the Dzyaloshinskii-Moriya interaction is particular interesting, since it can be an analogy of other magnetic materials [72]. Moreover, it exists even at integer filling factors. The electron gas favors a uniform state due to the exchange interaction if the two orbitals are the same. At $\nu = -1, 3$, we simplified the system as a two-level toy model to study the transport properties of the electron gas. The phase diagram contains uniform phase, orbital skyrmion crystal phase and spiral phase at different biases. We concentrate on the density of states, collective modes and absorptions of the crystal phase. There is a gapless phonon mode corresponding to the density wave. The dispersion is isotropic, which is similar to a Wigner crystal. It also contains a pseudo-spin $x - y$ mode gapped by the Dzyaloshinskii-Moriya term, which is gapless in a spin skyrmion crystal. The frequency of electromagnetic absorption is calculated in the microwave region.

In the last chapter, we considered the ground state and the single-particle excitations in higher Landau levels of graphene bilayer. We studied the system in the four-band model in which we take $\gamma_3 = 0$, since the effective two-band model is not exact in higher Landau levels. Moreover, the eigen-energies and eigenvectors of the four-band model are verified to be very good approximations when the Landau level is not very high.

The ground states at 1/4 and 3/4 fillings in Landau levels $n = 1, 2, 3$ were first studied. We obtained a Z_2 symmetry of valley pseudo-spin in the ground states at 1/4 filling. In this case, the ground state is an Ising quantum Hall ferromagnet. Furthermore, we notice that the Ising ferromagnet does not only exist in graphene bilayer, but also generally in higher LLs in chiral stacking multi-layer graphene. At finite temperature, the domain walls in the system lead to a conductivity spike [80], which has been observed in experiment [77].

We extract the nonlinear σ model for the two-spin system in an arbitrary valley. In contrast with monolayer graphene, the spin skyrmions exist up to Landau level $n = 4$ in graphene bilayer, if the screening is not considered. We also study the general CP^3 skyrmion in the symmetric gauge. We find that: at small Zeeman coupling, the CP^3 skyrmion degenerates to a SSK without valley coherence, which supports our assumption in studying the nonlinear σ model. At large Zeeman coupling, the CP^3 skyrmion degenerate to a VSK without spin coherence. The valley skyrmion has a very special valley pseudo-spin texture that is different from any other skyrmion we have known. The reason of the extraordinary texture is that the orbital indices are different in the wave function spinors in the two valleys.

The Landau level screening in graphene bilayer is stronger than that in monolayer graphene. In Landau levels $|N| = 1, 2, 3$, we considered the phase transitions at different bias with screening correction. Our numerical results agree with the experiment [77] qualitatively. Then we added the screening corrections in the nonlinear σ model. We found that the screening is able to decrease the existence Landau level for the spin skyrmion, while the existence Landau level for the spin skyrmion in monolayer graphene is not changed by the screening. Furthermore, the screening effect not only decreases the transport gap significantly, but also flattens the excitation energy curve to be approximately linear to the magnetic field.

Our calculations were based on Hartree-Fock plus generalized random phase approximation approach. This method is well controlled and conserves all the conservations laws. This technique has been used widely to study the collective modes and absorptions in a variety of nonuniform phases both in theoretical and experimental aspects [10, 26, 64, 66, 75, 86, 87]. However, this approach provides the qualitative, if not quantitative, results, since the lattice quantum fluctuations are not considered. It is possible that some phases will become unstable when the fluctuations are considered. It may also be possible to find other states lower energy than what we have obtained. This consideration which is beyond my thesis could be the object of future work.

Appendix A

Program difficulties for the Laguerre polynomial

For a generalized Laguerre polynomial, $L_n^a(x)$, the value sometimes goes beyond the limit of the double precision ($L_n^a(x) > 10^{304}$), when n or x is large. Essentially, $L_n^a(x)$ is a polynomial with the highest order x^n, so $L_n^a(x)$ diverges at infinity. Nevertheless the Coulomb interaction elements never diverge, since the exponential decay inhibits the divergence. But when we calculate $L_n^a(x)$ at very large n with the GNU Scientific Library (GSL) special function, the value of $L_n^a(x)$ usually goes very large. And the function $gsl\_sf\_laguerre\_n$ in GSL is only defined as a double precision. So we have the program difficulty in calculating a large angular momentum system.

Fortunatly, we find another special function, which can reach a very large number in GSL, to replace the Laguerre polynomial. Use the confluent hypergeometric function of the second type U, or say Tricomi confluent hypergeometric function, which can be found in GSL with a very high precision format (gsl_sf_result_e10),

$$L_n^a(x) = \frac{(-1)^n}{n!} U(-n, a+1, x) \, . \tag{A.1}$$

The confluent hypergeometric function of the second type can be found, in GSL, as the function $gsl\_sf\_hyperg\_U\_int\_e10\_e$. And its value is given by two parameters, the mantissa u and the exponent b, i.e. $U = u \times 10^b$. The Coulomb interaction elements in

Eq. (2.9) can be converted to

$$\begin{aligned} V^{n_1,n_2,n_3,n_4}_{M_1,M_2,M_3,M_4} &= \frac{e^2}{\kappa\ell}\delta_{M_1-M_2+M_3-M_4}\int dk e^{-k^2}\left(\frac{k}{\sqrt{2}}\right)^{|n_1-n_2|+|n_3-n_4|+|m_1-m_2|+|m_3-m_4|} \\ & L^{|n_1-n_2|}_{\min(n_1,n_2)}\left(\frac{k^2}{2}\right)L^{|n_3-n_4|}_{\min(n_3,n_4)}\left(\frac{k^2}{2}\right)(-1)^{\min(m_1,m_2)+\min(m_3,m_4)} \\ & \frac{U\left(-\min(m_1,m_2),|m_1-m_2|+1,\frac{k^2}{2}\right)}{\sqrt{\min(m_1,m_2)!\max(m_1,m_2)!}} \\ & \frac{U\left(-\min(m_3,m_4),|m_3-m_4|+1,\frac{k^2}{2}\right)}{\sqrt{\min(m_3,m_4)!\max(m_3,m_4)!}}, \end{aligned} \tag{A.2}$$

where $m_i = M_i + n_i$. The two terms $L^{|n_1-n_2|}_{\min(n_1,n_2)}\left(\frac{k^2}{2}\right), L^{|n_3-n_4|}_{\min(n_3,n_4)}\left(\frac{k^2}{2}\right)$ are not necessary to be replaced by the confluent hypergeometric function, since the LL indices n_1, n_2, n_3, n_4 in our systems are small. Also, for the factorial, $169! > 10^{304}$. So we need to program the factorial as

$$n! = \exp\left[\sum_{i=1}^{n}\ln(i)\right]. \tag{A.3}$$

So the integrand in Eq. (A.2) should be programmed as

$$\begin{aligned} & L^{|n_1-n_2|}_{\min(n_1,n_2)}\left(\frac{k^2}{2}\right)L^{|n_3-n_4|}_{\min(n_3,n_4)}\left(\frac{k^2}{2}\right)(-1)^{\min(m_1,m_2)+\min(m_3,m_4)}\,u(m_1,m_2,k)\,u(m_3,m_4,k) \\ & \times\exp\left\{-k^2+(|n_1-n_2|+|n_3-n_4|+|m_1-m_2|+|m_3-m_4|)\ln\left(\frac{k}{\sqrt{2}}\right)\right. \\ & +\left[b(m_1,m_2,k)+b(m_3,m_4,k)\right]\ln 10 \\ & \left.-\frac{1}{2}\left[\sum_{i=1}^{\min(m_1,m_2)}\ln(i)+\sum_{i=1}^{\max(m_1,m_2)}\ln(i)+\sum_{i=1}^{\min(m_3,m_4)}\ln(i)+\sum_{i=1}^{\max(m_3,m_4)}\ln(i)\right]\right\}, \end{aligned} \tag{A.4}$$

where we define

$$U\left(-\min(m_1,m_2),|m_1-m_2|+1,\frac{k^2}{2}\right) = u(m_1,m_2,k)\times 10^{b(m_1,m_2,k)}, \tag{A.5}$$

$$U\left(-\min(m_3,m_4),|m_3-m_4|+1,\frac{k^2}{2}\right) = u(m_3,m_4,k)\times 10^{b(m_3,m_4,k)}. \tag{A.6}$$

Appendix B

Positive background of bilayer graphene

When we derive the Hamiltonian in bilayer graphene, we should figure out the background effects. Usually, in a bilayer system, the capacity energy arises from the interaction with the background. And the capacity energy, sometimes, plays an important role in the phase diagram of the system. We suppose that the positive charge is distributed on the background homogeneously on the planes $z = \pm d/2$. Suppose the density of positive charge on each plane is $n_0/2$, and the area of the sample is S, so the neutral condition gives

$$n_0 S = \nu N_\phi, \tag{B.1}$$

where ν is the filling factor and N_ϕ is the degeneracy of the Landau level. Here we do not consider Landau level mixing, and only the highest Landau level which is fully or partly filled is taken into account. We write the Hamiltonian related to the background as

$$H_+ = H_{+,+} + H_{e,+}, \tag{B.2}$$

where $H_{+,+}$ remarks the background-background interaction and $H_{e,+}$ remarks the electron-background interaction.

$H_{+,+}$ term contains the intra-layer and inter-layer interactions, U_{intra} and U_{inter} respectively. For the intra-layer term,

$$\begin{aligned} U_{intra} &= \frac{1}{2}\int d\mathbf{r}d\mathbf{r}'\frac{n_0^2}{4}e^2V\left(\mathbf{r}-\mathbf{r}'\right) \\ &= \frac{1}{4}\frac{1}{S}\sum_{\mathbf{q}}\int d\mathbf{r}d\mathbf{r}'n_0^2\frac{2\pi e^2}{\kappa q}e^{i\mathbf{q}\cdot(\mathbf{r}-\mathbf{r}')} \\ &= \frac{1}{4}Sn_0^2V\left(q=0\right), \end{aligned} \tag{B.3}$$

where the Coulomb potential, in this system is given by

$$V\left(\mathbf{u}-\mathbf{u}'\right)=\frac{1}{S}\sum_{\mathbf{q}}\frac{2\pi e^2}{\kappa q}e^{i\mathbf{q}\cdot(\mathbf{r}-\mathbf{r}')}e^{-q|z-z'|}. \tag{B.4}$$

and the Coulomb potential in momentum space is defiend by

$$V\left(\mathbf{q}\right)=\frac{2\pi e^2}{\kappa q}, \tag{B.5}$$

where κ is the dielectric constant. And for the inter-layer term,

$$\begin{aligned} U_{inter} &= \int d\mathbf{r}d\mathbf{r}'\frac{n_0^2}{4}\frac{1}{S}\sum_{\mathbf{q}}e^{i\mathbf{q}\cdot(\mathbf{r}-\mathbf{r}')}e^{-qd} \\ &= \frac{Sn_0^2}{4}\sum_{\mathbf{q}}\frac{2\pi e^2}{\kappa q}e^{-qd}\delta_{q,0} \\ &= \frac{Sn_0^2}{4}\left[V\left(q=0\right)-\frac{2\pi e^2 d}{\kappa}\right], \end{aligned} \tag{B.6}$$

where d is the distance between two layers. Hence the background-background interaction is given by

$$H_{+,+} = 2U_{intra}+U_{inter}=\frac{1}{4}Sn_0^2\left[2V\left(q=0\right)-\frac{2\pi e^2 d}{\kappa}\right]. \tag{B.7}$$

The electron-background interaction is given by

$$H_{e,+}=-\left(h_{eR,+R}+h_{eR,+L}+h_{eL,+L}+h_{eL,+R}\right), \tag{B.8}$$

where we suppose the index R to represent the right layer associated with $\chi_R(z) =$

$\delta(z-d/2)$ and the index L to represent the left layer associated with $\chi_L(z)=\delta(z+d/2)$, respectively. In Eq. (B.8) we consider the interaction between electrons (right layer) and background (right layer) $h_{eR,+R}$, between electrons (right layer) and background (left layer) $h_{eR,+L}$, between electrons (left layer) and background (right layer) $h_{eL,+R}$, and between electrons (left layer) and background (left layer) $h_{eL,+L}$. Then we calculate one by one.

$$\begin{aligned} h_{eR,+R} &= \sum_i \int d\mathbf{u}d\mathbf{u}' \frac{n_0}{2} \Psi^\dagger_{i,R}(\mathbf{u})\,\Psi_{i,R}(\mathbf{u})\, e^2 V(\mathbf{u}-\mathbf{u}') \qquad \text{(B.9)} \\ &= \frac{n_0}{2}\sum_i c_i^\dagger c_i \int dz dz' \chi_R^*(z)\,\chi_R(z) \int d\mathbf{r}d\mathbf{r}' \Phi^*_{i,R}(\mathbf{r})\,\Phi_{i,R}(\mathbf{r}) \frac{1}{S}\sum_{\mathbf{q}} \frac{2\pi e^2}{\kappa q} e^{i\mathbf{q}\cdot(\mathbf{r}-\mathbf{r}')} e^{-q|z-z'|}, \end{aligned}$$

where i here is the valley-spin-guiding-center combination index $i=(k,s,X)$, and Φ is the wave function spinor in the layer R. If we define the density function for electrons,

$$n_{iR,iR}(\mathbf{r}) = \Phi^*_{i,R}(\mathbf{r})\,\Phi_{i,R}(\mathbf{r})\,, \tag{B.10}$$

$$n_{iR,iR}(\mathbf{q}) = \int d\mathbf{r}\Phi^*_{i,R}(\mathbf{r})\, e^{-i\mathbf{q}\cdot\mathbf{r}}\Phi_{i,R}(\mathbf{r})\,, \tag{B.11}$$

and use

$$\int dz\chi_R^*(z)\,\chi_R(z)\left|z-\frac{d}{2}\right| = 0, \tag{B.12}$$

then we obtain

$$h_{eR,+R} = \frac{n_0}{2}\sum_i c_i^\dagger c_i V(q=0)\, n_{iR,iR}(q=0)\,. \tag{B.13}$$

In the same way,

$$h_{eL,+L} = \frac{n_0}{2}\sum_i c_i^\dagger c_i V(q=0)\, n_{iL,iL}(q=0)\,. \tag{B.14}$$

For the inter-layer electron-background interaction, we have

$$\begin{aligned} h_{eR,+L} &= \frac{n_0}{2}\sum_i c_i^\dagger c_i \int dz\chi_R^*(z)\,\chi_R(z) \int d\mathbf{r}d\mathbf{r}' \Phi^*_{i,R}(\mathbf{r})\,\Phi_{i,R}(\mathbf{r}) \frac{1}{S}\sum_{\mathbf{q}} \frac{2\pi e^2}{\kappa q} e^{i\mathbf{q}\cdot(\mathbf{r}-\mathbf{r}')} e^{-q\left|z+\frac{d}{2}\right|} \\ &= \frac{n_0}{2}\sum_i c_i^\dagger c_i V(q=0)\, n_{iR,iR}(q=0) - \frac{n_0}{2}\frac{2\pi e^2 d}{\kappa}\sum_i c_i^\dagger c_i n_{iR,iR}(q=0)\,, \qquad \text{(B.15)} \end{aligned}$$

where we use

$$\int dz\chi_R(z)\,|z+d/2|\,\chi_R(z) = d. \tag{B.16}$$

In the same manner,

$$h_{eL,+R} = \frac{n_0}{2}\sum_i c_i^\dagger c_i V\left(q=0\right) n_{iL,iL}\left(q=0\right) - \frac{n_0}{2}\frac{2\pi e^2 d}{\kappa}\sum_i c_i^\dagger c_i n_{iL,iL}\left(q=0\right). \tag{B.17}$$

Combine them together, we obtain the electron-background interaction

$$H_{e,+} = n_0\left[\frac{\pi e^2 d}{\kappa} - V\left(q=0\right)\right]\sum_i \left[n_{iR,iR}\left(q=0\right) + n_{iL,iL}\left(q=0\right)\right] c_i^\dagger c_i. \tag{B.18}$$

So the positive back ground brings an extra term in the Coulomb interaction Hamiltonian,

$$\begin{aligned} H_+ &= H_{+,+} + H_{e,+} = n_0\left[\frac{\pi e^2 d}{\kappa} - V\left(q=0\right)\right]\sum_i\sum_{j=R,L} n_{ij,ij}\left(q=0\right) c_i^\dagger c_i \\ &\quad + \frac{1}{2} S n_0^2\left[V\left(q=0\right) - \frac{\pi e^2 d}{\kappa}\right]. \end{aligned} \tag{B.19}$$

Based on the normalization condition of the wave function, we get

$$\begin{aligned} \sum_i\sum_{j=R,L} n_{ij,ij}\left(q=0\right) c_i^\dagger c_i &= \sum_i c_i^\dagger c_i \sum_{j=R,L}\int d\mathbf{r}\Phi_{i,j}^*\left(\mathbf{r}\right)\Phi_{i,j}\left(\mathbf{r}\right) \\ &= \sum_i c_i^\dagger c_i \\ &= N_\phi \sum_{k,s}\rho_{(k,s);(k,s)}\left(\mathbf{q}=\mathbf{0}\right), \end{aligned} \tag{B.20}$$

where ρ is the density operator defined in Eq. (4.6). Drop the constant term, we finally obtain the background effect,

$$H_+ = n_0 N_\phi\left[\frac{\pi e^2 d}{\kappa} - V\left(q=0\right)\right]\sum_{k,s}\rho_{(k,s);(k,s)}\left(\mathbf{q}=\mathbf{0}\right) + \frac{1}{2} S n_0^2 V\left(q=0\right). \tag{B.21}$$

This term, actually, should cancel the Hartree term at $q=0$ partly, which means the divergency in both two terms should cancel each other, and the left part is the so-called capacitive energy.

Bibliography

[1] K. S. Novoselov, A. K. Geim, S. V. Morozov, D. Jiang, Y. Zhang, S. V. Dubonos, I. V. Grigorieva, and A. A. Firsov, *Electric Field Effect in Atomically Thin Carbon Films.* Sience **306**, 666 (2004).

[2] N. D. Mermin, H. Wagner, *Absence of Ferromagnetism or Antiferromagnetism in One- or Two-Dimensional Isotropic Heisenberg Models.* Phys. Rev. Lett. **17**, 1133-1136 (1966).

[3] M. I. Katsnelson, K. S. Novoselov and A. K. Geim, *Chiral tunnelling and the Klein paradox in graphene.* Nature Phys. **2**, 620 (2006).

[4] Kentaro Nomura and Allan H. MacDonald, *Quantum Hall Ferromagnetism in Graphene.* Phys. Rev. Lett. **96**, 256602 (2006).

[5] Y. Zhang, Z. Jiang, J. P. Small, M. S. Purewal, Y.-W. Tan, M. Fazlollahi, J. D. Chudow, J. A. Jaszczak, H. L. Stormer, and P. Kim, *Landau-Level Splitting in Graphene in High Magnetic Fields.* Phys. Rev. Lett. **96**, 136806 (2006).

[6] K. S. Novoselov, Z. Jiang, Y. Zhang, S. V. Morozov, H. L. Stormer, U. Zeitler, J. C. Maan, G. S. Boebinger, P. Kim, and A. K. Geim, *Room-Temperature Quantum Hall Effect in Graphene.* Science **315**, 1379 (2007).

[7] K. v. Klitzing, G. Dorda, and M. Pepper, *New Method for High-Accuracy Determination of the Fine-Structure Constant Based on Quantized Hall Resistance.* Phys. Rev. Lett. **45**, 494-497 (1980).

[8] A. H. Castro Neto, F. Guinea, N. M. R. Peres, K. S. Novoselov, and A. K. Geim, *The electronic properties of graphene.* Rev. Mod. Phys. **81**, 109 (2009).

[9] Kun Yang, S. Das Sarma, A. H. MacDonald, *Collective modes and skyrmion excitations in graphene SU(4) quantum Hall ferromagnets.* Phys. Rev. B **74**, 075423 (2006).

[10] S. E. Barrett, G. Dabbagh, L. N. Pfeiffer, K. W. West, and R. Tycko, *Optically Pumped NMR Evidence for Finite-Size Skyrmions in GaAs Quantum Wells near Landau Level Filling* $\nu = 1$. Phys. Rev. Lett. **74**, 5112 (1995).

[11] Y. P. Shkolnikov, S. Misra, N. C. Bishop, E. P. de Poortere, and M. Shayegan, *Observation of Quantum Hall "Valley Skyrmions".* Phys. Rev. Lett. **95**, 066809 (2005).

[12] A. F. Young, C. R. Dean, L. Wang, H. Ren, P. Cadden-Zimansky, K. Watanabe, T. Taniguchi, J. Hone, K. L. Shepard, and P. Kim, *Spin and valley quantum Hall ferromagnetism in graphene.* Nat. Phys. **8**, 550 (2012).

[13] J. Lambert and R. Côté, *Quantum Hall ferromagnetic phases in the Landau level* $N = 0$ *of a graphene bilayer.* Phys. Rev. B **87**, 115415 (2013).

[14] D. A. Abanin, S. A. Parameswaran, and S. L. Sondhi, *Charge* $2e$ *Skyrmions in Bilayer Graphene.* Phys. Rev. Lett. **103**, 076802 (2009).

[15] M. O. Goerbig, *Electronic properties of graphene in a strong magnetic field.* Rev. Mod. Phys. **83**, 1193 (2011).

[16] Y. Barlas, K. Yang and A. H. MacDonald, *Quantum Hall Effects in Graphene-Based Two-Dimensional Electron Systems.* Nanotechnology **23**, 052001 (2012).

[17] D. Yoshioka, *The Quantum Hall Effect.* Springer-Verlag, Berlin (2002).

[18] E. V. Castro, K. S. Novoselov, S. V. Morozov, N. M. R. Peres, J. M. B. Lopes dos Santos, J. Nilsson, F. Guinea, A. K. Geim, and A. H. Castro Neto, *Electronic properties of a biased graphene bilayer.* J. Phys.: Condens. Matter **22**, 175503 (2010).

[19] B. Partoens and F. M. Peeters, *From graphene to graphite: Electronic structure around the K point.* Phys. Rev. B **74**, 075404 (2006).

[20] J.-C. Charlier, X. Gonze, and J.-P. Michenaud, *First-principles study of the electronic properties of graphite.* Phys. Rev. B **43**, 4579 (1991).

[21] Edward McCann and Vladimir I. Fal'ko, *Landau-Level Degeneracy and Quantum Hall Effect in a Graphite Bilayer.* Phys. Rev. Lett. **96**, 086805 (2006).

[22] Benjamin E. Feldman, Jens Martin, and Amir Yacoby, *Broken-symmetry states and divergent resistance in suspended bilayer graphene.* Nat. Phys. **5**, 889 (2009); Y. Zhao, P. Cadden-Zimansky, Z. Jiang, and P. Kim, *Symmetry Breaking in the Zero-Energy Landau Level in Bilayer Graphene.* Phys. Rev. Lett. **104**, 066801 (2010).

[23] K. S. Novoselov, E. McCann, S. V. Morozov, V. I. Fal'ko, M. I. Katsnelson, U. Zeitler, D. Jiang, F. Schedin and A. K. Geim, *Unconventional quantumHall effect and Berry's phase of* 2π *in bilayer graphene.* Nature Phys. **2**, 177 (2006).

[24] S. L. Sondhi, A. Karlhede, S. A. Kivelson and E. H. Rezayi, *Skyrmions and the crossover from the integer to fractional quantum Hall effect at small Zeeman energies.* Phys. Rev. B **47**, 16419 (1993).

[25] R. Côté, *Methode.* Unpublished.

[26] R. Côté and A. H. MacDonald, *Collective modes of the two-dimensional Wigner crystal in a strong magnetic field.* Phys. Rev. B **44**, 8759 (1991); *Phonons as collective modes: The case of a two-dimensional Wigner crystal in a strong magnetic field.* Phys. Rev. Lett. **65**, 2662 (1990).

[27] Zyun F. Ezawa, *Quantum Hall Effects: Field Theoretical Approach and Related Topics, Second Edition.* World Scientific, Singapour (2007).

[28] R. Rajaraman, *Solitons and Instantons.* North-Holland, Amsterdam (1989).

[29] Wenchen Luo, R. Côté, *Zeeman coupling and screening corrections to skyrmion excitations in graphene.* Phys. Rev. B **88**, 115417 (2013).

[30] L. Brey, H. A. Fertig, R. Côté, and A. H. MacDonald, *Charged pseudospin textures in double-layer quantum Hall systems: Bimerons and meron crystals.* Phys. Rev. B **54**, 16888 (1996).

[31] I. Mihalek and H. A. Fertig, *Landau-level mixing and skyrmion stability in quantum Hall ferromagnets.* Phys Rev. B **62**, 13573 (2000).

[32] H. A. Fertig, Luis Brey, R. Côté, A. H. MacDonald, A. Karlhede, and S. L. Sondhi, *Hartree-Fock theory of Skyrmions in quantum Hall ferromagnets.* Phys. Rev. B **55**, 10671 (1997).

[33] K. Moon, H. Mori, Kun Yang, S. M. Girvin, A. H. MacDonald, L. Zheng, D. Yoshioka, and Shou-Cheng Zhang, *Spontaneous interlayer coherence in double-layer quantum Hall systems: Charged vortices and Kosterlitz-Thouless phase transitions.* Phys. Rev. B **51**, 5138 (1995).

[34] M. O. Goerbig, R. Moessner, and B. Douçot, *Electron interactions in graphene in a strong magnetic field.* Phys. Rev. B **74**, 161407(R) (2006).

[35] X.-G. Wu and S. L. Sondhi, *Skyrmions in higher Landau levels.* Phys. Rev. B **51**, 14725 (1995).

[36] Naokazu Shibata and Kentaro Nomura, *Coupled charge and valley excitations in graphene quantum Hall ferromagnets.* Phys. Rev. B **77**, 235426 (2008); J. Phys. Soc. Jpn. 78, 104708 (2009).

[37] Csaba Töke, P. E. Lammert, V. H. Crespi, and J. K. Jain, *Fractional quantum Hall effect in graphene.* Phys. Rev. B **74**, 235417 (2006).

[38] R. Côté, J.-F. Jobidon, and H. A. Fertig, *Skyrme and Wigner crystals in graphene.* Phys. Rev. B **78**, 085309 (2008).

[39] B. Douçot, M. O. Goerbig, P. Lederer, and R.Moessner, *Saturation of spin-polarized current in nanometer scale aluminum grains.* Phys. Rev. B **78**, 195327 (2008).

[40] H. A. Fertig, L. Brey, R. Côté, and A. H. MacDonald, *Charged spin-texture excitations and the Hartree-Fock approximation in the quantum Hall effect.* Phys. Rev. B **50**, 11018 (1994).

[41] Wenchen Luo, *Topological excitations in monolayer and bilayer graphene.* Master thesis, (2009).

[42] J. G. Checkelsky, L. Li, and N. P. Ong, *Zero-Energy State in Graphene in a High Magnetic Field.* Phys. Rev. Lett. **100**, 206801 (2008); X. Du, I. Skachko, F. Duerr, A. Luican, and E. Y. Andrei, *Fractional quantum Hall effect and insulating phase of Dirac electrons in graphene.* Nature (London) **462**, 192 (2009); J. G. Checkelsky, L. Li, and N. P. Ong, *Divergent resistance at the Dirac point in graphene: Evidence for a transition in a high magnetic field.* Phys. Rev. B **79**, 115434 (2009); L. Zhang, J. Camacho, H. Cao, Y. P. Chen, M. Khodas, D. E. Kharzeev, A. M. Tsvelik, T. Valla, and I. A. Zaliznyak, *Breakdown of the* $N = 0$ *quantum Hall state in graphene: Two insulating regimes. ibid.* **80**, 241412 (2009); L. Zhang, Y. Zhang, M. Khodas, T. Valla, and I. A. Zaliznyak, *Metal to Insulator Transition on the N=0 Landau Level in Graph.* Phys. Rev. Lett. **105**, 046804 (2010).

[43] A. H. MacDonald and S. M. Girvin, *Quasiparticle states in the fractional quantum Hall effect.* Phys. Rev. B **34**, 5639 (1986).

[44] S. Melinte, E. Grivei, V. Bayot, and M. Shayegan, *Heat Capacity Evidence for the Suppression of Skyrmions at Large Zeeman Energy.* Phys. Rev. Lett. **82**, 2764 (1999).

[45] Norio Kumada, Anju Sawada, Zyun F. Ezawa, Satoshi Nagaham, Hirofumi Azuhata, Koji Muraki, Tadashi Saku, and Yoshiro Hirayama, *Doubly Enhanced Skyrmions in* $\nu = 2$ *Bilayer Quantum Hall States.* J. Phys. Soc. Jpn. **69**, 3178 (2000).

[46] E. V. Gorbar, V. P. Gusynin, V. A. Miransky, and I. A. Shovkovy, *Broken symmetry* $\nu = 0$ *quantum Hall states in bilayer graphene: Landau level mixing and dynamical screening.* Phys. Rev. B **85**, 235460 (2012).

[47] Jiamin Xue, Javier Sanchez-Yamagishi, Danny Bulmash, Philippe Jacquod, Aparna Deshpande, K. Watanabe, T. Taniguchi, Pablo Jarillo-Herrero and Brian J. LeRoy, *Scanning tunnelling microscopy and spectroscopy of ultra-flat graphene on hexagonal boron nitride.* Nature Materials **10**, 282-285 (2011).

[48] K. Shizuya, *Electromagnetic response and effective gauge theory of graphene in a magnetic field.* Phys. Rev. B **75**, 245417 (2007); R. Roldán, M. O. Goerbig, and J.-N. Fuchs, *The magnetic field particle-hole excitation spectrum in doped graphene*

and in a standard two-dimensional electron gas. Semicond. Sci. Technol. **25**, 034005 (2010).

[49] I. L. Aleiner and L. I. Glazman, *Two-dimensional electron liquid in a weak magnetic field.* Phys. Rev. B **52**, 11296 (1995).

[50] Michael M. Fogler, *High Magnetic Fields: Applications in Condensed Matter Physics and Spectroscopy*, edited by C. Berthier, L.-P. Levy, and G. Martinez, Springer-Verlag, Berlin (2002).

[51] Y. Barlas, R. Côté, K. Nomura, and A. H. MacDonald, *Intra-Landau-Level Cyclotron Resonance in Bilayer Graphene.* Phys. Rev. Lett. **101**, 097601 (2008).

[52] Y. Barlas, R. Côté, J. Lambert, and A. H. MacDonald, *Anomalous Exciton Condensation in Graphene Bilayers.* Phys. Rev. Lett. **104**, 096802 (2010).

[53] R. Côté, Jules Lambert, Y. Barlas, and A. H. MacDonald, *Orbital order in bilayer graphene at filling factor* $\nu = -1$. Phys. Rev. B **82**, 035445 (2010).

[54] E. McCann, *Asymmetry gap in the electronic band structure of bilayer graphene.* Phys. Rev. B **74**, 161403(R) (2006).

[55] S. Ghosh and R. Rajaraman, *Quantum Hall solitons with intertwined spin and pseudospin at* $\nu = 1$. Phys. Rev. B **63**, 035304 (2000).

[56] J. Bourassa, B. Roostaei, R. Côté, H. A. Fertig, and K. Mullen, *Pseudospin vortex-antivortex states with interwoven spin textures in double-layer quantum Hall systems.* Phys. Rev. B **74**, 195320 (2006).

[57] C.-H. Zhang and Y. N. Joglekar, *Wigner crystal and bubble phases in graphene in the quantum Hall regime.* Phys. Rev. B **75**, 245414 (2007); *Influence of Landau-level mixing on Wigner crystallization in graphene.* **77**, 205426 (2008).

[58] K. Shizuya, *Pseudo-zero-mode Landau levels and collective excitations in bilayer graphene.* Phys. Rev. B **79**, 165402 (2009).

[59] R. Côté, Wenchen Luo, Branko Petrov, Yafis , and A. H. MacDonald, *Orbital and interlayer skyrmion crystals in bilayer graphene.* Phys. Rev. B **82**, 245307 (2010).

[60] D. S. L. Abergel and V. I. Fal'ko, *Optical and magneto-optical far-infrared properties of bilayer graphene.* Phys. Rev. B **75**, 155430 (2007); D. S. L. Abergel and T. Chakraborty, *Long-Range Coulomb Interaction in Bilayer Graphene.* Phys. Rev. Lett. **102**, 056807 (2009).

[61] D. Lilliehöök, K. Lejnell, A. Karlhede, and L. Sondhi, *Quantum Hall Skyrmion with Higher Topologicla Charge.* arXiv:cond-mat/9704121v1 (1997).

[62] D. Lilliehöök, *Inter-Landau-level skyrmions versus quasielectrons in the $\nu = 2$ quantum Hall effect.* Phys. Rev. B **62**, 7303 (2000).

[63] Yu. V. Nazarov and A. V. Khaetskii, *Quantum Phase Transition in the Skyrmion Lattice.* Phys. Rev. Lett. **80**, 576 (1998).

[64] L. Brey, H. A. Fertig, R. Côté, and A. H. MacDonald, *Skyrme Crystal in a Two-Dimensional Electron Gas.* Phys. Rev. Lett. **75**, 2562 (1995).

[65] A. A. Koulakov, M. M. Fogler, and B. I. Shklovskii, *Charge Density Wave in Two-Dimensional Electron Liquid in Weak Magnetic Field.* Phys. Rev. Lett. **76**, 499 (1996); M. M. Fogler, A. A. Koulakov, and B. I. Shklovskii, *Ground state of a two-dimensional electron liquid in a weak magnetic field.* Phys. Rev. B **54**, 1853 (1996); R. Moessner and J. T. Chalker, *Exact results for interacting electrons in high Landau levels. ibid.* **54**, 5006 (1996); M. M. Fogler and A. A. Koulakov, *Laughlin liquid to charge-density-wave transition at high Landau levels. ibid.* **55**, 9326 (1997).

[66] R. Côté, C. B. Doiron, J. Bourassa, and H. A. Fertig, *Dynamics of electrons in quantum Hall bubble phases.* Phys. Rev. B **68**, 155327 (2003).

[67] L. Brey, H. A. Fertig, R. Côté, and A. H. MacDonald, *Skyrme and meron crystals in quantum Hall ferromagnets.* Phys. Scr., **T66**, 154 (1996).

[68] O. Poplavskyy, M. O. Goerbig, and C. Morais Smith, *Local density of states of electron-crystal phases in graphene in the quantum Hall regime.* Phys. Rev. B **80**, 195414 (2009).

[69] Yafis Barlas, R. Côté, and Maxime Rondeau, *Quantum Hall to Charge-Density-Wave Phase Transitions in ABC-Trilayer Graphene.* Phys. Rev. Lett. **109**, 126804 (2012).

[70] R. Côté, J. P. Fouquet, and Wenchen Luo, *Biased bilayer graphene as a helical quantum Hall ferromagnet.* Phys. Rev. B **84**, 235301 (2011).

[71] I. Dzyaloshinskii, J. Phys. Chem. Solids **4**, 241 (1958); T. Moriya, *Anisotropic Superexchange Interaction and Weak Ferromagnetism.* Phys. Rev. **120**, 91 (1960).

[72] X. Z. Yu, Y. Onose, N. Kanazawa, J. H. Park, J. H. Han, Y. Matsui, N. Nagaosa, and Y. Tokura, *Real-space observation of a two-dimensional skyrmion crystal.* Nature (London) **465**, 901 (2010).

[73] Jung Hoon Han, Jiadong Zang, Zhihua Yang, Jin-Hong Park, and Naoto Nagaosa, *Skyrmion lattice in a two-dimensional chiral magnet.* Phys. Rev. B **82**, 094429 (2010).

[74] Jin-Hong Park and Jung Hoon Han, *Zero-temperature phases for chiral magnets in three dimensions.* Rev. Rev. B **83**, 184406 (2011).

[75] R. Côté, A. H. MacDonald, Luis Brey, H. A. Fertig, S. M. Girvin, and H. T. C. Stoof, *Collective Excitations, NMR, and Phase Transitions in Skyrme Crystals.* Phys. Rev. Lett. **78**, 4825 (1997).

[76] R. Côté and Manuel Barrette, *Validity of the two-component model of bilayer and trilayer graphene in a magnetic field.* Phys. Rev. B **88**, 245445 (2013).

[77] Kayoung Lee, B. Fallahazad, J. Xue, T. Taniguchi, K. Watanabe, E. Tutuc, *Chemical potential and quantum Hall ferromagnetism in bilayer graphene mapped using double bilayer heterostructures.* arXiv:1401.0659, (2014).

[78] Wenchen Luo, R. Côté and Alexandre Bédard-Vallée, to be published.

[79] Vladimir I. Fal'ko and S. V. Iordanskii, *Topological defects and goldstone excitations in Domain walls between ferromagnetic quantum Hall liquids.* Phys. Rev. Lett. **82**, 402 (1999).

[80] T. Jungwirth and A. H. MacDonald, *Resistance spikes and domain loops in Ising quantum Hall ferromagnets.* Phys. Rev. Lett. **87**, 216801 (2001).

[81] E. P. De Poortere, E. Tutuc, S. J. Papadakis, M. Shayegan, *Resistance Spikes at Transitions Between Quantum Hall Ferromagnets.* Science **290**, 1546 (2000).

[82] Koji Muraki, Tadashi Saku, and Yoshiro Hirayama, *Charge excitations in easy-axis and easy-plane quantum Hall ferromagnets.* Phys. Rev. Lett. **87**, 196801 (2001).

[83] Hongki Min and A. H. MacDonald, *Chiral decomposition in the electronic structure of graphene multilayers.* Phys. Rev. B **77**, 155416 (2008).

[84] T. Misumi and K. Shizuya, *Electromagnetic response and pseudo-zero-mode Landau levels of bilayer graphene in a magnetic field.* Phys. Rev. B **77**, 195423 (2008).

[85] J. Martin, B. E. Feldman, R. T. Weitz, M. T. Allen, and A. Yacoby, *Local Compressibility Measurements of Correlated States in Suspended Bilayer Graphene.* Phys. Rev. Lett. **105**, 256806 (2010).

[86] R. Tycko, S. E. Barrett, G. Dabbagh, L. N. Pfeiffer, and K.W.West, *Electronic states in gallium arsenide quantum wells probed by optically pumped NMR.* Science **268**, 1460 (1995).

[87] R. M. Lewis, Yong Chen, L. W. Engel, D. C. Tsui, P. D. Ye, L. N. Pfeiffer, and K. W. West, *Evidence of a First-Order Phase Transition Between Wigner-Crystal and Bubble Phases of 2D Electrons in Higher Landau Levels.* Phys. Rev. Lett. **93**, 176808 (2004).